Rare-earth ion doped chalcogenide waveguide amplifiers

Kunlun Yan

May 2018

A thesis submitted for the degree of Doctor of Philosophy of
The Australian National University

Laser Physics Centre
Research School of Physics and Engineering
College of Physical and Mathematical Sciences
The Australian National University

© Copyright by Kunlun Yan 2018
All Rights Reserved

Declaration

The contents of this thesis are the result of original research and have not been submitted for a higher degree to any other university or institution. This thesis is entirely my own work, unless explicitly stated otherwise.

Kunlun Yan

May 2018

Kunlun Yan

Acknowledgements

I would like to express my sincere gratitude to my supervisors A/Prof. Steve Madden, Dr. Rongping Wang and Prof. Barry Luther-Davies, for their continuous support of my Ph.D study and related research. This thesis could not have been possible without their guidance and support. For everything you’ve done for me, thank you.

My sincere thank also goes to Dr. Khu Vu who guided me and gave me suggestions from the first day I entered Laser Physics Centre till now. I would like to thank Dr. Duk for his help in waveguide fabrication, and thank Dr. Zhingyong Yang for glass fabrication.

I thank our technical staff Sukanta for his help in film deposition, Craig and John for their assistance in fixing equipments used in the lab. I also thank our department administrator Sonia for her kind help. Also, I want to acknowledge my colleagues in ANFF for providing the fabrication facility.

I am very grateful to have a group of friend, Xin Gai, Ivy, Joseph, Ting Wang, Niko, Zhisong Qu, they make my student life so much more enjoyable.

Last, I would like to thank my family. Thank my parents for their tireless love and support over these years. Thank my beloved wife Pan for her encouragement, constant support and love. Thank you.

Publications

1. **Kunlun Yan**, Khu Vu, Rongping Wang, and Steve Madden, "Greater than 50% inversion in Erbium doped Chalcogenide waveguides", Optics Express, 24, 20, 23304-23313, 2016.
2. **Kunlun Yan**, Khu Vu, and Steve Madden, “Internal gain in Er-doped As_2S_3 chalcogenide planar waveguides”, Optics Letters, 40, 5, 796-799, 2015.
3. **Kunlun Yan**, Khu Vu, Zhiyong Yang, Rongping Wang, Sukanta Debbarma, Barry Luther-Davies, and Steve Madden. “Emission properties of erbium-doped Ge-Ga-Se glasses, thin films and waveguides for laser amplifiers”, Optical Materials Express, 4, 3, 464-475, 2014.
4. **Kunlun Yan**, Rongping Wang, Khu Vu, Robert Elliman, Kidane Belay and Barry Luther-Davies. “Photoluminescence in Er-doped Ge-As-Se Chalcogenide Thin Films”, Optical Materials Express, 2, 9, 1270-1277, 2012.
5. Rongping Wang, **Kunlun Yan**, Mingjie Zhang, Xiang Shen, Shixun Dai, Xinyu Yang, Zhiyong Yang, Anping Yang, Bin Zhang, and Barry Luther-Davies, “Chemical environment of rare earth ions in $Ge_{28.125}Ga_{6.25}S_{65.625}$ glass-ceramics doped with Dy^{3+}”, Applied Physics Letters, 107, 161901, 2015.
6. Rongping Wang, **Kunlun Yan**, Zhiyong Yang, Barry Luther-Davies, “Structural and physical properties of $Ge_{11.5}As_{24}S_{64.5-x}Se_{64.5-(1-X)}$ glasses”, Journal of Non-crystalline Solids, 427, 16-19, 2015.
7. Vu K, **Yan K**, Jin Z, Gai X, Choi D, Debbarma S, Luther-Davies B, Madden S. “Hybrid waveguide from As_2S_3 and Er-doped TeO_2 for lossless nonlinear optics”, Optics Letters, 38, 11 1766-1768, 2013.
8. Xinyu Yang, Mingjie Zhang, **Kunlun Yan**, Liyuan Han, Qin Xu, Haitao Liu, Rongping Wang, "Controllable Formation of the Crystalline Phases in Ge–Ga–S Chalcogenide Glass-Ceramics", Journal of American Ceramic Society, doi:10.1111/jace.14492

Abstract

Chalcogenide glass waveguide devices have received a great deal of attention worldwide in the last few years on account of their excellent properties and potential applications in mid-infrared (MIR) sensing and all-optical signal processing. Waveguide propagation losses, however, currently limit the potential for low power nonlinear optical processing, and the lack of suitable on chip integrated MIR sources is one of the major barriers to integrated optics based MIR sensing. One approach to overcome the losses is to employ rare-earth ion doped waveguides in which the optical gain can compensate the loss, in such a way that the conversion efficiency of nonlinear effects is increased significantly. For infrared applications, the long wavelengths potentially attainable from rare-earth ion transitions in chalcogenide hosts are unique amongst glass hosts. New rare-earth ion doped chalcogenide sources in the MIR range could benefit molecular sensing, medical laser surgery, defence etc. Despite these promising applications, until now, no one has succeeded in fabricating rare-earth ion doped chalcogenide amplifiers or lasers in planar devices.

This work develops high quality erbium ion doped chalcogenide waveguides for amplifier and laser applications. Erbium ion doped As_2S_3 films were fabricated using co-thermal evaporation. Planar waveguides with 0.35 dB/cm propagation loss were patterned using photolithography and plasma etching on an erbium ion doped As_2S_3 film with an optimised erbium ion concentration of $0.45x10^{20}$ ions/cm^3. The first demonstration of internal gain in an erbium ion doped As_2S_3 planar waveguide was performed using these waveguides. With different film deposition approaches, promising results on intrinsic lifetime of the Er^{3+} $^4I_{13/2}$ state were achieved in both $ErCl_3$ doped As_2S_3 films (2.6 ms) and radio frenquency sputtered Er^{3+}:As_2S_3 films (2.1 ms), however, no waveguide was fabricated on these films due to film quality issues and photopumped water absorption issues.

The low rare-earth ion solubility of As_2S_3 is considered the main factor limiting its performance as a host. Gallium-containing chalcogenide glasses are known to have good rare-earth ion solubility. Therefore, a new glass host material, the Ge-Ga-Se system, was investigated. Emission properties of the bulk glasses were studied as a function of erbium ion doping. A region between approximately 0.5 and 0.8 at% of Er^{3+} ion was shown to provide sufficient doping, good photoluminescence and adequate lifetime to envisage practical planar waveguide amplifier devices. Ridge waveguides based on high quality erbium ion doped Ge-Ga-Se films were patterned. Significant signal enhancement at 1540 nm was observed and 50 % erbium ion population inversion was obtained, in waveguides with Er^{3+} concentration of 1.5×10^{20} ion/cm^3. To the Author’s knowledge, this is the highest level of inversion ever demonstrated for erbium ions in a chalcogenide glass host and is an important step towards future devices operating at 1550 nm and on the MIR transitions of erbium ions in chalcogenide glass hosts. Photoinduced absorption loss caused by upconversion products in the waveguides is the remaining hurdle to achieving net gain. Further research is needed to find suitable compositions that possess high rare-earth ion solubility whilst avoiding the detrimental photoinduced losses.

Table of contents

Abbreviations

Abbreviations

AO: acousto-optic

ASE: amplified spontaneous emission

BPM: beam propagation method

CCD: charge-coupled device

CVD: chemical vapour deposition

CW: continuous wave

DI water: deionisation water

DPSD: differential power spectral density

EDS: energy dispersive x-ray spectroscopy

ESA: excited state absorption

ETU: Energy transfer up-conversion

FDM: finite difference method

FDTD: finite-difference time-domain method

FEM: The finite element method

FSO: Free-Space Optical Communication

FWHM: full width at half maximum

FWM: four wave mixing

GLS: gallium lanthanum sulfide

ICP: inductively coupled plasma

LAN: local area network

MAN: metropolitan area network

MIR: mid-infrared

MoL: method of lines

MPR: multi-phonon relaxation

NA: numerical aperture

NIR: near-infrared

NLO: nonlinear optic

OPA: optical parametric amplifier

OPO: optical parametric oscillator

OSA: optical spectrum analyser

PL: photoluminescence

PLE: photoluminescence excitation spectroscopy

PML: perfect matching layer

QCL: quantum cascade lasers

RF: radio-frequency

RIE: reactive ion etching

RMS: Root-mean-square

RMSE: root-mean-square error

SC: supercontinuum source

SEM: scanning electron microscope

TE mode: transverse electric mode

T_g: glass transition temperature

TM: transition metal

TM mode: transverse magnetic mode

TOX: thermally oxidized silicon

TV: television

UV: ultraviolet

V/A: volts/amps

WAT: weak absorption tail

WDM: wavelength division multiplexing

Chapter 1

Introduction

1.1 General introduction

1.1.1 Integrated optics

Integrated optics has been a hot topic as electronics has been slowly supplemented by, and, in some cases, even replaced by, optics particularly in telecommunications systems since the 1980s. The original inspiration for this concept came from electronic integrated circuit technology [1], which displayed phenomenal advances in technological capability and cost reduction and is now truly ubiquitous. Thus, it is easy to understand that the main objectives of integrated optics are essentially similar to those of integrated electronics, namely that bulk components can be eliminated, and multiple functionalities can be integrated on one stable robust, mass producible, low cost device. Like optical fibres, the basic concept in optical integrated circuits is light confinement. In planar waveguides, light propagates within a region embedded in a planar substrate or within a portion of a film deposited upon a planar substrate due to the higher refractive of channel to that of the substrate/surrounds. This thin film type optical circuit aims to perform multiple functions by integrating laser light sources, functional components such as switches, modulators, filters, amplifiers, interconnecting waveguides, and detectors all on single substrate. By integration, mass producible, low cost, compact, stable and highly functional optical systems can be achieved [2].

To attain the full suite of desired functions in an integrated optical device, the functions and capabilities that have to be realised in a planar geometry include:

- On chip laser source (continuous wave (CW) and mode locked) capability
- Optical amplification
- Large and ultrafast second and/or third order optical nonlinearity
- Electronic control of refractive index for tuning/switching/modulation
- Acousto-optic effects for widely tunable filters
- Tight bending capability to make compact devices
- Low loss interfaces to standard optical fibres for the spectral range of interest
- Wide transmission range

- Stable photosensitivity for performance tuning and Bragg grating devices
- Light detection capability

Realising all of these different functionalities in a single material system is extremely challenging (InP integrated technology perhaps coming closest [3]), and so hybridisation methods are likely required.

It is now that clear one key challenge is finding a host material which can enable the most critical subset of the functions mentioned above and that has a clear route to hybridise with other materials easily to obtain the rest, and also that has compatibility with current electronic fabrication technology. Additionally, it should also enable high yield, high volume, low cost production. Currently, several different materials are used in commercial high performance integrated devices, such as silicon dioxide, silicon (oxy) nitride, polymers, lithium niobate, silicon, and indium phosphide. Each material has its advantages and disadvantages. Despite the plethora of existing platforms and the massive investments currently being made, there are several technology gaps still hindering the applicability of integrated optics at a broad level i.e. beyond telecoms. These include good nonlinear optic (NLO) performance, MIR transmission, having a wide choice of gain wavelengths and usable acousto-optic (AO) capability. Chalcogenide glasses, with high refractive index, high third order nonlinearity, MIR transparency, low phonon energies, and high AO coefficients offer opportunity in all these areas. Therefore, it is worthwhile considering chalcogenide glasses as a major component in a new hybrid platform for integrated optics.

1.1.2 Highly nonlinear waveguide device limitations

Highly nonlinear waveguides fabricated from chalcogenide glasses are proving extremely effective for all-optical signal processing of high-speed telecommunications signals e.g. [4-9]. To achieve the most efficient processors, the natural response is to maximise the nonlinear response of the waveguide which requires the most nonlinear material along with a waveguide design that gives the smallest mode area. When combined these lead to a large nonlinear coefficient, γ, of the waveguide, given by equation (1.1):

$$\gamma = 2\pi n_2/\lambda A_{eff} \tag{1.1}$$

where n_2 is the third order optical nonlinearity of the material, λ denotes the wavelength of operation and A_{eff} is the mode area of the waveguide [10]. Recently reported

$Ge_{11.5}As_{24}Se_{64.5}$ (at%) nanowires ≈500×630 nm in cross-section achieved mode effective areas of 0.25 μm^2 and γ values of 130-150 $W^{-1}m^{-1}$ [11], which is amongst the highest nonlinearity reported for any materials system and is the highest for a glass based system [4]. However, nanowires experience significant propagation losses because of the strong interaction of the optical fields to the etched sidewalls even when they have been fabricated using optimized processes that produce the lowest roughness (<2 nm Root-mean-square (RMS)) [11]. Typically the losses achieved for highly nonlinear chalcogenide nanowires are >1.5 dB/cm whilst significantly lower values (<0.2 dB/cm) have been achieved in $As_{40}S_{60}$ (at%) [12, 13] with ~1 μm^2 mode effective area and 0.42 dB/cm in a sub 1 micron squared Ge-Sb-S [14] rib waveguides. However, as the nonlinear phase shift for a given amount of input power also depends on the effective length (i.e. the loss limited interaction length) then often better performance is obtained using longer lower loss devices as the γ scales almost linearly with A_{eff} (i.e. width/height) whereas the loss scales essentially exponentially with waveguide dimension [15, 16]. These losses strongly limit nonlinear performance. For example, a commonly used nonlinear process in all-optical processing is four wave mixing (FWM). Based on the analytical expression for FWM conversion efficiency from Batelgelj [17], with the assumption of negligible pump depletion, and in the low power regime at the optimum length, the converted internal signal power in a waveguide is given by equation (1. 2):

$$P_{DFWM} = \frac{4}{27}\,\eta P_S \left[\frac{\gamma P_{pump}}{a}\right]^2 \qquad (1.\ 2)$$

where P_{DFWM} is the idler power generated by a signal power P_s and a degenerate pump power P_{pump}, γ is the waveguide nonlinear parameter, η is the pump-signal frequency spacing dependent phase mismatch efficiency parameter, and a is the loss of waveguide. Clearly, from this equation there is an inverse square dependence of the overall idler conversion power on the propagation loss of waveguide, so a significant improvement can be expected at the output with waveguide loss reduction [17]. One key means of reducing loss is to compensate it with gain, and in fact performing FWM in an optical amplifier is advantageous and results in large increases in efficiency [18-23].

Thus, a method of overcoming the waveguide losses is desirable to enhance the efficiency of all-optical processing. One approach is to employ a rare-earth ion doped nonlinear waveguide in which optical gain compensates the loss. The 1.55 μm emission arising from the $^4I_{13/2} \rightarrow {}^4I_{15/2}$ transition in the trivalent state of the erbium ion has been widely used to create optical fibre and waveguide amplifiers in oxide glass hosts [24-29]. Hence it should, in principle, be possible to use gain to compensate the optical losses in a chalcogenide waveguide as a route to improving the efficiency of all-optical processing.

1.1.3 MIR sensing opportunity

One of the major challenges for MIR sensing is the availability of either high power broadband sources, or widely tunable lower power laser devices. The best known route to obtain high power and high brightness broad band sources is supercontinuum generation [30, 31]. However, to generate broadband MIR supercontinuum, it is optimal to use a pump around 4 microns with femtosecond pulses [32-34]. Currently no such commercial mode locked laser exists and so there is an opportunity for a suitable device there, especially one integrated with an SC generator. In terms of tunable devices, currently, quantum cascade lasers (QCLs) and optical parametric oscillator/amplifier (OPO and OPAs) serve as the main workhorse in MIR photonics. For QCLs, the huge amount of heat produced in CW mode laser consumes up to 70 % of the injected electrical power, with the given relatively small active area ~100 μm^2, brings challenges to realise higher power single-mode infrared light [35], although QCLs with output power up to several watts are readily available [36]. However, the narrow tuning ranges of QCLs and the fact they cannot be mode locked to generate high peak power fs pulses set limitations to their applications. OPOs that offer wide tunability and multiwatt output power are now commercially available, but the excitation required by parametric generation needs to be narrow linewidth and linear polarized, which are significant constraints on the pump [37]. Also, OPOs are always expensive and physically large.

Chalcogenide ceramic lasers based on Cr^{2+}:ZnSe are commercially available within a broad wavelength range in the near- and mid-infrared. But issues arise from thermal lensing and quenching from multiphonon emission is becoming a challenge when higher power output is required [35]. A bulk optics mode locked Cr^{2+}:ZnSe laser with pulse duration from 40-150 fs, providing over 1 W output power in the range of 2.1-2.6 μm is available from IPG Photonics, and lasers with longer operation wavelength up to 5 μm are available based on liquid nitrogen cooled Fe^{2+}:ZnSe [38].

Rare-earth ion doped devices as an alternative to the technologies discussed above have important characteristics. For example, the absorption and emission wavelengths of rare-earth ions are relatively insensitive to the host material and correspond to readily available diode laser wavelengths for low cost pumping. The metastable state lifetimes of rare-earth ions are long, and the quantum efficiency can be high. Besides this, different rare-earth ions offer the opportunity to get a wide range of emission wavelengths and often wide tuning ranges which almost cover the entire spectrum from visible to 12 μm [35, 39, 40]. Rare-earth ions also offer an excellent path for mode locking to produce high peak power ultra-short pulses on account of their large emission bandwidth, and mode locking in rare-earth ion doped fibre lasers has been extensively demonstrated and today dominates the commercial femtosecond laser market in the guise of the Yb^{3+} doped silica fibre laser.

These excellent properties lead to a significant opportunity for rare-earth ions in MIR laser/amplifier applications where there are few other options. In addition, there are numerous telecommunications based opportunities for rare-earth ion doped devices, not yet fully exploited by the now ubiquitous silica fibre based erbium ion doped optical amplifier. As an example, some of the most popular rare-earth ions with their potential lasing wavelengths in the infrared are listed in Table 1. 1.

Table 1.1 Rare-earth ions with their potential lasing wavelength from [41] with updated details in *italics*.

Rare-earth ions	IR emission wavelengths (μm)
Nd^{3+}	0.786, 0.919, 1.08, 1.37 [42]
Er^{3+}	0.822, 0.86, 0.987 [43, 44], 1.54 [45], 2.7, 3.5, 4.5 [46],
Tm^{3+}	1.21, 1.45, 1.81, 2.35 [47], (*3.8, 5.38* [48])
Ho^{3+}	0.76, 0.91 [44], 1.2, 2.9, 3.9 [49], (*2.1* [50], *3* [51])
Pr^{3+}	1.3, 1.6, 2.9, 3.4, 4.5, 4.8, 4.9, 7.2 [52, 53], (*5.5, 7.6* [54])
Dy^{3+}	1.3, 1.8, 2.3, 4.3 [55], (*3.0, 3.2, 4.5, 5.5, 7.6* [54])
Tb^{3+}	3.0, 4.8, 8.0 [46], (*10.5* [54])
Yb^{3+}	*0.975, 1.02, 1.14* [56]

It is well known that silica optical fibre becomes opaque quickly beyond 2 μm, and although laser operation up to 3.9 μm has been demonstrated in fluoride glass hosts, beyond 3 μm the multiphonon relaxation rates of fluoride glasses compete with the sharp-line luminescence. Laser emission centred at 3.5 μm with the longest wavelength emission at 3.78 μm was recently realised in an erbium ion doped ZBLAN fibre laser

[57], and 3.9 μm fibre laser was realised in a Ho^{3+}-doped ZBLAN fibre pumped by a dye laser at 640 nm [58], but no laser with longer operation wavelength than this was reported on ZBLAN so far. With rather lower phonon energies, chalcogenide glasses, therefore, offer the prospect of attaining longer wavelength higher efficiency lasing.

As noted above, there are clearly some important opportunities that could be addressed using rare-earth ion doped chalcogenide glasses, especially when the proven planar integration capabilities of chalcogenide are factored in. Therefore, rare-earth ion doped chalcogenide planar waveguides were chosen as the topic of this thesis.

1.2 Chalcogenide glasses and their applications

1.2.1 Chalcogenide glasses

A chalcogenide is a chemical compound that contains one or more of the chalcogen elements from Group 16 of the Periodic Table (normally referred as sulfur, selenium, and tellurium but excluding oxygen) covalently bonded to network formers such as arsenic, antimony, germanium, silicon, etc. The heavy elements are relatively weakly covalently bonded and this provides chalcogenide glasses with some important optical and physical properties. For example, low bond energy leads to [4, 59]:

- Chalcogenide glasses' band gaps located in the visible or near infrared.
- Relatively low glass transition temperature (T_g), from ~100-400 °C.
- Extended optical transparency (12 μm in sulfide to 20 μm in telluride).
- High polarizability leading to large second and third order optical nonlinearity.
- Low hardness offering high acousto-optic coefficients.

Typical transmission spectra of several classes of glass including chalcogenide glasses are shown in Figure 1.1. Due to large atomic masses and relatively weak bond strengths resulting in low phonon energies, chalcogenide glasses have a long wavelength cut-off that lies in the MIR [60]. The transparency edge is 12 μm for sulfide based glasses, 15 μm for selenide glasses and 20 μm for telluride glasses, whilst silica becomes opaque at 4 μm and the transparency of ZBLAN drops quickly beyond 6 μm. This offers enormous opportunities to chalcogenide glasses in MIR applications.

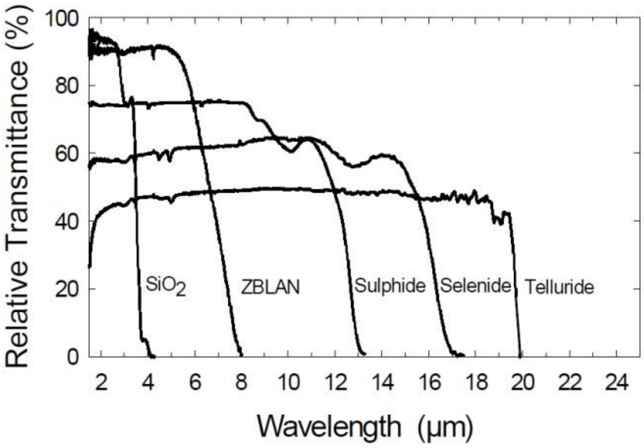

Figure 1.1 Transmission spectra for several glasses (optical path length of about 2-3 mm) [61].

There are a number of optical properties chalcogenide glasses possess that have made them of interest for several decades. High linear refractive index (2-3.5) and low absorption suggest that compact optical circuits made from sub-wavelength, single mode waveguides can be fabricated for telecommunications and MIR science. The low phonon energies present in chalcogenide glasses permit radiative transitions for rare-earth ion dopants that are not possible in silica and phosphate glasses due to multiphonon quenching, making them promising rare-earth ion host materials for IR amplifiers and lasers. The high photosensitivity present in many chalcogenide glasses enables direct optical patterning of planar waveguides, gratings and other photonic devices. The high optical non-linearity displayed by many chalcogenide glasses combined with low multi-photon absorption has been used for some of the most successful all-optical signal processing demonstrations of telecommunications signals [4, 9, 11, 62-66]. Finally, the wide range of glass-forming and compositions allow material properties to be fine-tuned for specific applications. In Table 1.2, some basic properties of chalcogenide, tellurite, silica and fluoride glasses are shown for comparison.

Table 1.2 Basic properties of chalcogenide glass in context with other optical glasses [67].

Property	Chalcogenide	Tellurite	Silica	Fluoride
Refractive index (RI)	2.1-3.5	1.8-2.3	1.46	1.5
Thermal coefficient of RI /10^{-6} °C^{-1}	~20-60 [68] (@4.515 μm)	~-20 [69] (@1.5 μm)	~12 [70] (@1 μm)	~-10 [71] (@1.53 μm)
Highest phonon energy / cm^{-1}	≥250	~800	~1000	~500
Transmission range / μm	0.8-20	0.4-5	0.2-2.5	0.2-7.0
Bandgap / eV	1-3	~3	~10	~10
Nonlinear refractive index (n_2) / m^2 W^{-1}	$3\text{-}10\times10^{-18}$	$3\text{-}6\times10^{-19}$	$1\text{-}3\times10^{-20}$	$\sim10^{-21}$
Glass transition temperature (T_g) / °C	100-400	300-450	~1000	~300
Thermal expansion /10^{-7} °C^{-1}	~140-250	120-170	~5	~150
Density / kg m^{-3}	4500	5500	2200	5000

Note: the thermal property values for chalcogenide glass change rapidly with glass composition, the values shown in this table are for representative Ge-As-Se glasses.

Amongst the properties chalcogenide glasses possess, low phonon energies, long wavelength transparency and relatively high rare-earth ion solubility make chalcogenide glasses attractive in exploring laser sources in the near and MIR range. Based on the definition in ISO 20473:2007E (Optics and photonics — Spectral bands), the MIR refers to the spectral region from 3 μm up to 50 μm [72]. However, the wavelength range of 2–25 μm covers the important atmospheric windows, and the molecular fingerprints of numerous gases, liquids and solids [39], and has gained widespread acceptance as a working definition that is used hereafter in this thesis. Laser sources working in this range have great potential applications in various fields, and these applications will be illustrated in the following section.

1.2.2 Example applications and limiting performance factors of chalcogenide glasses

Besides the applications in integrated optics, nonlinear waveguide devices and MIR sensing mentioned in the general introduction part, there are other potential applications under intensive study as well.

(a) Remote molecular sensing

The MIR between 400 and 4000 cm^{-1} (25–2.5 μm) covers the important range for vibrational spectroscopy, making MIR technology attractive for chemical or biochemical sensors. The applications here span a huge range of fields through medicine, agriculture, climate and atmospheric monitoring, industrial process control, border security, petrochemicals, water quality monitoring, etc. MIR spectroscopy has been known and used for decades in some of these areas, but field deployment has been impossible due to the lack of low power, rugged, low cost instruments. This could be overcome with planar integration.

One of the most challenging but essential parts for integrated infrared optical sensing is the light source. For bulk optics based devices the thermal Globar© source can offer light with a huge spectral range, but the brightness is not sufficient enough for applications where high spatial resolution or long distance propagation is required [73], and it is not easily planar integratable. Quantum cascade lasers (QCL) provide diffraction-limited MIR beams with high brightness, but the tuning range is quite narrow meaning multiple sources need to be flip chip bonded increasing cost and complexity.

Wideband amplified spontaneous emission (ASE) sources (potentially with multiple dopants and cascade emission) are another option for white light sources. For example, the spectral range from 1540 nm to >2340 nm at −20 dB was achieved in Tm^{3+}–Ho^{3+} co-doped alumina-rich silica core fibre [74]. An ASE emission peak at 1880 nm with a 3-dB spectral width of almost 2000 nm was generated with Bi^{3+}–Tm^{3+} co-doped lithium-alumino-germano-silicate (LAGS) core fibre [75]. Praseodymium ion in chalcogenide fibre has also been demonstrated as an ASE source, offering an emission bandwidth spanning 3 μm to 5 μm at -20 dB [40, 76] with the potential for further emissions from other energy levels. High power is also possible in the MIR with rare-earth ions. For example, broad band emission around 2 μm with Multi-Watt output power was achieved in a Tm^{3+}-doped fibre amplifier (TDFA) [77]. A 24 W liquid-cooled CW 3 μm Er^{3+}-doped ZBLAN fibre laser has also been developed [78]. ASE waveguide based sources are clearly integratable, the challenge is how to span the wide range required for sensing of a general nature, though they could be useful for sensing in specific wavebands, for example for isotopic detection of methane.

Supercontinuum (SC) sources generated from dispersion engineered chalcogenide fibres or waveguides are able to offer continuous broadband emission in the MIR range with reasonable average power. For instance, broadband supercontinuum spanning from 1.8 μm to >7.5 μm with total power ~20 mW and source brightness > ×100 that of current synchrotrons was reported from a chalcogenide waveguide excited with ~320 fs pulses at 4 μm [32]. A supercontinuum with broader band extending from ~2 μm to >10 μm generated using a chalcogenide buried rib waveguide pumped with 330 femtosecond pulses at 4.184 μm was reported by the same group [34]. By launching ultra-short, high peak power pulses with centre wavelengths of 4.5 μm and 6.3 μm respectively, into a short piece of chalcogenide glass optical fibre, SC spanning 1.5-11.7 μm and 1.4-13.3 μm were generated, respectively, though at low average powers [30]. Also, MIR supercontinuum generation spanning from ~1.8 to ~10 μm within a dynamic range of 15 dB has been demonstrated from a 11-cm-long step-index chalcogenide fibre pumped with ~330 fs pulses at 4.0 μm from an optical parametric amplifier (OPA) [33]. Broadband high spatial coherence sources with wide emission range like this are clearly highly desirable for molecular sensing, and the potential for integration is clear. However, to expand the SC emission deep into the MIR, a mode locked MIR pump source is optimal as shown in the experiments cited above. Further, this needs to ultimately be integrated to control costs. Fortunately, MIR laser sources are possible with rare-earth ion doped waveguides in suitable hosts, and so the promise of an integrated pump source is real. The enormous number of transition lines in different rare-earth ions cover almost the whole MIR range from 2 to 10 μm, which potentially offer great support to SC generation as pump sources [35, 39].

(b) Free-space optical communications

Free-Space Optical Communication (FSO) systems are used for high rate communication between two fixed points over distances up to several tens of kilometres. In comparison to radio-frequency (RF) counterparts, FSO systems have high bandwidth, allowing much higher data rates. Besides applications such as, metropolitan area network (MAN) extension, local area network (LAN)-to-LAN connectivity, high definition television (TV) and medical image/video transmission, wireless video surveillance monitoring, FSO systems are considered as an efficient solution for the "last mile" problem to bridge the gap between the end user and the fibre optic infrastructure already in place. Currently, FSO link reliability is the biggest challenge preventing widespread adoption, especially at long ranges due to atmospheric turbulence-induced fading and sensitivity to weather conditions [79]. The advantages of MIR range sources for FSO communications arise from the usual λ^{-4} light scattering dependence (λ is wavelength), making the long wavelength region considerably more reliable in the dusty and smoky environments, characteristic of many urban areas and even battlefields [80]. The MIR between 3 to 5 μm is also considered a low loss atmospheric window and eye safe. Along with the ultra-high bandwidth and highly secure data transfer for both short and medium range, free-space optical communications at 3 to 5 μm has been seriously considered as a solution to the “last mile” communications problem. Thus, besides QCLs, emissions from rare-earth ion doped materials at 3 to 5 μm wavelengths are in great demand to fulfil this task.

(c) Medical laser surgery

Significant benefits are known to be possible with laser surgery compared with conventional mechanical cutting methods. For example, laser energy can seal small blood vessels, so using a laser enables dry field surgery. Also clear field of view, precise cutting control, and operating in a small area under a microscope could be realised with laser surgery. Furthermore, the use of femtosecond MIR pulsed sources to ablate tissue without heating has been shown to result in less tissue damage and better, faster healing [81-84]. There is also the opportunity to use wavelength specific reactions to target the specific biological tissue without damaging the surrounding tissues [85].

In medical laser surgery, strong absorption of energy in tissues occurs in both the ultraviolet and MIR wavelength regions, but because of the potential mutagenic effects of ultraviolet wavelengths, MIR lasers are preferred for many types of tissue [86]. Surgical lasers have been evaluated by means of achieving controlled removal of tissue with minimal collateral thermal injury. While water is the dominant chromophore in tissue, lasers operating at 2.1, 2.94, 6.1, 6.45 and 10.6 μm associated with strong water absorption are of greatest interest due to their ability to remove tissue effectively with little concomitant thermal damage. Among these, erbium ion doped lasers at 2.9 µm (exploiting the water OH-stretch mode) were used leading to a more efficient ablation of cartilage with significantly less thermal injury [87].

Alternative laser sources in the 6-8 μm range are in need, and pulsed lasers with proper pulse parameters are also of interest on account of the low thermal damage. Currently, options for surgical lasers are limited due to their continuous-wave operation and energy limitations [88-90]. This leaves open an opportunity for rare-earth ion doped chalcogenide IR laser sources. Low phonon energy and long wavelength transparency make rare-earth ion doped chalcogenide hosts a promising candidate in MIR laser sources, whilst the large gain bandwidths of rare-earth ion doped chalcogenide host also bring advantages in realising ultra-short fs pulsed laser sources.

(d) Defence

MIR technologies are used extensively for military purposes, including target acquisition, surveillance, night vision, homing and tracking. And also some high power MIR lasers, for example the Mid-Infrared Advanced Chemical Laser (MIRACL), were developed as directed energy weapons [91, 92]. Compared with lasers in the visible/NIR wavelength, MIR operation has immediate potential for target illumination and designation applications, because the visible/NIR wavelength based illuminators and designators have become less effective due to the availability of night vision sensors that can be obtained inexpensively and easily by adversaries [93].

Also, MIR technologies will benefit battlefield communication. Currently battlefield communications are dominated by radio-frequency technologies, but these technologies are confronted with issues such as simple eavesdropping, jamming and antiradiation munitions [94]. NIR free-space optical links are relatively immune to these issues but are degraded by fog and smoke, making it less dependable. Communication in MIR region is scattered much less by particulates even in fog and smoky conditions, enable reliable communication in such conditions [95].

In addition, the MIR laser wavelengths are considerably more eye safe than the NIR laser sources at the same power, because the MIR wavelengths are strongly absorbed by water and thus cannot reach the retina.

1.3 Rare-earth ion doped chalcogenide glasses

1.3.1 Introduction

Amongst all rare-earth ion elements, erbium ion (Er^{3+}) doped materials have attracted considerable attention because of their potential applications in optoelectronics, and their importance in the telecommunication area due to the 1.55 μm emission located at the low attenuation range of massively deployed silica-based fibre optics [96].

The 1.55 μm emission arising from the $^4I_{13/2} \rightarrow {}^4I_{15/2}$ transition in the trivalent state of erbium ion has been widely used to create optical fibre and waveguide amplifiers in oxide glass hosts [97-100]. There are some major differences between Er^{3+} doped chalcogenide glasses and Er^{3+} doped oxide glasses, resulting mainly from the low phonon energy of chalcogenide glasses. Compared with the oxides, the low characteristic phonon energy of the chalcogenide glasses hugely lowers the multi-phonon processes such as multi-phonon relaxation (MPR) or phonon-assisted parasitic transitions. This results in a range of processes being present in chalcogenide glasses that are not available in other hosts, for example, long lived states away from the traditional 1550 nm erbium (III) transition band allows both extra transitions not seen in oxides (typically but not exclusively in the MIR) and a range of up conversion, cross-relaxation, and excited state absorption based processes which have far higher efficiency than in oxide hosts. Some chalcogenide glasses, such as Ga-containing chalcogenide or chalcohalide glass [101-104], can also accept high doping levels (1-2 at%) without clustering and this makes it feasible to achieve high gain in a relatively short device. Additionally, the non-equilibrium growth of thin films via methods such as co-evaporation or co-sputtering allows the possibility of highly doped films in hosts where clustering prohibits the formation of useful bulk glasses. Details on options for film deposition and waveguide fabrication can be found in Section 3.2.3 and 4.4, respectively. Hence it should, in principle, be possible to use optical gain to compensate the optical losses in a chalcogenide waveguide as a route to improving the efficiency of all-optical processing, and to realise MIR waveguide based laser or amplifier devices.

1.3.2 History of rare-earth ion based chalcogenide laser and amplifier devices

There have by now been many reports on the luminescence properties of erbium ion doped chalcogenide glasses and a smaller amount of work on thin films and waveguides. At the commencement of this thesis, however, there had been only three demonstrations of fibre or waveguide amplifiers and a further two bulk glass based devices using rare-earth ion doped chalcogenide glasses, in spite of the good progress that has been made on rare-earth ion doped bulk glasses. The first laser action in a rare-earth ion doped chalcogenide glass was demonstrated by Schweizer et al. in 1996 [105]. In their experiment, CW lasing at 1.08 µm was achieved through a 1.42 mm thick neodymium-doped gallium lanthanum sulfide (GLS) glass with a concentration of 1.5 mol% (2.6×10^{20} ions/cm^3) Nd_2S_3 when pumped with a Ti:sapphire laser either at 0.815 or 0.890 µm. Laser action ceased at high pump powers, due to thermal lensing effect. In the next year, laser action at 1.080 µm was obtained in a 22 mm long GLS glass fibre under excitation at 0.815 µm [106]. The multimode GLS fibre with a 14 µm core doped with 0.05 mol% Nd_2S_3, was fabricated using the rod-in-tube method. Self-pulsing behaviour was noticed in the experiment but the cause for this was unknown. In 2000, optical amplification at 1.34 µm with a gain coefficient of 0.81 dB/mW was achieved in a single-mode Pr^{3+} doped Ga-Na-S (GNS) fibre [107]. The fibre, doped with 750 ppm Pr^{3+}, had an attenuation loss of 1.2 dB/m at 1.31 µm was fabricated using the extrusion method. By pumping a 6.1 m long fibre at 1.017 µm, a net gain of 32 dB was achieved when the pumping power was 90 mW.

In 2002, Mairaj et al. reported lasing at 1075 nm from a neodymium ion doped Ga-La-S glass channel waveguide written using a focused UV-laser beam (λ=244 nm) [108]. The maximum measured refractive index change after treatment was Δn~$+10^{-3}$. A lasing experiment was performed on a 0.5 mol% Nd_2S_3 doped 16 mm long waveguide with propagation loss estimated 0.5 dB/cm. Single mode laser operation at output slope efficiency of 17% with respect to absorbed power was obtained.

Laser action also has been demonstrated in neodymium ion doped GLS glass microspheres (1.5 mol% Nd^{3+} doped) [109]. Chalcogenide spheres of ~100 µm diameter were fabricated, and the Q factor from this sphere was of the order of 10^4. Under excitation at 808 nm, single and multimode laser action was demonstrated at wavelengths between 1075 and 1086 nm with a pumping threshold of 82 mW. Resonant peaks shift to longer wavelengths with the increasing of excitation power was observed, and both thermal and third order nonlinear effects were thought responsible for this resonant wavelength shift.

Since these demonstrations there has been no gain or lasing demonstrated in chalcogenide hosts at wavelengths of 1.40 µm or longer. High power MIR amplified spontaneous emission from rare-earth ion doped chalcogenide fibres was reported by the Naval Research Laboratory [40, 76, 110]. In their experiment, a 150 µm core, 250 µm cladding Pr^{3+}-doped selenide fibre was pumped using a 1.97 µm diode laser. ASE emission from 3.2-5.8 µm was achieved. Rise and fall times of the emission from this fibre source were also studied and it was claimed that the temporal response could be tailored by selectively modifying the composition of the fibre material.

In addition to rare-earth ions, transition metal (TM^{2+}) ion doped polycrystalline chalcogenide hosts also offer properties such as ultra-broadband gain, low saturation intensities and large pump absorption coefficients. This has, until now made them the gain media of choice for cost effective broadly tunable lasing in the shorter waveband of the MIR. Amongst the family of TM ion doped chalcogenide glasses, Cr^{2+}:ZnS/Se and Fe^{2+}:ZnS/Se are the best performers on account of their better thermal properties. With

Cr^{2+} and Fe^{2+} doped chalcogenide materials, the 1.9-6 μm spectral range is potentially accessible, though with some limitations/compromises. Lasers with high output powers (average power of 18 W in gain switched lasing [111] and 30 W in pure CW at 2.4 μm [112]), large tunable range (over 1800-3100 nm [113]), short-pulse (~40 fs from a graphene passive mode-locked laser with 250 mW average output power at 2.4 μm [114]), multi-Joule long-pulse output energy (2.1 J output energy from a low temperature pulsed Fe^{2+}:ZnSe laser at wavelength of 4.1 μm [115]), and narrow spectral linewidth (<100 kHz with spectral region from 2.12 to 2.58 μm [116]) were also realised with TM ion doped chalcogenide glasses[112]. Therefore, it is reasonable to say that currently this is certainly one of the most effective routes for room temperature lasing in the 1.9-3 μm and perhaps even ultimately the 1.9–5 μm spectral range though at minimum thermoelectric cooling is required to access the longer wavelength range. New schemes for gain element thermal management due to the high potential for thermal lensing are the key to improve output power in the future and improve the practical usability of such sources, especially the Fe^{2+}:ZnSe which have to operate at low temperatures (<-80 °C).

1.3.3 Rare-earth ion doped chalcogenide materials

Amongst chalcogenide hosts, there has been a particular focus has on those containing Ga, such as Ga-La-S (GLS), Ge-Ga-S and Ge-Ga-Se [46, 117-123], since they have been shown to accept high Er^{3+} concentrations without clustering. For example, Schweizer et al. [117] studied the properties of the Er^{3+} doped GLS glass system for MIR applications. Tonchev et al.[118], reported 1550 nm photoluminescence (PL) decay lifetime around 1.5-2 ms with 975 nm pumping in $(As_2Se_3)_{1-x}(GaSe)_x$ (with Ga from 0 to 5 at%) bulk glass doped with Er_2S_3 (1% Er^{3+}). They found that the PL decay lifetime increased linearly with Ga concentration from about 1.5 ms to 2 ms with the addition of Ga up to 5%. Allen et al. [119] studied the photoluminescence characteristics of a series of Er^{3+} doped chalcogenide glasses and found that all samples exhibited lifetimes in the 1–4 ms range. The Ga-Ge-As-Se glass had the shortest lifetimes of 1–1.5 ms for 980 nm pumping, whilst Ga-Ge-Se and Ga-Ge-S samples had the highest values of 2–4 ms. A strong correlation between the Er^{3+} ion and Ga concentrations that affects the properties of Er^{3+} doped Ge-Ga-Se glasses was found in [120]. Kasap et al. examined the optical and photoluminescence properties of Er^{3+} doped Ge-Ga-S glasses of near stoichiometric compositions ($Ge_{28}Ga_{6.2}S_{65.3}$:$Er_{0.5}$ at%) and calculated a lifetime around 2.6 ms using the Judd–Ofelt theory [121]. However, Ga-containing bulk glasses pose significant problems during the thin film deposition required to make waveguides. In particular, upon melting these glasses tend to phase separate into a non-volatile Ga-S(Se) phase leading to significant deviations from the starting composition in the film, typically the film being gallium poor. As a result, to the best of our knowledge there have been no reports of stable, high quality thin films or waveguides (loss of less than 1 dB/cm) made from Ga-containing chalcogenide glasses. Chalcohalide glasses are also reported with high rare-earth solubility and promising PL emissions in MIR [104, 124, 125], however, due to the lack of experience in chalcohalide film deposition and waveguide fabrication in our group, no research on chalcohalide was conducted in this thesis.

There have, however, been many demonstrations of high quality chalcogenide thin films and waveguides in other chalcogenide hosts such as As_2S_3, Ge-Sb-S and $Ge_{11.5}As_{24}Se_{64.5}$ (at%) [4, 11, 13, 14]. For example, loss values as low as 0.05 dB/cm at 1550 nm have been measured for un-doped 4 μm wide As_2S_3 rib waveguides etched into 2.5 μm thick films, whilst losses for highly nonlinear dispersion-engineered As_2S_3 waveguides with a nonlinearity, $\gamma \approx 10\ W^{-1}m^{-1}$ are now as low as 0.3 dB/cm [13]. Recently, $Ge_{11.5}As_{24}Se_{64.5}$ (at%) nanowires (585×575 nm) with extreme nonlinearity coefficient of $\gamma = 130\ W^{-1}m^{-1}$ and moderate losses of ≈1.65 dB/cm were also reported [65]. Propagation loss as low as 0.42 dB/cm was demonstrated in submicron $Ge_{23}Sb_7S_{70}$ (at%) waveguides (700×600 nm ribs with 290 nm etch depth) using chlorine plasma etching [14]. These materials, have to date, proven to be the most suitable for planar waveguides [4, 11]. However, doping of rare-earth ions into bulk glasses with these compositions is difficult because the absence of Ga means the solubility of rare-earth ions in such glasses is low. As_2S_3 bulk glass doped with Er_2S_3 to give 0.1 at% Er concentration produced complex narrow line structures in the PL spectrum that are similar to those found in crystalline material such as Er^{3+}:YAG [126], implying low erbium ion solubility in As_2S_3 bulk glass; while for the ternary $Ge_{33}As_{12}Se_{55}$ (at%) glass, erbium ion clustering was observed at concentrations above 0.2 wt% [127]. Unfortunately, useful waveguide based devices require ~1-5 at% doping levels in order to obtain the ~1dB/cm gain required for practical devices.

Interestingly, there is strong evidence that some films can incorporate larger amounts of rare-earth ions compared with bulk samples when prepared by physical vapour deposition methods. This is most probably due to the fact that films are created in strongly non-equilibrium conditions by condensing a vapour onto a cold substrate.

This means that single isolated rare-earth atoms (or ions) are immediately incorporated into the film thereby inhibiting clustering. This contrasts sharply with the situation used to create a bulk glass where the dopant has to be soluble in the molten host. Lyubin et al. [128] reported that co-thermal evaporation of erbium with As_2S_3 produced films with Er^{3+} concentration as high as 4 at% without any signs of clustering and led to strong PL emission under Ar^+ laser excitation at 514 nm. Vigreux-Bercovici et al. [129] also reported sputtering of a 3% Er^{3+}:As_2S_3 composite target to produce a thin film that had 1.5 μm transition lifetime of 4 ms. Whilst this is encouraging, the problem of etching rare-earth ions doped films remains and hence it is sometimes attractive to introduce the dopant after waveguide fabrication using ion implantation. In this approach a chalcogenide host that makes the most stable low loss waveguides can be employed. Fick et al. observed a strong Er^{3+} emission at 1.54 μm from erbium ion implanted As_2S_3 and $As_{24}S_{38}Se_{38}$ (at%) films with a lifetime of 2.3 ms [130]. In Ivanova’s work [131], the PL properties of Ge-S-Ga films ion implanted with relatively low energy (320 keV) ions at different fluences was investigated. They reported that the PL efficiency reduced with increasing Er^{3+} concentration and that thermal annealing at 230 °C approximately doubled the PL efficiency at all doses.

Whilst rare-earth ion doped chalcogenide bulk glasses have been intensively investigated, e.g. [119, 120, 122, 127, 132], as noted above, at the outset of this work there have been only five demonstrations of gain or lasing in chalcogenide glasses. Despite the many rare-earth elements added in bulk glass and the rich vein of possible transitions at longer wavelengths, there have since been no further demonstrations of amplifiers or lasers. A brief collation of representative measured NIR and MIR emissions of various rare-earth ion doped chalcogenide glasses and fibres are shown in Table 1.3.

Table 1.3 Collation of the MIR emission of rare-earth ion doped chalcogenide glasses and fibres.

Dopant(s)	Host glass	Excitation / µm	Emission / µm	Transition	Reference
Er^{3+}	As_2S_3	1.48	1.54	$^4I_{13/2}\rightarrow{}^4I_{15/2}$	[133]
	GLS	0.66/0.81	2.0/2.75/3.6/4.5		[117]
	GeGaSbS	0.804	4.3-4.8	$^4I_{9/2}\rightarrow{}^4I_{11/2}$	[134]
Ho^{3+}	GeGaAsS/Se	0.9	1.6	$^5I_5\rightarrow{}^5I_7$	[135]
	GeAsS	0.905	1.2/2.0/2.9	$^5I_6\rightarrow{}^5I_8$ /$^5I_7\rightarrow{}^5I_8$ /$^5I_6\rightarrow{}^5I_7$	[136]
	GLS	0.76/0.9/2	1.2/1.25/1.67/2/2.2/2.9/3.9/4.9		[137]
Tm^{3+}	GeAsS	0.698/0.8	1.2/1.4/1.8	$^1H_5\rightarrow{}^3H_6$ /$^3H_4\rightarrow{}^3F_4$ /$^3F_4\rightarrow{}^3H_6$	[138]
	GeGaS-CsI	0.8	1.48/1.8/2.3/2.8		[139]
	GLS	0.7/2	3.8/5.38	$^3H_5\rightarrow{}^3F_4$ / $^3F_{2,3}\rightarrow{}^3H_4$	[48]
Dy^{3+}	GeAsS GeGaS	0.808	1.33/1.75/2.9/4.38/5.27 (No spectrum)		[140]
	GeGaS	0.798	2.9 (Tm^{3+}/Dy^{3+} co-doped)	$^6H_{13/2}\rightarrow{}^6H_{15/2}$	[141]
	GaSbS	1.32	2.95/3.59/4.17/4.4		[142]
	‘selenide’		~4.5	$^6H_{11/2}\rightarrow{}^6H_{13/2}$	[103]
	GeAsGaSe	1.3	3.0/3.2/4.5/5.5/7.6		[54]
Pr^{3+}	‘selenide’		3.5-5.5		[41]
	GeAsGaSe	2	3.4/4.0/4.8/5.2/7		[54]
Tb^{3+}	GeAsGaSe	1.97	3.1/4.7/4.8/7.5/10.5		[54]
	GLS	2	4.8/8.1(No spectrum)	$^7F_5\rightarrow{}^7F_6$ /$^7F_4\rightarrow{}^3F_5$	[48]

1.3.4 Potential issues for rare-earth ion doped chalcogenide glasses

Whilst chalcogenide glasses have much promise as outlined above, there are also potential issues that need to be outlined and considered in the forthcoming work. For example, it is well known that in erbium ion doped silicon, photoluminescence can be excited and observed via the energy transfer from an electron-hole pair trapped at an erbium-related defect state in the silicon band gap. In detailed studies, the reverse process was also observed. In the erbium ion doped silicon system, energy transfer from excited erbium ion back to the electronic system of the silicon host was observed and named energy back-transfer. Obviously, this process is detrimental for devices such as amplifiers or lasers, for it depopulates the excited ions in a non-radiative way and causes thermal degradation.

A similar phenomenon has been noticed in rare-earth ion doped chalcogenide glasses. In Gu et al.'s study [143], careful investigation via PL and photoluminescence excitation spectroscopy (PLE) in Er^{3+} doped As_2S_3 and $Ge_{33}As_{12}Se_{55}$ (at%) glasses, remarkably broad PLE spectra for the 1550 nm emission extending from the Urbach absorption edge to beyond 1000 nm were observed [143, 144]. Similar features were also observed in the PLE spectrum of a 1-μm-thick Er^{3+}-doped $As_{40}Ge_{10}Se_{25}S_{25}$ (at%) film deposited on silicon substrates using radio frequency (RF) sputtering [145]. This feature indicated that, like what happened in rare-earth ion doped silicon, there was another energy transfer mechanism by which energy can be directly transferred in either direction between the chalcogenide host and rare-earth ions. Whilst this energy transfer mechanism potentially enables flexible pumping wavelengths and more distantly the possibility of direct electrical pumping, the back-transfer process could also prevent rare-earth ion doped devices from attaining gain.

Alternately, Ivanova et al. examined the conductivity properties of erbium ion doped Ga-Ge-S-Se glasses, and also estimated the efficiency of the energy back transfer process to the chalcogenide matrix by careful lifetime measurement in erbium ion doped Ga-Ge-S glasses [146-148]. Samples were exposed to sub-bandgap light, the un-doped sample showing no change in conductivity; while the sample doped with erbium had a significant increase in conductivity. It was believed that the erbium was excited to an energy state above the band gap by a multi-photon mechanism and then interacted with electrons in the glass matrix to generate additional free electrons thereby increasing the conductivity. In conclusion, it was pointed out: energy transfers from an excited erbium ion to the host (energy back-transfer) may also be possible. This obviously brings an obstacle to realise an amplifier or laser based on rare-earth ion doped chalcogenide glasses.

Ion-to-ion interaction is another issue to be confronted in rare-earth ion doped materials. With high rare-earth dopant concentrations, the distance between rare-earth ions becomes small enough that electric dipole-dipole interactions between different rare-earth ions takes place. The strength of this interaction is strongly related to the distance between the related ions with a $1/r^6$ relationship, where r is the inter-ion distance [149]. The occurrence of this phenomenon can drop the fraction of excited rare-earth ions significantly at a given pump power, which will in turn degrade the performance of the device. Publications concerning these phenomena have been reported in variety of host materials, while one representative of chalcogenide glasses, sulfide glasses, was claimed to suffer more severe ion-to-ion interaction [150]. In that work, both Er^{3+}/Ce^{3+} co-doped tellurite and sulfide glasses were prepared. Up-conversion emission at 816 nm increased and the lifetime of the $^4I_{13/2}$ state decreased with increasing cerium concentration, implying the occurrence of the $^4I_{13/2}:^4I_{13/2} \rightarrow ^4I_{15/2}:^4I_{9/2}$ process. While similar phenomena were observed in the tellurite glasses, they were much weaker, indicating that sulfide glasses suffered more serious ion-to-ion interactions, which even quenched the $^4I_{13/2}$ state population. Thus, ion-to-ion interaction was thought to be another issue preventing researchers from achieving gain in Er and potentially other doped chalcogenide devices.

Impurity multiphonon relaxation is suggested as an additional method of non-radiative depopulation of the excited state in the MIR, besides lattice multiphonon relaxation [39]. In gallium-lanthanum-sulfide (GLS) glass, large oxide additions (La_2O_3) increase glass stability to avoid crystallization during fibre drawing. With the appearance of La_2O_3, a mixed sulfur-oxygen species is formed leading to a vibrational absorption at 8.6 µm (1163 cm^{-1}), and this value is thought a more realistic phonon energy in this oxysulfide glass instead of the value of ~425 cm^{-1}. With this number, only 4 phonons are required to prevent the ~ 2 µm emission, thus it is easy to explain that GLS glasses have failed to lase in MIR. In more covalent chalcogenide glasses such as Ge-As-Se, Ge-Sb-Se, oxide exists as an impurity manifesting extrinsic absorption bands in the infrared spectra of glasses. For example, As-O and Ge-O impurity have vibrational absorption band centred at ~7.9 µm (~1266 cm^{-1}). These extrinsic impurities close to a rare-earth ion in a glass host lattice could cause impurity multiphonon relaxation of the rare-earth ion excited states in an analogous way to lattice multiphonon relaxation by means of local independent oscillators. In this scenario, the probability of non-radiative emission by impurity multiphonon decay matters. Oxide impurities at low level of 200 ppmw had great impact on the photoluminescence spectrum in Pr^{3+}-doped GeS_2-based glasses was also reported in [151]. Of course the magnitude of this effect is directly proportional to the impurity concentration and it does not affect all the rare-earth ions in the material, but it can have sufficient impact to prevent gain being demonstrated. In Section 5.2 of this thesis, the PL of RF sputtered Er^{3+}:As_2S_3 films drops almost down to zero in some conditions, which is believed due to the existence of O-H impurities which are resonant in energy with the desired transition. This has also been documented in tellurite glass planar waveguide amplifiers as a mechanism preventing gain [152]. Thus in any investigation into rare-earth ion doped gain, material optimisation is necessary to rule out contaminant species as significant contributors to non-radiative decay.

In the decades following the initial demonstration of the chalcogenide laser, and despite considerable efforts, no successful result beyond 1300 nm has been reported. With the huge potential applications in MIR sensing, and all optical signal processing and telecommunications, erbium ion doped chalcogenide amplifiers and lasers were intensively studied, but no significant results have been achieved. In addition to this, to date only one explanation has been proffered as to why rare-earth ion doped chalcogenide glasses do not perform as expected. This is due to absorption and non-radiative decay of excited rare-earth ion by extrinsic phonons due to impurities in the chalcogenide glass host as mentioned above [39].

1.4 Problem under study

As has been laid out above, since the first demonstration of a laser using Nd^{3+} at 1080 nm and Pr^{3+} at 1300 nm in both bulk glass and fibres, no real progress has been made on other ions or longer wavelengths in chalcogenide hosts. Given the clear MIR capabilities of chalcogenide glasses and their potential as all optical processing hosts at 1550 nm, this clearly needs to be investigated. Likewise, planar waveguide based lasing devices have not prospered despite some promising looking initial results in thin films. In neither case has much been said in the literature about the reasons why progress has not been achieved, apart from the reason of extrinsic non-radiative decay [39].

Therefore, the plan for this thesis was to investigate these two issues. The ion of choice for the studies was erbium, as it provides gain at 1.5 µm for optical signal processing applications, as well as MIR transitions at 2.9, 3.4 µm and 4.5 µm. In addition, it has potentially efficient multiple pump photon upconversion to the visible where the interactions with the band gap may be studied. The objective of this study was to make working rare-earth ion doped chalcogenide waveguide amplifiers and lasers at 1.5 µm, and potentially demonstrate MIR amplification in a planar format.

1.5 Outline of this work

This thesis studies both the materials and waveguide structures for rare-earth ion doped chalcogenide glasses. Several deposition modalities are covered, comparisons made to bulk glasses, and waveguide devices fabricated and tested. The remainder of this thesis is organized as follows:

Chapter 2 introduces comprehensively the important properties of rare-earth ions, focussing especially on erbium ion and characterisation methods of rare-earth ions in hosts. Factors related with lifetime and emission properties are discussed. Important processes in rare-earth ion doped glasses, such as energy migration processes, concentration quenching and solubility of rare-earth ions in chalcogenide hosts are also discussed.

Chapter 3 focuses on As_2S_3, the main workhorse of this thesis. Optical and structure properties such as transmission, absorption, dispersion and Raman spectrum of As_2S_3 are introduced at the first part. Bulk As_2S_3 was fabricated by melt-quenching method, and then erbium ion doped As_2S_3 films were deposited using co-thermal evaporation. The physical and optical properties of the obtained films are detailed. The influence of thermal and light post-treatment and even higher temperature (above the transition temperature of As_2S_3) post-treatment on the emission properties of erbium ion are studied. Cooperate up-conversion phenomena in erbium ion doped As_2S_3 film were observed and investigated as well. With all this information, an optimised erbium ion concentration was arrived at, and this concentration was applied in the following chapter.

Chapter 4 covers the basic theory of light propagation in waveguide, waveguide design and simulations. Performance of erbium ion doped As_2S_3 waveguide amplifier was also simulated using the OptiSystem commercial software, and promising results were achieved. Several methods of waveguides fabrication are detailed. Photolithography combined with inductively coupled plasma reactive ion etching was applied in this work to pattern erbium ion doped As_2S_3 waveguides. Erbium ion doped As_2S_3 waveguides with a low loss of 0.35 dB/cm were achieved, and for the first time internal gain from 1570 to 1630 nm was observed in an erbium ion doped chalcogenide waveguide amplifier. Neodymium ion doped As_2S_3 waveguides were also fabricated and tested, but no gain/lasing was observed. Given the test results and information from Raman spectroscopy, neodymium ion clustering in the As_2S_3 host was thought the main reason for failure.

Chapter 5 introduces different approaches to realise better population inversion in erbium ion doped As_2S_3 waveguides. $ErCl_3$ and Er_2S_3 were used in film deposition instead of erbium metal, however in both cases film quality became an issue that prevented further progress. RF sputtering of As_2S_3 together with a piece of erbium foil was also performed. The PL intensity from obtained sputtered films (after thermal post-treatment) was even stronger than the PL intensity from the film on which internal gain was achieved. However, due to the columnar growth habit RF sputtering has, the O-H contained in the column-structure quenched PL rapidly, so no amplification result was achieved from this waveguide.

Chapter 6 reports the research results on erbium ion doped chalcogenide glasses and waveguide amplifiers based on Ge-Ga-Se hosts, which are known to have better rare-earth ion solubility than As_2S_3. A series of erbium ion doped Ge-Ga-Se glasses was synthesised, and their optical properties are measured and analysed. Waveguide structures were patterned on erbium ion doped Ge-Ga-Se films deposited using co-thermal evaporation, and the optical properties were characterized. The film deposition equipment was modified to overcome the particulates on deposited film, after that high quality films were finally deposited. With these high quality films, erbium ion population inversion up to 50% was achieved, but appearance of photo-darkening phenomenon was observed in amplification experiments which presented a hurdle to realising a working rare-earth ion doped chalcogenide waveguide amplifier in practice.

Chapter 7 summarises the main challenges, achievements of the work then suggests future work to further advance the field of rare-earth ion doped chalcogenide waveguide devices.

Chapter 2

Rare-earth ions in chalcogenide glasses

2.1 Introduction to rare-earth ions

The rare-earth elements (also referred to as the lanthanides) are a set of seventeen elements in the Periodic Table, specifically the fifteen lanthanides, as well as scandium and yttrium. In the lanthanide series, the 4*f*-shell is consecutively filled from cerium ($4f^15d^16s^2$) to lutetium ($4f^{14}5d^16s^2$). Compared with the 4*f*-electons, the more distant $5d^1$- and $6s^2$-electrons with lower ionization energies can be removed much more easily and this explains the similar reactivates that the lanthanides share. After removing the $5d^1$- and $6s^2$-electrons, the 4*f*-electrons are still shielded by 5*s*- and 5*p*-electrons, therefore, they are relatively insensitive to the host environment. The 4*f* electron shell has a series of energy levels which are annotated by the orbital angular momentum number L, the overall spin S, and the total angular moment J. These levels are known as the *LSJ* levels, and written as $^{2s+1}L_j$. In a neutral environment, these multiple energy levels are degenerate and electric dipole transitions between different levels are forbidden. But if rare-earth ions are subjected to the crystal field of a host matrix, then despite the 5*s*- and 5*p*-electron shielding, there is still sufficient interaction between the 4*f*-electrons and the crystal field to affect the energy levels [153]. As a result, a series of discrete energy levels are created, and a radiative electric dipole transition between different multiplets is then allowed to occur. Because of the weak oscillator strength of the electric dipole transition under these circumstances, narrow emission lines are observed in crystalline hosts for all the rare-earth ions, and the emission wavelengths are only slightly influenced by individual ligand systems. One crucial advantage supporting rare-earth ion luminescence is the long lifetimes of their excited states which are directly correlated to the low probabilities of forbidden transitions. As an example of interest in this research, Figure 2.1 shows the effect of spin-orbit and crystal field interactions on the energy levels of erbium ions in a solid host [154]. All the possible inter-level emission wavelengths are calculated based on the data from single crystal erbium oxide [155], and the detailed results are shown in Table 2.1.

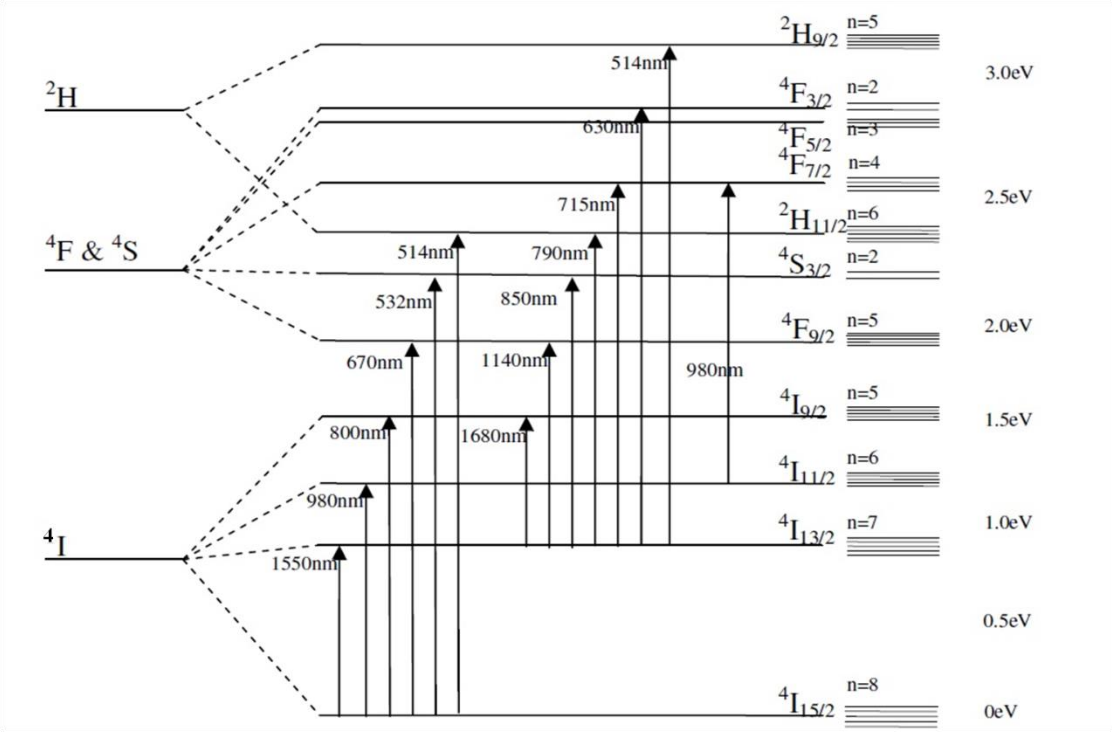

Figure 2.1 Energy levels of Er^{3+} quantum energy with effect of spin-orbit and crystal splitting and excitation wavelengths from $^4I_{15/2}$, $^4I_{13/2}$ and $^4I_{11/2}$ to various levels [154], see Table 2.1

Table 2.1 Calculated possible inter-level emission wavelengths in μm with data of Er_2O_3 crystal [155].

	$^4I_{15/2}$	$^4I_{13/2}$	$^4I_{11/2}$	$^4I_{9/2}$	$^4F_{9/2}$	$^4S_{3/2}$	$^2H_{11/2}$
$^4I_{13/2}$	1.548						
$^4I_{11/2}$	0.992	2.759					
$^4I_{9/2}$	0.815	1.719	4.562				
$^4F_{9/2}$	0.664	1.162	2.008	3.587			
$^4S_{3/2}$	0.554	0.862	1.253	1.728	3.333		
$^2H_{11/2}$	0.528	0.802	1.131	1.504	2.589	11.59	
$^4F_{7/2}$	0.494	0.725	0.983	1.253	1.926	4.56	7.52
$^4F_{5/2}$	0.457	0.648	0.847	1.04	1.465	2.61	3.37
$^4F_{3/2}$	0.499	0.632	0.82	0.999	1.385	2.37	2.98
$^2H_{9/2}$	0.412	0.561	0.704	0.832	1.083	1.6	1.86

For Er^{3+}, the $^4I_{13/2}$ energy level is treated as the metastable excited state as it has essentially the longest excited state lifetime of the accessible levels in most hosts. The radiative lifetime decay from this level to the ground state $^4I_{15/2}$ is relatively long, up to tens of milliseconds in some host materials, though in low phonon energy materials such as tellurite and chalcogenide glasses, the $^4I_{11/2}$ and $^4I_{9/2}$ state lifetimes become comparable to the lifetime of the $^4I_{13/2}$ state [46]. Therefore, several different pumping schemes were proposed. Typically, in higher phonon energy hosts such as silica, an excitation laser at 980 nm is used in a three energy level system. Ions are excited from the ground state $^4I_{15/2}$ to the excited state $^4I_{11/2}$, and then decay to a metastable state $^4I_{13/2}$ quickly due to the interaction between the excited erbium ions and the thermal phonons in the host material. As erbium ions accumulate in the long lived $^4I_{13/2}$ energy level, population inversion and therefore optical gain is achievable for this scheme. Pumping with 1490 nm is another option. In this scheme, erbium ions are excited into the top of the $^4I_{13/2}$ manifold directly by absorbing pump photons. These excited ions then de-excite down through the sublevels which are broadened to the point of strong overlap by thermal phonons to form a population inversion between the lower energy part of the $^4I_{13/2}$ manifold and the ground state $^4I_{15/2}$. In this case, the energy level $^4I_{13/2}$ is considered to be effectively split into two parts that play different roles in the process. Therefore, in this pumping scheme, the erbium ions are treated as a quasi-three energy level system. However, as the pump photon energies lie inside the excited state manifold, there is some pump stimulated emission and this places limits on the maximum inversion achievable. It is also possible to pump Er^{3+} via the even higher energy levels at 800 nm and 670 nm.

2.2 Properties and characterization of rare-earth ions in glasses

2.2.1 Lifetime of rare-earth ions in an excited energy level

The lifetime, τ, of an excited energy level is the inverse of the probability per unit time of the exit of an ion from that excited level. In the ideal case, the decay of the population in a given level drops exponentially with a time constant equal to the lifetime. There are a number of pathways for the excited state decays. The total probability is equal to the sum of the individual pathway probabilities. Each pathway can, therefore, be considered to have a separate lifetime. Usually they are classified as a radiative lifetime τ_r or non-radiative lifetime τ_{nr}. The total lifetime can then be written as:

$$1/\tau = W_{tot} = W_r + W_{nr} \tag{2.1}$$

The overall emission probability for an excited energy level depends upon the relative sizes of W_r (radiative emission) and W_{nr} (the probability of non-radiative emission) per unit time, which will be elaborated in the following parts, (a) and (b), respectively.

(a) Radiative Relaxation

Radiative relaxation refers to the situation that excited ions decay to a lower state by emitting a photon. When two energy levels, i and j, are sufficiently close they become thermally linked and their relative populations are expressed by Boltzmann's distribution law [156, 157]:

$$\frac{N_i}{N_j} = exp\left(-\frac{\Delta E_{ij}}{k_B T}\right) \tag{2.2}$$

where $N_{i,j}$ are the population of upper and lower states, ΔE_{ij} is the energy difference between state N_i and N_j, k_B is the Boltzmann constant and T is the absolute temperature. Obviously, if ΔE_{ij} is big enough, the ratio of the population between the upper and lower states becomes essentially zero. This means the two energy levels are not thermally coupled and the relaxation between these two levels can occur with relatively high probability via photon emission or other non-radiative routes. There are two types of mechanisms for photon emission, depending on whether population inversion between these two levels has been formed, they are known as spontaneous or stimulated emission.

(b) Phonon Relaxation

In reality, non-radiative emission has many contributing components, such as, lattice multiphonon decay and impurity/defect multiphonon decay processes, expressed mathematically as:

$$W_{tot} = W_r + W_{mp} + \sum W_{imp} \tag{2.3}$$

where W_{mp} is lattice multiphonon decay rate and $\sum W_{imp}$ is the sum of all impurity multiphonon decay rate [39]. Whilst the exact mechanisms underlying some of these decay processes can be complex, the model described by Layne [158] has usually been found to be an acceptable approximation for W_{mp}. Under this description, if the energy gap to the nearest lower Stark manifold of the rare-earth ions is ΔE, then normally p phonons from the lattice are needed to bridge this gap, where $p = \Delta E/\hbar\omega_{lattice}$. For energy gaps that can be bridged by a few phonons, the multiphonon rate can be expressed empirically as follows [39, 159]:

$$W_{mp}(T) = \beta[1 + n(T)]^p e^{-\alpha\Delta E} \tag{2.4}$$

where $n(T)$ is the number of thermally generated phonons per lattice mode at absolute temperature T, which can be defined through the Bose-Einstein equation as:

$$n(T) = [exp(\hbar\omega/kT) - 1]^{-1} \tag{2.5}$$

β is a material constant, ΔE is the energy gap between two successive levels, and α is expressed by

$$\alpha = -(\hbar\omega)^{-1} ln(\epsilon) \tag{2.6}$$

where, ϵ is the coupling constant.

α, β and ϵ are dependent on the host but independent of the specific electronic level of the rare-earth ion from which the decay occurs. Typical non-radiative parameters for different glass hosts are shown in Table 2.2.

It is clear for a given glass host, the probability of non-radiative relaxation between two energy levels depends on the energy gap ΔE and how many phonons are required to bridge this gap. Amongst all the host materials listed in Table 2.2, chalcogenide glasses have the lowest minimum phonon energy, and the five to seven orders of magnitude lower multiplicative β factor. This determines that chalcogenide glasses have the lowset non-radiative relaxation probability, therefore longer wavelength emissions that could not be realised in other hosts due to high phonon energy could be expected in chalcogenide hosts.

Table 2.2 Typical non-radiative parameters for different glass hosts (a from [67]; b from [160]).

Glass	β (s^{-1})	α (cm)	$\hbar\omega$ (cm^{-1})	ϵ
Phosphate[a]	$5.4x10^{12}$	$4.7x10^{-3}$	1200	0.0036
Silicate[a]	$1.4x10^{12}$	$4.7x10^{-3}$	1100	0.0057
Germanate[a]	$3.4x10^{10}$	$4.9x10^{-3}$	900	0.012
Tellurite[a]	$6.3x10^{10}$	$4.7x10^{-3}$	700	0.037
Fluoride[a]	$1.88x10^{10}$	$5.77x10^{-3}$	500	0.056
Borate[b]	$2.9x10^{12}$	$3.80\ x10^{-3}$	1400	0.0048
Ge-Ga-S[b]	$8.13x10^{5}$	$2.83\ x10^{-3}$	350	0.371
Ge-As-S[b]	$2.56x10^{6}$	$2.95\ x10^{-3}$	350	0.356
La-Ga(Al)-S[b]	$1x10^{6}$	$2.9\ x10^{-3}$	350	0.362
Chalcogenide[a]	$1x10^{6}$	$2.9x10^{-3}$	300	0.419

2.2.2 Absorption and emission cross-section

(a) Absorption cross-section

Absorption cross-section can be established by direct light transmission measurements. To obtain an absorption spectrum, a broadband light source is usually used in conjunction with a monochromator to provide wavelength discrimination. When a sample is illuminated with beam of intensity $I_0(\lambda)$, the output power intensity $I(L,\lambda)$ can be written according to the Beer-Lambert law:

$$I(L,\lambda) = I_0(\lambda) exp(-\alpha(\lambda)L) \tag{2.7}$$

where $\alpha(\lambda)$ is the absorption coefficient and L is the optical path length of the sample along the propagation direction. The absorption cross-section $\sigma_a(\lambda)$ is then defined as the absorption coefficient, $\alpha(\lambda)$, normalised by the ion concentration, N:

$$\sigma_a(\lambda) = \frac{\alpha(\lambda)}{N} = \frac{1}{NL} ln \frac{I_0(\lambda)}{I(L,\lambda)} \tag{2.8}$$

(b) Emission cross-section

The estimation of the emission cross-section is more complicated than the absorption cross-section. When it is not straightforward to measure both the absorption and stimulated emission cross-sections for a rare-earth ion doped material, the Einstein *A* and *B* coefficients for a two-level system are often employed to calculate one from the other. In a two level system, both lower state (level 1) and upper state (level 2) are split into multiple components, and the following relationship holds [161]:

$$g_1 \int v^2 \sigma_a(v) dv = g_2 \int v^2 \sigma_e(v) dv \tag{2.9}$$

where g_i is the degeneracy of level i, v is the photon frequency, σ_a and σ_e are absorption and emission cross-sections, respectively. This equation is a more general form of the Ladenburg-Fuchtbauer relationship [162], and the validity condition in a rare-earth ion system is that either the two levels must be equally populated, or all the transitions must have the same rate. Unfortunately, erbium ion doped glasses cannot meet either of these conditions. The manifold width of the $^4I_{15/2}$ and the $^4I_{13/2}$ states of erbium ion doped glass are typically a few meV (300-400 cm^{-1}), which is larger than kT=200 cm^{-1} at room temperature. In addition, low temperature absorption and emission measurements indicate the transition strength is sensitive to the Stark levels involved, making it impossible for all transitions to have the same rate. If an emission spectrum is captured and the metastable state radiative lifetime is accurately measured, then a formula derived from the Ladenburg-Fuchtbauer relationship can be applied to calculate the emission cross-section [97, 161]:

$$\frac{1}{\tau_e} = \frac{8\pi n^2}{c^2} \int v^2 \sigma_e(v)\, dv = 8\pi n^2 c \int \frac{\sigma_e(\lambda)}{\lambda^4} d\lambda \tag{2.10}$$

where τ_e is the radiative lifetime of metastable state, n is the refractive index of the host material, c is the light velocity in vacuum, and σ_e is emission cross-section. This method is known to work well for erbium ion doped fluorophosphate glass [161].

On the other hand, a relationship between absorption and emission cross-sections was proposed by McCumber in 1964 [156], as follows:

$$\sigma_e(v) = \sigma_a(v) exp\left(\frac{\varepsilon - hv}{kT}\right) \tag{2.11}$$

where σ_e is the stimulated emission cross-section, v is the photon frequency, h is Plank's constant, k is the Boltzmann constant, and ε is the effective energy required to excite one Er^{3+} from the lower state of interest to the upper state of interest at temperature T. The only assumption required by this theory is the time needed to establish a thermal distribution within each manifold must be shorter than the lifetime of the manifold. Thus, an accurate value of ε is essential to calculate emission cross-sections.

Miniscalco and Quimby [161] suggested a simple method for approximation of ε by using the room temperature absorption and emission spectrum half-width. The ion distribution between the ground level and excited level can be described as follows [161]:

$$\frac{N_1}{N_2} = exp\left(\frac{\varepsilon}{kT}\right) \tag{2.12}$$

where N_1 and N_2 are the equilibrium population of ground level and excited level at temperature T. For Er^{3+}, if all eight Stark components of the ground state $^4I_{15/2}$ and seven Stark components of the excited state $^4I_{13/2}$ are known, the ion distribution can also be expressed as [161]:

$$\frac{N_1}{N_2} = \frac{1}{exp(-E_0/kT)} \times \frac{1+\sum_{j=2}^{8} exp(-E_{1j}/kT)}{1+\sum_{j=2}^{7} exp(-E_{2j}/kT)} \tag{2.13}$$

where E_0 is the separation between the lowest components of each manifold, E_{ij} is the energy difference between the jth and the lowest component of level i. The electronic structure could be simplified by assuming the Stark levels for a given manifold are equally spaced, which means $E_{ij}=(j\text{-}1)E_i$. This reduces the unknown parameters from 14 to 3: E_0 and the manifold spacing ΔE_1 and ΔE_2. From low temperature measurement results, the absorption and emission peaks corresponding to the transition between the lowest components of each manifold, therefore, the average value of absorption and emission peaks are taken as the value of E_0. Also the seven ΔE_1 spaced levels are chosen based on the low-energy half-width of the room temperature emission spectrum, while the six ΔE_2 spaced levels are chosen from the high-energy half-width of the room temperature absorption spectrum accordingly. With these three parameters (E_0, ΔE_1 and ΔE_2), the N_1/N_2 value is calculated, then according to equation 2.12, the parameter ε, which is essential to emission cross-section calculation, could be extracted. The accuracy of the calculated emission cross-section using this method was verified by Miniscalco and Quimby in Al/P-silica fibre and fluorophosphate glasses [161]. This method is also widely applied on rare-earth ion doped chalcogenide glass hosts with reasonable accuracy [48, 120, 163, 164].

(c) Maximum pump efficiency

Knowing the absorption and emission cross-sections, the fraction of ions in the $^4I_{13/2}$ metastable state can be estimated as a function of excitation wavelength. Under high-power excitation, the expression for the maximum achievable excited state fraction is [97]:

$$\eta_{max} = \frac{n_2}{n} = \frac{\sigma_a(\lambda_p)}{\sigma_a(\lambda_p)+\sigma_e(\lambda_p)} \tag{2.14}$$

where n is the total Er^{3+} concentration, n_2 is the population of the $^4I_{13/2}$ state, σ_a is the absorption cross-section, σ_e is the emission cross-section and λ_p is the excitation wavelength.

2.2.3 Judd-Ofelt theory

In order to determine the transition probabilities or oscillator strength of any particular transitions between energy levels in rare-earth ions, a theory was proposed independently by Judd and Ofelt in the 1960s [165, 166], since termed the Judd-Ofelt theory. Since its proposal, it has been widely applied to calculate $4f$ transition intensities of rare-earth ions doped in many hosts. This method is based on three Judd-Ofelt parameters $\Omega_{2,4,6}$ calculated from experimental data normally obtained from ground state absorption spectra. With these three parameters, important spectroscopic characteristics like the spontaneous emission probabilities, the radiative lifetimes, the oscillator strengths, the branching ratios and the quantum efficiency of the levels can be evaluated.

The relationship between transition oscillator strength and integrated absorption for a particular transition is given by:

$$f = \frac{mc}{\pi e^2 N}\frac{9n}{(n^2+2)^2}\int k(\lambda)d\lambda \tag{2.15}$$

where N is the number density of rare-earth ions in the glass, m and e are the mass and charge of electron, c is the vacuum velocity of light, n is the refractive index, and $k(\lambda)$ is absorption coefficient at wavelength λ, which can be measured from experiment [146].

On the other hand, the oscillator strength of a transition from a level J to a level J' can be expressed theoretically as follows:

$$f(J{:}J') = \frac{8\pi^2 mc}{3h(2J+1)\lambda n^2} \times [\chi_{ed}S_{ed}(J{:}J') + \chi_{md}S_{md}(J{:}J')] \tag{2.16}$$

where h is the Planck's constant, $S_{ed}(J{:}J')$ and $S_{md}(J{:}J')$ are the electric and magnetic dipole transition line strengths, respectively; $\chi_{ed} = n\,(n^2+2)^2/9$ and $\chi_{md} = n^3$ are the local field correction factors for electric dipole moment transition and for magnetic dipole moment transition, respectively [167].

The contribution given by electric dipole to the line strength can be expressed as follows, based on Judd-Ofelt theory:

$$S_{ed}(J{:}J') = \sum_{t=2,4,6} \Omega_t \left| \langle 4f^N(SL)J \| U^{(t)} \| 4f^N(S'L')J' \rangle \right|^2 \qquad (2.17)$$

While the line strength resulting from magnetic dipole transitions is expressed by:

$$S_{md}(J{:}J') = \frac{h^2}{16\pi^2 m^2 c^2} \left| \left\langle 4f^N(SL)J \right\| \overrightarrow{L} + \overrightarrow{2S} \left\| 4f^N(S'L')J' \right\rangle \right|^2 \qquad (2.18)$$

where the three terms $\langle \| U^{(t)} \| \rangle$ are the reduced matrix elements of the unit tensor operator whose values depend on the rare-earth ion type, and details are given in ref [168]. The coefficients $\Omega_{2,4,6}$ are intensity parameters which depend on the glass matrix. By fitting experimentally obtained oscillator strengths with this theoretical expression via least squares fitting, the Judd-Ofelt parameters $\Omega_{2,4,6}$ can be extracted. These parameters then allow one to characterise all aspects of emission from the ions in that host.

As the $\Omega_{2,4,6}$ parameters do not depend on the rare-earth ion transition levels, the spontaneous emission probabilities between J and J' can be calculated from the following equation:

$$A(J'{:}J) = \frac{64\pi^4 e^2}{3h(2J'+1)\lambda^3} \times [\chi_{ed} S_{ed}(J'{:}J) + \chi_{md} S_{md}(J'{:}J)] \qquad (2.19)$$

If there is more than one transition related with level J', the ratio among each transition can be determined by:

$$\beta(J;J') = \frac{A(J;J')}{\sum_{J'} A(J;J')} \qquad (2.20)$$

and the radiative transitions rates can be calculated by:

$$W_J^R = \frac{1}{\tau_R} = \sum_{J'} A(J;J') \qquad (2.21)$$

Although the unambiguous interpretation of J-O parameters has always been challenging, in general, it is agreed that smaller values of the Ω_2 parameter indicates chemical bonds that have ionic rather than covalent character, while low Ω_4 and Ω_6 values may be due to high rigidity of the host matrix [121]. Also it is believed that parameter Ω_2 is related with asymmetry of the crystal field on the rare-earth ion, the larger the Ω_2 the more asymmetric the glass host [169].

Typical values for J-O parameters in some glasses are summarized [169] in Table 2.3. (Added information a is cited from ref [170], b is from [136], and c is from [171]).

Table 2.3 Typical value of Judd-Ofelt parameters in some glasses.

Glass	Ω_2 (x10^{-20} cm^2)	Ω_4 (x10^{-20} cm^2)	Ω_6 (x10^{-20} cm^2)
Fluorophosphate	2.90	1.63	1.26
Germanate	4.81	1.41	0.48
Silicate	4.23	1.04	0.61
Aluminate	5.60	1.60	0.61
Fluoride	2.90	1.27	1.11
Phosphate	3.89	1.01	0.55
Tellurite	5.05	1.45	1.22
Bismuth	3.86	1.52	1.17
Chalcogenide (Ge-Ga-S)[a]	6.9±0.1	2.19±0.02	1.05±0.01
Chalcogenide (Ge-As-S)[b]	6.98	2.53	0.78
Chalcogenide (GeGaSbS)[c]	8.7	2.5	1.4

Amongst all the rare-earth ion host materials listed in Table 2.3, the big Ω_2 values chalcogenide glasses have imply their covalent character of chemical bonds. Also, the relatively high Ω_4 values of chalcogenide glasses indicate the less rigidity of the host matrix. As a result of the widely varying J-O values for the same rare-earth ion in different host materials, the emission parameters also vary widely. Taking Er^{3+} for example, in silicate hosts the ${}^4I_{13/2}$ energy level lifetime can exceed 10 ms [172], while in chalcogenide glass host the number drops to around 4 ms [119], but still long enough for applications such as amplifiers and lasers. In Table 2.4, the reported emission properties of Er^{3+} in different glass hosts are summarised.

Table 2.4 Emission properties of $^4I_{13/2}\rightarrow{}^4I_{15/2}$ transition of erbium ion in different host materials [2, 154, 173], and FWHM refers to full width at half maximum.

Glass hosts	Refractive Index at 1.5 µm	Peak emission cross-section / cm^2	Emission FWHM bandwidth / nm	Lifetime / ms	Maximum Er^{3+} concentration	Max phonon energy / cm^{-1}
Silica	~1.5	$7x10^{-21}$	20	12	$\sim 3x10^{19}$ ions/cm^3	1200
Alumina	~1.7	$6x10^{-21}$	55 [174]	8	$>3.4x10^{20}$ ions/cm^3 [175]	1000
Aluminosilicate	~1.6	$6x10^{-21}$	43	10	500 ppm ($\sim 1x10^{19}$ ions/cm^3)	1100
Phosphosilicate	~1.6	$6x10^{-21}$	27	10	2.5 at% ($\sim 5x10^{20}$ ions/cm^3)	1200
Tellurite [176, 177]	~2.1	$13x10^{-21}$	80	4	$1x10^{21}$ ions/cm^3 (10 mol% in TeO_2-WO_3-La_2O_3 [178])	700
Chalcogenide (sulfide based) [130]	~2.4-3	$15x10^{-21}$	45	2.5	$1x10^{19}$ ions/cm^3	400
ZBLAN [179]	1.5	$4.2x10^{-21}$	82	9	$7.9x10^{20}$ ions/cm^3	500

Among these hosts, erbium ion doped chalcogenide glass has the highest refractive index, emission cross-section, and the lowest maximum phonon energy, along with reasonable full width at half maximum (FWHM) bandwidth and erbium ion solubility. All of these make chalcogenide glasses competitive candidate for erbium ion doped amplifier/lasers.

2.3 Energy migration processes in rare-earth ion doped materials

2.3.1 Ion-Ion interactions

At low dopant concentration, the average distance between two adjacent ions is sufficiently large that the interactions between separate ions can be neglected. As the dopant concentration increases, the average inter-ion distance decreases, and thus ion-ion interactions involving excited state energy transfer start to occur. Such interactions can occur between rare-earth ions of the same or different species. Within the same rare-earth ion type, ion-ion interaction leads to either a non-radiative loss mechanisms or luminescence from unwanted transitions. Between different rare-earth ions, it can offer new pumping schemes to extend the selection of pumping sources, or a means to de-excite targeted energy levels in four or more state lasing mechanisms [154], and also in 3 level systems, e.g. Ce^{3+} & Eu^{3+} with Er^{3+} in TeO_2 for 980 nm pumping [180, 181].

Ion-ion interactions due to multipolar interactions between neighbouring rare-earth ions have been carefully studied. Based on Auzel's research [149], the probability for energy transfer between two ions at a sufficiently large distance R can be written as:

$$P = \frac{1}{\tau_s}\left(\frac{R_0}{R}\right)^6 \qquad (2.22)$$

where τ_s is the actual lifetime of the sensitizer (the ion which is being first directly excited) excited state, including multiphonon non-radiative decay, and R_0 is the critical transfer distance for which excitation transfer and spontaneous deactivation of the sensitizer have equal probability.

However, Dexter pointed out that this theory could be extended to include higher multipole and exchange interactions [182]. Thus, the energy transfer probability for electric multipolar interactions can be modified as follows:

$$P = \frac{1}{\tau_s}\left(\frac{R_0}{R}\right)^s \qquad (2.23)$$

where s=6 for dipole-dipole interactions, s=8 for dipole-quadrupole interactions, and s=10 for quadrupole-quadrupole interactions [149].

Normally, in a single rare-earth ion containing system, a number of different ion-ion interactions may occur, the most important of which are outlined in the following section. The erbium ion is chosen as an example to illustrate the mechanism of each process.

2.3.2 Up-conversion process

Up-conversion emission is an important phenomenon in rare-earth ion doped materials. Emissions of higher energy than that of the excitation light are seen, which is due to the so called anti-Stokes emission or up-conversion process. There is quite a number of possible up-conversion mechanisms in rare-earth ion doped materials, of which the most important include: energy transfer up-conversion (ETU), excited state absorption (ESA), cooperative sensitization, cooperative luminescence and 2-photon absorption excitation [149, 154].

(a) Energy transfer up-conversion (ETU)

The process of up-conversion by sequential energy transfers, also named APTE (for 'addition de photon par transferts d'energie') by Auzel [149]. In this case, energy transfers from one ion already in some excited state to another excited ion, which may be in a different excited state, to promote it to a higher energy state. Resonance or phonons may be involved to help match the energy difference in a real case. In an Er^{3+} ion system for example, with 1490 nm excitation, two ions are excited into the $^4I_{13/2}$ metastable state. If ETU occurs, then one ion will transfer its energy to the other and decay to the ground state, whilst the one receiving the energy will be promoted to the higher energy level $^4I_{11/2}$, corresponding then to the 800 nm emission. The process can also apply to ions in different excited states, for example, an ion in the $^4I_{11/2}$ level can receive energy from an excited ion in the $^4I_{13/2}$ level and be further promoted to the $^4S_{3/2}$ level to radiate 530 nm. The schematic energy level diagram for ETU process is shown in Figure 2.2 (a).

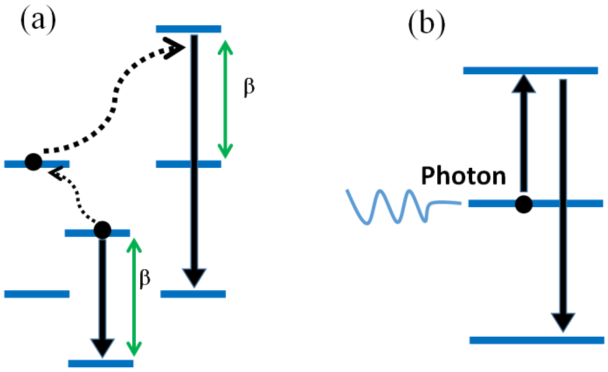

Figure 2.2 Schematic energy level diagram showing the ETU (a) and ESA (b) [149].

In ETU then, only the matching of the energy difference between the upconversion level and the de-excitation levels involved matters rather than the absolute energy, therefore this process applies potentially to many up-conversion wavelengths [149].

(b) Excited state absorption (ESA)

In this process, an ion in an excited state absorbs another pump or signal photon, and is further excited into a higher energy level. Obviously, this process requires the availability of an energy level which is roughly a pump or signal photon energy above the current level to occur. For example, in the Er^{3+} system, an ion in the $^4I_{13/2}$ state absorbs another 1490 nm photon and promotes to the $^4I_{9/2}$ state. The upper state excited ion could return to the metastable level by multiphonon relaxation or radiative decay, or back to the ground state with a high energy photon emission, 800 nm emission in the case of Er^{3+}. The schematic energy level diagram for this process could be found in Figure 2.2 (b). ESA reduces the excitation efficiency as pump photons are lost to either heat or emission at unwanted wavelengths. In the case of signal photons, it can also clamp the extent of the gain window. Examples of this process are shown in ref. [183, 184].

(c) Cooperative sensitization

In cooperative sensitization, two ions in the metastable state give their energy to a third ion thereby decaying to the ground state. The third ion which accepts the energy will be promoted to an excited state around the sum of the energies of the de-excited ions from its ground state. An Yb^{3+}/Tb^{3+} co-doped system makes a good example of this process. Tb^{3+} ions at ground state accept energy from two Yb^{3+} ions of the $^2F_{5/2}$ excited states, and then the Tb^{3+} ions is promoted to the $^5D_4$ excited state, while the two Yb^{3+} ions return to their $^2F_{7/2}$ ground state. Example of this process could be found in ref [185].

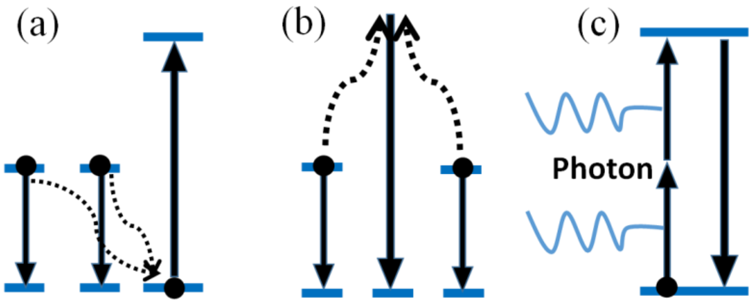

Figure 2.3 Schematic energy level diagram showing the cooperative sensitization (a), cooperative luminescence (b) and 2-photon absorption excitation (c) [149, 154].

Cooperative luminescence is a radiative process in which two metastable level ions simultaneously de-excite to emit one photon with the sum of their excitation energies [149]. Two-photon absorption excitation is that where the ion absorbs two photons simultaneously to promote it into a higher energy state. Due to the lack of interaction with the medium, the efficiency of these two processes is relatively low. Research on these phenomena can be found in ref [186]. Schematic energy level diagrams of cooperative sensitization, cooperative luminescence and 2-photon absorption excitation are shown in Figure 2.3.

From Auzel's reports [149], the relative efficiency of ETU is much higher than the other processes, almost two orders of magnitudes higher than the efficiency of two-step absorption and three orders of magnitudes higher than that of cooperative sensitization. The efficiency of different up-conversion processes in some materials is listed in Table 2.5.

Table 2.5 Comparison of efficiency of different 2-photons up-conversion processes [187]

Mechanism (section)	Efficiency /cm^{-2} W^{-1}	Example
A.P.T.E (ETU) [2.2.2(a)]	$\sim 10^{-3}$	YF_3:Yb^{3+}:Er^{3+}
Excited state absorption (ESA) [2.2.2(b)]	$\sim 10^{-5}$	SrF_2:Er^{3+}
Cooperative sensitization [2.2.2(c)]	$\sim 10^{-5}$	YF_3:Yb^{3+}:Tb^{3+}
Cooperative luminescence [2.2.2(c)]	$\sim 10^{-8}$	Yb^{3+} PO_4
Second-harmonic generation (SHG)	$\sim 10^{-11}$	KDP
2-photon absorption and emission [2.2.2(c)]	$\sim 10^{-13}$	CaF_2:Eu^{2+}

KDP refers to Potassium Dihydrogen Phosphate (KH_2PO_4).

Although each up-conversion process has its own mechanisms, in reality, different up-conversion processes may occur simultaneously, and the final emission is always a combination of all processes involved.

2.3.3 Energy transfer

An ion in the metastable state may also interact with a nearby ground state ion, promoting it to the metastable state by passing over its energy. This can occur with both radiative and non-radiative pathways. In the radiative pathway, one ion decays from the metastable state to the ground state by emitting a photon which is immediately absorbed by the adjacent ground state ion promoting it into the metastable state. Schematic energy level diagram for this process is shown in Figure 2.4(a). This can cause a distortion of the emission spectrum as energy can be lost or gained [154] and also the so called ‘radiative trapping’ phenomenon that leads to a longer apparent lifetime especially in highly doped or large-volume samples [188]. On most occasions, the non-radiative energy transfer mechanism is more important, in which the energy transfers without emission and absorption of photons. Phonons are often involved to bridge the energy gap when the energy between related ions is not equal. This interaction can be explained by either the short-range exchange or long-range electric multipolar mechanisms [188]. Although radiative emission may still occur from the second ion that receives the energy, the probability of non-radiative decay is increased with each successive transfer, and hence this is always considered as a loss mechanism.

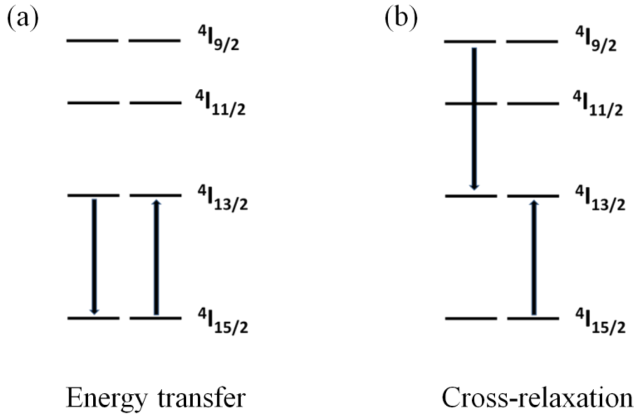

Figure 2.4 Schematic energy level diagram for energy transfer (a), and cross-relaxation (b), in Er^{3+} ion [154].

2.3.4 Cross relaxation

Cross-relaxation is the process where an ion at a higher excited state gives part of its energy to another ion at the ground state such that both end up in a metastable state. Schematic energy level diagram for this process is shown in Figure 2.4(b). Taking erbium ion as an example, the energy gap between the $^4I_{9/2}$ state and the $^4I_{13/2}$ state is similar to the gap between the $^4I_{13/2}$ state and the $^4I_{15/2}$ state, thus an ion in the $^4I_{9/2}$ state may give part of its energy to an ion in the $^4I_{15/2}$ ground state and then decay to the $^4I_{13/2}$ state, whilst the ground state ion receives the energy and is promoted to the $^4I_{13/2}$ metastable state. Obviously, this process may increase the population of the metastable state by the decay of ions from the higher excited state and also ion promotion from the ground state.

2.4 Concentration quenching

Concentration quenching is usually the term used to sum up the effects of the previously described ion-ion interactions which result in the decrease of rare-earth ion fluorescence efficiency with increasing concentration of the ion. In highly doped samples, the average distance between neighboring ions is short, thus the ion-ion interaction processes mentioned above (see Section 2.3) occur and the efficiency of fluorescence is degraded. Concentration quenching also manifests itself as a shortening of the metastable state lifetime, and the relation between lifetime and concentration has been expressed by an empirical formula [189, 190]:

$$\tau^{obs} = \frac{\tau_0}{1+(\rho/Q)^p} \tag{2.24}$$

where τ_{obs} is the observed fluorescence lifetime, τ_0 is the ideal fluorescence lifetime with zero concentration, ρ is the rare-earth ion concentration, Q is the quenching concentration and p is a phenomenological parameter characterizing the steepness of the corresponding quenching curve. Normally, the concentration Q with a lifetime τ equal to $\tau_0/2$ is defined as the quenching concentration in this material. Quenching concentrations of Er^{3+} in several different hosts are listed in the Table 2.6 [189].

Table 2.6 Quenching concentrations of Er^{3+} in several different hosts.

Type of glass	Q / ions cm^{-3}	τ_0 / ms	p
Sol-gel silicate $80SiO_2$-$20TiO_2$-$0.5Yb_2O_3$-$10Al_2O_3$ waveguide (mol%) [189]	$1.4x10^{20}$	6.4	1.27
Al_2O_3-GeO_2-SiO_2 fibre [191]	$1x10^{20}$	9.6	1.27
Borosilicate [192]	$8x10^{19}$	9.9	1.55
Phosphate [193]	2-$3x10^{19}$	14	2
Aluminate $58.5GaO$-$27.5Al_2O_3$-$8.4MgO$-$5.6SiO_2$ (wt%) [194]	$4x10^{18}$	7.6	0.97
Germanate $70GeO_2$-$24PbO$-$6PbF_2$ (wt%) [194]	$5.2x10^{18}$	7.3	1.74
Sulfate Ga_2S_3-GeS_2-La_2S_3 [195]	$3.2x10^{20}$	2.2	1.29
Alkali-borosilicate BGG 31 [195]	$<5.8x10^{19}$	>0.96	unknown
$Ge_{25}Ga_{10}Se_{65}$ (at%) (data from this work)	$3.6x10^{20}$	1.69	1.415

In this table BGG 31 refers to BaO-GeO2-Ga_2O_3 glass, Q is the quenching concentration, τ_0 is the ideal fluorescence lifetime with zero concentration and p is the phenomenological parameter characterizing the steepness of the corresponding quenching curve.

Amongst the host materials, chalcogenide glasses have the shortest lifetime due to their high value of Judd-Ofelt parameters and high refractive index [196]. In Ga containing chalcogenide glasses the quenching concentration is one of the highest, which means high dose rare-earth ions can be doped in Ga containing chalcogenide hosts to achieve high gain in a short length, which is favourable for compact devices.

2.5 Solubility of rare-earth ion in glasses

Rare-earth ions in any host may form crystalline or amorphous precipitates when the concentration exceeds a critical value. This can be in the form of clusters of rare-earth ions in compounds, alloys or glasses within the host matrix. Such processes are detrimental to photoluminescence either by ion-ion interactions between essentially bonded rare-earth ions or the formation of other compounds that are not optically active in the host. Rare-earth ion solubility varies with host material. Maximum concentrations for silicate glasses and phosphate glasses are in the range of 4-$9x10^{20}$ ions/cm^3 [154].

Tellurite glass is known to have high rare-earth ion solubility and can contain erbium ion of around 5 at% (~1x10^{21} ions/cm^3) without any evidence of clustering [176]. As the workhorse of the chalcogenide glass system, bulk As_2S_3 is considered to have a low erbium ion solubility [197]. In Gu et al.'s report, bulk samples of Er^{3+} doped As_2S_3 with nominal Er^{3+} concentrations from 0.02 to 4 wt% (~6x10^{20} ions/cm^3) were prepared. Unfortunately, in the X-ray pattern, the sample with the highest Er_2S_3 dopant concentrations exhibited weak, sharp-line X-ray diffraction pattern which were consistent with the polycrystalline Er_2S_3 source materials, indicating the existence of precipitates and cluster in the host material [143]. Amongst the family of chalcogenides, gallium-containing materials have been proven to have better rare-earth ion solubility. In the Ge-Ga-Se/S system, Er^{3+} ion of up to 2 at% (~ 2x10^{20} ions/cm^3) illustrated that erbium ion could be well dispersed and optically active [198, 199], implying the potential in compact planar waveguide amplifiers.

2.6 Conclusion

This chapter covered the basic theory of rare-earth ion doped materials. Concepts related to rare-earth ion doped materials such as lifetime, absorption/emission cross-section and maximum pump efficiency were discussed in detail. Judd-Ofelt theory was introduced as a tool to predict the transition probabilities or oscillator strength of transitions between energy levels. Energy migration processes in rare-earth ion doped materials were catalogued by their mechanisms. Concentration quenching and solubility of rare-earth ion in glasses, including chalcogenide glasses, were discussed.

Chapter 3

Co-thermal evaporation of erbium ion doped As_2S_3 waveguides

3.1 Diarsenic trisulfide: As_2S_3

3.1.1 Background of As_2S_3

Diarsenic trisulfide (also known as and hereafter referred to as arsenic trisulfide), As_2S_3, as a member of chalcogenide family, has been well studied in the past several decades. Besides the generic chalcogenide properties it possesses, as a bulk glass it has particularly good chemical stability and resistance to crystallization, a high optical damage threshold, usefully large optical nonlinearity, a relatively large optical bandgap, and can easily be deposited by thermal evaporation. These characteristics have made it the subject of many studies since the 1970s in bulk glass, fibre and waveguide forms.

The first study resulted from the desire to make glass with transparency beyond 3-5 µm, initially using sulfur-based glasses by Frerichs in the 1950s [200]. Jerger and Fraser of Servo Corporation then developed useful As-S based glasses in 1953 [201].

The first As-S core-clad fibres were fabricated by Kapany and Simms in the early 1960s, though with a relatively high loss of around 20,000 dB/km at 5.5 µm [202]. The loss of chalcogenide fibres was subsequently reduced significantly over the intervening years to 35 dB/km at 2.44 µm in an As_2S_3 unclad fibre in Kanamori et al.'s report of 1984 [203].

As_2S_3 also became the workhorse material for studies into planar waveguide nonlinear optics e.g. [4, 62, 64, 66, 204-206]. Various methods have been used to realise high quality waveguides based on As_2S_3 films. In Zoubir et al.'s report, channel waveguides were laser written in As_2S_3 thin films [207]. By using focused femtosecond pulses from a 25-MHz repetition rate Ti:sapphire laser, 2 cm long waveguides were fabricated with refractive index differentials $\Delta n > 10^{-2}$. The obtained waveguides showed reasonable light confinement ability by confining more than 70% of the launched light exiting the film end face in the channel waveguide. Wet etching is another way to fabricate chalcogenide glass waveguides. In Su et al.'s report, a focused laser beam was applied to form waveguide patterns on an As_2S_3 film deposited using thermal evaporation [208]. The exposed and unexposed As_2S_3 thin films had different etching rates in I_2 and CS_2 solutions, as a result, a ridge waveguide structure was obtained with this method. However, rough surfaces were observed on the scanning electron microscope (SEM) image of the etched ridge waveguide, leading to an average loss of 5.5±0.5 dB/cm at 1330 nm. As_2S_3 waveguides fabricated through hot embossing were demonstrated in [209]. The propagation loss of such waveguides was reported at 0.52 dB/cm for the transverse electric (TE) polarization and 0.41 dB/cm for the transverse magnetic (TM) polarization at 1550 nm for a waveguide cross-section dimension of 3.8 × 1 µm. Dry etching has proven to be a promising way to fabricate chalcogenide waveguides. Ruan et al. reported As_2S_3 rib waveguide losses as low as 0.25 dB/cm at 1550 nm achieved using dry etching with CF_4 and O_2. With the obtained waveguides, a phase shift $\sim\pi$ due to self phase modulation has been obtained using a ~40 W peak power pulse in a 5 cm long waveguide [12]. Madden et al. using a different dry etching recipe (using CHF_3 instead of CF_4), and obtained As_2S_3 rib waveguides with loss <0.05 dB/cm, which is the current lowest loss in chalcogenide waveguides [13].

3.1.2 Properties of As_2S_3

(a) Optical transparency

The transmission spectrum of a 37 mm optical path length As_2S_3 sample and of a 2 mm optical path length As_2S_3 plate are shown in Figure. 3.1. The useful transmission window for planar devices made from As_2S_3 is from ~0.8-8 µm. At the short wavelength side, below 0.7 µm, the Urbach absorption edge and the weak absorption tail (WAT) occur inducing a fast increase in absorption. Also an absorption band at 4 µm, corresponding to the S-H vibrations, appears in the curve as well.

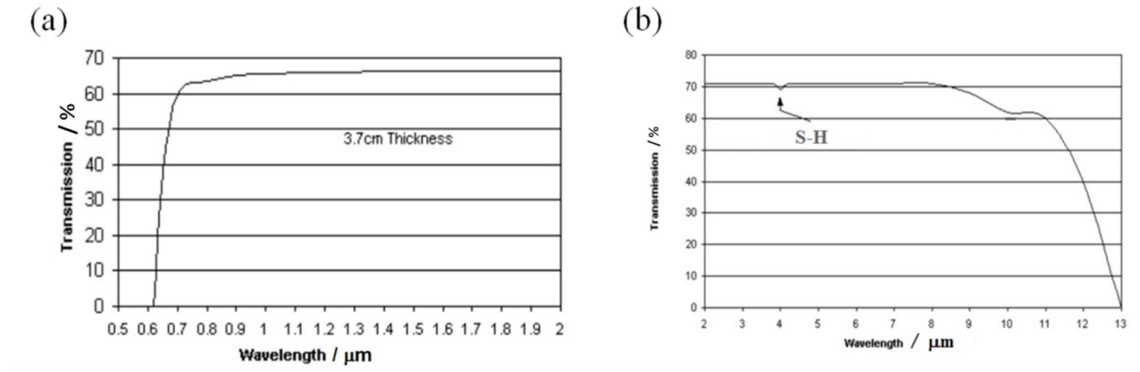

Figure 3.1 Absorption edge from a 37 mm optical path length As_2S_3 sample (a); transmission spectrum (uncorrected for reflection losses) from a 2 mm optical path length As_2S_3 sample (b) [210].

(b) Refractive index

The refractive index of bulk As_2S_3 is 2.438 at 1.53 µm, and drops with increase of wavelength [211]. The high refractive index enables strong optical field confinement and hence small waveguide bend radius and small optical mode area with enhanced optical intensities. These are critical characteristics for application in integrated optics and efficient nonlinear interactions. The zero dispersion wavelength for As_2S_3 material lies in the MIR at 4.9 µm, and there is strong normal dispersion at telecommunication wavelengths (1.55 µm) of ~-360 ps nm^{-1} km^{-1}. Thus dispersion engineering is normally required to shift the zero dispersion wavelengths in practice for telecoms NLO applications [212]. Figure 3.2 shows the refractive index and dispersion curve for As_2S_3.

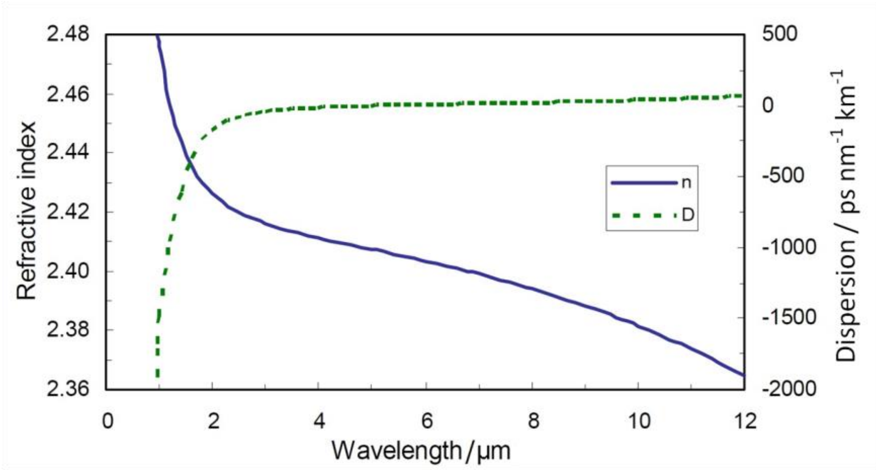

Figure 3.2 Refractive index and dispersion curve of As_2S_3 [59].

(c) Raman spectrum

Raman spectroscopy provides information about bond structure via molecular vibrations, and thus is widely used for sample identification and quantification in materials science. A typical Raman spectrum of bulk As_2S_3 glass has been reported in the literature [213-216], and Raman spectrum of an in-house made bulk As_2S_3 glass under 830 nm excitation measured in our lab is shown in Figure 3.3. The spectrum is strongly dominated by the band at 345 cm^{-1} attributed to the symmetric stretching vibrational mode of $AsS_{3/2}$ pyramids. Besides this strong bond, there are two weak shoulders at 315 cm^{-1} and 390 cm^{-1} on both sides of the 345 cm^{-1} band, which can be associated with asymmetric stretching modes of $AsS_{3/2}$ pyramids and As-S-As bridges, respectively. In the small Raman shift range, small bands at 190 cm^{-1} and 235 cm^{-1} corresponding to weak bonds that can be attributed to the bending modes of $AsS_{3/2}$ pyramids and S_8 and As_4S_4 molecules. The small band around 495 cm^{-1} associated with the S-S stretching vibration in S_8 rings indicates the presence of excess sulfur in this bulk glass.

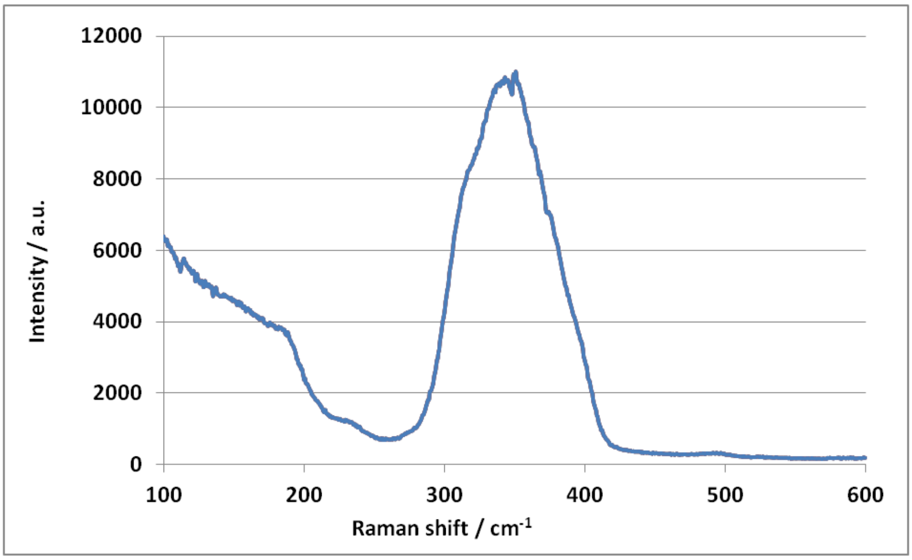

Figure 3.3 Raman spectrum of an in-house made bulk As_2S_3 glass under 830 nm excitation.

3.2 Erbium ion doped As_2S_3

3.2.1 Research in erbium ion doped As_2S_3 glasses

As the workhorse material for planar waveguides in the chalcogenide glass family, rare-earth ion doped As_2S_3 for amplification and lasing applications in the NIR and MIR range was promising and studied for decades. Besides properties that are preferable for a rare-earth ion dopant in a chalcogenide glass, such as low phonon energy (350 cm^{-1})

and wide transparency window, As_2S_3 has the advantage of a band gap in the green, meaning all tail absorption processes are low at common rare-earth ion pump wavelengths (e.g. 808, 980, 1064 nm). Unfortunately, bulk As_2S_3 glass cannot be doped without clustering at high enough concentrations for planar waveguide amplifiers [118, 197] to date blunting the advantages offered by the material. Thin films, however, offer an alternative perspective as they are formed under highly non-equilibrium conditions where there is insufficient time and thermal energy for clusters to form in the deposited film, leading to new opportunities for doped devices.

There are investigations on rare-earth ion (and particularly erbium ion) doped As_2S_3 films and waveguides [128, 130, 217]. Fick et al. investigated Er^{3+} doped As_2S_3 films formed using thermal evaporation and subsequent ion implantation [130]. Emission cross-sections up to 1.6×10^{-20} cm^2 were measured for the $^4I_{13/2} \rightarrow {}^4I_{15/2}$ transition that is two times higher than for Er^{3+} doped silica glass. A 2.3 ms lifetime of the $^4I_{13/2}$ metastable state under 983 nm pumping was achieved from planar samples with Er^{3+} concentration of ~5×10^{18} ions/cm^3. Due to the low phonon energies of chalcogenide glasses, a relatively long lifetime of the $^4I_{11/2}$ excited state was measured of the order of 0.25 ms. Improvements in PL intensity of up to almost 10x were seen in some cases after annealing the films just below the glass transition temperature at 165 °C for 2 hours. Lifetime was also improved by the post implant anneal but only by about 10%.

Highly erbium ion doped films (~4 at%) were produced using co-evaporation of As_2S_3 and Er_2S_3 by Lyubin et al. [128]. Emission at 1.54 μm, was about 3x the intensity that of similarly doped GeGaS bulk glass. A linear PL intensity dependence on the excitation laser intensity was observed. Photostructural transformation phenomena were also studied by using an installation with two linearly polarized lasers, an.Ar^+ laser (488 nm, 10 mW), acting as the inducing beam, and a He–Ne laser (633 nm, 0.1 mW) working as a probing beam. They concluded that although the transparency of the Er^{3+}-doped film decreased, the photodarkening effect in the doped film was smaller than in the non-doped film.

Fuchs et al. [217] studied the spectral properties of Er^{3+} doped As_2S_3 films deposited using RF sputtering. An As_2S_3 glass disc with a piece of erbium metal partly covering its surface was used as sputtering target. After thermal annealing at 150 °C, a 4 ms PL decay lifetime of the 1.55 μm emission was measured when pumped at 977 nm,. The annealing also led to an increase in the PL intensity of up to 40x when measured in slab waveguide geometry. Erbium ion concentrations were estimated at ~1 at% for the highest doped sample which had inferior PL performance compared to the lower doped samples with unknown concentrations.

Despite these promising results, and other work on alternative chalcogenide host materials, there has been, however, no report of amplification in erbium ion doped chalcogenide glass devices. To realise amplification in chalcogenide glasses, the emission properties in rare-earth ion doped chalcogenide glass must be well understood and available methods used to fabricate low loss waveguides. The Laser Physics Centre at the Australian National University has significant expertise in depositing and processing As_2S_3. As stated above (see Section 3.1.1), an As_2S_3 rib waveguide with record low loss of 0.05 dB/cm was achieved by photolithography and plasma etching [13] providing a good base for rare-earth ion doped amplifier studies in As_2S_3. Given the facilities and experience available, it was decided to make the first step with erbium ion doped As_2S_3.

3.2.2 Fabrication of bulk As_2S_3 glass

The As_2S_3 used here was fabricated using the conventional melt-quenching method, either in house or commercially sourced from Amorphous Materials Inc. In this method, high purity arsenic and sulfur (*5N*) were weighed inside a dry nitrogen glove box and loaded in the required proportions into a pre-cleaned quartz ampoule. The ampoule was then sealed under vacuum (~10^{-4} Pa) using an oxygen-hydrogen torch, and introduced into a rocking furnace for melting of the contents at ~800 °C. The melt was then homogenized for periods typically exceeding 12 hours, before the ampoule was removed from the rocking furnace and water-quenched. The resulting glass boule was subsequently annealed at a temperature typically 20 °C below its glass transition temperature (T_g) of ~180 °C, before being slowly cooled down to room temperature. A piece of bulk As_2S_3 made in-house (without elemental purification) is shown in Figure 3.4. The starting elements may also be purified before glass making to remove oxygen, water, and carbon contaminants. Details on starting element purification can be found in ref [218].

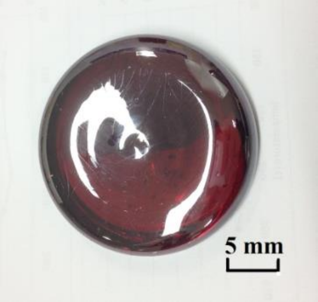

Figure 3.4 Typical in-house made bulk As_2S_3 glass.

3.2.3 Erbium ion doped As_2S_3 film deposited using co-thermal evaporation

Different methods, such as RF sputtering [219], pulsed laser deposition [220, 221], chemical vapour deposition (CVD) [222], solvent based spinning [223, 224] or thermal evaporation [225] may be used for film deposition. Each method has its own advantages and drawbacks. Among these approaches, thermal evaporation is one of the most popular film fabrication methods for low loss waveguide devices [4, 13]. However, for most ternary and quaternary glasses (and especially those containing gallium and rare-earth ions), a large contrast in the saturated vapour pressure of these elements and their various compounds in the melt lead to severe difficulty in controlling the film composition using thermal evaporation. This usually leads to significant differences between the properties of as-deposited films and the bulk glass, often producing nearly rare-earth- [128, 130], and Ga-free films. Besides the stoichiometry of the film, physical parameters like refractive index of as-deposited films were found to be markedly different from bulk counterparts [225]. This also results in the films being highly photosensitive [213]. The significant difference between as-deposited films and bulk glass is likely because films are fabricated in non-equilibrium conditions. Therefore, an approach that can release the excess internal energy stored in the films and relax them back to the thermal metastable equilibrium state is required.

It has been reported that at room temperature the relaxation time for non-annealed As_2S_3 films made by electron beam evaporation to the equilibrium state is of the order of one year [226], but thermal annealing can accelerate this procedure. Also thermal annealing can remove the photo-structurally-induced photosensitivity, but residual photosensitivity remains, the origin of which is still not entirely clear [227, 228]. Also one should note that so far no film with properties identical to its bulk counterpart has been fabricated [229] [213].

As_2S_3 bulk glass cannot be doped sufficiently with rare-earth ion to avoid clustering, so whilst it evaporates above T_g [13, 227, 230], it is not a suitable starting point for erbium doped thin films. As a result co-thermal evaporation method was instead chosen to dope the film. Crushed As_2S_3 glass and an erbium source (Er metal pieces in this Chapter, Er_2S_3 and $ErCl_3$ in Chapter 5) were used in film deposition. The two sources had their own shutters and evaporation rate monitors, and thus theoretically any desired doping concentration could be achieved. An internal schematic of the co-thermal evaporation chamber manufactured by Angstrom Sciences is shown in Figure 3.5. Here the resistively heated boat at the bottom centre of the diagram was used to evaporate the As_2S_3, and one of the smaller furnaces in the group of five in the centre of the diagram was used for the erbium.

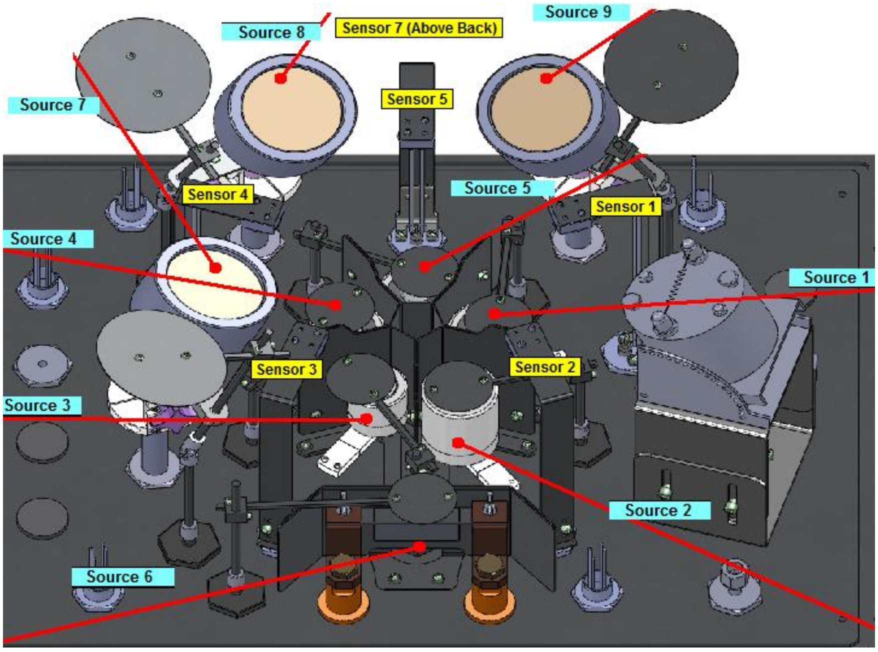

Figure 3.5 Internal view of the co-thermal evaporation chamber manufactured by Angstrom Sciences: 6 sources for co-thermal evaporation, and 3 guns for RF sputtering.

In the first experiment, erbium metal was used as the dopant. High purity As_2S_3 (made from 5*N* elements) and erbium metal were loaded into resistively heated sources. Each source had one quartz microbalance thickness monitor overhead to monitor the evaporation rate, and another monitor was placed above the shutter at the same height as the wafer to check the film thickness. Evaporation was performed at a vacuum level around ~$1x10^{-5}$ Pa and with a source-wafer distance of ~40 cm. After reaching a pressure set point of ~$6x10^{-4}$ Pa, the temperature of each source was slowly increased to ~280 °C over a 20 minute period to bake out the evaporants before ramping to the evaporation temperature and setting the individual rates. The erbium metal source was also ‘cleaned’ by heating up at evaporated temperature for 10-15 minutes with shutter closed to remove the possible contamination due to surface oxidation. Typical evaporation rates for As_2S_3 and erbium were fixed at 0.1 nm/s and 0.001 nm/s, respectively. After the desired evaporation rates were achieved, the shutter covering the wafers was opened and the evaporation started. When the film thickness read from the film thickness monitor reached the desired thickness set point, the system automatically closed all the shutters and ramped down the power for both sources gradually and allowed them to cool to <100 °C before venting the chamber.

It is well known that as-deposited As_2S_3 films degenerate easily through crystallization via surface diffusion under the influence of room light [231, 232], therefore, as soon as the films were removed from the chamber, a ~100 nm thick SU-8 (SU-8 2 from MicroChem Corp. diluted 1:4 with SU-8 GBL developer) layer was spin-coated and ultraviolet-cured (UV) on the film to prevent As_2S_3 evaporation at high temperature during the following thermal post-treatment and As_2O_3 crystallite formation on the surface [233, 234].

As previously noted, one of the issues in deposited films is that the as-deposited films are not identical with their bulk glass counterparts in terms of refractive index, bandgap, etc. [213, 225]. As a result of the highly non-equilibrium deposition conditions, thermally-evaporated As_2S_3 films tend to contain significant chemical and structural disorder such as As–As and S–S homopolar bonds, which are at lower concentrations in stoichiometric bulk glasses [213, 235].

Thermal annealing is a simple way to accelerate the relaxation of a film towards its metastable equilibrium state. During heat treatment, it has been reported that the properties of films tend to change and finally reach a condition close to their bulk counterpart [213]. In this research, thermal treatment of as-deposited films was carried out at temperatures of 130 °C for 24 hours in a vacuum oven (~10 Pa), which is below the glass transition temperature (T_g ~180 °C) and low enough to prevent cracking of the film after thermal treatment due to the large mismatch in thermal expansion coefficient of As_2S_3 (~$23x10^{-6}$/°C) and SiO_2 (~$0.5x10^{-6}$/°C).

Besides thermal treatment, it was reported that optical treatment with light illumination around the optical bandgap of the films, evolves the structure of the film in a similar way to thermal treatment [234]. Light treatment was carried out in the following way: the emission of an array of 100 W tungsten halogen reflector spotlamps was filtered using green band-pass gel filter (G28 from Lee Filters) to produce a spectrum extending from 500-570 nm which overlapped with the bandgap of As_2S_3 films. Then full 4-inch diameter wafers were exposed under the uniform light with an illumination intensity of 2-3 mW/cm^2 for 48 hours in the ambient atmosphere. In later experiments, the halogen lamps were replaced with green LED floodlights providing a uniform illumination ~8-10 mW/cm^2.

The thickness and linear refractive index (n) of the films were measured using a spectroscopic reflectometer (SCI FilmTek 4000) applying a Tauc-Lorentz model to fit the acquired data. In the FilmTek 4000 system, spectroscopic reflection data (400-1650 nm) were gathered at two different angles (normal incidence and ~70° incidence). The Lorentz oscillator parameters and the Tauc bandgap were the free variables used in a nonlinear fitting procedure to least squares fit to the measured reflectance data, and an iterative error minimization procedure employed to fine tune the model parameters and thickness. The system was capable of 1 part in 10^5 index/thickness accuracy for a layer of silica on silicon. Therefore, with this system, important film parameters such as thickness, optical bandgap of the material, and refractive index and dispersion from 400-1650 nm could be obtained.

The as-deposited, thermal and light treated films were tested in terms of thickness, refractive index at 1550 nm and bandgap, using the SCI FilmTek 4000 and the results are summarized in Table 3.1.

Table 3.1 Properties of As_2S_3 films with different treatment methods.

Type of treatments	Thickness / nm	Refractive index @1550 nm	Bandgap / eV
As-deposited	892	2.35	2.325
Thermal treatment (130 °C for 24 hours)	877	2.41	2.337
Light treatment (green light with intensity of 2-3 mW/cm^2 for 48 hours)	881	2.43	2.265

From the results, the film thickness decreased from 892 nm for an as-deposited film down to 877 nm and 881 nm after thermal or light treatment, respectively. This change is believed to be due to the consolidation of the films during the thermal or light treatment. The refractive index at 1.55 µm increased from 2.35 for an as-deposited film to 2.41 in the thermally treated sample, and 2.43 for the post-light-treatment sample, which is almost the refractive index of their bulk counterpart, indicating that both thermal and light treatment offered the similar effects that brought the as-deposited film back towards the bulk condition. As for the energy of bandgap, thermal treatment gave film a tiny increment, while the light treatment dropped it from 2.325 eV down to 2.265 eV, the reasons for this are unclear at present.

3.3 Characterization of erbium ion doped As_2S_3 films

3.3.1 Raman spectrum of erbium ion doped As_2S_3 film deposited using thermal evaporation

For Er^{3+} doped As_2S_3 films, the Raman spectrum was measured to check whether there were any structural changes between the doped film and its un-doped and bulk counterparts. The Raman spectrum of a 600 nm thick film with $1.8x10^{20}$ ions/cm^3 Er^{3+} doping (thermally treated at 130 °C for 24 hours) on a 1.5 μm thick thermally oxidized silicon (TOX) substrate was measured in a Horiba Jobin Yvon 64000 spectrometer system with a 50x NIR objective with numerical aperture (NA) of 0.75. A 630 nm laser was employed as the excitation source, and a charge-coupled device (CCD) detector installed on the spectrometer recorded Raman spectra. The power of the 630 nm excitation laser was set ~1 mW to avoid damage the sample surface. For comparison, bulk As_2S_3 glass and an As_2S_3 film without erbium ion doping (thermal treated at 130 °C for 24 hours) were also measured and the spectra are shown in Figure 3.6 with vertical offsets to aid viewing.

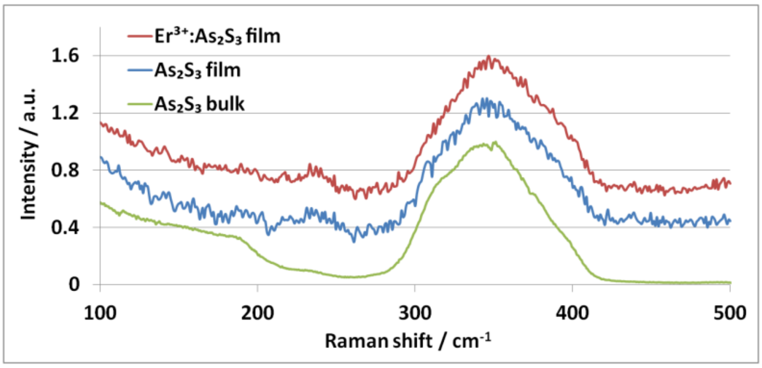

Figure 3.6 Raman spectra of: bulk As_2S_3 glass; As_2S_3 film (thermal treated at 130 °C for 2 hours) and Er^{3+}:As_2S_3 film (thermal treated at 130 °C for 2 hours), the spectra were recorded under 630 nm excitation.

Due to the small thickness of film, the signal to noise ratio dropped and a much longer acquisition time was required to get a reasonable spectrum. The band at 345 cm^{-1}, attributed to the symmetric stretching vibrational mode of $AsS_{3/2}$ pyramids, still dominates the whole spectrum. The shoulder at 315 cm^{-1} is hard to distinguish, while another shoulder around 390 cm^{-1} associated with asymmetric stretching modes of $AsS_{3/2}$ pyramids and As-S-As bridges is still traceable. Weak bands at 190 cm^{-1} and 235 cm^{-1} corresponding the bending modes of $AsS_{3/2}$ pyramids and S_8 and As_4S_4 molecules are still clear to see, but, it is obvious that the band at 235 cm^{-1} is stronger in films than in the bulk glass counterpart, indicating more S_8 and As_4S_4 structure are formed during film deposition. This is common in thin films [236, 237]. The Raman spectra from films with and without 0.6 at% erbium ion are very similar within the limits of low signal to noise ratio in Figure 3.6, implying the added erbium ions have no significant effect on the molecular structure of film.

3.3.2 Optical properties of erbium ion doped As_2S_3 film

(a) Lifetime and PL spectrum of erbium ion doped As_2S_3 films

There are two types of lifetime that are used to describe the decay curve. One is the 1/e lifetime of the captured decay curve, which is defined as the time to 36.8% of the fluorescence intensity after the pumping is turned off and includes all effects impacting the radiative decay. The other is the underlying (hereafter referred to as intrinsic) radiative lifetime, which is the lifetime the fluorescence has in the absence of population dependent processes, though this is still affected by some ion-ion interactions it is the best measurable approximation to the actual radiative lifetime.

To accurately measure the lifetime of thin films, an all-fibre confocal setup first proposed in [152] was used, the scheme of which is shown in Figure 3.7. Pumping power at 1490 nm or 980 nm was delivered to the edge of the film via a lens tipped fibre with 14 μm working distance. The lensed fibre produced a 2.5 μm $1/e^2$ diameter spot and was aligned to the edge of the film to couple the 1490 nm (or 980 nm) pump laser which was directly modulated with ~10 ms long pulses. The fluorescence was then coupled back into the lensed fibre and then the emission component around 1550 nm extracted with the pump power rejected by a chain of three 1490 nm (or 980 nm)/1550 nm wavelength division multiplexers (WDMs) providing in excess of 90 dB pump rejection. Detection was accomplished with a connectorised 150 μm diameter InGaAs diode and a fast, low noise Signal Recovery Inc. transimpedance amplifier. Data was captured on a PC equipped with a 16 bit analog to digital converter, and custom software enabled arbitrary amounts of trace averaging to remove noise [152]. The rise and fall time of the complete light modulation and detection system was less than 20 μs allowing accurate lifetime measurement even for sub-ms lifetimes. It should be noted that the capability of recording the photoluminescence intensity during lifetime measurement made the system usable in studying the relationship of PL versus pump power.

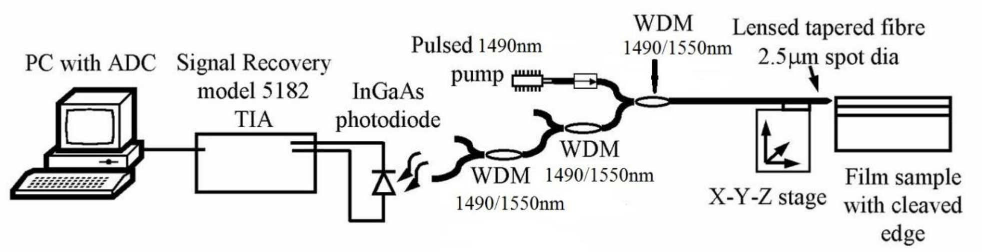

Figure 3.7 Optical set-up for PL lifetime measurement of Er^{3+}:As_2S_3 film [152].

Generally, the 1/e and intrinsic lifetimes are different, and the 1/e lifetime is always pump intensity dependent. The intrinsic lifetime is approximated as the measured decay rate of the PL once it decays >10-100x from its starting value. At this point, intensity dependent effects become weak and the number of excited ions has significantly reduced eliminating many of the ion-ion effects.

For the 1.8x10^{20} ions/cm^3 Er^{3+} doped As_2S_3 films pumped at 1490 nm with 350 kW/cm^2 intensity, the 1/e and intrinsic lifetime are 0.7 ms, and 0.9 ms, respectively. The difference between these two lifetimes indicates the presence of ion-ion interactions. The 1.55 µm PL decay curve of an Er^{3+}:As_2S_3 film is shown in Figure 3.8(a). If the 1.55 µm emission is strong enough not to fall into the noise floor of an optical spectrum analyser (OSA), replacing the photodiode with an OSA, the PL spectrum of the film can be obtained. A 1.55 µm emission spectrum from a 600 nm thick erbium ion doped As_2S_3 film is shown in Figure 3.8(b), where a broad emission band with peak centred at 1538 nm is clearly seen.

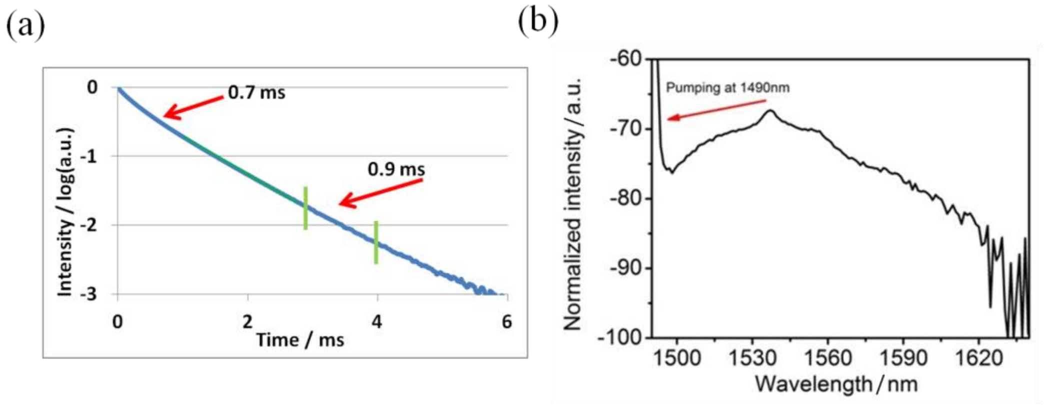

Figure 3.8 1.55 µm PL decay curve of an Er^{3+}:As_2S_3 film (a), and a PL spectrum of 1.55 µm emission (b), from as-deposited erbium ion doped As_2S_3 films under excitation at 1490 nm.

The dependence of lifetime and PL intensity on pump intensity was investigated in an Er^{3+}:As_2S_3 film with 1.8×10^{20} ions/cm^3 erbium ion concentration, and the results are shown in Figure 3.9. From the results, the 1/e lifetime drops from 0.7 ms under an excitation intensity of 10 kW/cm^2 to around 0.6 ms when the excitation intensity reaches 415 kW/cm^2. This dependence of the 1/e lifetime on the pump power indicates both ion-ion energy exchange effects and excited state processes are occurring when high excitation power is involved. The occurrence of ion-ion energy exchange effects may also be reflected in the trend of PL intensity increases with excitation power. If the sample is not close to the saturation region, the PL output power would be expected to be linear with pump power in the absence of energy exchange effects. The quadratic trend relationship between PL intensity and pump power observed (Figure 3.9 (b)) instead of a linear relationship indicates that radiative and non-radiative ion-ion energy exchange interactions are present in film. When measuring the PL emission with high pump intensity, weak green light (~10^{-13} W from the OSA spectrum) was observed to be emitted from the film edge with the naked eye in a dark environment, which is a clear sign that up-conversion is occurring. To determine the exact processes participating requires a much more thorough examination and will be reported later in Section 3.4.

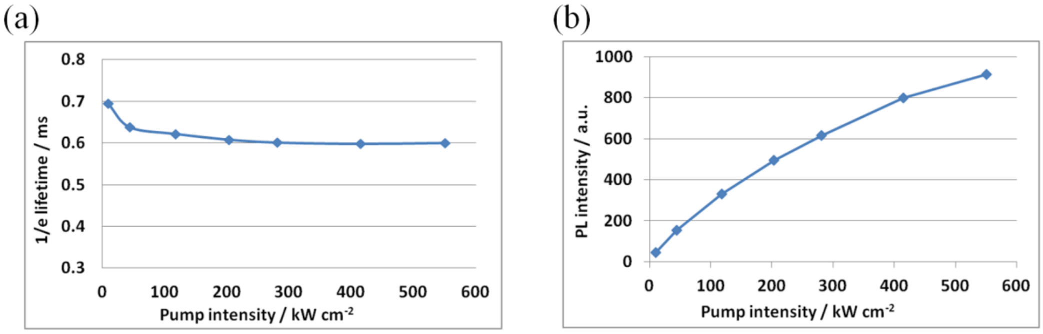

Figure 3.9 1/e lifetime (a), and 1.55 µm emission intensity (b), versus excitation intensity at 1490 nm of an Er^{3+}:As_2S_3 film after 2 hours 130 °C thermal treatment.

(b) Effects of "standard" thermal post-treatment practices on erbium ion doped As_2S_3 films

Thermal annealing in rare-earth ion doped materials would be expected to reduce the defects in the host material and also 'activate' the doped rare-earth ions provided the solubility limit of the glass has not been exceeded. Several reports [129, 130, 217] showed significant 1.5 µm PL intensity enhancement in rare-earth ion doped chalcogenide glasses after thermal treatment (up to 40x in Fuchs's report) [217]. Also a longer lifetime of the $^4I_{13/2}$ state of Er^{3+} was anticipated and has been observed [129, 130] after this treatment.

Lifetimes of the $^4I_{13/2}$ state of Erbium ions in Er^{3+}:As_2S_3 films (~$2x10^{20}$ ions/cm^3) after thermal or light treatment were measured under two different excitation wavelengths, 980 nm and 1490 nm, respectively. With the lifetime measurement set-up described in Section 3.3.2(a), the error of lifetime measurement is about ±0.005 ms. The results are shown in Table 3.2 with a pump intensity estimated at 200 kW/cm^2. The difference between 1/e and intrinsic radiative lifetime as noted earlier (see Section 3.3.2(a)) indicates the presence of some non-radiative decay, energy exchange mechanism, or up-conversion process. It is clear that 1490 nm and 980 nm excitation give similar results. This is somewhat surprising, given the $^4I_{11/2}$ state would normally has a lifetime similar to that of the $^4I_{13/2}$ state in a low phonon energy host [46] and so some "energy storage" effect would be expected that manifests as a longer 1550 nm lifetime for 980 nm pumping [238]. The reasons for this are not clear, but one upside is that this means that an accelerated decay is occurring from the $^4I_{11/2}$ state may enhance pumping efficiency for the higher inversion 980 nm pumping mechanism. There is little difference between the results for thermal treatment and light treatment compared to the as-deposited case, indicating that the long and medium range glass structure has little impact on the rare-earth ion performance.

Table 3.2 Lifetimes of the $^4I_{13/2}$ state of erbium ion in Er^{3+}:As_2S_3 films after thermal or light treatment.

	Excitation @ 1470 nm		Excitation @ 980 nm	
Treatment of Er^{3+}:As_2S_3 films	1/e lifetime / ms	Intrinsic lifetime / ms	1/e lifetime / ms	Intrinsic lifetime / ms
As-deposited	0.47	0.65	0.48	0.66
Thermal annealing (130 °C, 24 hours under vacuum)	0.5	0.69	0.56	0.72
Light annealing (500-570 nm green light, ~3mW/cm^2, 48 hours, in ambient atmosphere)	0.49	0.64	0.49	0.65

(c) Propagation loss and absorption band of erbium ion doped As_2S_3 film

Measurements of film loss and Er^{3+} absorption band (range from 1450 nm to 1650 nm) were performed using a Metricon 2010 prism coupler, tunable laser sources, and an InGaAs camera. The scattering streaks from the TE fundamental slab guided mode was imaged and captured using a cooled high sensitivity InGaAs camera at wavelengths between 1450 and 1650 nm and then the propagation loss was calculated using custom image processing software by analysing the decay of the normalized and background corrected scattering streak versus distance. A representative beam streak is shown in Figure 3.10(a). The resulting optical loss of the 1.8×10^{20} ions/cm^3 Er^{3+} doped As_2S_3 film (after 2 hours 130 °C thermal treatment) is shown in Figure 3.10(b).

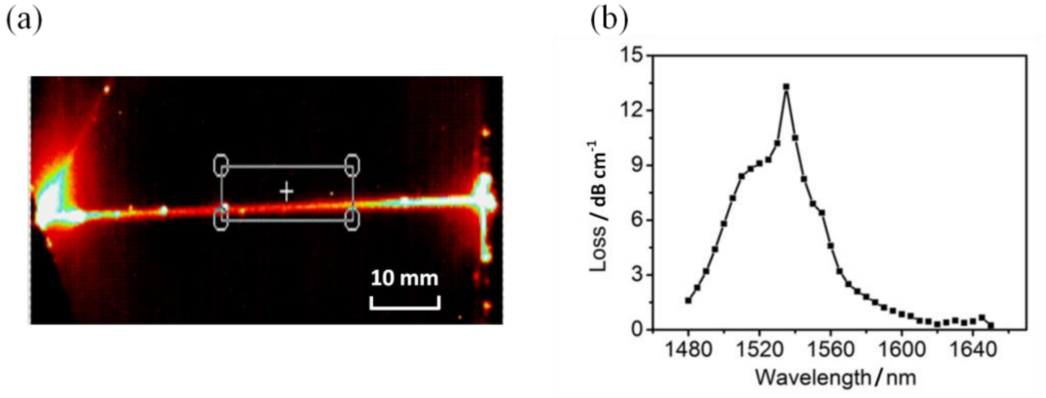

Figure 3.10 Beam streak in an Er^{3+}:As_2S_3 film at 1500 nm, light entered on the right side and exited on the left at the edge of the wafer (a), and the absorption curves (b) of an Er^{3+} doped As_2S_3 film.

The absorption band peak due to the $^4I_{15/2}\rightarrow{}^4I_{13/2}$ transition of Er^{3+} lay at 1538 nm, which is slightly red-shifted from the 1532 nm usually observed in oxide glass hosts [239-241], and blue-shifted from that observed in Er_2O_3 crystal [155]. This red-shift in absorption band is normal in chalcogenide glass host materials [46, 102, 242] and could be explained by the nephel-auxetic effect (‘electron cloud expanding’), that is, rare-earth ion radiative absorption and emission tend to red-shift slightly with increasing covalency of the lattice [39]. The obtained red-shift of the absorption curve and weaker absorption tail at shorter wavelength indicated a longer excitation wavelength for optimum pumping is required than for the normal 1480 nm oxide host pump lasers.

3.4 Up-conversion properties of erbium ion doped As_2S_3 film

Detailed investigation of the up-conversion processes present in the material enable a better prediction of the emission properties and potentially available optical gain, so attempts were made to quantify the various up-conversion products, and their dependencies on pump intensity and doping concentration. The starting point was measurement of the emission spectrum across a wide range (400-1700 nm) that is able to cover all necessary emissions and up-conversion bands. Due to the wide range, two different detectors (Ocean Optics HR4000 spectrometer and an Ando AQ6317 OSA) were employed in the optical set-up. For a better accuracy, these two detectors were supposed to work at the same time, corresponding to the same excitation intensity. The scheme of the set-up for this measurement is shown in Figure 3.11. In the measurement, erbium ion doped As_2S_3 film is pumped with 1490 nm excitation through a clean, cleaved edge via a lensed silica fibre. Emission captured by the same lensed fibre is recorded using the OSA for the 700-1700 nm range. Emission is also captured by a 250 micron core silica fibre from the top of the excited film edge, then passes through a short-pass filter placed in a pair of collimators and finally is analysed using an Ocean Optics HR4000 spectrometer to cover the 400-1000 nm range. As the OSA and Ocean Optics spectrometer have a spectral overlap across 600-1000 nm, and given that the OSA has power calibration and normalization, then an Ocean Optics white light source is used as a transfer reference to cross-calibrate power and level the response spectrum of the Ocean Optics spectrometer.

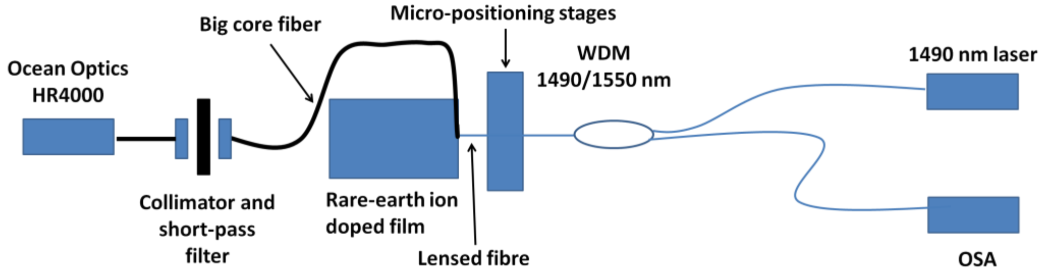

Figure 3.11 Optical set-up for wideband erbium ion emission in an Er^{3+}:As_2S_3 film from visible to NIR.

The combined spectra collected by both detectors versus pump power are shown in Figure 3.12. The PL band at 1540 nm arises from the $^4I_{13/2}\rightarrow{}^4I_{15/2}$ emission. The sharp peak at 1490 nm is the remnant pump laser, while the other bands around 980 nm, 805 nm, 670 nm, 540 nm and 520 nm correspond to the emission from the $^4I_{11/2}$, $^4I_{9/2}$, $^4F_{9/2}$, $^4S_{3/2}$ and the $^2H_{11/2}$ energy states to the ground state, respectively, and potentially some higher inter-level transitions. Possible radiative transitions of Er^{3+} are shown in Table 3.3, including the related energy levels, wavelength and calculated spontaneous emission probabilities based on $98(0.15Ga_2S_3\text{-}0.85GeS_2)\text{-}2Er_2S_3$ (mol%) glass in ref [146].

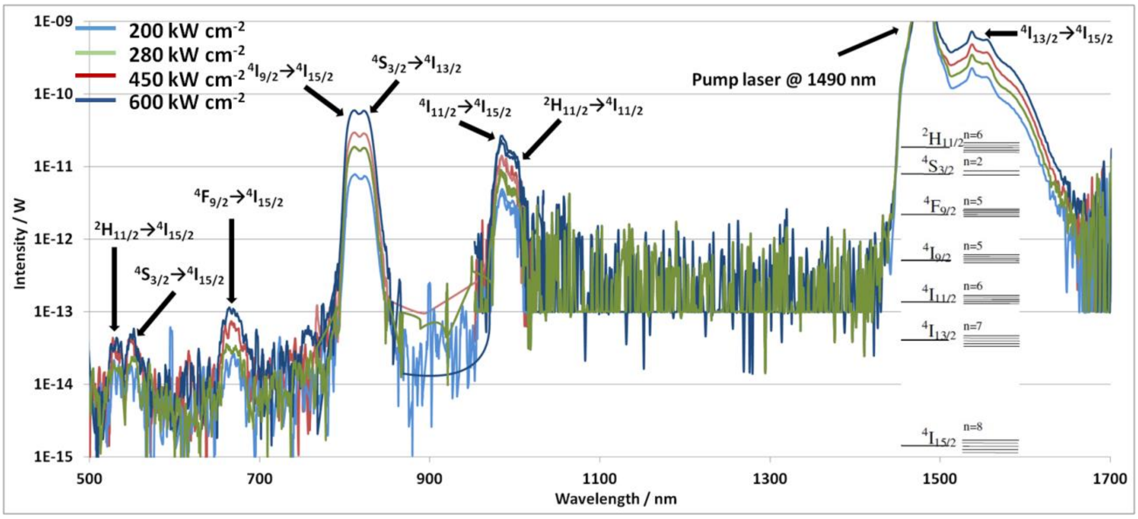

Figure 3.12 Emission spectrum of an Er^{3+}-doped As$_2$S$_3$ film (after 2 hours 130 °C thermal treatment) pumping at 1490 nm from visible to NIR versus pump power.

Table 3.3 Possible radiative transitions of Er^{3+} and calculated spontaneous emission probabilities [*A(J;J′) (s^{-1})*] based on 98(0.15Ga$_2$S$_3$-0.85GeS$_2$)-2Er$_2$S$_3$ glass in ref [146].

Emission wavelength / µm	Transition		*A(J;J′) (s^{-1})*
	Initial state	Final state	
0.525	$^2H_{11/2}$	$^4I_{15/2}$	14370
0.546	$^4S_{3/2}$	$^4I_{15/2}$	2371
0.656	$^4F_{9/2}$	$^4I_{15/2}$	4718
0.78	$^2H_{11/2}$	$^4I_{13/2}$	--
0.803	$^4I_{9/2}$	$^4I_{15/2}$	513
0.848	$^4S_{3/2}$	$^4I_{13/2}$	964
0.98	$^4I_{11/2}$	$^4I_{15/2}$	1029
1.05	$^2H_{11/2}$	$^4I_{11/2}$	--
1.15	$^4F_{9/2}$	$^4I_{13/2}$	444
1.25	$^4S_{3/2}$	$^4I_{11/2}$	77
1.45	$^2H_{11/2}$	$^4I_{9/2}$	--
1.53	$^4I_{13/2}$	$^4I_{15/2}$	508
1.7	$^4I_{9/2}$	$^4I_{13/2}$	94
1.7	$^4S_{3/2}$	$^4I_{9/2}$	156
2.0	$^4F_{9/2}$	$^4I_{11/2}$	397
2.7	$^4I_{11/2}$	$^4I_{13/2}$	99
3.6	$^4F_{9/2}$	$^4I_{9/2}$	73
4.5	$^4I_{9/2}$	$^4I_{11/2}$	6

-- Data unavailable

The erbium ion concentration in this sample is relatively high, at 1.8x10^{20} ions/cm^3, leading to a drop in the average distance between ions, and therefore to enhanced ion-to-ion interactions due to the r^6 (r is the distance between neighbour ions) dependence [149]. With high excitation intensity, ions in the $^4I_{13/2}$ metastable state with a relatively long lifetime of 0.9 ms have a high probability of promotion to the $^4I_{9/2}$ energy state via ETU, ESA and cooperative up-conversion processes (see Section 2.3.2). At this point erbium ions may experience several different transitions. Firstly, erbium ion can radiatively decay to the ground state with corresponding emission of 805 nm photons. Ions in the $^4I_{9/2}$ state may also decay to the $^4I_{11/2}$ state by multiphonon relaxation or radiative decay with a longer wavelength emission that could not be recorded with the OSA. Ions in the $^4I_{11/2}$ energy state explained the 980 nm emission in the spectra. An intrinsic lifetime of 0.5 ms was measured for the $^4I_{9/2}$ excited state, and this lifetime allows the possibility that ions in the $^4I_{9/2}$ excited state receive energy from another ion in the metastable state $^4I_{13/2}$ via an ETU process and elevate to the higher $^2H_{11/2}$ energy level, which results in the 520 nm emission. The energy difference between the $^2H_{11/2}$ and the $^4S_{3/2}$ levels is small, therefore ions at the $^2H_{11/2}$ level can non-radiatively decay to the $^4S_{3/2}$ level quickly with the help of host phonons. The small intensity 540 nm emission is assigned to the radiative decay from the $^4S_{3/2}$ state to the $^4I_{15/2}$ ground state. The emission band at 670nm could be explained by the radiative decay from the $^4F_{9/2}$ state to the ground state, on which excited states accumulate by phonon assisted non-radiative decay from the $^4S_{3/2}$ upper energy level. It is worth to note that emissions of 540 nm and 520 nm are located in the bandgap of the As_2S_3 host material, which implies emissions in this wavelength range would suffer extremely high absorption by the host. As a result of this, the 540 nm and 520 nm emission intensity in these spectra may be much lower in intensity than the real value. Also in chalcogenide glass hosts, the intensity of the 980 nm emission is much smaller than the 805 nm emission, which is different from the results in most oxide glasses [175]. This could be explained as follows, based on the erbium ion energy level system (see Fig 2.1), the 980 nm emission arises from the radiative decay from the $^4I_{11/2}$ state to the ground state, and the population in the $^4I_{11/2}$ state is due to the decay of ions from the $^4I_{9/2}$ state to the $^4I_{11/2}$ state. Due to the low phonon energy of chalcogenide glass hosts, the probability of this decay is rather lower than that in high phonon energy hosts like oxide glasses, which in turn lead to a weak emission at 980 nm.

It is worth noting that whilst the high intensity emissions at 980 and 805 nm are present, their power spectral density is still at least an order of magnitude lower than that at 1540 nm. These energy transfer processes are then causing some loss of pump efficiency and to an extent depopulating the metastable level: $^4I_{13/2}$, the first excited state.

As mentioned previously (Section 2.3), all the up-conversion emissions observed are caused by a combination of the up-conversion processes, such as energy transfer up-conversion (APTE or ETU), excited state absorption (ESA), etc. Besides the first-order up-conversion from the metastable state, second-order cooperative up-conversion processes are also occurred, which lead to the observed green emission at 520 and 540 nm, due to the $^2H_{11/2}\rightarrow{}^4I_{15/2}$ and $^4S_{3/2}\rightarrow{}^4I_{15/2}$ transitions, respectively.

Although all these three processes lead to a similar short wavelength emission, there are significant differences between them. For example, in ETU, two ions in the first excited state ($^4I_{13/2}$) interact to populate the $^4I_{9/2}$ state, and the $^4I_{11/2}$ state is populated due to rapid nonradiative or radiative decay from the $^4I_{9/2}$ state. Therefore, the rate of up-conversion depends quadratically on the concentration of ions in the $^4I_{13/2}$ state (i.e. dopant concentration both for the population and the degree of interaction via separation), and therefore also quadratically on the pump power. In contrast, excited state absorption (ESA) involved only one excited ion, this process is independent of erbium ion concentration but only related with pump intensity.

In order to determine which of these mechanisms is responsible for the observed up-conversion luminescence, one popular method is to measure the luminescence intensity of the different bands as a function of pump power. With the data analysed quantitatively, the up-conversion coefficient and ESA cross-section could be determined [175].

To accomplish this task, the optical set-up shown in Figure 3.11 was modified. An optical attenuator was inserted in the pump laser line to control precisely the excitation power and enable the power to be tuned over a big range (>30 dB) as was required to obtain a good fit [175]. In the lensed fibre output side, a power meter with -110 dBm sensitivity was used instead of the OSA to record the power of 1.5 µm emission, and two more 1490/1550 nm WDMs were applied to remove completely the residual pump power. Narrow band-pass optical filters and a Si detector with a low noise trans-impedance amplifier having gain of 10^9 V/A (volts/amps), and a lock-in amplifier system were employed to record the pump power dependence of emission from the up-conversion processes. The experimental results are plotted in Figure 3.13.

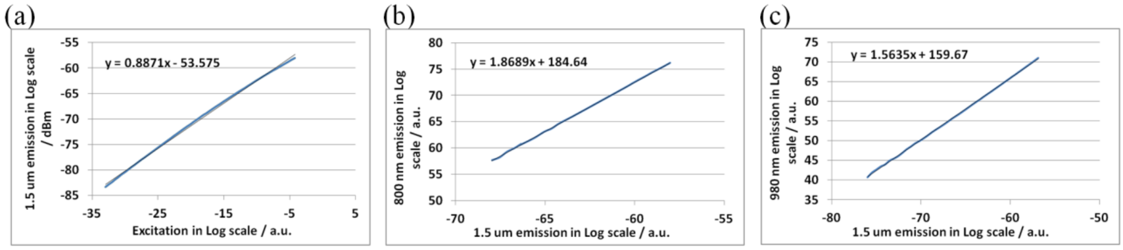

Figure 3.13 Luminescence intensity at 1.5 μm (a), 800 nm (b)and 980 nm (c) vs. excitation power and 1.5 μm emission of an erbium ion doped As_2S_3 film, on $\log_{10}$ scales.

The 1.5 μm emission intensity versus pump power at 1490 nm of a $1.8x10^{20}$ /cm^3 erbium ion doped As_2S_3 film is plotted in Figure 3.13 (a), in $\log_{10}$ scale. A linear trend is found between 1.5 μm emission and pump power, but the slope is 0.887 from the fitted line, implying processes such as energy transfer and up-conversion, that can reduce 1.5 μm photon emission yield, are occurring. PL intensity at 800 nm and 980 nm versus that at 1.5 μm are shown in Figure 3.13 (b) and (c), respectively, and both curves can be linear fitted with slopes of 1.87, and 1.56, respectively. Both slopes are smaller than 2 as might be expected if no non-radiative decay and/or second-order up-conversion occurs. Due to the long lifetime of the $^4I_{11/2}$ state (intrinsic lifetime of 0.84 ms) in this sample, ions in the $^4I_{11/2}$ state may be promoted to the $^4F_{9/2}$ state by photon absorption or energy transfer, which depletes the population of the $^4I_{11/2}$ state, resulting in a slope less than 2. Similar phenomena can occur at 800 nm. With a long $^4I_{9/2}$ state lifetime of 0.59 ms, ions could be further excited to the $^4S_{3/2}$ state from which the 540 nm emission arise to the ground state.

Since the ions can reach the $^4S_{3/2}$ state via second-order up-conversion or a 3-photon process, then it is also possible to decay from the $^4S_{3/2}$ state to the $^4I_{13/2}$ state and give out emission around 800 nm. The zoomed in 800 nm emission spectrum shown in Figure 3.14 supports this assertion. The broad 800 nm emission band can be divided into two bands almost overlapping each other. The one centred at 810 nm is proposed to be associated with the $^4I_{9/2}$ state to the ground state transition, whilst the other one located at 830 nm is thought to arise from the decay between the $^4S_{3/2}$ state and the $^4I_{13/2}$ state.

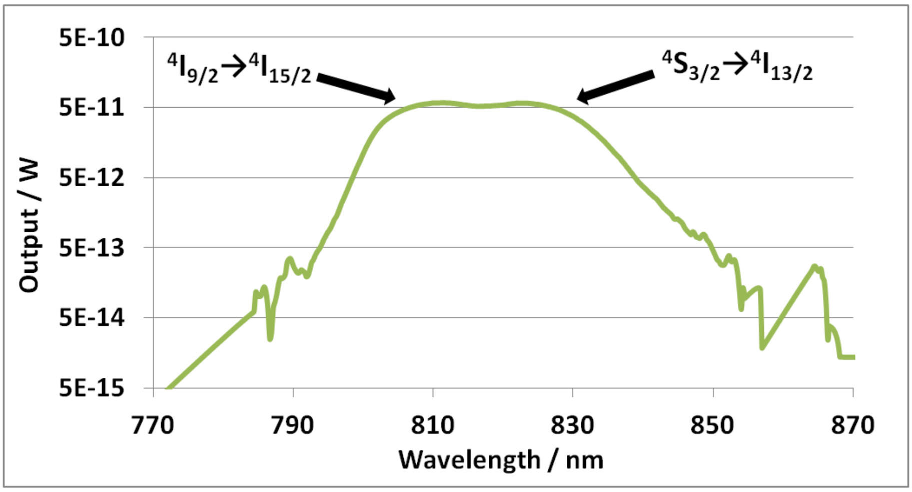

Figure 3.14 Emission spectrum at 800 nm of an erbium ion doped As_2S_3 film of 1.8×10^{20} ions/cm^3 Er^{3+} concentration after 2 hours 130 °C thermal treatment.

In this research, even with the maximum pump power the diode laser can reach, ASE saturation was not evident, and therefore it was difficult to calculate the up-conversion efficiency by modelling with rate equations under steady-state conditions [175]. A result showing such saturation behaviour was achieved in an erbium ion doped TeO_2 reference film with ~$2.2\text{x}10^{20}$ ions/cm^3 concentration, but the reasons behind the different behaviour in erbium ion doped As_2S_3 films are still unclear.

3.5 High temperature thermal post-treatment on erbium ion doped As_2S_3 film

It is well known that high temperature thermal treatment often yields positive effects on rare-earth ion doped materials. With the energy from thermal treatment, dopants are able to ‘re-bond’ and be ‘active’ and better incorporate themselves into the host material. But at the same time, given the known low solubility of erbium ion in bulk As_2S_3 [118, 197], the question naturally arises as to whether the thermal or light post-treatment process used to restore the film towards the bulk state causes erbium ion precipitation.

Therefore, the question of whether thermal treatment up to and above T_g helps or hinders is relevant, and gives insight into the effects of the “standard” 130 °C 24 hours thermal treatment typically applied to As_2S_3 films. Based on previous experiments in the ANU’s Laser Physics Centre, thermal treatment of chalcogenide films at temperatures beyond the T_g, will not damage the film directly in terms of film quality observed in dark field microscopy, provided the thermal treatment occurs in a vacuum below T_g and an inert atmosphere above T_g.

Several small pieces (10x10 mm) of erbium ion doped As_2S_3 films of 0.6 at% Er^{3+} concentration ($1.8x10^{20}$ ions/cm^3) were cleaved and prepared for different thermal treatments. One of the Er^{3+}:As_2S_3 films was also measured as deposited and then subjected to the standard 130 °C 24 hour thermal treatment under vacuum and remeasured for comparison. Figure 3.15 presents the results.

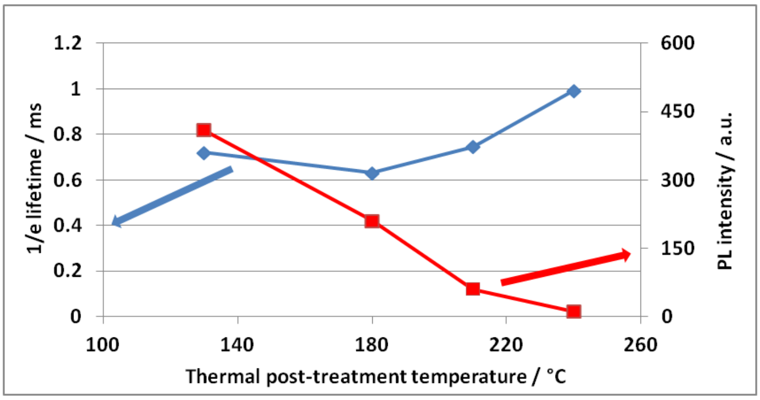

Figure 3.15 Results of thermal treatment on 0.6 at% Er^{3+} doped As_2S_3 films. Samples were thermally treated for 1 hour at temperature indicated, except 130 °C data point which is for 24 hours under vacuum.

There are two interesting features from Figure 3.15. Firstly, it is apparent that as the thermal post-treatment temperature rises, the lifetime of the active erbium ions is increasing by up to ~50%. This indicates that the erbium ions are not optimally incorporated into the glass matrix after deposition nor after the standard thermal treatment. Secondly, the PL intensity drops markedly as the thermal post-treatment temperature exceeded ~130 °C and drops rapidly to zero as the glass T_g (~180 °C) is exceeded. For reference purposes, the sample measured before and after the 130 °C 24 hour thermal post-treatment under vacuum exhibited about a 30% reduction in PL intensity at the $1.8x10^{20}$ ions/cm^3 doping used. It is not clear how much of the drop in PL intensity due to the 2 hours thermal post-treatment at 130 °C is attributable to erbium ion diffusion and clustering as opposed to changes induced by the large structural rearrangement of the host glass, but the reduction is tolerable given the known benefits to the glass stability and properties [213].

3.6 Concentration effects in erbium ion doped As_2S_3 films

Er^{3+}:As_2S_3 films with different erbium ion concentrations were deposited using co-thermal evaporation. Bulk As_2Se_3 (*5N*) and metallic erbium were used as starting materials. The deposition details were described previously (see Section 3.2.3), and the only difference was the evaporation temperature of erbium metal source. During deposition, the erbium metal target temperature was decreased from 1070 °C to 1030 °C and 990 °C, respectively, to drop the erbium metal evaporation rate to a half and a quarter of its previous value of 0.001 nm/s (see Section 3.2.3), whilst the power and rate for As_2S_3 target was kept as previously at 0.1 nm/s. By doing so, samples with 0.15 at%, 0.3 at% and 0.6 at% erbium ion doped concentrations were fabricated. It is worth pointing out that with the current deposition system, the erbium ion concentration in the as-deposited As_2S_3 films could not go lower than 0.15 at% because the erbium metal target evaporation rate here was at the measurement limit.

All the as-deposited wafers were coated with a 120 nm thick SU-8 layer to protect from contamination, and were subjected to 130 °C thermal post-treatment in a vacuum for 24 hours, and then two days of light post-treatment with 500-570 nm green light (~3mW/cm^2) in ambient atmosphere to try to ensure the Er^{3+}:As_2S_3 films were fully relaxed toward the condition of their bulk counterpart.

Lifetime and PL intensity versus excitation intensity for different concentrations of Er^{3+} in these Er^{3+}:As_2S_3 films were measured and are plotted in Figure 3.16. From the results, the 0.15 at% sample has the longest lifetime of 1.2 ms, the lifetime of the 0.3 at% sample drops to 0.9 ms, while the highest doped sample has the shortest lifetime of about 0.5 ms. Also lifetimes are relatively independent of pump power: taking the 0.15 at% sample as an example, the 1/e lifetime only fell from 1.23 ms (excitation intensity of 50 kW/cm^2) to 1.17 ms (excitation intensity of 1100 kW/cm^2), and the PL decay curve showed a single exponential nature. Conversely, with increasing erbium ion concentration, the lifetime drops significantly, indicating strong ion-ion interaction induced photoluminescence quenching occurs. In the PL intensity curves in Figure 3.16(b), the PL intensity of all three samples increases with excitation intensity, but in a quadratic way rather than linear way, especially at high excitation intensity, indicating that even in the 0.15 at% doped sample ion-ion interaction occurs as well. Also, the PL intensity of the 0.3 at% sample is less than double that of the value of the 0.15 at% sample, implying the PL yield per erbium ion drops at higher concentrations. In the most heavily doped 0.6 at% sample (1.8x10^{20} ions/cm^3), the film edge is easily damaged with high excitation power. This phenomenon is assumed to be due to the higher absorption with the greater doping, coupled with a higher degree of ion-ion interaction and energy migration, meaning a large amount of the pump energy absorbed is transferred to defects or phonons, which in turn damages the film edge by local temperature elevation. Therefore, there are no data recorded at excitation intensities over 400 kW/cm^2 for the 0.6 at% film.

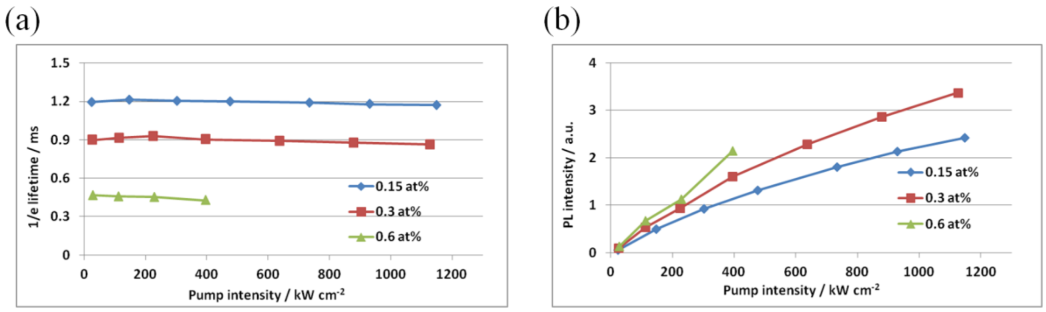

Figure 3.16 1/e lifetimes (a), and PL intensities (b), of Er^{3+}:As_2S_3 films with different erbium ion concentrations.

Again, high temperature thermal post-treatment was applied to the 0.15 at% sample for 1 hour at each fixed temperature. The high temperature thermal post-treatment results are shown in Figure 3.17. With higher thermal post-treatment temperatures, the lifetime increases from 1.23 ms up to 1.88 ms after thermal post-treatment at 280 °C, while the PL intensity drops to low values indicating perhaps erbium ion diffusion and precipitation. These results provide conclusive evidence that the optimum additive of erbium ion in As_2S_3 is < 0.15 at%.

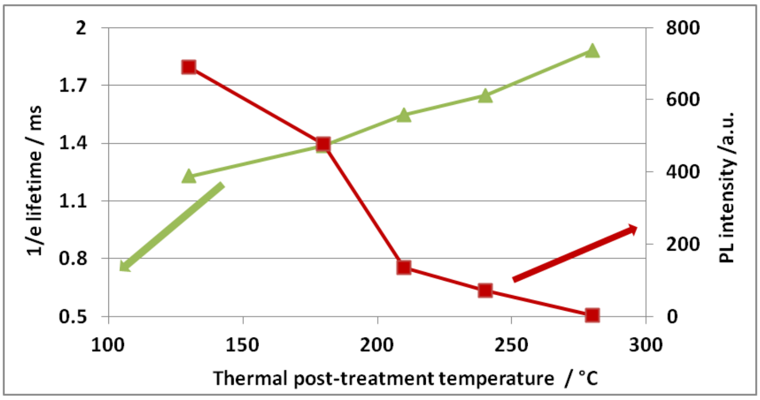

Figure 3.17 Results of thermal post-treatment of 0.15 at% Er^{3+} doped As_2S_3 films. Samples are post-treated for 1 hour at the temperature indicated, except for the 130 °C data point which is for 24 hours under vacuum.

3.7 Conclusion

This chapter reported the fabrication of erbium ion doped As_2S_3 films by co-thermal evaporation. Both structural and optical properties of the obtained films were investigated in detail. Wideband emission spectra of an Er^{3+}:As_2S_3 film were measured. Emissions due to up-conversion and second-order up-conversion were characterised. Influence of $>T_g$ thermal post-treatment on lifetime and PL intensity in erbium ion doped As_2S_3 film was studied and analysed. By comparing the performance of samples with different erbium ion concentrations, it is found that the optimal erbium ion concentration observed to date in an As_2S_3 film made using thermal evaporation is about 0.15 at%. However, it was also pointed out the solubility limit of erbium ion in As_2S_3 is below this value.

Chapter 4

Erbium ion doped As_2S_3 waveguide amplifiers

This chapter reports the fabrication of waveguide amplifiers based on erbium ion doped As_2S_3 films using photolithography and reactive ion etching, as well as the performance of the obtained waveguide amplifiers. Optical waveguide theory is briefly discussed first, and the waveguide design and simulation for the devices are covered. Waveguide fabrication is briefly described and then the propagation losses of the obtained erbium ion doped waveguides as well as the absorption properties of erbium ions in the waveguides, are characterised. Excitation experiments are finally performed to study the amplification property of the waveguides.

4.1 Basic theory and simulation methods

4.1.1 Maxwell's equations for optical waveguides

It is well known that the propagation of light can be described by Maxwell's equations [243] as follows:

$$\nabla \cdot \mathbf{E} = \frac{\rho}{\varepsilon_0} \tag{4.1}$$

$$\nabla \cdot \mathbf{B} = 0 \tag{4.2}$$

$$\nabla \times \mathbf{E} = -\frac{\partial \mathbf{B}}{\partial t} \tag{4.3}$$

$$\nabla \times \mathbf{B} = \mu_0 \left(\mathbf{J} + \varepsilon_0 \frac{\partial \mathbf{E}}{\partial t} \right) \tag{4.4}$$

where $\boldsymbol{E}$ and $\boldsymbol{B}$ are the electric and magnetic fields respectively, ε_0 is the free space permittivity, μ_0 is the free space permeability. ρ represents electric charge density and $\boldsymbol{J}$ is the electric current density. If the light is propagating in a pure dielectric medium, (i.e. a medium with no conductivity or charges), no magnetic effects are present, and in the further case of an isotropic and linear system, then Maxwell's equations reduce to:

$$\nabla \times \mathbf{E} = -\mu_0 \frac{\partial \mathbf{H}}{\partial t} \tag{4.5}$$

$$\nabla \times \mathbf{H} = \varepsilon_0 n^2 \frac{\partial \mathbf{E}}{\partial t} \tag{4.6}$$

where $\mathbf{H} = \frac{1}{\mu_0}\mathbf{B}$, and the *n* is the refractive index distribution of the propagation media. If the medium is optically inhomogeneous its properties are position-dependent, *n*=*n*(*r*). The wave equations for **E** and **H** can be derived as [244]:

$$\nabla^2 \mathbf{E} + \nabla\left(\frac{1}{n^2}\nabla n^2 \mathbf{E}\right) - \varepsilon_0 \mu_0 n^2 \frac{\partial^2 \mathbf{E}}{\partial^2 t} = 0 \tag{4.7}$$

$$\nabla^2 \boldsymbol{H} + \frac{1}{n^2}\nabla n^2 \times (\nabla \times \boldsymbol{H}) - \varepsilon_0 \mu_0 n^2 \frac{\partial^2 \boldsymbol{H}}{\partial^2 t} = 0 \tag{4.8}$$

Normally, these two full vectorial equations describe all coupled components of the electric and magnetic fields, and each component cannot be reduced to a scalar equation. Although the dielectric medium for amplification may encounter intensity-dependent refractive index, for the characterization of light propagation in the waveguide, the numerical solutions consider linear refractive index. In many structures, for example the waveguides used in this thesis, the lack of cylindrical symmetry prevents analytical solutions, thus numerical methods must be used to calculate the eigenvalues of the eigenmode equations which describe the propagating modes of the waveguide.

4.1.2 Simulation of optical waveguide

Accurate modelling of waveguide-based devices plays several significant roles in the advancement of optical devices, including optimization of current designs, shortening of the design and fabrication cycle, and evaluation of new device concepts. So far, modelling techniques for optical guided-wave propagation can be divided into two groups: time-harmonic (e.g. monochromatic continuous wave (CW) operation) and general time-dependent (e.g. pulsed operation) [245]. Excepting short pulse high intensity cases, where significant nonlinear effects occur, time-harmonic methods are usually accurate tools when implemented to an appropriate level of exactness.

In this work, to complete the design of waveguide amplifiers, modal analysis was essential. Factors such as the number of modes supported by the waveguide, their propagation constants, mode intensity distribution, modal excitation in response to a given input field, and the overlap between the mode distribution and the erbium ion doped area especially, can readily be extracted using modal analysis. Different simulation methods, for example the finite difference method, finite element method, mode-matching technique, beam propagation method (BPM), method of lines (MoL), coupled mode theory, and the finite-difference time-domain method (FDTD), are commonly used to compute the electromagnetic modes of waveguides [245].

The key objective for mode solvers is to determine the value of the propagation constant and the corresponding mode field distribution for each mode the structure supports in a given waveguide cross-section at a specified operating wavelength. The finite difference and finite element methods (based on variational principles) have found wide acceptance in the community with demonstrated accuracy even for high refractive index contrast full vectorial cases. They possess advantages such as arbitrary structure, arbitrary shape of waveguides, graded meshes, and numerically stable solution methods for this method are readily available [246]. Detailed discussion on these two methods can be found in [245-248].

4.2 Waveguide design

4.2.1 Waveguide geometry

Planar waveguide structures are primarily and widely used to integrate photonic technologies to the chip scale and gain the same sorts of benefits enjoyed by the silicon integrated circuit industry. Compared to fibres, they enable multi-functional multi-material integrated devices, and also combine higher light confinement and high refractive index contrast. The most common types of waveguide are the buried channel and ridge based devices, which are shown in Figure 4.1(a) and (b), respectively. A typical structure of a buried channel device uses three different refractive index materials and can be described with two geometric parameters, Width and Height. A generalised ridge waveguide is composed of four different materials and can be described by three geometric parameters, Width, Height and Etch depth as shown in Figure 4.1(b). Normally, buried channel devices have better optical confinement and thus have smaller bending radii and therefore advantages in realizing high density photonic circuits. Ridge waveguides have lower propagation losses due to reduced interaction of the mode with the waveguide sidewall and offer fabrication opportunities unavailable to buried channel devices [249].

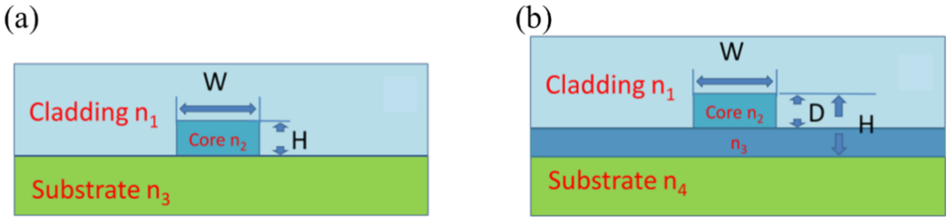

Figure 4.1 Structures of: buried channel waveguide (a), and ridge waveguide (b). In this figure, W is the width, H is the height and D represents the etch depth of waveguide.

In this work, there are particular considerations that make the ridge waveguide advantageous. These stem mainly from the desire to make the waveguides by lithography and dry etching where one material cannot easily be etched as this is an established route to low loss devices in chalcogenide glasses [13, 250].

(a) Waveguide width and etch depth

A structure that is as simple and easily achievable as possible is preferred. In waveguide design, the total film thickness should not be too big, which will bring issues in film deposition, thermal treatment and film etching, therefore based on experience with annealing of chalcogenide glass films, the film thickness was fixed at around 1.3 µm.

Modal effective refractive index was studied as a function of etch depth for waveguides of different widths (1, 2 and 3 µm), and the results are shown in Figure 4.2. In simulation, the refractive index of the thermally oxidized silicon (TOX) substrate is 1.445, the core (take As_2S_3 as an example here and fix $n_2=n_3$) is 2.41 with an air cladding ($n_1=1$). In a 1 µm width waveguide, the etch depth needs to be above 300 nm to stop the TE_0 mode leaking into the slab, and 550 nm for the TM_0 mode. In the wider waveguides, 2 and 3 µm, smaller etch depths are required to confine properly the modes but high order modes start to be guided. In the 2 µm waveguide, if the etch depth is controlled in a range of 350 nm to 550 nm, single mode propagation at 1550 nm is feasible, which is preferable for our application. For the 3 µm waveguide, high order modes are guided at almost every etch depth. Therefore, in the following part, attention is directed primarily to the 2 µm wide waveguide.

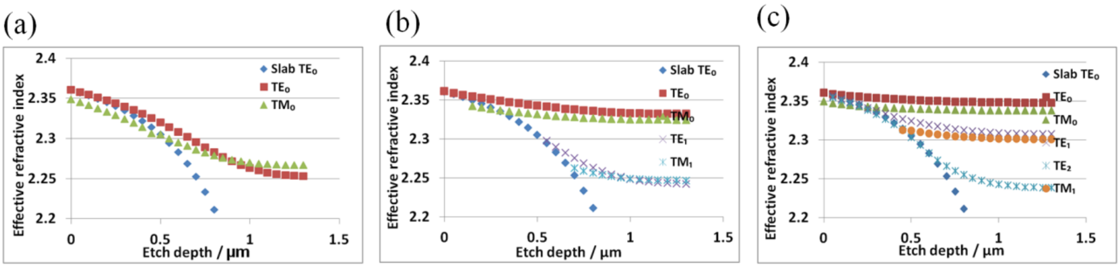

Figure 4.2 Etch depth versus effective refractive index of supporting modes for: 1 µm (a); 2 µm (b) and 3 µm (c) As_2S_3 waveguide.

(b) Bend and junction loss

The bending loss has to be taken into consideration during design of integrated devices. A large bend radius would make the device less compact, while too small a bend radius can introduce considerable extra loss. Therefore, a bending loss simulation was completed to quantify the minimum bend radius the structure could reach without causing significant loss. Commercial software Rsoft-FemSim was employed here to undertake this task. In simulations, a 0.5 µm perfect matching layer (PML) was applied at the domain edge and leaky modes were enabled in the calculation which relied on a conformal transform method to simulate the bend [251]. The imaginary part of the effective refractive index was used to calculate the bending loss using the following formula:

$$loss = 4\pi \times n_{im} \times 4.3429/\lambda \qquad (4.9)$$

where n_{im} is the imaginary part of the effective refractive index, and λ is the wavelength. In Figure 4.3, both the fundamental TE_0 and TM_0 mode bending loss in the 2 µm wide structure are shown.

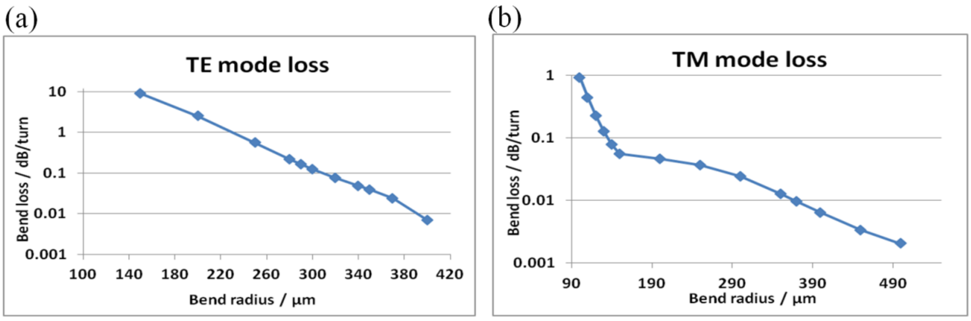

Figure 4.3 The bending loss of the fundamental mode: TE_0 mode (a) and TM_0 (b) mode in the 2 µm wide structure.

From the results in Figure 4.3, bending losses of both TE and TM modes increase with decreasing bend radius in a roughly exponential way. For any radius above 400 µm, the bending loss is less than 0.01 dB per turn for both modes, which is negligible in a real device. Similar bending loss curves were calculated for the 3 µm waveguide, and the results are shown in Figure 4.4. Therefore, allowing a safety factor, a 400 µm radius could be set as a minimum threshold to the occurrence of significant bending loss. It should also be noted that, the bending loss here is purely through radiation. There is also the mode shape shift introduced by the bending structure which causes a mode overlap loss at the entrance and exit of any bends which is referred as junction loss. The junction loss for 2 µm and 3 µm waveguides were calculated and are shown in Figure 4.5.

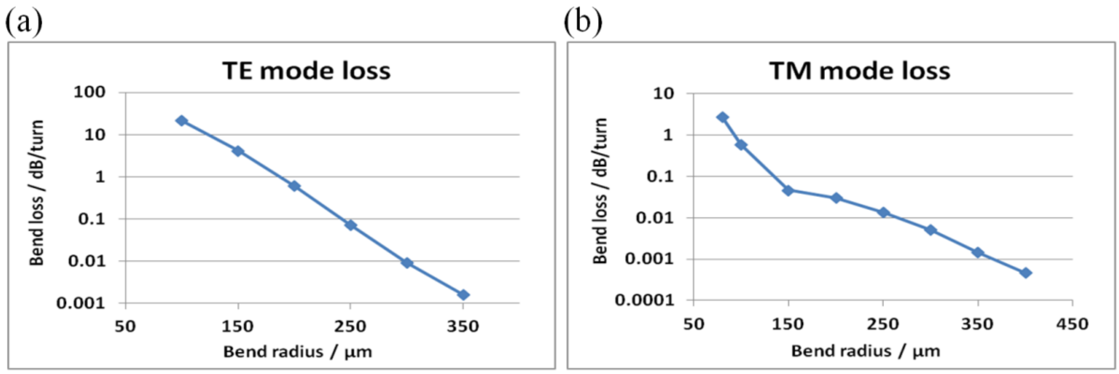

Figure 4.4 The bending loss of the fundamental mode: TE$_0$ (a) and TM$_0$ mode (b) in the 3 µm width structure.

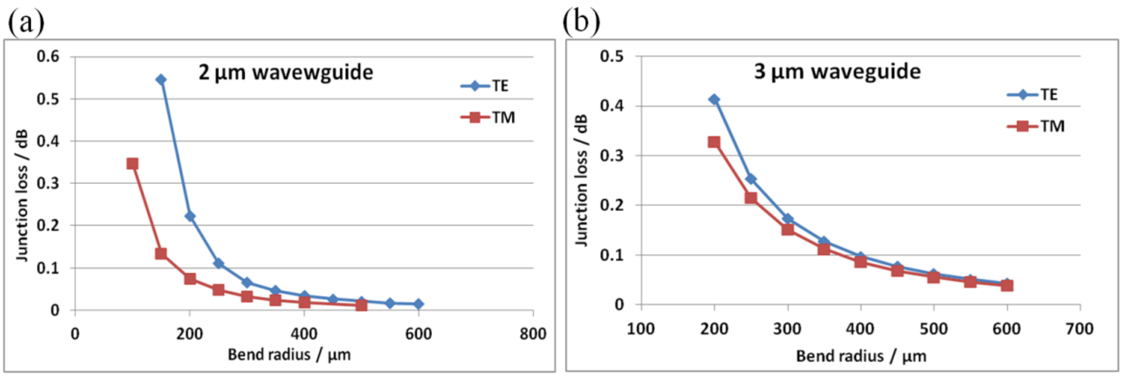

Figure 4.5 The junction loss in: 2 µm (a) and 3 µm (b) width structure.

Junction loss drops almost exponentially with the increase of bend radius. For the 2 µm waveguide, junction loss is below 0.01 dB when the bend radius is over 400 µm for the TM mode, and over 600 µm for the TE mode. In a 3 µm waveguide, due to the bigger mode area the junction loss is little bigger than 2 µm waveguide with the same bend radius, but still down to ~0.03 dB when the bend radius exceeds 600 µm for both TE and TM mode.

(c) Hybrid integrated waveguide structure

A significant barrier exists towards fabricating the designed waveguides in rare-earth ion doped materials, namely that there are no volatile halides or hydrides that can be used to transport the etched rare-earth atoms [252]. The involatile erbium etch products cause roughness as they tend to form micro-masks which then result in rough etched surfaces and sidewalls. For example, Figure 4.6 shows the results of etching pure TeO_2 and Er^{3+}:TeO_2 using an optimised hydrogen/methane/argon mix in an inductively coupled plasma (ICP) reactive ion etching (RIE) system [152]. The degradation of the etching quality is unacceptable, and an alternative solution is required. To avoid this issue, a hybrid integrated waveguide structure is proposed. In a hybrid integrated waveguide structure, more than one materials are combined to achieve more flexibility and better performance.

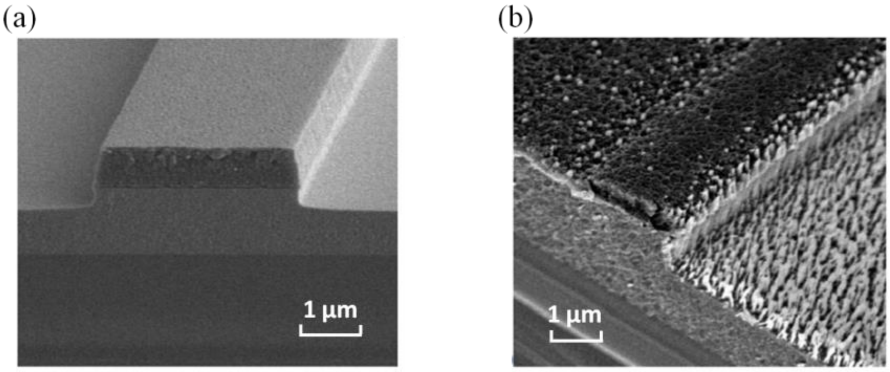

Figure 4.6 Images of etched: un-doped TeO_2 (a) and Er^{3+}:TeO_2 (b) waveguides [152].

Here, a strip loaded waveguide was investigated comprising an erbium ion doped As_2S_3 slab and an un-doped As_2S_3 loading strip. In this structure, H=1350 nm total thickness was used, with h =500 nm etch depth and 50 nm pure As_2S_3 left as a buffer, and the Er^{3+} doped As_2S_3 layer is 800 nm thick. A small overlap reduction between the mode and the doped area is the price to avoid the issue of etching erbium ion doped As_2S_3 directly. The cross-section of the finalised rib waveguide structure is shown in Figure 4.7, and the TOX refers to thermally oxidized silicon substrate.

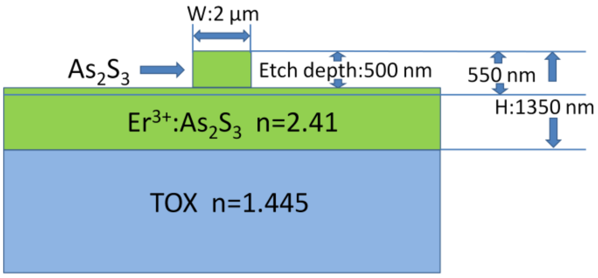

Figure 4.7 The cross-section of the finalised ridge waveguide structure to avoid etching Er^{3+}:As_2S_3 directly, and TOX is the thermally oxidized silicon substrate.

With this finalised ridge waveguide structure, the properties of the propagation modes in this waveguide were simulated in the following section.

4.2.2 Mode properties of the hybrid integrated waveguide structure

In the waveguide design, besides parameters such as effective refractive index, mode area and the mode distribution, two more specific parameters are also of interest. Firstly, the overlap between the optical mode distribution and the erbium ion doped area (see Figure 4.7) is important. This overlap is less than unity because of field penetration into the un-doped "strip loading" layer in the two layer structure, which in turn decreases gain and the pump efficiency. Therefore, a structure with a large overlap is preferable. Secondly, the coupling loss from an input fibre into the waveguide is of considerable interest and may be calculated from the mode overlap formulism [244].

Simulations were performed using a public domain Matlab finite difference code written by Fallahkhair et al., 2008 [253]. The Matlab finite difference mode solver is a full-vector simulation based on the transverse magnetic field components. It is versatile and reprogrammable to allow custom properties to be calculated. Waveguides of the structure shown in Figure 4.7 were modelled with variable widths of 1 µm, 2 µm, 3 µm and 4 µm, respectively, matching the widths on the standard waveguide test mask used at the Laser Physics Centre, in the Australian National University. In calculations, a grid size of 20 nm was applied with a 10 µm × 5.35 µm window, and the wavelength used in calculations was 1.55 µm. In the simulation, a perfectly matched layer (PML) was applied at the domain edge. The resulting TE and TM mode distributions for different waveguide widths are shown in Figure 4.8. Effective refractive index, mode area (defined as in [254]), overlap between optical mode distribution and the erbium ion doped area and coupling loss from lensed fibre (2.5 µm of $1/e^2$ diameter with 14 µm working distance) to waveguide were obtained from calculation and are summarised in Table 4.1.

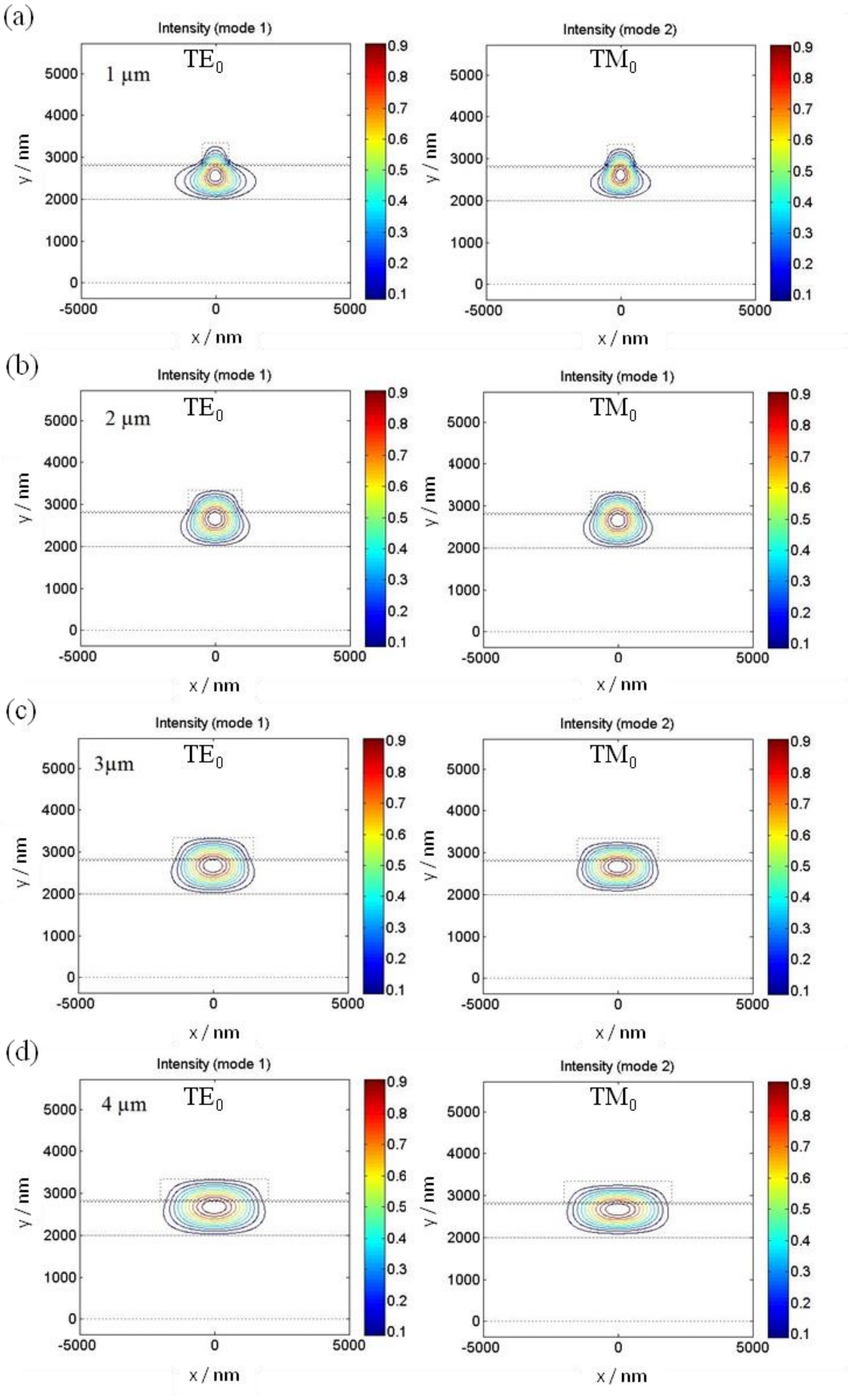

Figure 4.8 Simulations of the TE and TM mode distributions for waveguide structure depicted in Figure 4.7 with different waveguide widths: 1 µm (a); 2 µm (b); 3 µm (c) 4 µm (d). The horizontal dotted black line in each figure represents the structure of waveguide. Note the colour bar scale represents major electric field component normalised to unity peak value.

Table 4.1 Simulation results of mode effective refractive index, mode area, the overlap between mode and Er^{3+} doped area and fibre-waveguide coupling loss for the waveguide structure depicted in Figure 4.7.

	TE_0				TM_0			
Waveguide width / µm	Mode effective refractive index	Mode area / μm^2	Overlap between mode and Er^{3+} doped area / %	Coupling loss / dB	Mode effective refractive index	Mode area / μm^2	Overlap between mode and Er^{3+} doped area / %	Coupling loss / dB
4	2.355	3.31	65.5	1.76	2.342	2.97	67.9	1.90
3	2.351	2.64	66.5	1.56	2.338	2.34	68.4	1.68
2	2.342	2.04	70.0	1.61	2.329	1.75	70.1	1.78
1	2.319	1.97	85.0	1.92	2.302	1.75	81.3	2.09

Based on the results shown in Table 4.1 and Fig 4.8, wider waveguides have bigger mode area (unsurprisingly but in a sub-linear manner) and less overlap of the mode with the erbium ion doped area. They also, however, have lower interaction with the sidewalls which should produce lower scattering losses. The 1 µm and 2 µm waveguides both have significantly better overlap than the other widths, but the 1 µm waveguide has the highest coupling loss due to the mismatch between waveguide mode area and the output spot size of the lensed fibre. Narrow waveguides also have increased sidewall overlap and will suffer more bending losses as discussed in the previous section (see Section 4.2.1), and so the best choice is the 2 µm wide waveguide.

4.3 Simulation of amplification performance of erbium ion doped As_2S_3 waveguide amplifier

4.3.1 Rate equation for an erbium ion doped waveguide system

The dynamics of energy level populations in laser gain media are often modelled using a system of rate equations. These are differential equations, describing the temporal evolution of level populations under the influence of optically induced and non-radiative transitions. To predict the performance of an $Er^{3+}:As_2S_3$ waveguide amplifier, simulation based on rate equations was performed. Laser diodes working at 980 and 1480 nm are both practically used for Er^{3+} doped fibre amplifiers, and it was reported that 980 nm pumping was shown to have better gain characteristics and lower noise figure [255, 256]. In chalcogenide glasses, due to the low phonon energy, the lifetime of the $^4I_{11/2}$ state is long (intrinsic lifetime of 0.84 ms, see Section 3.4), resulting in significant up-conversion processes when pumping at 980 nm. To avoid this, in this thesis, the amplification experiment was carried out with 1480 nm excitation. With 1480 nm excitation, the erbium ion works as a quasi-three level energy system (see Section 2.1). In this case, the stark levels of the $^4I_{13/2}$ state are divided into two energy groups, the upper energy level and lower energy level. Erbium ions in the ground state absorb pump photons and are promoted into the upper part of the $^4I_{13/2}$ excited state. These then rapidly decay non-radiatively due to interactions with the thermal phonon bath and through electron-electron energy loss processes to the metastable state, the lower energy part of the $^4I_{13/2}$ level. With the ion accumulation in the lower $^4I_{13/2}$ energy level, a population inversion between it and the ground state $^4I_{15/2}$ is formed. During this process, basic up-conversion effects are taken into consideration in the model, therefore, the higher excited state $^4I_{9/2}$ is also in the picture. As the pump energy is approximately equal to the $^4I_{9/2}$ - $^4I_{13/2}$ energy difference, ions in the lower $^4I_{13/2}$ energy level may get further excited (by absorbing another pump photon (ESA) or accepting energy from neighbouring excited ions (co-operative upconversion)) and be promoted to the $^4I_{9/2}$ energy state. Further processes can also occur from this state but were not included in the model. A detailed energy level diagram of erbium ion in a glassy host and the main processes modelled with 1480 nm excitation are shown in Figure 4.9.

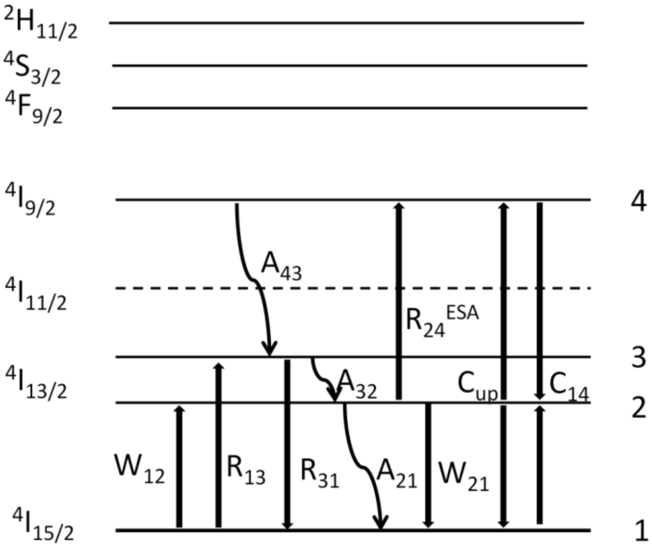

Figure 4.9 Energy level diagram of erbium ion in a glassy host with all potential energy transfer mechanisms. In this diagram, R_{ij} and W_{ij} are the pump and signal stimulated rates, the A_{ij} are the nonradiative rates from level *i* to *j*, A_{21} is the fluorescence rate, ESA is excited state absorption, C_{up} is the homogeneous upconversion coefficient, and the C_{14} is cross-relaxation coefficient. R_{13} and W_{21} represent the primary pump and primary PL, respectively.

To describe ion state populations in an erbium ion doped glass, a quasi-three level energy system is used as described above, the rate equations would normally be written as follows:

$$\frac{\partial N_1}{\partial t} = -W_{12}N_1 - R_{13}N_1 + R_{31}N_3 + A_{21}N_2 + W_{21}N_2 + C_{up}N_2^2 - C_{14}N_1N_4 \qquad (4.10)$$

$$\frac{\partial N_2}{\partial t} = W_{12}N_1 - A_{21}N_2 - W_{21}N_2 + A_{32}N_3 - 2C_{up}N_2^2 + 2C_{14}N_1N_4 - R_{24}^{ESA}N_2 \qquad (4.11)$$

$$\frac{\partial N_3}{\partial t} = R_{13}N_1 - R_{31}N_3 - A_{32}N_3 + A_{43}N_4 \qquad (4.12)$$

$$N_1 + N_2 + N_3 + N_4 = N_{Er} \qquad (4.13)$$

In the above equations with reference to Figure 4.9, R_{ij} and W_{ij} are the pump and signal stimulated rates, and the A_{ij} are the nonradiative rates from level *i* to *j*. A_{21} is the fluorescence rate. C_{up} is the homogeneous upconversion coefficient, and the C_{14} is cross-relaxation coefficient. The N_i represents the ion population at each energy level, and N_{Er} is the total erbium ion population. The equations are normally solved numerically using Runge-Kutta or similar methodologies.

4.3.2 Simulation of erbium ion doped As_2S_3 waveguide amplifiers

Optiwave Corporation has commercially released a fully self-consistent model of Er^{3+}-Yb^{3+} codoped waveguide amplifiers based on the propagation and rate equations. This is embodied in the Optisystem software suite and was employed here to implement the simulation work. The amplification scheme used in the simulation is shown in Figure 4.10. A CW laser at 1538 nm with low output power of -30 dBm is used as a signal source; a high power pump laser at 1480 nm with 200 mW output power is used as a pump source; an optical spectrum analyser and WDM analyser are used to capture the output spectrum and record the results. The core part of this design is the Er^{3+}-Yb^{3+} codoped waveguide. Parameters required by simulation are measured from the fabricated erbium ion doped As_2S_3 waveguides or from the literature [123, 257], and the parameters used in the simulation are shown in Table 4.2.

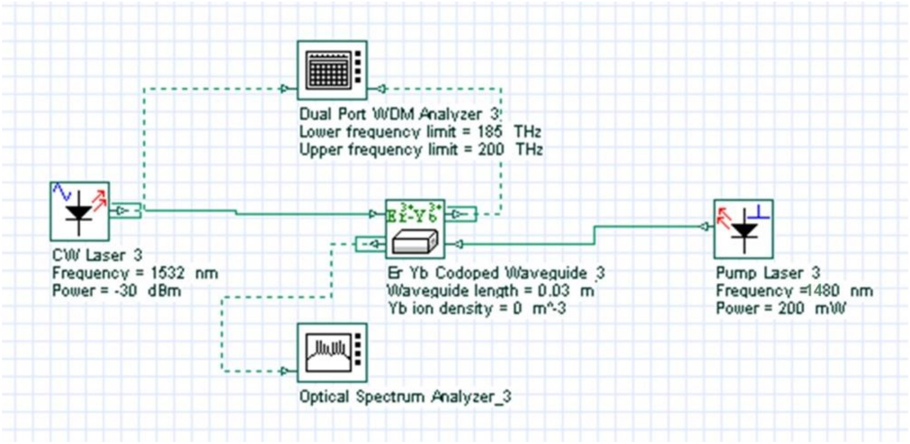

Dual Port WDM Analyzer 3
Lower frequency limit = 185 THz
Upper frequency limit = 200 THz

CW Laser 3
Frequency = 1532 nm
Power = -30 dBm

Er Yb Codoped Waveguide 3
Waveguide length = 0.03 m
Yb ion density = 0 m^-3

Pump Laser 3
Frequency =1480 nm
Power = 200 mW

Optical Spectrum Analyzer_3

Figure 4.10 Schematic optical set-up for Er^{3+}-Yb^{3+} waveguide amplifier pumping modelling using the OptiSystem software [258].

Table 4.2 Parameters used in the OptiSystem software [258] simulation (some of them cited from [123, 257]). Detailed definition of A_{32}, A_{43}, C_{up} and C_{14} could be found in Figure 4.9.

Name and description	Value used in simulation
Waveguide length	3 cm
Signal background loss	1 dB/cm (@1300 nm)
Pumping background loss	1 dB/cm (@1300 nm)
Wavelength to calculate	1538 nm
Refractive index data file	2.41 @1550 nm
Er^{3+} ion density	$6x10^{26}$ ions m^{-3}
Yb^{3+} ion density	0 ions m^{-3}
Er^{3+} metastable lifetime	1.3 ms
ESA cross-section value at 1480 nm	$3x10^{-25}$ m^2 [123]
A_{32}	$1x10^8$ s^{-1}
A_{43}	$2x10^4$ s^{-1} [123]
C_{up}	$4x10^{-23}$ m^3 s^{-1} [257]
C_{14}	$2x10^{-24}$ m^3 s^{-1} [257]
Noise centre frequency	1550 nm
Noise bandwidth	60 nm
Noise threshold	-100 dB

Note: A_{32}, the nonradiative rates from level 3 (upper level of $^4I_{13/2}$ state) to level 2 (lower level of $^4I_{13/2}$ state), is fixed as $1x10^8$ s^{-1} to make sure the rapidly decay between these two levels.

As this model is designed for an Er^{3+}-Yb^{3+} codoped waveguide, the Yb^{3+} density was set to be 0 atoms/m^3 in simulation for the absence of Yb^{3+} ion. It has to be pointed out that in this model, any process occurring above the $^4I_{9/2}$ state (known to occur here as discussed in Section 3.4) is not taken into consideration, because short lifetime of the $^4I_{9/2}$ state in silicate glasses. However, in chalcogenide glass due to the low phonon energy, the lifetime of $^4I_{9/2}$ state is long enough (intrinsic lifetime of 0.59 ms was measured on an erbium ion doped As_2S_3 film, see Section 3.4) to support further up-conversion processes, which could be confirmed from emission bands at 520 and 540 nm in the wideband emission spectrum described later in Section 4.4.2. Due to the limitation of this model, influences of energy levels above the $^4I_{9/2}$ state are not considered in the following simulations.

Firstly, the small signal gain at three different signal wavelengths (1540 nm, 1555 nm and 1580 nm) were simulated for Er^{3+}:As_2S_3 waveguides with different excitation powers at 1480 nm. The simulation results are presented in Figure 4.11. Clearly, the results for the three different wavelengths share a similar trend, and the 1540 nm signal has the best performance lying closest to the erbium ion gain peak. With a 1540 nm signal, net gain can be achieved with pump power as low as 20 mW, and then the gain saturates at its maximum value of 11dB at for a 100 mW pump. The 1555 nm signal has a similar trend to the 1540 nm one, but less gain at 7 dB in total; while the 1580 nm signal barely exhibits gain even with its best performance, which can be explained by the relatively small emission cross-section of erbium ion in chalcogenide glass hosts at this wavelength.

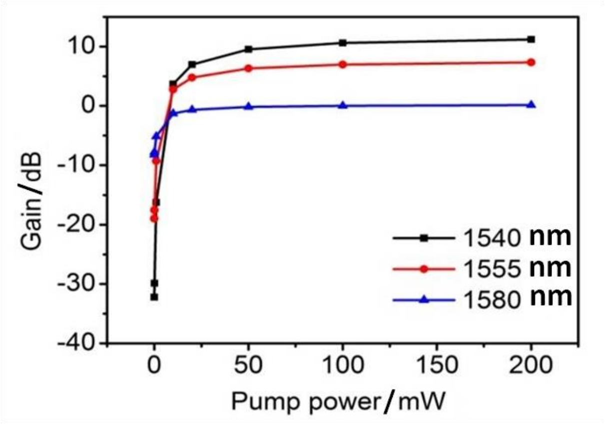

Figure 4.11 Simulated signal gain spectra versus pump power at different wavelengths of a 30 mm long Er^{3+}:As_2S_3 waveguide amplifier with Er^{3+} concentration of $6x10^{26}$ ions m^{-3}.

The gain spectrum under different excitation powers, ranging from 0.01 mW up to 200 mW, in the waveguide was also simulated and is shown in Figure 4.12. From the results, the peak gain occurs at 1540 nm, and 50 mW can be considered the maximum required pump power. Based on simulations, gain of 11 dB at 1540 nm in a 30 mm long waveguide could be expected, corresponding to 3.67 dB/cm. The high level of performance for low pump powers even with 1 dB/cm propagation loss is a consequence of the high gain cross-section in chalcogenide glass hosts and the small mode area afforded by the high refractive index contrast. Clearly performance of this order would be attractive for compact devices such as amplifiers or laser arrays powered off a single pump, or for ultrahigh repetition rate on chip mode locked lasers.

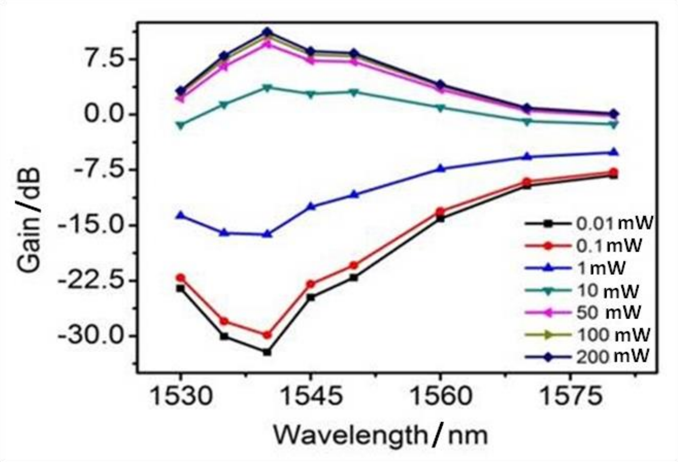

Figure 4.12 Simulated gain spectra with different pump powers of an Er^{3+}:As_2S_3 waveguide amplifier.

4.4 Waveguide fabrication

4.4.1 Waveguide fabrication introduction

At present, the usable length of chalcogenide planar waveguides is determined by the loss of the waveguide at the pump wavelength. Reduction of the mode area, as required to maximise nonlinear optics effects, is challenging since waveguide loss usually increases super-linearly with the waveguide cross-section decrease, due to scattering induced by side wall surface roughness [16, 259]. Besides careful design of the waveguide structure to weaken the negative effects from rough surfaces and sidewalls, another method to overcome this issue is improved process technology. Since the first reports of waveguides made from chalcogenide glasses appeared in the 1970s from researchers in Russia [260] and Japan [261, 262], various ways of fabricating waveguides have been proposed. Some of the most popular methods are described below.

(a) CW direct laser writing

Direct laser writing in chalcogenide materials due to their photo-darkening effect, which refers to the phenomenon that when chalcogenide glass is illuminated by light of energy above its bandgap, the optical absorption edge of illuminated material will shift to longer wavelength. This property in chalcogenide glasses has been used to fabricate waveguides since the 1970s. In 1979, Zembutsu et al. [262] reported waveguides based on As-Se-S-Ge thin films using irradiation with a 1.06 µm Nd^{3+}:YAG laser. The refractive index change between the irradiated area and un-irradiated area was about

0.03 at 1.06 µm wavelength which they believed was large enough to fabricate a 3-D waveguide (curved waveguide and optical directional coupler). The best propagation loss of 0.4 dB/cm at 1.064 µm was achieved in an $As_{40}Se_{10}S_{40}Ge_{10}$ (at%) film, and they believed with an optimised film composition an even lower loss waveguide was achievable. In Turnbull et al.'s work [263], 5 µm width waveguides were fabricated by exposure to 514.5 nm CW light from an Ar^{3+} laser on sputtered $Ge_5As_{34}Se_{61}$ (at%) films with an approximate dosage of 100 J/cm^2 on the sample. The propagation losses of the obtained waveguides ranged 3.5 to 6.4 dB/cm at 1.3 µm, and scattering from micro-cracks at the glass–substrate interface was speculated as the dominant source of the loss. Nicolas et al. [264] reported a refractive index change of 0.04 induced in an As_2Se_3 film by exposure to 633 nm He–Ne laser through a photomask. In waveguide fabrication, an incident CW power of 1.0 mW, focused using an f=11 mm aspheric lens, at a translation speed of 4 mm/min were thought ideal writing parameters, with which good lateral confinement, single-mode output, and high injection efficiency were achievable. The measured average propagation loss of the waveguides was 0.5±0.1 dB/cm for the TE mode and 1.1±0.1 dB/cm for the TM mode at 8.4 µm, respectively.

Clearly, using the photodarkening property of chalcogenide glasses for waveguide fabrication is a simple approach. However, with this method only low refractive index contrast is achievable, and often the waveguides fabricated with this method are not stable when heated or exposed to even long term ambient light.

(b) Femtosecond direct writing

Femtosecond lasers irradiating within the Urbach-tail region were also used to direct write chalcogenide waveguides [265-267]. Zoubir et al. [207] wrote waveguides in As_2S_3 films with femtosecond laser pulses from a 25-MHz repetition rate Ti:sapphire laser, with an 40 nm spectral bandwidth centred at 800 nm, producing 20-nJ pulses of 30-fs duration with 4.5% pulse-to-pulse stability. In the waveguide, a refractive index difference bigger than 10^{-2} was achieved. The structure change induced by Ti:sapphire laser illumination was investigated using Raman spectroscopy. A buried single mode waveguide within a Tm^{3+}-doped $75GeS_2 15Ga_2S_3 10CsI$ (mol% GGSI) glass substrate was realised using femtosecond laser direct writing [267]. Single mode guidance at 1039 nm, with a minimum propagation loss of 0.86 dB/cm at 1039 nm, was reported. It was pointed out that high stress could be induced in waveguides directly written using low-repetition rate ultrafast laser systems [268].

(c) UV direct writing

UV direct writing is also thought a useful way for waveguide fabrication. In Mairaj et al.'s work [269], waveguides were written on Ga:La:S bulk glass with continuous wave UV (244 nm) light providing spatially uniform fluence (±5%) in the range of 1.1 J/cm^2 to 3.6 J/cm^2. Propagation losses of the obtained waveguides was 0.2±0.1 dB/cm at 1.3 µm, with a positive change of refractive index of 10^{-3}. Lin et al. [270] reported channel waveguides with ~ 10^{-2} refractive index difference achieved by irradiating As_2S_8 films under a UV light (300–436 nm) with an intensity of 58 mW/cm^2 . After proper annealing, propagation loss of 0.76 dB/cm was achieved at 1310 nm.

Similar to the photo-darkening and femtosecond methods, the refractive index contrast obtained using UV direct writing is limited.

(d) Ion implantation

Ion implantation has also been trialled as a method for fabricating chalcogenide glass waveguides. Meneghini et al. [271] fabricated channel waveguides on As_2S_3 films through implanting helium ions at an energy of 113 keV, a dose of $2x10^{16}$ ion/cm^2, and an average current density of 1 µA/cm^2. The ion range distribution calculated using commercial software was 671 nm and the straggling width was 332 nm (half-width at half-maximum). Also a metallic mask was applied in front of the film in order to define the structure of the final waveguides. Confinement of 1.3 µm light in the implanted channel was achieved, and this was explained by the refractive index increase of As_2S_3 due to helium implantation. However, the propagation loss of this waveguide was not measured due to the too low level of the scattering loss over the buried channel waveguide.

In Qiu et al.'s work [272], gallium lanthanum sulphide (GLS) and gallium lanthanum oxysulfide (GLSO) glass waveguides were fabricated using Ar^+ ion implantation at 60 MeV and $2x10^{12}$ ions/cm^2. The beam current density in the experiment was chosen at about 10 nA/cm^2 to minimise charging and heating effects during irradiation. Waveguides with a refractive index distribution of 'well + barrier' type were obtained, where the 'well' region had an increased refractive index because of the ionisation effect of electronic energy deposition, followed by the appearance of a 'barrier' region due to the energy deposition into nuclear displacements. Propagation losses of 2.0 dB/cm for GLS and 2.2 dB/cm for the GLSO glass were achieved.

It is well known that, ion implantation is an energy and time-consuming method, and, with this method, the metallic mask used to define the waveguide structure is not trivial to fabricate. Also the roughness caused by the high energy ion injected into chalcogenide films is another issue needing careful consideration.

(e) Wet etching

Wet-etching is a well-known technology for waveguide fabrication from many host materials, and it has also been applied in processing chalcogenide waveguides. In DeCorby et al.'s report [273], waveguides based on As_2S_3 films were patterned directly using photo-exposure through a mask followed by selective wet etching. Shallow ridge waveguides (with ridge width of 3.8 µm), with losses as low as 0.26 dB/cm at 1530 nm, were produced. As_2S_3 glass ridge waveguides were also fabricated with wet-etching in Su et al.'s work [208]. The as-deposited As_2S_3 film was irradiated with a 2 mW 532 nm laser with a spot diameter on the order of 2 µm. This 532 nm laser irradiation induced a change not only in structure but in physicochemical properties as well, offering the possibility that, with a properly chosen selective etching liquid, the etching rate for exposed and unexposed parts could be very different. The film was then wet etched using CS_2 solution with iodine as an oxidising reactant. The average loss obtained for the ridge waveguide was 5.5±0.5 dB/cm at 1330 nm. In this fabrication process no mask was required.

However, the drawback illustrated by wet etching methods is that many chalcogenide glasses are attacked by alkaline resist developers which leads to a relatively rough sidewalls which in turn increases the scattering losses [250]. Precise control of waveguide dimensions is another difficulty that needs to be overcome, along with the non-ideal cross-sectional profile resulting from isotropic etching.

(f) Lift-off techniques

The lift-off method was proposed to overcome the issues caused by etch induced sidewall roughness, in which a chalcogenide glass film is deposited onto a pre-patterned resist structure with undercut. In Frantz et al.'s report [274], waveguides were patterned by a lift-off technique on a gallium lanthanum sulphide (GLS) glass film deposited using radio-frequency (RF) magnetron sputtering. The root mean square (RMS) surface roughness of a slab waveguide was sufficiently small to provide low scattering losses. Estimated propagation loss for the final lift off waveguide was 2.4±0.4 dB/cm at 1650 nm. High-index contrast $Ge_{23}Sb_7S_{70}$ (at%) strip waveguides and small core $Ge_{23}Sb_7S_{70}$

(at%) rib waveguides (1.2 µm in width, 500 nm in height) have been fabricated using the lift-off method in Hu et al.'s report [275]. The obtained strip waveguides had good wafer-scale uniformity with loss of 2-6 dB/cm, while the rib waveguides had a lower loss of 0.5 dB/cm.

Other processes, for example, thermal reflow, have been utilised to smooth the sidewall roughness and then decrease loss. Although, with lift-off methods, the quality and loss of waveguides are both improved, scattering from rough sidewalls is still thought to be the main source of the loss.

(g) Reactive ion etching

Reactive ion etching refers to a method that removes material by exposing the materials to a bombardment of ions which both chemically and physically remove material from the exposed surface. In reactive-ion etching, high-energy ions are generated in low pressure plasma, typically using an RF electromagnetic field. The ions bombard the wafer surface and react with it forming volatile etch products that are pumped away. Several etching parameters, such as pressure, gas flow, gas composition, and RF power, can be chosen to meet different requirements and vary the degree of etch anisotropy. High quality chalcogenide waveguides with low loss were fabricated using this method. Ridge As_2S_3 waveguides produced using dry etching with CF_4 and O_2 have been reported by Ruan et al. [12]. High index contrast rib waveguides ($\Delta n \sim 1$) were obtained with a minimum propagation loss of 0.25 dB/cm at 1.5 µm. Madden et al. subsequently reported on the fabrication of etched As_2S_3 chalcogenide planar rib waveguides using CHF_3 and O_2 [13]. Optical loss as low as 0.05 dB/cm at 1550 nm was achieved, which is the lowest loss in chalcogenide waveguides ever reported so far and comparable to losses obtained in even mature low index contrast germanosilicate technologies suitable for dense integration.

Besides all the methods mentioned above, there are some other approaches that could be used to fabricate chalcogenide glass waveguides, such as ion exchange [276]; fibre-on-glass [277]; physical sputter etching [278]; hot embossing [279, 280], etc. However, each of them has its own drawback. For example, the fibre-on-glass and hot embossing always need to heat the materials up to T_g, which will may enable the rare-earth ions to cluster; with ion exchange an ionic species is required for exchange that is not normally present in chalcogenides, and with physical sputter etching methods, it is hard to get low loss chalcogenide waveguides preferable for amplification devices.

4.4.2 Erbium ion doped As_2S_3 waveguide fabrication

Low passive losses in rare-earth ion doped planar waveguides are highly desirable as they both maximise the external gain through lower signal losses, and also allow for longer devices through lower pump passive losses with correspondingly higher amplifier gain and saturated output power. Therefore, a method that could fabricate low loss waveguides is important. To date, the best As_2S_3 waveguide with loss as low as 0.05 dB/cm was fabricated by UV lithography combined with inductively coupled plasma reactive ion etching (ICP-RIE) [13]. The high quality waveguides and the availability of facilities such as UV lithography and plasma etching made this method attractive.

Based on the waveguide design discussed above (see Section 4.2.1), As_2S_3 bilayer films were deposited by thermal evaporation on a <100> oriented 100 mm silicon wafer with 2 μm of thermal silicon dioxide (TOX) as a bottom cladding: first an erbium ion doped As_2S_3 layer with 800 nm thickness (erbium metal was used as the erbium ion source), followed by an un-doped As_2S_3 layer of 550 nm. Before going to the UV lithography, the as-deposited film was thermal treated at 130 °C for 24 hours followed by green light treatment for 48 hours to push the film’s properties back toward its bulk counterpart (see Section 3.2.3) [233, 234]. A 100 nm layer of SU-8 was spun and cured on the film before putting it into the annealing oven. This SU-8 layer benefits films in two ways: firstly, this thin SU-8 layer protects the films from O_2 to prevent film quality degradation by oxidation and surface diffusion [232]. Secondly, it is well known that chalcogenide glass films are readily attacked by alkaline developers. Fortunately, this SU-8 layer acting as a protective coating beneath the resist prior to patterning can protect the films from this attack.

After thermal and green light treatment (see Section 3.2.3), the refractive index of erbium ion doped As_2S_3 films can reach 2.41 at 1550 nm which is close to value of its bulk counterpart (2.43). Nominal waveguide widths on the chrome mask were 1, 2, 3 and 4±0.1 μm. Photoresist coating and development was carried out in an SVG 8600 series track to ensure repeatability, and resist exposure was undertaken in a Karl Suss Mask Aligner (MA-6) with a 350 W mercury arc lamp filtered to provide just the 365 nm i-line emission (~4 mW/cm^2 intensity). The resist was 1 μm thick Clariant AZ MIR 701 and it was developed for 60 seconds in a single puddle using AZ 326 MIF developer after a 1 minute post exposure bake at 110°C on a vacuum contact hotplate.

Following development, a 1 minute 110°C hard bake was applied in ambient atmosphere.

All the etching work was performed in an ICP system (PlasmaLab 100 from Oxford Instruments). This ICP system has a load lock chamber and sample chamber which are pumped separately. The base pressure of the system is around ~$2x10^{-6}$ Torr (~$2.67x10^{-4}$ Pa) and the system can pump up to 100 sccm of gas and still maintain 8 mTorr (~1.1 Pa) pressure. Gases used in etching were controlled by mass flow controllers. Etching depth and etching rate were monitored live by an in-situ laser interferometer operating at 677 nm. The coated SU-8 layer was removed by exposing the film to O_2 and Ar plasma in the ICP system (200 W ICP power, 20 W forward power and 10 mTorr (~1.3 Pa) pressure).

Previously, a combination of CF_4 and O_2 were employed to etch As_2S_3 [231]. However, the etching results indicated that this combination had different etching rates for different phases present in the As_2S_3 films which is known to be inherently nanoscale phase-separated [250, 281]. This leads to rough etched surfaces which are undesirable. Based on experimental results, the main cause for this roughness was due to the high proportion of reactive fluorine in CF_4 which gave different etching rates for some phases of the thermally post-treatment As_2S_3 host material. Therefore, CHF_3 was employed instead to reduce the concentration of fluorine and also to provide some sidewall and surface passivation via the deposition of fluorocarbon polymers [13]. This resulted in significantly lower waveguide losses. Thus, in this work, CHF_3 was used as the etching gas, and the details of the etching process was described in [13].

After etching, the residual resist was removed by using AZ Quikstrip wet stripping. Normally, inorganic polymer is thought a good option for top protective cladding. However, broad absorption bands inorganic polymer possesses are close to the wavelengths of our interest, therefore, the waveguides were used with an air top-cladding instead (see Figure 4.7). Whilst this made them more prone to damage and limited their life, it was deemed an acceptable compromise in most testing instances. After hand cleaving with a diamond scriber, the waveguides were ready to measure. A schematic of the whole fabrication procedure is shown in Figure 4.13. Figure 4.14 shows an optical micrograph of the end facet of a finished 2 µm width waveguide.

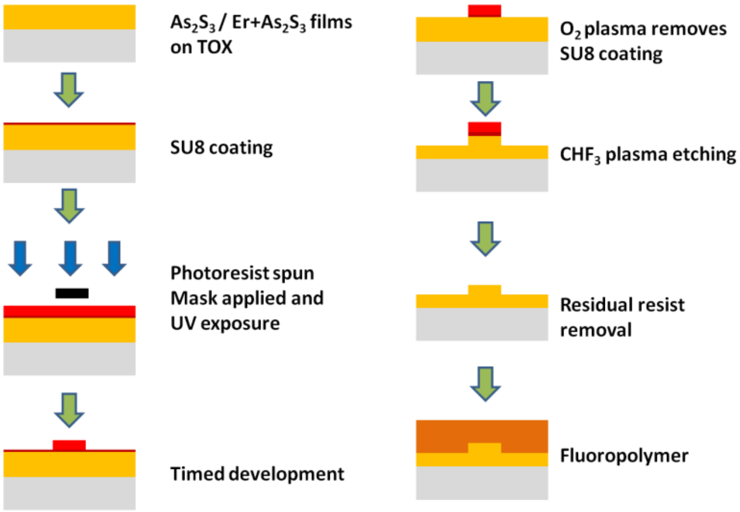

Figure 4.13 As_2S_3/Er^{3+}:As_2S_3 (after thermal post-treatment) waveguide fabrication procedure using photolithorgraphy. TOX refers to thermally oxidized silicon.

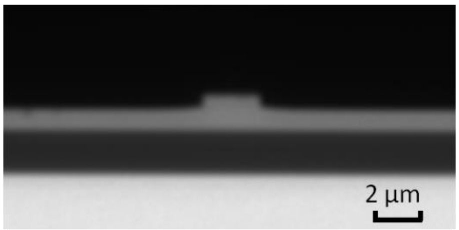

Figure 4.14 Image of the end facet of a 2 μm width Er^{3+}:As_2S_3 waveguide depicted in Figure 4.7.

4.5 Characterization of erbium ion doped As_2S_3 waveguides

To test the waveguides both passively and in a pumped configuration, an in-house supercontinuum (SC) source was used as a probe/signal source. The SC source was generated in a photonic crystal fibre driven by 10 ps pulses from a mode-locked Nd^{3+}:YVO4 laser [282, 283]. This was coupled into the waveguides through a lensed fibre, with wavelength range from 300 nm to 2000 nm and total power up to around 200 mW. Transmission spectra using this SC source were recorded using an optical spectrum analyser (Ando AQ 6317) and the supercontinuum spectrum is shown in Figure 4.15. The SC source was heavily attenuated (<-30 dBm/nm) during the experiment to avoid bleaching the Er^{3+} absorption in waveguide samples.

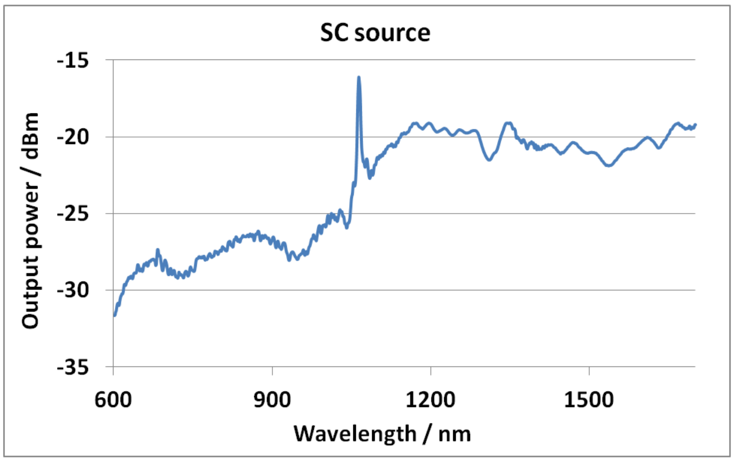

Figure 4.15 Spectrum of the SC source used as signal source in this thesis.

4.5.1 Propagation loss and absorption of erbium ion doped As_2S_3 waveguides

The first concern regarding the obtained Er^{3+} doped As_2S_3 waveguide is its propagation loss and Er^{3+} absorption spectrum, which can both be derived from loss spectra of the waveguide. Loss spectra were measured using the SC system described above (see Section 4.5) as a probe source, and recorded with the described OSA (see Section 4.5) on the output side of the waveguides. The set-up for this measurement is shown in Figure 4.16. The attenuated SC source was delivered to waveguides by a lensed fibre from Oz Optics. The lens focused the SC source to a spot size of 2.5 μm ($1/e^2$) diameter at 14 μm distance from the tip. On the output side of the waveguide, another lensed fibre was positioned to collect the output signal. Both lensed fibres were mounted on 3 axis piezo enhanced micro-positioning stages for hands-off alignment. Reference fibre to fibre SC spectra were recorded at the start and end of each measurement session to mitigate any drift in the SC spectrum shape.

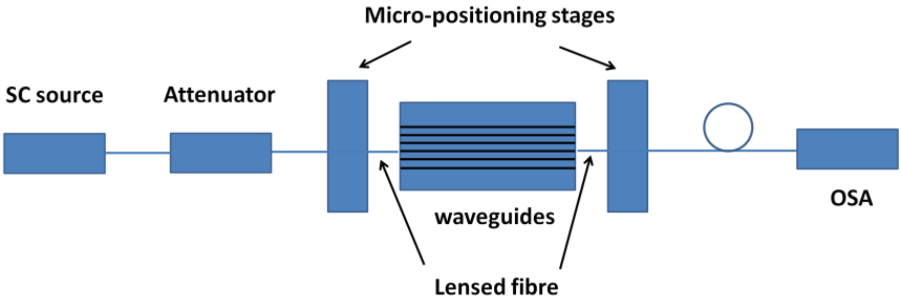

Figure 4.16 Optical set-up for Er^{3+}:As_2S_3 waveguides loss measurement.

The typical insertion loss spectrum of a 180 mm long, 3 µm width serpentine waveguide, with 2 mm radius bends, with 0.15 at% erbium ion is shown in Figure 4.17 after normalising out the SC spectrum using a lensed fibre to lensed fibre measurement as the reference. Two absorption bands are visible in the spectrum; one located at 980 nm, corresponding to the absorption of $^4I_{15/2} \rightarrow ^4I_{11/2}$ transition; and the other located at 1540 nm which is ascribed to the absorption of $^4I_{15/2} \rightarrow ^4I_{13/2}$ transition.

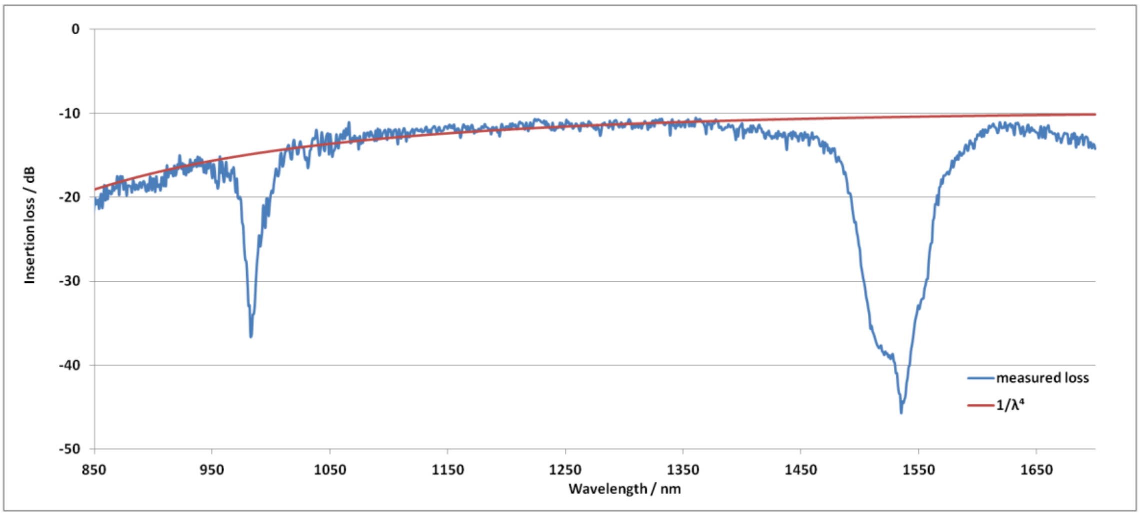

Figure 4.17 The insertion loss spectrum of a 180 mm long 3 µm width Er^{3+}:As_2S_3 serpentine waveguide with 0.15 at% erbium ion concentration. The red fitted curve represents the loss due to Rayleigh scattering.

Besides the erbium ion absorption bands, the background also provides information on the loss of this waveguide at different wavelengths. The waveguide loss spectrum indicates an estimated background propagation loss of about 0.35 dB/cm at 1550 nm after correcting for coupling losses (calculated at 2.35 dB/facet from mode overlap using a Matlab code based on the finite difference method and reflection [253]), and shows an excellent fit to a $1/\lambda^4$ curve, where λ is the wavelength. This indicates that the loss is dominated by Rayleigh scattering off nanoscale inhomogeneities and is unusual for As_2S_3 waveguides which typically show loss curves dominated by $1/\lambda^2$ responses from sidewall scattering. From the fit, the erbium ion absorption was extracted. The absorption band at 1540 nm is 34 dB in this 180 mm long waveguide, leading to a 1.9 dB/cm absorption of erbium ion in this 0.15 at% (0.45×10^{20} ions/cm^3) doped waveguide.

The absorption band centred at 1540 nm was also extracted, normalized and is plotted in Figure 4.18. A normalized erbium ion absorption band for a TeO_2 waveguide [152] is also plotted in Figure 4.18 for comparison. One immediately striking difference is in the short wavelength absorption edge, where with As_2S_3 as a host, the absorption at the usual erbium ion pump wavelengths in the 1480-1490 nm range is considerably weaker than in TeO_2. This suggests that a pump wavelength in the 1505-1510 nm range may be required for efficient pumping. The wavelength of the maximum absorption is also red shifted as expected, and this could be explained by the nephel-auxetic effect [39], which was discussed in Section 3.3.2(c).

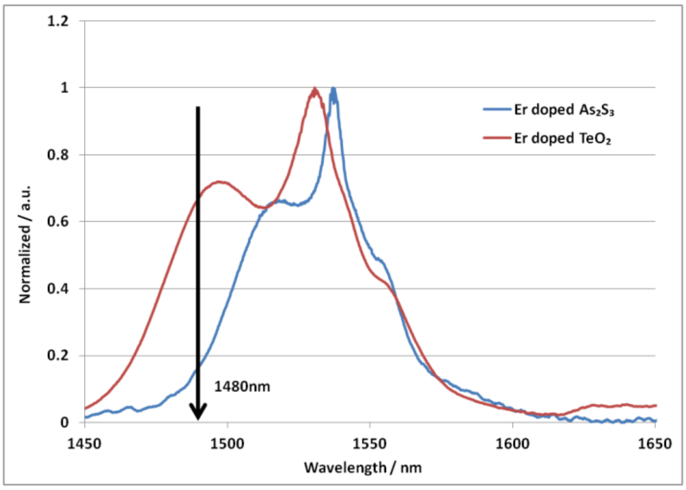

Figure 4.18 Normalized absorption bands from 1450 to 1650 nm in Er^{3+}:As_2S_3 and Er^{3+}:TeO_2 waveguides. The black vertical arrow shows the position of the usual Er^{3+} 1480 nm pumping wavelength.

4.5.2 Amplification measurements of erbium ion doped As_2S_3 waveguides

In the interests of clarity, it is noted that the raw internal gain of a waveguide amplifier is considered to be the enhancement factor minus the rare-earth ion absorption, where the enhancement factor is the ratio of the output power with pump on, minus the amplified spontaneous emission (ASE) to the output power with the pump off. This is the definition used later to measure the internal gain and represents actual signal amplification due to the material processes down the waveguide length indicating the likely gain available if propagation losses are low (presumed to be the case for any useful amplifier). Raw transparency occurs when the internal gain equals 1, that is it offsets the rare-earth ion absorption exactly, and gain exists when it exceeds unity. Net internal gain results when the division by the waveguide propagation losses leaves a number above unity and means more power exits the waveguide than entered it.

Excitation experiments on waveguides were performed with the set-up shown in Figure 4.20. The excitation laser was centred at 1490 nm with a maximum output power of 200 mW exiting the SMF-28 output connector. This was combined with the attenuated SC source (see Section 4.5) which acted as a probe signal via the 10% port of a 10/90 coupler and then was delivered to the waveguide through a lensed fibre as previously described. On the output side of the waveguide, the signal was collected by another aligned lensed fibre, then was passed through two 1490/1550 nm WDMs which provided roughly 30 dB attenuation for the excitation power at each WDM. After removing the remnant excitation power, the signal spectrum was recorded by an OSA. A bi-directional pumping setup can also easily be formed by adding another excitation laser to the output side via the first WDM.

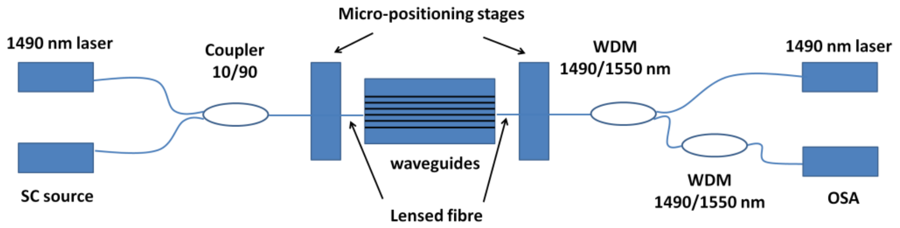

Figure 4.20 Optical set-up for excitation experiments on Er^{3+}:As_2S_3 waveguides with 1490 nm uni- or bi-directional pump with a SC probe source (see Figure 4.15 for output spectrum of this SC source).

It is worth noting that in the set-up described here, the loss from the lens tipped fibres themselves is about 1.8 dB (which was zeroed off to a lens tipped fibre to lens tipped fibre measurement, consequently it had no effect on the waveguide insertion loss), and the overlap loss due to the mismatch of the modes between the lensed fibre and the waveguide and surface reflection are about 2.35 dB/facet in total based on calculation. Therefore, this set-up comes with a total insertion loss of about 6.5 dB.

The test results are plotted in Figure 4.21 for a 55 mm long, 2 µm width, 0.15 at% Er^{3+} doped As_2S_3 straight waveguide uni-directionally pumped at 1490 nm. The sharp drop of power below 1520 nm and above 1640 nm is due to the cut-off of the 1490/1550 nm WDM applied here. The erbium ion absorption band at 1540 nm bleaches with increase of excitation power. From Figure 4.21, excitation of 70 mW at 1490 nm in the waveguide gives the best performance of this waveguide. Any further increase of pumping power only resulted in photosensitive, where the spectrum is degraded with additional dips and spikes, and thus spectra with higher excitation power are not given in Figure 4.21.

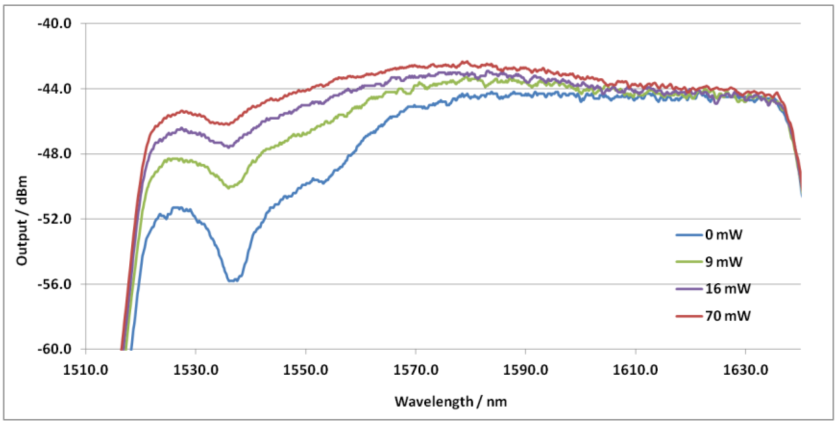

Figure 4.21 Excitation results for a 55 mm length, 0.15 at% Er^{3+}:As_2S_3 waveguide, uni-directionally pumped at 1490 nm with SC probe (see Figure 4.15).

To reiterate, enhancement is the ratio of output power with pump on, minus the ASE, to the output power with the pump off. Therefore, to get a clear enhancement, ASE spectra also have to be recorded under the identical condition only with the SC source turned off. The same set-up was employed to measure three spontaneous emission spectra under excitation of 9 mW, 16 mW and 70 mW, respectively, and the results are shown in Figure 4.22.

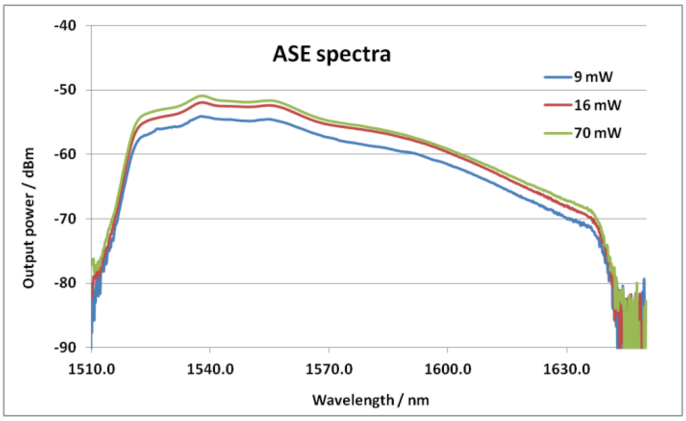

Figure 4.22 Amplified spontaneous emission (ASE) spectra for a 55 mm length, 0.15 at% erbium ion doped As_2S_3 waveguide, with uni-directional pump at 1490 nm.

Enhancement factor spectra were then extracted from the excitation spectra, ASE spectra and the zero excitation power spectra. The erbium ion absorption curve was obtained from the insertion loss spectrum and the waveguide propagation loss fitting curve. This was then applied to the enhancement factor curve to obtain an internal gain curve, which is shown in Figure 4.23.

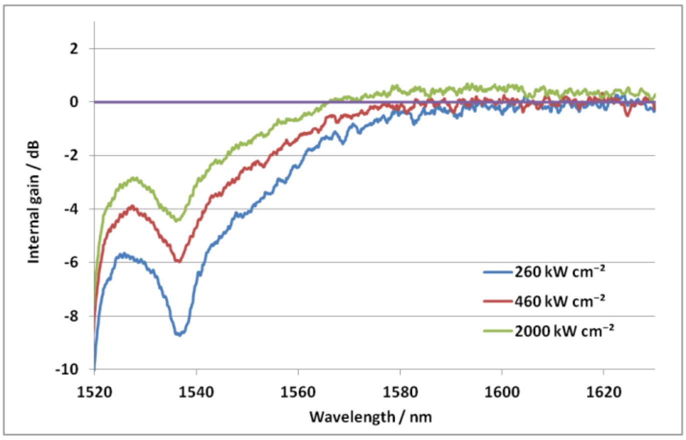

Figure 4.23 Internal gain characteristics for different 1490 nm pump intensities working uni-directionally in a 0.15 at% Er^{3+}:As_2S_3 waveguide of 55 mm length.

A small internal gain (~0.7 dB) from 1570 to 1630 nm was observed, the first time to the Author's knowledge that any internal gain has ever been reported in an erbium ion doped chalcogenide bulk glass, fibre or thin film based waveguide amplifier. That internal gain shows first at the longer wavelengths can be explained simply by the emission cross-section inhomogeneous broadening and the correspondingly low absorption cross-section there. However, it is clear that at the absorption peak wavelength 1538 nm, the device is still about 4.3 dB below the optical transparency line even for the best performance spectrum in Figure 4.23. Considering the 10 dB absorption at 1538 nm of this 55 mm long waveguide, it is reasonable to estimate that roughly 30% of total erbium ions are inverted in this waveguide. Details of the erbium ion inversion estimation method can be found in Section 6.4.

It was not possible to utilize the full pump power as photosensitive effects began to occur, characterized by the presence of mode coupling gratings and the appearance of deep mode coupling dips in the spectrum. Whilst this complicated matters, it was however clear that the gain spectrum was not increasing at any significant rate with additional pump power. Similarly switching to 1505 nm pumps did not produce a better result.

For comparison, an 18 mm length, 0.6 at% Er^{3+}:As_2S_3 waveguide was also pumped under the same conditions and the result is shown in Figure 4.24. About 8 dB optical enhancement is found at 1540 nm when only 5 mW pump power applied, which is believed to have been due to the ASE. No further optical enhancement occurs even when the pump power is pushed up to 100 mW. Also it is clear the ASE level of this sample (~-65 dBm) is much lower than that of the 0.15 at% Er^{3+}:As_2S_3 sample (~-51dBm), and both of these values were measured with 2 nm optical bandwidth.

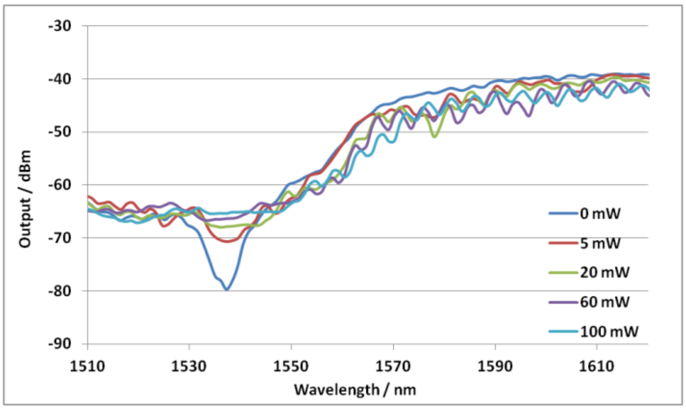

Figure 4.24 Excitation results for an 18 mm length 0.6 at% Er^{3+}:As_2S_3 waveguide with uni-directional pump at 1490 nm.

Given the evident non bleachable absorption in the excitation spectra, it is suggested that there could be significant clustering in this 0.6 at% Er^{3+}:As_2S_3 waveguide. Even the 0.15 at% Er^{3+}:As_2S_3 waveguide appears to have a significant degree of clustering and further improvements to the deposition process are required to attain net gain.

4.6 Co-thermal evaporation of neodymium ion doped As_2S_3

It is well known that it is more difficult to achieve optical gain in a quasi-three-level energy system like Er^{3+} than in a four-level energy system like Nd^{3+}, due to the absence of the ground state absorption at the emission wavelength in a four level energy system. Referring to Figure 4.25, Nd^{3+} ions in the $^4I_{9/2}$ ground state absorb 808 nm photons and are excited to the $^4F_{5/2}$ state, and then by phonon emission rapidly decay to the upper lasing $^4F_{3/2}$ state. 1.06 µm emission occurs when ions transfer from the $^4F_{3/2}\rightarrow{}^4I_{11/2}$ levels, and the ions in the $^4I_{11/2}$ level are quickly de-excited to the ground state $^4I_{9/2}$, again, due to a phonon mediated process. Due to the long lifetime of the $^4F_{3/2}$ state and the efficient nonradiative decay between the $^4I_{11/2}$ and the $^4I_{9/2}$ energy levels, a population inversion is easily formed between the $^4F_{3/2}$ and the $^4I_{11/2}$ energy levels. High gain is possible due to the lack of absorption at the emission wavelength. Therefore, it would be interesting to know whether population inversion in Nd^{3+} doped As_2S_3 waveguides could be obtained.

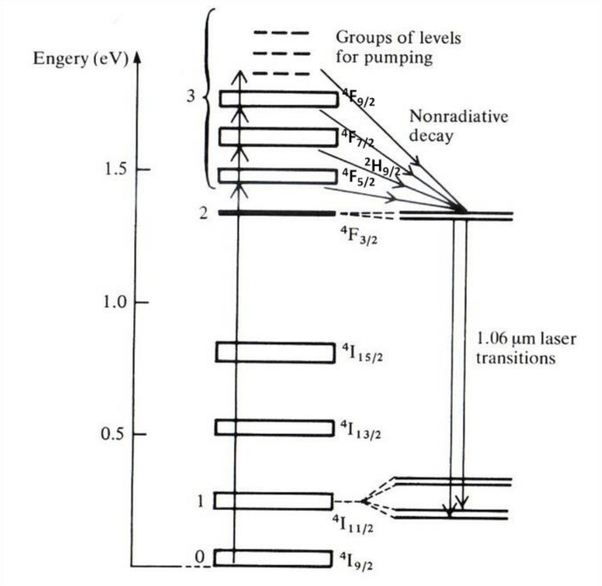

Figure 4.25 Energy level diagram of Nd^{3+} ions.

4.6.1 Neodymium ion doped As_2S_3 film deposited using co-thermal evaporation

Much work on neodymium doped chalcogenide glasses, fibres and waveguides has been reported. The first attempt of measuring absorption and emission spectra of neodymium ions in chalcogenide glasses was made by Reisfeld et al. in 1977 [42]. Chalcogenide glasses of composition $0.7Ga_2S_3$-$0.27La_2S_3$-$0.03Nd_2S_3$ (mol%) were prepared. Absorption and emission spectra of these glasses were measured and compared to commercial neodymium ion doped silicate glass. Higher absorption intensity and lower nonradiative relaxation rate were observed compared with their silicate counterparts [42]. In Mori et al.'s paper [284], Nd^{3+} doped Ge–As–Ga–Sb–S (core) and Ge–As–S (cladding) fibre was drawn by the rod-in-tube method. Under 890 nm pumping, internal gain of 6.8 dB at 1.083 μm was achieved from a 50 mm length fibre with doping concentration of 1000 ppm. Net signal gain was not obtained due to the high transmission loss of the fibre. Laser action in a neodymium ion doped chalcogenide glass was demonstrated for the first time in a Ga-La-S host glass by Schweizer et al. [105]. 1.083 μm laser action was achieved with a 1.42 mm thick sample of Ga-La-S glass doped with 1.5 mol% Nd_2S_3 (2.6xl0^{20} ion/cm^3) neodymium ions, under excitation wavelengths of 815 nm and 890 nm from a Ti:sapphire laser. In the following year, laser action at 1.08 μm from a 22 mm long 0.05 mol% Nd_2S_3 doped Ga-La-S fibre fabricated using the rod-in-tube technique was reported by the same group [106]. In Mairaj et al.'s report [108], channel waveguide structures were directly written using a focused UV-laser beam in neodymium ion doped Ga-La-S glass. A lasing experiment was performed on a 0.5 mol% Nd_2S_3 (8.7xl0^{19} ion/cm^3) doped 16 mm long waveguide.

Single mode laser operation at 1075 nm with output slope efficiency of 17% with respect to absorbed power was obtained. Attenuation in the laser device was estimated by the Findlay–Clay method combined with a separate calculation involving the slope efficiency, and the upper limit of the propagation loss was found to be about 0.5 dB/cm. Most of the work has focused on the Ga-La-S glass system because of its high rare-earth ion solubility, and there were few reports on other more frequently used glasses for waveguides such as As_2S_3.

In this work, Nd^{3+} doped As_2S_3 films were deposited in a similar manner to that of the co-thermally evaporated erbium ion doped As_2S_3 films, with the substitution of neodymium powder instead of erbium metal. Evaporation was performed at a vacuum level around ~$3x10^{-7}$ Torr (~$4x10^{-5}$ Pa). After reaching the pressure set point, a slow increase of the neodymium powder temperature showed evaporation commenced at a temperature of ~ 1000 °C, and the rate reached 0.001 nm/s at 1130 °C. For the film deposition, the neodymium temperature was set at ~ 1060 °C and the rate of As_2S_3 was set at 0.1 nm/s to target a final neodymium ion concentration of ~0.3 at%.

After deposition, a 120 nm SU-8 protective layer was coated on the obtained Nd^{3+}:As_2S_3 film, then thermal post-treatment (at 130 °C for 24 hours under vacuum) and light post-treatment (500-570 nm green light with ~3mW/cm^2 intensity for 48 hours)were carried out. The obtained film was characterized using the SCI Filmtek 4000. After thermal and light post-treatment, the film refractive index was 2.41 at 1550 nm and the bandgap was 2.27 eV, measured from a 1.48 μm thick film. These results indicated the Nd^{3+} doping had little effect on the host glass As_2S_3 which exhibited a refractive index of 2.41 at 1550 nm and bandgap of 2.34 eV (see Section 3.23).

4.6.2 Characterization of the neodymium ion doped As_2S_3 film

Based on the energy level diagram of Nd^{3+} ions shown in Figure 4.25, the lifetime of the upper $^4F_{3/2}$ energy level related with the 1.08 μm emission is of most concern. However, due to lack of high isolation pump/signal WDMs working at this wavelength, the $^4F_{3/2}$ energy level lifetime could not be measured.

The Nd^{3+}:As_2S_3 film emission spectrum was collected using a Horiba Jobin Yvon 64000 spectrometer. The excitation laser operated at 830 nm, which is not the optimum wavelength to excite Nd^{3+} ions from the ground state up to the $^4F_{5/2}$-$^2H_{9/2}$ levels, but it still lays in the long wavelength edge of the absorption band. An InGaAs detector cooled using liquid nitrogen was installed on the spectrometer to record the emission spectrum. The PL spectrum from a 1.3 µm thick neodymium ion doped As_2S_3 film is recorded in Figure 4.26.

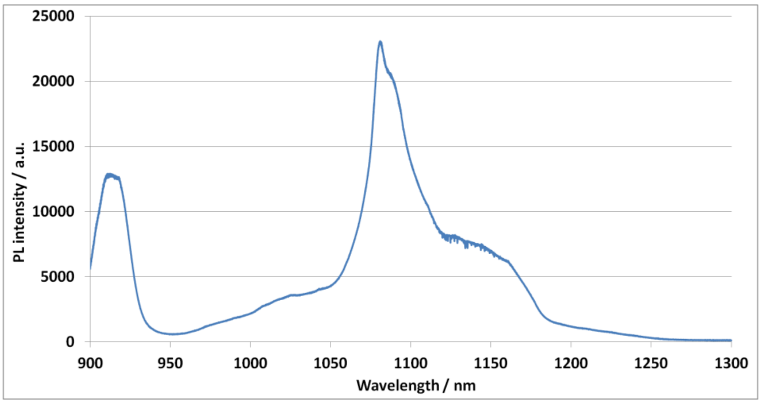

Figure 4.26 Emission spectrum of a 1.3 µm thick Nd^{3+} doped As_2S_3 film pumped at 830 nm.

There are two main features in the emission spectrum of the Nd^{3+}:As_2S_3 film: the major one is located at 1080 nm with broad shoulder arising from the $^4F_{3/2} \rightarrow {}^4I_{11/2}$ transition, and another band centred at 916 nm is associated with energy decay from the $^4F_{3/2}$ to the $^4I_{9/2}$ levels (see Figure 4. 25). The distinct broadening of the fluorescence band of the long wavelength 1080 nm emission is thought to be due to the variation of environments surrounding the rare-earth ions [285, 286], that is non-homogeneous broadening. The same phenomenon is also noticed in silica-based glass. For example, in Ainslie et al.’s report [287], significant emission spectrum broadening was observed in some of the high Nd^{3+} doped (up to 15 wt% of $NdCl_3$) SiO_2-$A1_2O_3$-P_2O_5 glasses. Also, the peak wavelength at 1.08 µm, is roughly 10–20 nm longer than that found for Nd^{3+}-doped silicate, fluoride and phosphate-based glass fibres [284]. A similar wavelength red shift is also noticed in erbium ion doped chalcogenide glass hosts [238], which is discussed in Section 3.3.2(c).

Similar to the approach used to pattern the erbium ion doped As_2S_3 films to make waveguides, two layers of neodymium ion doped and un-doped As_2S_3, respectively, of designed thickness were deposited on thermally oxidized silicon (TOX) wafers, followed by standard lithography and plasma etching with CHF_3. Ridge waveguides with the structure shown in Figure 4.27 were achieved.

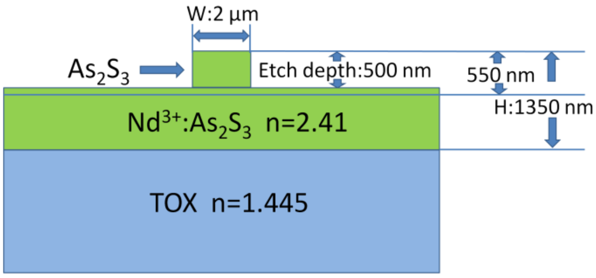

Figure 4.27 Typical structure of a 2 µm Nd^{3+} doped As$_2$S$_3$ waveguide (Tox is thermally oxidized silicon).

Propagation losses and the neodymium ion absorption spectrum of the obtained waveguides were measured using the SC source described in Section 4.5. To avoid bleaching the neodymium ion absorption, a 20 dB optical attenuator was connected in the beam path before the SC light was launched into the waveguides. The transmission spectrum of this SC source was then recorded with, and without, the waveguide present using an optical spectrum analyser (Ando AQ 6317) at the waveguide output side. The transmission spectrum of an 8 mm long, 3 µm wide waveguide is shown in Figure 4.28.

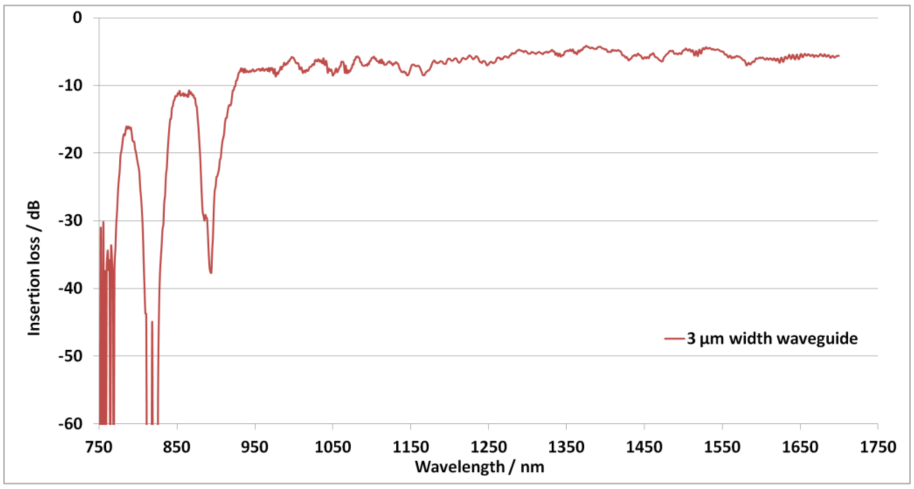

Figure 4.28 Absorption spectrum of an 8 mm long, 3 µm wide Nd^{3+} doped As$_2$S$_3$ waveguide after thermal and light post-treatment.

Two absorption bands are clearly observed in the absorption spectrum of Nd^{3+}:As$_2$S$_3$ waveguide. The strongest one is located at ~820 nm corresponding to the absorption of ions from the $^4I_{9/2}$ to the $^2H_{9/2}$-$^4F_{5/2}$ excited levels. The band centred at 890 nm arises from the transition $^4I_{9/2} \rightarrow {}^4F_{3/2}$ (see Figure 4.25). More absorption bands at shorter wavelengths, associated with exciting the ions to even higher energy levels, are not observed in this spectrum because of the intrinsic bandgap absorption in the host glass. The absorption band at ~820 nm, with a broad shoulder (from 790 nm to 850 nm), enables the PL spectrum to be obtained with excitation of 830 nm as mentioned before (see Section 4.6.2). The ~820 nm absorption band is so strong that only a few photons were collected by the detector making the spectrum noisy, therefore, it is not possible to quantify its absorption strength. From Figure 4.28, the 890 nm absorption band is ~ 32 dB/cm in this 8mm long Nd^{3+}:As_2S_3 waveguide. Comparing this value with the absorption information in ref [105], the estimated Nd^{3+} concentration in this As_2S_3 waveguide is ~ 0.4 at% ($1.2x10^{20}$ ions/cm^3), which is a little higher than the number ~0.3 at% ($0.9x10^{20}$ ions/cm^3) estimated from film deposition rate. With such a high absorption at the pump wavelength, the effective pumped length is short, which brought practical difficulties in making accurate gain measurements.

The propagation loss of this waveguide could also be estimated from the insertion loss curve. The total insertion loss for this 8 mm long waveguides is 4.9 dB at 1300 nm, a wavelength far away from the absorption bands. Subtracting the fibre-to-waveguide coupling loss of 1.55 dB/facet due to mode mismatch calculated by the finite difference method, and a reflection loss of 0.75 dB/facet from the waveguide-to-air interface, the propagation loss of this waveguide is estimated to be about 0.4 dB/cm. Although it is not realistic to calculate waveguide propagation loss accurately with such a short waveguide, due to uncoupled light bleed through, from the result it is still safe to say the propagation loss of this waveguide is reasonably low and suitable for a potential waveguide amplifier/laser. In the range from 1 μm to 1.7 μm, the propagation loss shows almost no dependence on the wavelength. This phenomenon is different from that in the un-doped As_2S_3 waveguides, where $1/\lambda^2$ dependence is typical indicating the effects from roughness of the waveguide sidewalls [280]. It is also different from the trend in the previous erbium ion doped As_2S_3 waveguide, where a strong $1/\lambda^4$ relationship is evident indicating nanoscale scattering off film inhomogeneities (see Section 4.5.1). The flat curve obtained here may indicate a high quality waveguide with smooth sidewalls and of a homogeneous nature at the nanoscale, or may arise due to wavelength independent scattering from an unknown source.

Having no suitable WDMs, gain measurements were not feasible, so a lasing measurement was attempted using an 806 nm diode laser pumping an 8 mm long 2 μm wide waveguide (structure of this waveguide is depicted in Figure 4.27) with an optical set-up as in Figure 4.29. The 806 nm laser with a beam diameter of 2 mm was coupled into a single mode fibre (SMF 28) via a 10x objective lens with NA of 0.2. Then the excitation laser was delivered to the waveguides through a lensed fibre. On the output side, another lensed fibre was positioned to collect all the signals from the waveguide, and an OSA was connected to this lensed fibre to record all the data. The laser cavity was formed by the facet reflections of the waveguide.

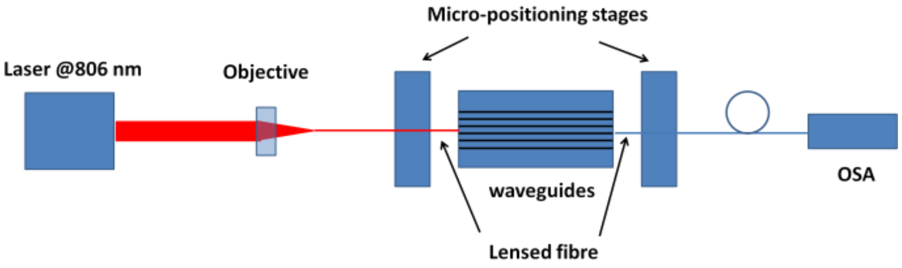

Figure 4.29 Optical set-up for lasing measurement in a ~0.4 at% Nd^{3+} doped As_2S_3 waveguide with 806 nm pump (OSA is optical spectrum analyser).

The obtained ASE spectra under different excitation powers are shown in Figure 4.30. The sharp peak at 808 nm is the residual pumping energy, and the bands at 922 nm and 1080 nm correspond to the emissions of $^4F_{3/2} \rightarrow {}^4I_{9/2}$ and $^4F_{3/2} \rightarrow {}^4I_{11/2}$, respectively.

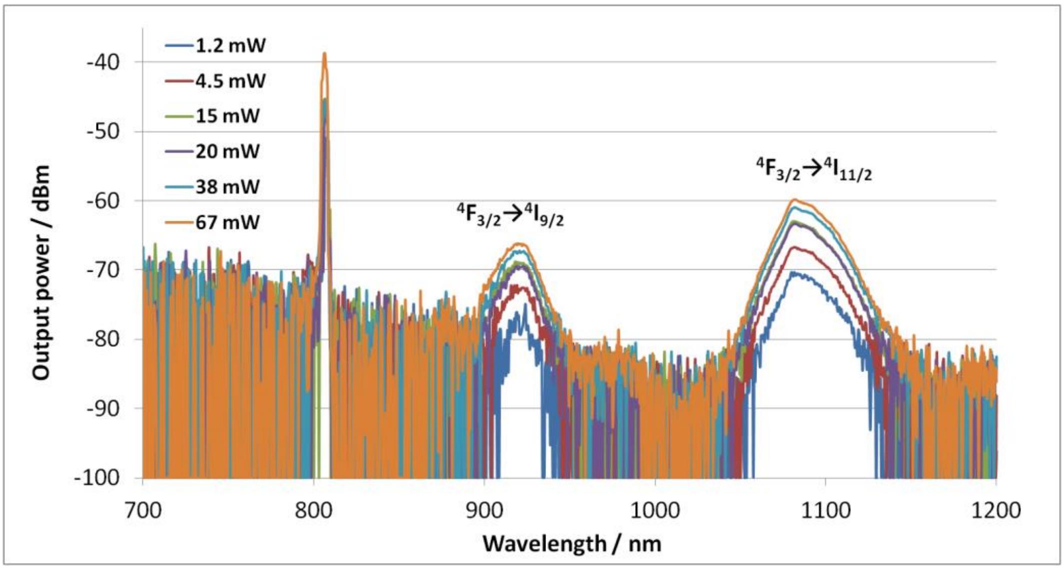

Figure 4.30 Amplified spontaneous emission (ASE) spectra of an 8 mm long, 2 µm wide, ~0.4 at% Nd^{3+} doped As_2S_3 waveguide with 808 nm excitation at increasing power.

Unfortunately, except for the ASE spectrum (see Figure 4.30), no lasing was observed even under the maximum excitation power. The reasons for this less preferable performance may be multi-fold. Firstly, the reflectivity of each end facet of the waveguide is estimated to be 15.7 % (-8.04 dB), which introduces significant intracavity loss for a waveguide laser. However, given the doping level (0.4 at%) of Nd^{3+}, sufficient gain should have been available to overcome this. Secondly, the high pump absorption (which could not be properly quantified) leads to a short effective gain length, but the low output pump power indicating no bleaching in excitation which is a signature of clustering. Lastly, from the spectrum, the absolute ASE level of this waveguide is quite low even compared to erbium ion in an As_2S_3 film (compare ~-50 dBm for Er^{3+}:As_2S_3 (Figure 4.22) with ~-60 dBm for Nd^{3+}:As_2S_3 (Figure 4.30) with 2 nm optical bandwidth), although due to the lack of ground state absorption meaning it should be higher ASE level than that of Er^{3+}:As_2S_3. Considering the low rare-earth ion solubility in As_2S_3, and the broadening of the PL emission shoulder from the film PL spectrum, neodymium ion clustering is possible in this case.

Given the excitation results of Er^{3+} & Nd^{3+} doped As_2S_3 waveguides, it is highly suspected that rare-earth ion clustering occurs during the film deposition. The evaporation of metals (more than 40 elements by 1969) has been studied in detail in the past [288], and it is established that during evaporation from the metal, single atoms are emitted together with polyatomic complexes, which become overgrown with atoms in the region of high vapour density close to the source. In addition, as the plume of evaporant expands and cools, polyatomic complexes could be formed by atomic collisions if conditions are favourable to the removal of the heat of condensation. Although no direct evidence was found to prove the existence of polyatomic rare-earth complexes during film deposition, the non bleachable Er^{3+} absorption in 0.6 at% Er^{3+} doped As_2Se_3 waveguide, and small rare-earth particles formed on the edge of alumina crucible after evaporation, indicating the high possibility of polyatomic evaporation. Based on the research [289], the relative equilibrium vapour pressure of the dimer, P_2, is given by the expression:

$$\frac{P_2}{P} = const\ e^{\frac{\Delta H_0}{RT}\left(\frac{1-\alpha}{\alpha}\right)} \qquad (4.14)$$

where P is the vapour pressure of the monomer, R is the gas constant, T is the absolute temperature, and $\alpha=\Delta H_0/D_0$, where D_0 is the dissociation energy of the dimer, and ΔH_0 is the heat needed to evaporate an atom at 0 K. As for metals, $\alpha>1$, means the proportion of dimers in the saturated vapour increases with temperature. Therefore, working on this premise, it is suggested that a lower evaporation temperature would: a) reduce the percentage of evaporated polyatoms and condensed clusters through a less dense plume, and b) a lower rare-earth ion concentration would reduce the likelihood of any post-treatment induced clustering. However, to achieve a reasonable rare-earth ion concentration with lower evaporation temperature means a large area source is required, certainly much larger than the half inch diameter crucible source used here. Another option is to use a plasma assisted reactive evaporation device that combines an evaporation source and a high density plasma source [290]. These two sources are installed in a coaxial configuration, where the material evaporated from the evaporation source is transported through the plasma source and then condenses on the substrate. With the help of the plasma, the dimers can be dissociated to ensure monatomic rare-earth ion deposition. However, limited by the chamber and facility available, it was not possible to try these options. Consequently, no further progress was made on thermally evaporated films.

4.7 Conclusion

In this chapter, the basic theory of planar optical waveguides was discussed. Methods for waveguide mode simulation were introduced, and the amplification performance of an erbium ion doped As_2S_3 waveguide amplifier was simulated by Optisystem based on rate equations and the waveguide simulation data. Erbium ion doped As_2S_3 waveguides with loss of 0.35 dB/cm at 1.55 µm were fabricated using standard photolithography and plasma dry etching. With the obtained 55 mm length, 2 µm wide, 0.15 at% Er^{3+}:As_2S_3 waveguides, for the first time, internal gain from 1570 to 1630 nm was achieved in an erbium ion doped chalcogenide glass or in a chalcogenide thin film based waveguide amplifier. ASE signals at 900 nm and 1100 nm were observed in neodymium ion doped As_2S_3 waveguide fabricated using thermal evaporation. However, due to the lack of proper wavelength division multiplexing (WDMs) and pump laser, lasing in this waveguide was not achieved. Erbium ion clustering and low rare-earth ion solubility in thermal evaporated As_2S_3 film are thought the main reasons for the limited internal gain achieved in the amplification experiment. Therefore, different film fabrication approach (RF sputtering in Chapter 5) and different host material with better rare-earth ion solubility (Ge-Ga-Se material in Chapter 6) are tried in the following chapters.

Chapter 5

Different approaches to fabricate erbium ion doped As_2S_3 waveguides

Although limited internal gain was achieved from 1570 to 1630 nm in an erbium ion doped As_2S_3 waveguide deposited using thermal evaporation with metallic erbium as the dopant, the maximum erbium ion inversion was estimated at around 30%. Higher erbium ion inversion is required to make practical devices. From excitation experiments and high temperature thermal post-treatment results in Chapter 4, the low erbium ion population inversion level appeared to be due to erbium ion clustering in As_2S_3 films. Therefore, in this chapter, several different approaches are introduced to attempt to eliminate the erbium ion clustering.

5.1 Co-thermal evaporation of ErX_n (X=S/Cl) with As_2S_3

It is known that in rare-earth ion doped chalcogenide materials, films offer certain opportunities over bulk glasses in hosting rare-earth ions. In bulk glass fabrication, the melt-quenching method with long rocking time provides high quality homogeneous glasses. At the same time, long rocking time also offers rare-earth ions time and energy input to migrate. Therefore, the rare-earth ion solubility in a host material caps the limit on the highest concentration of rare-earth ion that can be incorporated in the host glasses without clustering. On the other hand, thin films (by thermal evaporation or other methods) are usually produced in a non-equilibrium condition by rapidly condensing vapor onto a cold substrate which gives insufficient time for the material to revert back to their metastable equilibrium state. Therefore, higher concentrations of rare-earth ion than the actual solubility limit could be incorporated, provided that the film is not then subjected to elevated temperatures or other forms of energy input that can cause bond rearrangement or material diffusion. Therefore, as discussed in Chapter 4, the clustering in the low concentration of erbium ion doped sample (0.15 at%) stemmed from the metal erbium evaporation source. One possible way to prevent the formation of erbium metal clustering is to use erbium compounds instead of erbium metal in film evaporation. By using compounds such as $ErCl_3$ and Er_2S_3, the direct formation of erbium ion clustering should be reduced due to the erbium ion being already bonded with -Cl or –S.

For this experiment, the two candidates that could be used to replace erbium metal are $ErCl_3$ and Er_2S_3. $ErCl_3$ is the obvious first choice as it has a lower evaporation temperature than Er_2S_3 (melting temperature of $ErCl_3$ is 1529 °C compared to 1730 °C for Er_2S_3). In the deposition chamber the evaporation temperature should be somewhat below the standard melting temperature due to the low pressure. It was reasonable to assume that for the same evaporation rate, $ErCl_3$ would need a lower temperature than Er_2S_3 does. This provides more space to operate and less potential heat load in the chamber. The maximum operating temperature for the available alumina crucibles used in the evaporation was 1500 °C. Thus, $ErCl_3$ was the first to be deposited to test the hardware capability.

5.1.1 Co-thermal evaporation of $ErCl_3$ with As_2S_3

$ErCl_3$ has been used as a source of Er^{3+} in various host materials. For example, Shojiya et al. [291] studied the upconversion luminescence from Er^{3+} in chloride glasses using $ErCl_3$ as an active Er^{3+} source. Photoluminesence properties of Er^{3+} in oxyfluoride glass ceramics were investigated by Zeng et al. [292], and $ErCl_3$ was one of the erbium compounds used in this report. Soundararajan et al. [293] reported the optical properties of erbium ion doped fluorochlorozirconate glasses, where active Er^{3+} were added as $ErCl_3$.

There are only a few papers on $ErCl_3$ utilization in chalcogenide glass hosts. In Allen et al.'s work on the photoluminescence measurement of erbium ion doped GaGeS and GeGaSe glasses [119], $ErCl_3$ was employed instead of Er_2S_3 for its lower melting temperature, thereby simplifying the glass preparation. However, the Er^{3+} introduced as $ErCl_3$ had less promising performance: no discernible lifetime was observed in the $ErCl_3$-doped samples, and the PL spectrum showed limited optical activity of Er^{3+} ion. In reality, researchers are reluctant to use $ErCl_3$ in chalcogenide glasses as the Cl^- in the host might act as a quenching centre and it is considered to cause instability in the glass structure [119, 294]. Despite Allen's results, it is decided to try using $ErCl_3$ in this instance as the experiments are with As_2S_3 not Ga-Ge-S/Se.

High purity (*5N* elements) As_2S_3 and $ErCl_3$ components were loaded into a resistively heated tantalum boat and resistively heated alumina crucible, respectively.

Evaporation was performed at a pressure ~1x10^{-5} Pa. After reaching the pressure set point, the $ErCl_3$ temperature was increased slowly; at the same time the rate sensor for $ErCl_3$ was carefully monitored to record the $ErCl_3$ evaporation temperature. According to the rate sensor (a quartz microbalance thickness monitor), $ErCl_3$ started to evaporate at about 620 °C. During deposition, the $ErCl_3$ temperature was fixed at 650 °C to get a stable evaporation rate of 0.001 nm/s, whilst keeping the As_2S_3 rate at 0.1 nm/s to ensure the final Er^{3+} concentration was around 0.2 at% (~0.6x10^{20} ions/cm^3). After all the desired evaporation rates were achieved, the shutter covering the wafers was opened and evaporation started. When the film thickness read from the film thickness monitor reached the final thickness set point, the system closed the shutters for both sources and films automatically, ramped down the power for both sources gradually and allowed them to cool to <100°C before venting the chamber.

To protect the As_2S_3 from surface crystallisation, a 100 nm thick SU-8 layer was coated on the surface and cured as soon as the as-deposited films were removed from the chamber. Another set of films with a higher Er^{3+} concentration of ~0.4 at% (~1.2x10^{20} ions/cm^3) were deposited in the same way by doubling the $ErCl_3$ evaporation rate from 0.001 nm/s to 0.002 nm/s.

Optical properties of the films were measured using the FilmTek 4000, and the lifetimes of the erbium ion doped As_2S_3 films were measured in the all-fibre confocal setup described previously (in Section 3.3.2) under 1490 nm excitation. The results for the as deposited film are listed in Table 5.1.

Table 5.1 Physical properties of as-deposited Er^{3+}:As_2S_3 films with $ErCl_3$ as dopant.

Er^{3+} concentration in As_2S_3 film	Thickness / nm	Bandgap / eV	RI @ 1550 nm
Low doped (0.2 at%)	931	2.29	2.32
High doped (0.4 at%)	718	2.30	2.32

The film refractive index of 2.32 at 1550 nm and the bandgap around 2.3 eV are identical to the values previously obtained from as-deposited As_2S_3 films (see Section 3.2.3), indicating that low concentration of $ErCl_3$ has no clear effects in As_2S_3 film formation.

1/e, intrinsic lifetime and PL intensity of the Er^{3+}:As_2S_3 films under 20 kW/cm^2 excitation were measured, and are shown in Table 5.2. From the results, 0.2 at% $ErCl_3$

doped As_2S_3 film has the best lifetimes, which are 2.5 ms (1/e) and 2.6 ms (intrinsic lifetime), respectively. The lifetime drops with doubling of the Er^{3+} concentration, but is still 1.4 ms, longer than the previous best data of the erbium metal doped 0.15 at% As_2S_3 film. The much longer lifetimes obtained in $ErCl_3$ doped films implies less erbium ion clustering is formed in this $ErCl_3$ doped As_2S_3 film than in erbium metal doped As_2S_3 films using co-thermal evaporation. Using compounds like $ErCl_3$ might be a possible way to eliminate the clustering.

Table 5.2 Lifetimes of as-deposited Er^{3+}:As_2S_3 films with $ErCl_3$ as dopant.

Er^{3+} concentration in As_2S_3 film	1/e lifetime / ms	Intrinsic lifetime / ms	PL intensity / mV
Low doped (0.2 at%)	2.5	2.6	~10
High doped (0.4 at%)	1.4	1.6	~2
Er^{3+} (metal):As_2S_3 (0.15 at% reference)	1.2	1.4	~50

The PL intensity from these $ErCl_3$ doped As_2S_3 films was relatively weak. The PL intensity of the 0.2 at% $ErCl_3$ doped sample was 1/5 and the 0.4 at% film was only 1/25 of that of the 0.15 at% erbium metal doped As_2S_3 film. In further investigation, a high density of particulates with an average size of 10 μm diameter was found to cover the whole film. An image of the particulates in $ErCl_3$ doped As_2S_3 films taken in dark field mode is shown in Figure 5.1. These particulates may act as defects and source of absorption, and quench the PL emission immediately. It is also possible that these particulates are $ErCl_3$ condensate, meaning a proportion of the material never got into the film leading to a low concentration of active Er^{3+} and thus a weak PL intensity. More particulates were found on the 0.4 at% doped film than the 0.2 at% film, suggesting that these particles are $ErCl_3$ concentration related. To verify this assumption, an As_2S_3 film without $ErCl_3$ doping was deposited under the identical conditions to the $ErCl_3$ doped As_2S_3 films and was inspected again. The new As_2S_3 film was almost particle-free under microscope. This indicated clearly that $ErCl_3$ is the cause of the particles. The mechanism of particle formation and the role of the $ErCl_3$ in this are still unknown, but the high density of particles make the films unusable for waveguide amplifiers, and so no further investigations were performed.

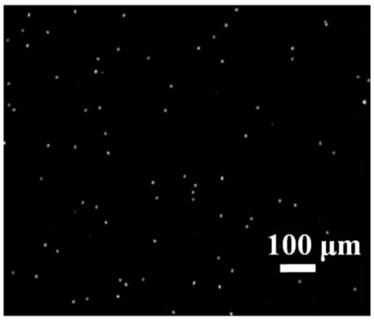

Figure 5.1 Particulates in co-thermal evaporated $ErCl_3$ doped As_2S_3 films taken with an optical microscope in dark field mode.

5.1.2 Co-thermal evaporation of Er_2S_3 with As_2S_3

Given the particulate issues described above, the alternative compound Er_2S_3 was investigated. Unlike $ErCl_3$, Er_2S_3 was widely used in chalcogenide glasses for Er^{3+} doping as it can easily be incorporated in the chalcogenide glass host matrix, especially so in sulfur containing materials. For example, in Kasap et al.'s report [121], optical and PL properties of powdered Er^{3+}-doped GeGaS glasses of various mean sizes of near-stoichiometric composition ($Ge_{28}Ga_{6.2}S_{65.3}$:$Er_{0.5}$ with $2.1x10^{20}$ ions/cm^3 Er^{3+} ions), were examined carefully, where Er_2S_3 was employed as the dopant source. The radiative lifetime for the $^4I_{13/2}$ energy level was calculated 2.6 ms using Judd–Ofelt theory, and the estimated maximum emission cross-section at 1.53 μm was $15.5x10^{-21}$ cm^2. Tonchev et al. [295] reported both the thermal stability and optical properties of $(GeS_2)_{75}(Ga_2S_3)_{25}$ glasses doped with large amounts of Er_2S_3 (1.8 to 2.4 mol% of Er_2S_3). Samples were synthesized with the melt-quenching method, and the measured ~ 1540 nm PL decay times were in the 1.13-1.55 ms range decreasing with increasing erbium ion content. In Allen et al.'s work [119], besides $ErCl_3$, in another set of GeGaS and GeGaSs samples, Er_2S_3 was chosen as the dopant. Er_2S_3 doping concentration varied in the range of 0.3-3 at%. PL spectra and decay lifetime of 1.54 μm emission were measured under 980 nm excitation. The Er_2S_3-doped samples exhibited the $^4I_{13/2}$ energy level lifetimes in the 1-4 ms range. The PL efficiency measurements showed quenching occurred at Er^{3+} concentration greater than 1 at%. Er_2S_3 was also used in erbium ion doped film deposition. Lyubin et al. reported the co-thermal evaporation with Er_2S_3 to fabricate Er^{3+}-doped As_2S_3 and As_2Se_3 films [128]. The chalcogenide glasses were evaporated from a quartz crucible, while a tungsten boat was used to evaporate the Er_2S_3 powder on account of its high evaporation temperature. PL spectra at 1.54 μm of

Er^{3+} doped As_2S_3 and As_2Se_3 films were recorded under Ar^+-laser excitation, and a linear PL intensity dependence on the exciting laser beam intensity was also observed.

In this research, the Er_2S_3 doped As_2S_3 film deposition procedure was similar to the previous $ErCl_3$ doped As_2S_3 film deposition procedure, which was described in Section 5.1.1, except replacing the $ErCl_3$ from the resistively heated alumina crucible with high purity Er_2S_3 (5*N*) powder. A test run of evaporating Er_2S_3 was commenced before the Er_2S_3 doped As_2S_3 film deposition, to establish the Er_2S_3 evaporation rate-temperature relationship. In the test run, even heating the alumina crucible up to its maximum temperature of 1500 °C, there was still no sign of Er_2S_3 evaporation, indicating Er_2S_3 had a much lower vapour pressure than $ErCl_3$. After cooling down the system and venting the chamber, the alumina crucible loaded with Er_2S_3 was found to have been damaged, as shown in Figure 5.2 (a). It is known that Al_2O_3 and phosphate are added in silicate glasses to improve the dispersion of rare-earth ion in glass matrix. In this experiment, the alumina crucible may react with Er_2S_3 which caused the damage of alumina crucible [296-298].

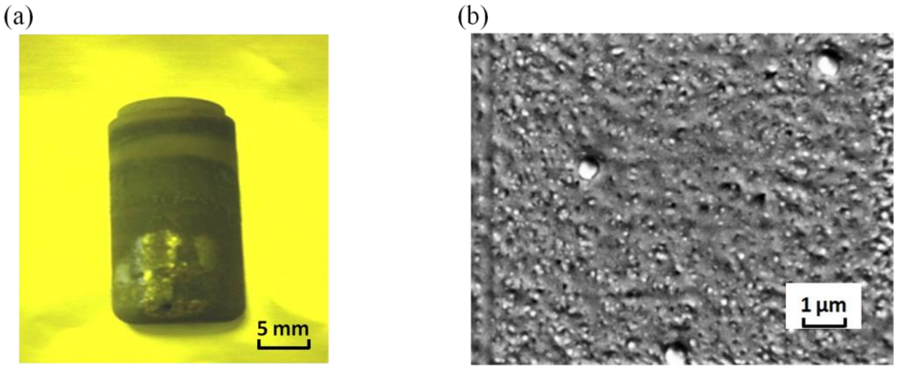

Figure 5.2 Damaged Al crucible in Er_2S_3 evaporation (a); scanning electron image of an as-deposited Er_2S_3 doped As_2S_3 film with tantalum boat (b).

Obviously, an evaporation boat for Er_2S_3 powder that can stand even higher temperature (more than 1500 °C) was needed. Therefore, a tantalum boat was used in the following deposition, and As_2S_3 was relocated to an alumina crucible. With this new arrangement, evaporation of Er_2S_3 was observed from rate sensor when 80% of full power (300 W) was applied to the tantalum boat.

However, in the following lifetime measurement, no 1.55 μm emission signal was obtained from this film. The film surface was clearly rough under optical microscope inspection. A scanning electron microscope (SEM) image of the film surface is shown in Figure 5.2 (b) with magnification of 2×10^4 confirming the poor surface quality. It is speculated that the high temperature of the Er_2S_3 source (>1500 °C) radiatively heated the wafer located 40 cm above the source. Prior unpublished experiments within the Laser Physics Centre have established that at much above 70 °C wafer temperature, the film quality of As_2S_3 films degrades rapidly. Three viable ways are proposed to resolve this problem. Firstly, a cooling system could be employed to prevent the substrate wafer temperature increase caused by heating of Er_2S_3 source. However, given that the wafers are on a planetary style rotation carousel, this is a nontrivial implementation. Secondly, the distance between the Er_2S_3 source and substrate wafer could be increased. In the current chamber there is insufficient room to get more than approximately another 10 cm of throw distance, likely insufficient to resolve the issue given the ~10x3 cm size of the source. Lastly, a water-cooled shield could be placed over the source leaving only the emitting aperture exposed to reduce the heat load. Due to the complexity of the deposition system, (6 thermal sources plus three sputter guns) there are no spare feedthroughs available to be able to try this option. Consequently, no further progress was made on thermally evaporated Er_2S_3 doped As_2S_3 film fabrication, and its viability, as a method to fabricate high performance waveguide amplifier is still an open question.

5.2 Radio-frequency (RF) sputtering of erbium ion doped As_2S_3 films

5.2.1 Introduction to RF sputtering chalcogenide glass films

RF sputtering of chalcogenide glasses using argon has been reported as a promising method to deposit device-quality films [217, 279, 299, 300]. Typically, sputter deposition is performed at pressures of 0.1-1 Pa, and involves creating a plasma (usually in an inert gas like argon) by applying an RF voltage between a cathode, (which is the target holder), and anode (which refers to the gun shield and the rest of the vacuum chamber). With the bombardment by high energy ions, the target surface ejects atoms or atom clusters that diffuse away and finally condense on the substrate wafer to form films. The stoichiometry of the deposited films can be controlled through adjusting the sputtering parameters, typically the chamber pressure, sputtering power and gas flow.

There are reports on rare-earth ion doped chalcogenide glass films fabricated by RF sputtering. In Nazabal et al.'s report [300], Tm^{3+} doped $Ga_5Ge_{20}Sb_{10}S_{65}$ (at% 2S2G) films were fabricated using RF sputtering. The sputtering was performed in an Ar pressure of $3.7x10^{-2}$ to $3.7x10^{-3}$ Torr (~0.49-4.9 Pa), and the RF power varied between 20 and 50 W applied on a 2-3 mm thick 80 mm diameter target. The composition of the films was found to be comparable to the bulk glass target with only a slight increase of gallium. Lifetime of the $^3H_4$ energy level of Tm^{3+} was measured under 800 nm excitation and was found to be about 50 μs in a 0.1 at% doped sample, which was shorter than the value of 120 μs from 2S2G powders with 0.05 at% Tm^{3+} doped concentration. It was suspected that the presence of impurities or defects in the films induced this discrepancy. Thin films of Er^{3+} doped As_2S_3 and $Ge_{33}As_{12}Se_{55}$ (at%) have also been fabricated using RF sputtering in Fuchs et al's work [217]. Sputtering targets were fabricated from Er^{3+} doped bulk samples (25 mm in diameter) and from commercial un-doped targets (50 mm in diameter) with erbium metal pieces placed on the target surface. The sputtering was performed at pressure of $3x10^{-2}$ Torr (~4 Pa), and the applied RF power was 20 W. A PL lifetime of 4 ms of the $^4I_{13/2}$ energy level was measured on the obtained Er-doped As_2S_3 films under 977 nm excitation. However, in the $Ge_{33}As_{12}Se_{55}$ (at%) waveguides fabricated using wet etching, insertion losses at 1.3 μm (well out of the Er^{3+} absorption band) were larger than 30 dB, which was thought due to the large porosity induced by column-like structure in the film which produced strong light scattering.

5.2.2 Erbium ion doped As_2S_3 film deposited using RF sputtering

At the Laser Physics Centre of the Australian National University, the facility used for co-thermal evaporation can also function as a sputtering chamber, containing three RF sputtering guns. A 3-inch commercial As_2S_3 powder sintered target was used in the first experiment, and a piece of erbium foil stuck onto the As_2S_3 target surface acted as an erbium ion source. The chamber configuration can be found in Figure 3.5, and the As_2S_3 target with erbium foil attached on its surface is shown in Figure 5.3. Argon was used for the creation of the sputtering plasma. During the deposition process, the substrate was mounted on a 150-mm diameter rotatable holder. The glass target was loaded into the 3-inch magnetron which was mounted 45° off vertical and facing upwards with a distance of 100 mm between the target and substrate. Parameters such as Ar flow, RF sputtering power and sputtering rate were optimised for film quality. The final parameters used in the deposition are listed in Table 5.3.

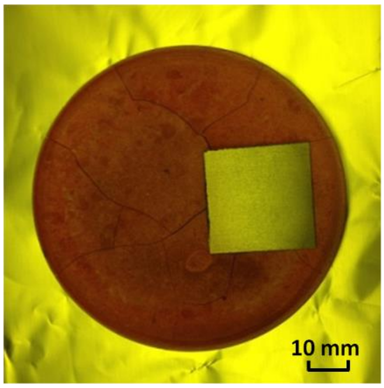

Figure 5.3 A 3-inch As_2S_3 RF sputtering target with a piece of erbium metal on the surface acted as erbium ion source.

Table 5.3 Parameters used in erbium ion doped As_2S_3 film deposition using RF sputtering.

Base chamber pressure	$1.5\mathrm{x}10^{-7}$ Torr (~$2\mathrm{x}10^{-5}$ Pa)
RF power	43 W
Ar flow	20 sccm
Sputtering pressure	2 mTorr (~0.26 Pa)
Sputtering rate	~0.1 nm/s
Wafer rotation speed	20 r/min

5.2.3 Characterisation of RF sputtered erbium ion doped As_2S_3

The as-deposited RF sputtered Er^{3+}:As_2S_3 films, coated with 100 nm SU-8 protective layer, were characterised using the FilmTek. Film thickness, refractive index and bandgap of the obtained films were measured at the film centre, as well as the film edge, to check the uniformity of the whole film. This measurement was repeated on the same film after 24 hours of 130 °C vacuum thermal post-treatment. The measurement results of the as-deposited film, and the film after thermal treatment, are shown in Table 5.4.

Table 5.4 Physical properties of Er^{3+}:As_2S_3 film deposited using RF sputtering.

Measured spot position on film / mm	Thickness / nm	Bandgap / eV	RI @ 1550 nm
As-deposited, centre (0,0)	848	2.20	2.409
As-deposited, edge (35,0)	878	2.20	2.403
After thermal post-treatment, centre (0,0)	843	2.26	2.387

Compared with thermally evaporated films (see Section 3.2.3), RF sputtered films have a lower bandgap (2.20 eV vs. 2.32 eV), but a higher refractive index close to the bulk value (2.41 at 1550 nm vs. of 2.35). The RF sputtered film thickness increases from 848 nm (at film centre) to 878 nm (35 mm off centre), indicating that sputtering led to less uniformity in films. This phenomenon could be explained partly by the relatively short distance and the big angle between the target and the wafer, where the edge of the wafer is closer to the source and so collects more condensate. The thermal treatment applied has the opposite effect on RF sputtered films compared with what it does on co-thermally evaporated films. In the RF sputtered films, after 24 hours thermal post-treatment at 130 °C, the film bandgap increases up to 2.26 eV from 2.20 eV, while the refractive index drops to 2.387 from 2.409 in as-deposited film, coupled with a reduction in the thickness (the 6 nm reduction in thickness is certainly well within the accuracy/resolution of the instrument and so is considered real). The differences between RF sputtered and thermally evaporated films are thought to be micro-structure related, thus careful attention should be paid to this when using such films in a real device.

The lifetime and PL intensity were measured in as-deposited and thermal post-treated (at 130 °C for 24 hours in vacuum) RF sputtered Er^{3+}:As_2S_3 films, and the results are shown in Table 5.5. A 1.3 ms 1/e lifetime of the $^4I_{13/2}$ state of Er^{3+} was achieved from the as-deposited film, which is longer than the 1.16 ms in the previous 0.15 at% co-thermally evaporated Er^{3+}:As_2S_3 film in Section 3.6. After thermal post-treatment, the 1/e lifetime of RF sputtered Er^{3+}:As_2S_3 films increased to 1.9 ms, and the PL intensity was enhanced roughly 4.5 times. Clearly, thermal treatment enables some of the erbium ions to re-bond in a more ideal way reducing nonradiative transitions or causes defect/impurity state densities to be significantly reduced.

Table 5.5 Lifetime & PL intensity of the $^4I_{13/2}$ state of Er^{3+} in Er^{3+}:As_2S_3 film deposited using RF sputtering.

Er^{3+}:As_2S_3 films of different types	1/e lifetime / ms	Intrinsic lifetime / ms	PL intensity / mV
As-deposited	1.3	1.6	40
After annealing	1.9	2.1	180
Ref: Thermal deposition (0.15 at%) (see Section 3.6)	1.16	1.35	~300

As mentioned in Section 5.2.2, to dope erbium ion into the As_2S_3 films, a piece of erbium foil was stuck on the As_2S_3 target surface. Due to the different sputtering rates of the erbium foil and the As_2S_3 target, it was not possible to estimate the erbium ion concentration in the final Er^{3+}:As_2S_3 films based on the proportion of areas each material exposed to plasma. The available energy dispersive X-ray spectroscopy (EDX) also could not resolve clearly the erbium ion concentration at the 0.5 at% level and so was not of assistance.

Another potential method to estimate the Er^{3+} concentration in Er^{3+}:As_2S_3 film, is to compare its Er^{3+} absorption band intensity with a film of known Er^{3+} concentration in the same host. In the absence of clustering, the Er^{3+} absorption is proportional to its concentration [198, 301]. Prism coupling offers a widely used way to measure the absorption intensity of a film. However, good film quality is critical to getting an accurate absorption or propagation loss in prism coupling methods described in Section 3.3.2(c). Inspection under a microscope showed micro-sized particles with diameter ranging from 1 μm up to 4 μm covering the whole wafer at a much higher density than usual thermally evaporated As_2S_3 films. A micrograph of the particles on the RF sputtered Er^{3+}:As_2S_3 film taken in dark field mode with an optical microscope is shown in Figure 5.4. Given these particles would cause light scattering and an indeterminate propagation loss contribution, this measurement was not pursued.

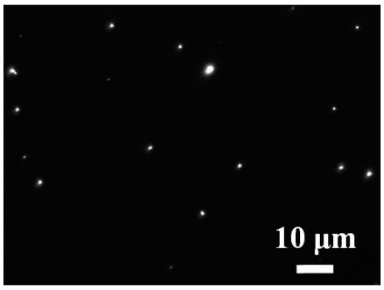

Figure 5.4 Particulates on RF sputtered Er^{3+}:As_2S_3 film, which was taken with microscopy in dark field mode. The micro-sized particulates have diameters ranging from 1 μm up to 4 μm.

It was thought, based on prior experience with other materials, that the particulate problem originated from the sintered powder nature of the As_2S_3 target and the visible cracks and graininess covering the whole target surface after use (see Figure 5. 3). Therefore, another 3-inch one-side polished As_2S_3 glass disc was purchased as a new target. Er^{3+}:As_2S_3 films with better quality (checked using microscope in dark field mode) were deposited under same conditions as previously described in Section 5.2.2 with this new As_2S_3 glass target. The lifetime and PL intensity of the as-deposited and thermally treated Er^{3+}:As_2S_3 films were measured, and the results are shown in Table 5.6.

Table 5.6 Lifetime and PL intensity of Er^{3+}:As_2S_3 film deposited using RF sputtering with the new As_2S_3 glass target.

Er^{3+}:As_2S_3 films of different types	1/e lifetime / ms	Intrinsic lifetime / ms	PL intensity / mV
As-deposited	1.18	1.45	~120
After annealing (130 °C for 24 hours in vacuum)	1.82	1.97	~440
Ref: Thermal deposition (0.15 at%) (see Section 3.6)	1.16	1.35	~300

The lifetime of the as deposited film using As_2S_3 glass target is at the same level as the previous films sputtered with the sintered As_2S_3 target, but the PL intensity increases significantly: from 40 mV to 120 mV for the as-deposited film, and 180 mV to 440 mV after thermal post-treatment, which is even stronger than the best co-thermal evaporated Er^{3+}:As_2S_3 film with 0.15 at% erbium ion described in Section 3.6. The erbium ion concentration in this waveguide is uncertain, but as will be discussed below it is subsequently estimated at 0.1 at%.

5.2.4 Pump-induced PL intensity decay in RF sputtered erbium ion doped As_2S_3 films

It was noticed that the PL intensity of RF sputtered Er^{3+}:As_2S_3 films dropped significantly during PL testing, and fell to almost zero after 48 hours of green light treatment (light wavelength of 550 nm with intensity of ~10 mW/cm^2 from a typical LED flood light in ambient air), the normal light treatment for photoinduced annealing of our As_2S_3 films. Interestingly, the reduced PL intensity of this RF sputtered Er^{3+}:As_2S_3 film could be restored to its original value if this sample was then thermally treated (130 °C in vacuum for 24 hours). It was also noticed that this process was repeatable, and the PL intensity cycled with different post-treatment types as shown in Figure 5.5. The T in x-axis refers to 24 hours thermal post-treatment under vacuum, and the L refers to 48 hours green light post-treatment (light wavelength of 550 nm with intensity of ~10 mW/cm^2) in ambient air.

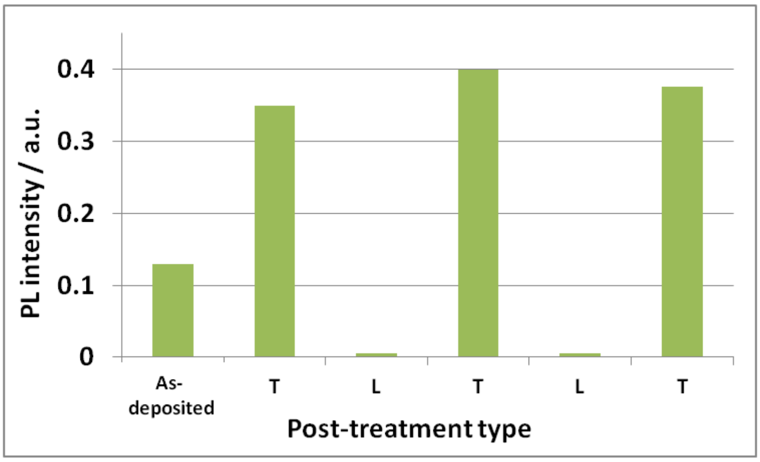

Figure 5.5 PL intensity cycled with light and thermal post-treatments of RF sputtered Er^{3+}:As_2S_3 film. T refers to 24 hours thermal post-treatment under vacuum and the L refers to 48 hours green light post-treatment (light wavelength of 550 nm with intensity of ~10 mW/cm^2) in ambient air.

To characterise the PL intensity change of RF sputtered Er^{3+}:As_2S_3 films with time in thermal and light post-treatment, the PL intensities of two Er^{3+}:As_2S_3 film samples (#1 & #2) were measured over time during sequential light & then thermal treatment processes, and the results are shown in Figure 5.6. During light treatment, the PL intensity of the Er^{3+}:As_2S_3 film dropped significantly in the first few hours and then slowed down to reach almost zero in about 60 hours. In subsequent thermal treatment, the PL intensity of the light treated Er^{3+}:As_2S_3 film increased quickly and reached its maximum value in ~20 hours.

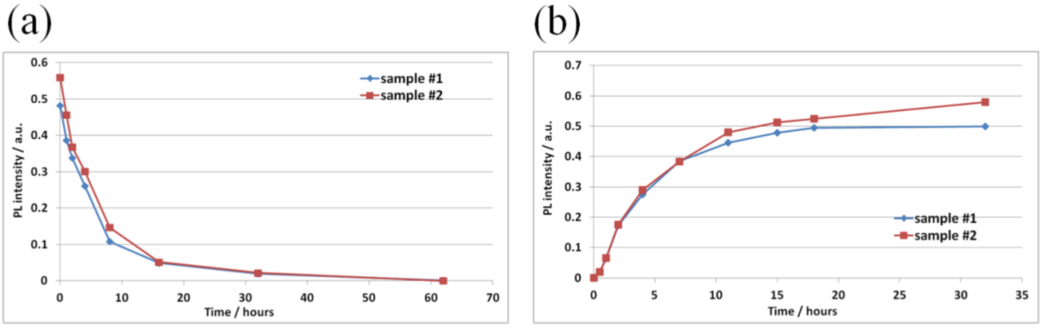

Figure 5.6 PL intensity of a RF sputtered Er^{3+}:As_2S_3 film drops in time during light post-treatment (a), and the PL intensity of the light post-treated Er^{3+}:As_2S_3 film increases in time during thermal post-treatment (b).

It was suspected that the green light and moisture in the atmosphere were responsible for the PL intensity change in Er^{3+}:As_2S_3 films. To figure out exactly what factors caused this phenomenon, 5 pieces of RF sputtered Er^{3+}:As_2S_3 film cleaved from the same wafer were put in 5 different conditions, and the PL intensity was monitored with time. The five different conditions were as follows:

1) Sample immersed in deionised water (DI water);

2) Sample immersed in DI water and irradiated with green light;

3) Set sample in ambient air and irradiated with green light;

4) Sample irradiated with green light in an N_2 atmosphere;

5) Set sample in a high vacuum chamber (~1x10^{-7} Torr, equals to ~1.33x10^{-5} Pa) and irradiated with green light through a glass window.

The green light in this experiment was the same light used in previous light post-treatment (centre wavelength at 550 nm with intensity of ~10 mW/cm^2).

From the results shown in Figure 5.7, Er^{3+}:As_2S_3 films in condition No.1 (DI water only) and No.5 (under green light irradiation in high vacuum) keep the PL intensity without obvious decay for a long time. PL intensities of Er^{3+}:As_2S_3 films in other conditions dropped significantly and the decay in sample No.2 (immersed in DI water with green light irradiation) is the most significant one. Therefore, it is clear that water (or moisture in air) and green light (550 nm) are essential for the PL intensity decay described in the beginning of this section. One may argue that the sample No.4 (N_2 flow with green light irradiation) is not supposed to decay that fast, because the moisture in air should be expelled by N_2 flow. However, in the test setup, chamber used to keep the sample and inject the N_2 flow in was not sealed perfectly, thus it is believed there was still moisture in that chamber which was sufficient to cause this PL intensity decay.

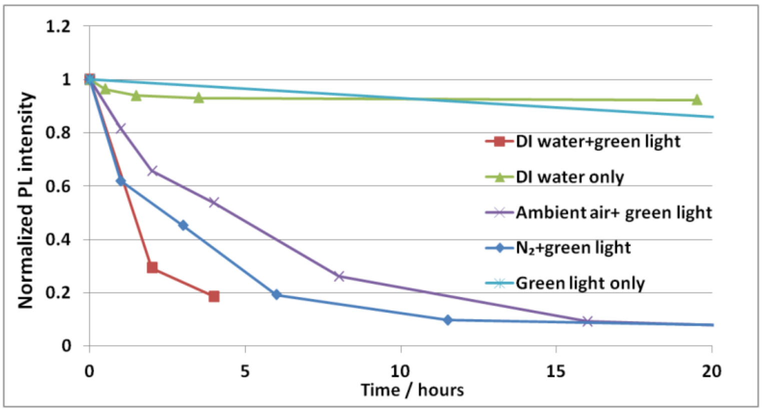

Figure 5.7 PL intensity of RF sputtered Er^{3+}:As_2S_3 films change in time under various storage conditions. DI water is deionised water.

To further enhance the evidence of water diffusion in waveguide, a undoped RF sputtered As_2S_3 film (no erbium ion contained in this film) was patterned into waveguides, and the propagation loss spectrum of a 2 μm wide waveguide was recorded after each thermal (noted as T in Figure 5.8) and green light post-treatment (noted as L in Figure 5.8), repeatedly, and is shown in Figure 5.8. An evident absorption band at 1430-1480 nm shows up after each light post-treatment and disappears after each thermal post-treatment. An absorption band at this wavelength is considered to be associated with the overtones of the O-H stretch vibration near 3600 cm^{-1} [302], which supports the assumption that moisture in air is one of the main factors contributing to this phenomenon.

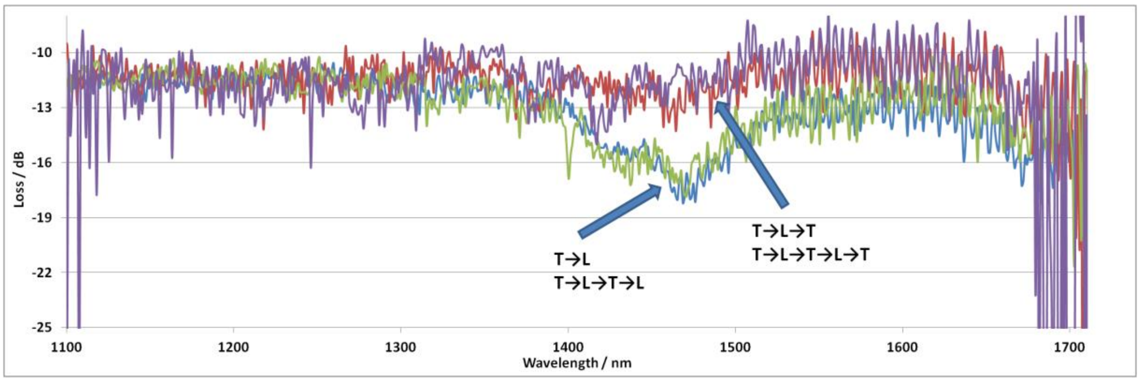

Figure 5.8 Loss spectra of a RF sputtered As_2S_3 waveguide after thermal/light post-treatment. These spectra were recorded with OSA and using SC source as probe source. In this figure, T refers to the thermal post-treatment and L refers to the light post-treatment, and the 'T→L' refers to a thermal post-treatment followed by another light post-treatment.

In order to get the erbium ion absorption spectrum in RF sputtered Er^{3+}:As_2S_3 film, a RF sputtered Er^{3+}:As_2S_3 film was patterned into waveguides, and the recorded spectrum of a 3 μm wide waveguide (the same structure as depicted in Figure 4.7 except the width changed from 2 μm to 3 μm) without post-treatment is shown in Figure 5.9. Absorption bands related to O-H stretch vibration and erbium ion are clear and overlap to each other at shoulder. From Figure 5.8, the O-H stretch vibration absorption band ends by 1520 nm, therefore it is still possible to get the erbium ion absorption value at wavelengths longer than that. The peak erbium ion absorption at 1540 nm was 6 dB for a 48 mm long waveguide, which results in absorption of 1.2 dB/cm. Compared with the previous number of 1.9 dB/cm from the 0.15 at% Er^{3+}:As_2S_3 waveguide deposited using co-thermal evaporation (see Section 4.5.1), the erbium ion concentration in this film is estimated about 0.1 at%.

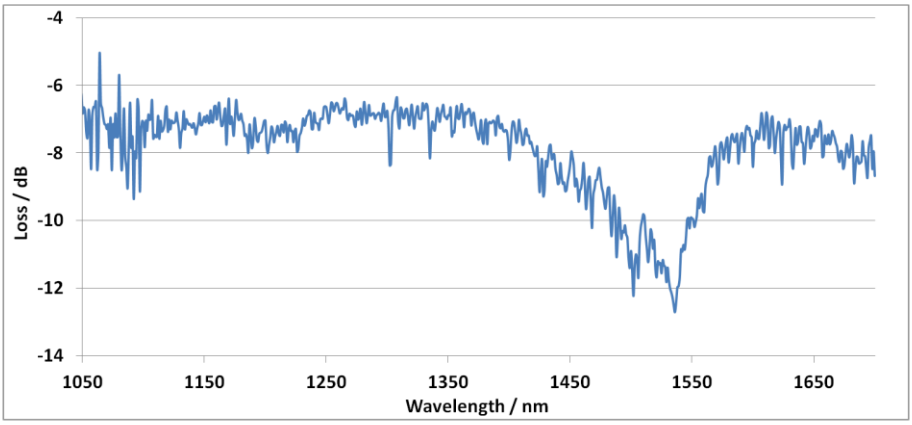

Figure 5.9 Spectrum of erbium ion absorption overlaps with O-H stretch vibration absorption of a 48 mm RF sputtered Er^{3+}:As_2S_3 waveguide.

There has been observation of degradation of PL intensity in Er^{3+} doped chalcogenide film deposited using RF sputtering. In Fuchs et al.'s reports [217], Er^{3+} doped As_2S_3 and $Ge_{33}As_{12}Se_{55}$ (at%) chalcogenide films were fabricated using RF sputtering. Column-like structure was found in Er^{3+}:$Ge_{33}As_{12}Se_{55}$ waveguide. No PL signal was observed from it, which was believed to due to the huge loss of the waveguide. It was also noticed that the PL intensity in the as-deposited Er^{3+}:As_2S_3 film was weak, but after thermal post-treatment, the PL intensity increased up to 40 times. Large PL intensity increase after thermal post-treatment is similar to observations in this research. Fuchs explained the absence of PL in Er^{3+}:$Ge_{33}As_{12}Se_{55}$ waveguides was due to light diffusion from columnar structure in the films. However, in the current experiment, columnar structure based light scattering cannot explain the PL intensity change in the RF sputtered Er^{3+}:As_2S_3 film after thermal and light treatment; also it cannot explain the appearance of the O-H stretch vibration absorption band in the RF sputtered As_2S_3 waveguide after green light treatment. Furthermore, it is clear that any columnar growth in the film must be densely packed as the waveguide losses are low, where the propagation loss is estimated ~0.4 dB/cm in this waveguide.

To explain the current measurement results, a modification was made on Fuchs's explanation. In green light post-treatment, due to the existence of nano columnar structure in RF sputtered Er^{3+}:As_2S_3 film, moisture from the air could easily diffuse into the film along the column boundaries or other types of nano pores resulting from the film growth. As the energy of the 550 nm green light (2.25 eV) is above the bandgap of Er^{3+}:As_2S_3 film (~2.2 eV), it has the capability to induce bond rearrangement and therefore potentially to form O-H bonds with film constituents. It is well know that O-H quenches erbium ion emission effectively [152], thus the PL intensity in Er^{3+}:As_2S_3 film drops, also the appearance of O-H absorption band after light post-treatment could be explained by this hypothesis. In thermal post-treatment, bonds between O-H and Er^{3+}:As_2S_3 are broken down with the help of thermal energy, and moisture is expelled from the film under vacuum, and thus the PL intensity recovers back to its high level and the O-H absorption band disappears in the RF sputtered Er^{3+}:As_2S_3 waveguide.

An obvious question raised from here is whether the decay of PL intensity observed under green light in air affects Er^{3+}:As_2S_3 waveguide amplifier performance. Excitation experiments on RF sputtered Er^{3+}:As_2S_3 waveguides were carried on in ambient air. Although no green light was irradiated directly on the waveguide in excitation experiments, green light due to up-conversion was observed in the Er^{3+}:As_2S_3 waveguide.

From the measured wideband PL spectrum from the erbium ion doped As_2S_3 co-thermal waveguides (see Figure 4.19), there are three up-conversion related bands that could act as ‘green light source’ here. The first one is centred at 530 nm ($^2H_{11/2}\rightarrow{}^4I_{15/2}$), the power level of this emission band is at $4x10^{-14}$ W with ~20 nm bandwidth based on the OSA recorded spectrum, and this data was taken with a 1 nm resolution bandwidth; the second one is at 550 nm ($^4S_{3/2}\rightarrow{}^4I_{15/2}$) with $6x10^{-14}$ W power level, ~30 nm bandwidth; the last one is 660 nm emission ($^4F_{9/2}\rightarrow{}^4I_{15/2}$) with $1.1x10^{-13}$ W power level, ~40 nm bandwidth. Summing all energy together and considering the effective mode area of the well confined waveguide is ~1 μm^2, the real ‘green light’ intensity is estimated ~1 mW/cm^2, almost the same order of intensity as the green light used for light post-treatment. Also, all data used here is from the recorded spectra, therefore the real green light intensity in the waveguide should be ~3 dB (0.9 dB for one side fibre-to-fibre from the current optical set-up, and 2.35 dB for fibre to waveguide mode mismatch and surface reflection) stronger than the above value.

To verify this assertion, the ASE spectra of a 48 mm long RF sputtered Er^{3+}:As_2S_3 waveguide were measured under 1490 nm excitation three times: immediately after the pump laser was turned on, and 5 and 10 minutes after the pump laser was turned on. The pumping intensity was ~2000 kW/cm^2, and the results are shown in Figure 5.10. About 3 dB drop of the ASE level is observed in the first 5 minutes, and another 1.5 dB drop in the following 5 minutes. This decrease of ASE level indicates similar effects as those seen in the PL measurements are being induced by upconverted green light, and this will seriously affect amplifiers & laser devices.

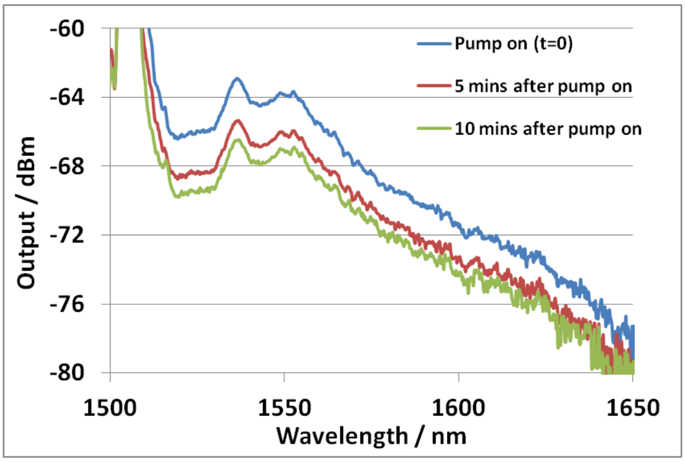

Figure 5.10 ASE spectrum of a 48 mm long RF sputtered Er^{3+}:As_2S_3 waveguide excited at 1490 nm.

Columnar structure is found in films fabricated using RF sputtering in many materials [303, 304], as well as in chalcogenide glass films [217, 305]. Coating a moisture barrier layer on the film to protect it is one option to resolve this issue, but reducing the columnar structure in the film would be a better solution. Either or both are essential for future research on erbium ion doped RF sputtered films, but neither was available at the time.

5.3 Conclusion

In this chapter, different approaches to realising erbium ion doped As_2S_3 waveguide amplifiers with reduced clustering were investigated. Erbium ion containing components ($ErCl_3$ and Er_2S_3) were chosen to replace the erbium metal in co-thermal evaporation. With $ErCl_3$, a long 1/e lifetime of the $^4I_{13/2}$ state of 2.6 ms was achieved in a low Er^{3+} doped (0.2 at%) sample, but the high density of 10 μm sized particles made the films unusable for waveguide amplifiers. The evaporation of Er_2S_3 was unsuccessful due to its high evaporation temperature which was beyond the upper limit of the available deposition system using the shielded alumina crucibles and with a tantalum boat resulted in very poor film quality. In RF sputtered Er^{3+}:As_2S_3 film, a 1/e lifetime of the $^4I_{13/2}$ state up to 2.1 ms was achieved in a thermally treated sample, but film quality became an issue that prevented the fabrication of suitable quality waveguides. With a glass As_2S_3 target, film quality was improved and the PL intensity from the obtained Er^{3+}:As_2S_3 film (after thermal post-treatment) was even stronger than that of the film on which internal gain was achieved in Section 4.5.3. However, due to the columnar growth of RF sputtering films water penetration and bonding to the glass matrix with the help of above band gap light quenched the PL rapidly. Whilst none of the above are fundamental issues and the results are promising, it was not possible to resolve these in the time available and with the equipment available.

Chapter 6

Erbium ion doped Ge-Ga-Se waveguides

Although internal gain was achieved in an erbium ion doped As_2S_3 waveguide amplifier as reported in Chapter 4, net gain in a rare-earth doped chalcogenide waveguide amplifier is still out of reach because of the clustering and the inability to disperse the clusters through thermal post-treatment due to the low intrinsic rare-earth ion solubility of As_2S_3. In this chapter, a new chalcogenide glass host, the Ge-Ga-Se system, which is known to have high rare-earth ion solubility, is investigated. Bulk glasses, thin films and waveguides based on erbium ion doped Ge-Ga-Se material were fabricated and characterised. Record erbium ion population inversion was achieved in these waveguides. But excitation laser upconversion pumped photoinduced absorption was encountered which presented a new hurdle to realising net gain.

6.1 Erbium ion doped Ge-Ga-Se bulk glasses

6.1.1 Background on Ge-Ga-Se glasses

Internal gain between 1570-1630 nm was achieved in an erbium ion doped As_2S_3 waveguide amplifier [133] in the work detailed in Chapter 4. The total erbium ion population inversion was, however, estimated only at ~30% from the absorption and enhancement curves, and this was still some way from realising a useful amplifier with net gain. Analysis revealed that thermally evaporated erbium ion doped As_2S_3 films showed clear signs of erbium ion clustering even at concentrations as low as 0.15 at% (~4-5×10^{19} ion/cm^3) (see Section 3.6 and 4.5.3). This erbium ion concentration is essentially the minimum usable doping level for a planar waveguide device. Under 1490nm pumping, the maximum inversion is 65% which limits the maximum possible internal gain to ~0.5 dB/cm, even before waveguide losses, ion-ion effects, etc. are considered which further reduce the gain. Long waveguides with lower doping are not a solution here, as the passive losses at the pump wavelength then become a problem (passive losses of ~3-5 dB are tolerable for the pump which limits amplifier length to perhaps 15 cm for the ~0.3 dB/cm propagation losses common for high refractive index contrast waveguides of this type [62]). Obviously, significant improvement is necessary to realise a useful high gain amplifier. Different approaches to doping erbium ions into

As_2S_3 films for better erbium ion homogeneity without thermal post-treatment, or the use of hosts with better intrinsic erbium ion solubility are considered promising solutions to this issue. The former was presented in Chapter 5. This chapter focuses on alternative hosts.

Among the family of chalcogenide glasses, gallium containing materials are known to have good rare-earth ion solubility. In As_2S_3, the three dimensional network can be interpreted using a [$AsS_{3/2}$] trigonal pyramidal units. The insufficient quantity of non-bridging sulfur in As_2S_3 that is needed to coordinate the isolated rare-earth ions, cannot meet the requirement of the large coordination number rare-earth ion needs to fit in, therefore, resulting in low rare-earth ion solubility [140, 306]. The incorporation of gallium as modifiers into chalcogenide glassy networks could dramatically increase the solubility of rare-earth ions due to the presence of edge-sharing [GaS_4] (or [$GaSe_4$] in selenium glass) tetrahedral structure, which provides a compensation for the negative charge of free S^{2-} (or Se^{2-} in selenium glass) ions by forming the chemical bonds with rare-earth ions [307-309].

Erbium ion doped Ga-containing chalcogenide bulk glasses were intensively investigated, and promising 1540 nm emission properties were obtained, e.g. [119, 198, 199]. Ikuta et al. measured PL intensity at 1540 nm in Er^{3+} doped stoichiometric $(GeSe_2)_{1-x}(Ga_2Se_3)_x$ chalcogenide glasses and concluded that Er^{3+} could be well dispersed and optically active up to 2 at% [198]. The importance of gallium for Er^{3+} activation was also studied, and the PL results indicated the critical gallium to erbium ion concentration ratio was about 5. Too much gallium in the glass may cause inhomogeneity. Allen et al. studied the optical characteristics of a series of Er^{3+}-doped chalcogenide glasses and found that under 980 nm excitation, the shortest 1550 nm emission decay time of 1–1.5 ms were observed in GaGeAsSe glasses, whilst the highest values of 2–4 ms were obtained in GaGeSe and GaGeS samples [119]. Koughia et al. examined the optical properties of erbium ion doped Ge-Ga-Se and Ge-Ga-S chalcogenide glasses [199]. The lifetime of the $^4I_{13/2}$ state of Er^{3+} in Ge-Ga-Se glass was predicted at 1.8 ms from Judd-Ofelt theory, but in experiments, with different excitation wavelengths (976 nm, 818 nm and 662 nm), longer lifetimes ranging from 2.7 to 3.1 ms were observed in a 2 at% erbium ion doped sample, and this discrepancy was explained by effective energy transfer in the Er^{3+} system when the self-absorption effect and the possible re-emission and re-absorption processes were taken into consideration. Also in another report, in Ge-Ga-Se glass system, it was suggested that a high ratio of

Ga^{III} to Er^{3+} ensured homogeneous distribution of Er^{3+}, whilst a low ratio led to the formation of clusters [120]. In the intermediate region, energy was shown to be able to efficiently migrate from one Er^{3+} to another. Tonchev et al. doped Er_2S_3 from 1.8 to 2.4 mol% into Ge-Ga-S glasses [295], and a broad PL emission band at ~1540 nm with decay time in the range of 1.13 to 1.55 ms was observed under 818 nm excitation. The PL decay time decreased rapidly with increasing Er^{3+} concentration in the range of study, at a linear rate of 0.7 ms/mol%. All of these works showed the potential of Ge-Ga-Se glass as a promising host for Er^{3+} doping due to the long 1.5 μm PL decay time and high dopant concentration possible.

To gain an initial understanding of the properties of the Er^{3+}:Ge-Ga-Se glass system, six pieces of $Er^{3+}:Ge_{25}Ga_{10}Se_{65}$ (at%) glass with different Er^{3+} concentrations were prepared. Absorption and emission properties of the obtained $Er^{3+}:Ge_{25}Ga_{10}Se_{65}$ glasses were investigated in order to determine the effect of Er^{3+} concentration and establish a baseline for the performance of Er^{3+} in these hosts to compare with thin films.

6.1.2 Erbium ion doped Ge-Ga-Se glasses synthesis and characterisation

In order to provide a benchmark for film based materials, erbium ion doped $Ge_{25}Ga_{10}Se_{65}$ (at%) chalcogenide glasses with different Er^{3+} concentrations (ranging from 0.1 at% (~3×10^{19} ion/cm^3) to 2 at% (~6×10^{20} ion/cm^3)) were prepared from high purity (5*N*) germanium, gallium, selenium and erbium metals using the conventional melt-quenching method. This composition ($Ge_{25}Ga_{10}Se_{65}$ (at%)) was chosen as it was expected to be a stoichiometry that should produce thin films with properties close to the bulk glass [225] and that had sufficient gallium to enable ~1 at% erbium ion to remain unclustered. The required amounts of these raw materials were weighed inside a dry nitrogen glove box and loaded into a pre-cleaned quartz ampoule. The ampoule was then sealed under vacuum (~10^{-4} Pa) using an oxygen-hydrogen torch, and introduced into a rocking furnace for melting of the contents at 950 °C. The melt was homogenized for a period not less than 12 hours, then the ampoule was removed from the rocking furnace and water quenched. The resulting glass boule was subsequently thermally treated at a temperature 20 °C below its glass transition temperature T_g of ~395 °C for 2 hours, before being slowly cooled down to room temperature. The obtained glass rods were cut into small pieces with ~2 mm thickness and then polished on both surfaces.

The room temperature Raman spectra of these Er^{3+}:$Ge_{25}Ga_{10}Se_{65}$ (at%) bulk glass samples were measured using a Horiba Jobin Yvon 64000 spectrometer employing a 632 nm laser as the excitation source. The 830 nm excitation source was avoided, because this wavelength could excite the erbium ions and thus lead to emissions which may overlap with the Raman signal. A CCD array detector was installed on the spectrometer to record Raman spectra. Raman spectra collected from erbium ion doped $Ge_{25}Ga_{10}Se_{65}$ (at%) bulk glass samples are shown in Figure 6.1 with vertical offsets to aid viewing.

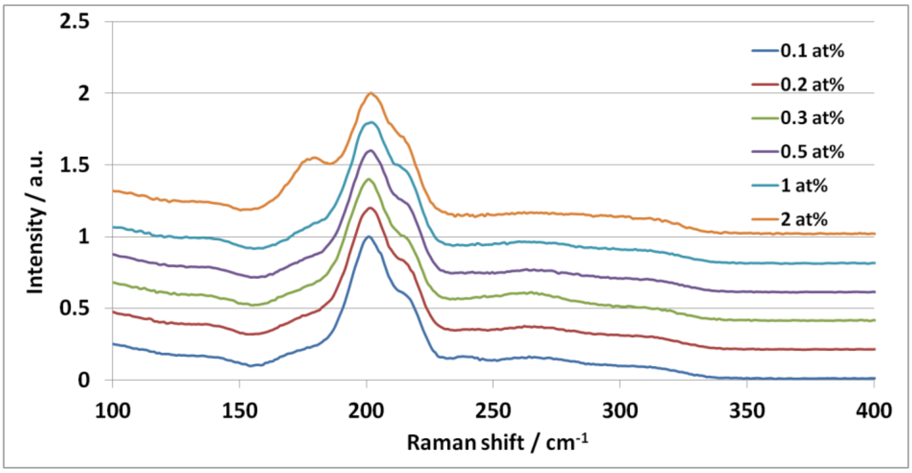

Figure 6.1 Raman spectra of Er^{3+}:$Ge_{25}Ga_{10}Se_{65}$ (at%) bulk glasses with Er^{3+} concentrations ranging from 0.1 at% to 2 at%, under excitation at 632 nm.

The main feature in the Raman spectra is the band with its maximum near 202 cm^{-1} with two shoulders near 177 and 217 cm^{-1}. According to reference [310], the strongest band rising near 202 cm^{-1} is attributed to the $v_1(A_1)$ symmetric stretching modes of corner-sharing [$GeSe_{4/2}$] tetrahedra. The shoulder at 217 cm^{-1} of the dominant band can be associated with the A^c_1 breathing vibrations of distorted fragments of the layered c-$GeSe_2$ structure containing edge-shared $Ge_2Se_{8/2}$ bi-tetrahedra. The Raman band at 177 cm^{-1} is probably related to stretching modes of Ge-Ge, Ga-Ga or Ge-Ga bonds (A_G vibration modes) in $Ge_2Se_{6/2}$, $Ga_2Se_{6/2}$ or $GeGaSe_{6/2}$ structural units. This 177 cm^{-1} band is much stronger in the 2 at% doped sample implying a significantly increased concentration of Ge-Ge, Ga-Ga homopolar bonds in this glass [311]. Although the band at 177 cm^{-1} in the 2 at% sample is evident, no sign of the evolution of this band in the 1 at% and below samples is visible, and the cause for this abrupt change is not clear.

Besides the obvious Raman bands discussed above, the broad Raman band of lower intensity (235-330 cm^{-1}), consisting of at least three weak bands with strong overlaps, can be assigned to the vibrations of Se-Se bonds (245, 265 cm^{-1}) and to the vibrations of $GeSe_4$ structural units (300 cm^{-1}). Additionally, for Ge-Ga-Se based chalcogenide glasses, the vibration modes of Ga-containing structural units, such as [$GaSe_4$] and [Se_3Ga-$GaSe_3$] are usually overlapping with Ge-containing structural units [$GeSe_4$] and [Se_3Ge-$GeSe_3$], due to the small difference between bond strength and atomic weights of Ga and Ge [310]. From Figure 6.1, the increasing of the erbium ion concentration from 0.1 at% up to 1 at% brought almost no significant change in Raman spectrum and therefore glass structure, whilst in the 2 at% Er^{3+} doped sample, a sign of more Ge-Ge, Ga-Ga homopolar bonds appears, indicating a local structure change occurs in this high doped sample. This is consistent with reports that the introduction of transition metals into the glass matrix may cause significant change of almost all glass parameters, but with rare-earth ions only mild change could be found [312, 313].

6.1.3 Optical properties of erbium ion doped Ge-Ga-Se glasses

Absorption spectra of Er^{3+}:$Ge_{25}Ga_{10}Se_{65}$ (at%) bulk glasses were recorded using a Cary 5000 UV-Vis-NIR spectrophotometer. The absorption curve of a 2.9 mm optical path length, 0.5 at% Er^{3+}:$Ge_{25}Ga_{10}Se_{65}$ sample, is shown in Figure 6.2 for example.

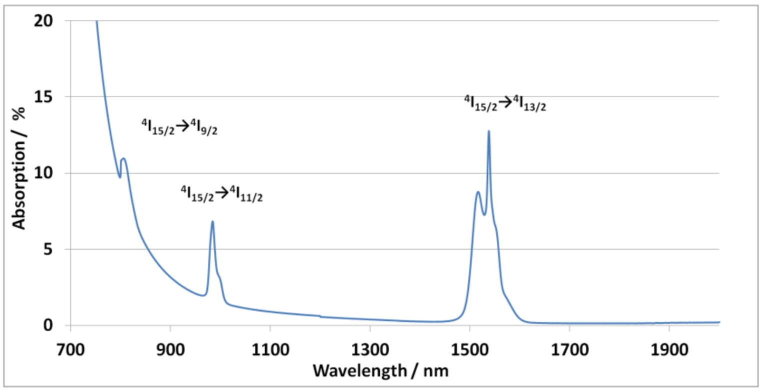

Figure 6.2 Absorption spectrum of a 2.9 mm optical path length 0.5 at% Er^{3+}:$Ge_{25}Ga_{10}Se_{65}$ bulk glass.

Three absorption bands show up in the spectrum in Figure 6.2 as expected. The strong band located at 1538 nm is due to the $^4I_{15/2} \rightarrow ^4I_{13/2}$ transition. The 980 nm feature corresponds to the absorption between the $^4I_{15/2}$ and the $^4I_{11/2}$ state, and the band at 805 nm is assigned to the $^4I_{15/2} \rightarrow ^4I_{9/2}$ transition. The increasing absorption starting from ~800 nm to short wavelengths is the weak absorption tail (WAT) that is formed by extrinsic impurities and intrinsic defects [39]. At even shorter wavelength the absorption increased exponentially as the band gap is reached, these effects preventing us observing the ground state absorptions of higher energy levels.

Absorption features at 1538 nm from all 6 samples with different erbium ion concentrations were extracted and are shown in Figure 6.3(a). The absorption spectra shape are essentially invariant except the intensity increases with increase of erbium ion concentration. The peak absorption value at 1538 nm was extracted and is plotted versus erbium ion concentration in Figure 6.3(b), from which a linear relationship (fitted line) between absorption and doped concentration up to 2 at% (~6×10^{20} ion/cm^3) is seen clearly, implying the erbium is not forming physical clusters at concentrations up to 2 at%.

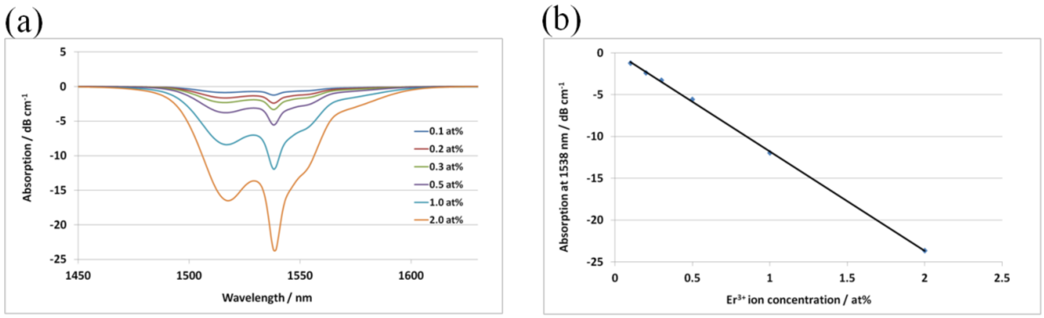

Figure 6.3 Absorption band centred at 1538 nm for different erbium ion concentrations in Er^{3+}:$Ge_{25}Ga_{10}Se_{65}$ bulk glasses (a); peak absorption value at 1538 nm versus erbium ion concentration in Er^{3+}:$Ge_{25}Ga_{10}Se_{65}$ bulk glasses (b).

6.1.4 PL and PL lifetime of erbium ion doped Ge-Ga-Se bulk glasses

The room temperature photoluminescence spectra (PL) of the Er^{3+}:$Ge_{25}Ga_{10}Se_{65}$ (at%) bulk glass samples were measured using the Horiba Jobin Yvon 64000 spectrometer employing an 830 nm laser as the excitation source. An InGaAs detector installed on the spectrometer recorded PL spectra up to 1600 nm. The $^4I_{13/2}$ excited state lifetime of Er^{3+} in Er^{3+}:$Ge_{25}Ga_{10}Se_{65}$ (at%) glass was measured under 1490 nm excitation, using the all fibre confocal arrangement previously described in Section 3.3.2. With 1490 nm excitation, the effect of the possible transitions involved in higher excited states on the measured $^4I_{13/2}$ level lifetime was reduced significantly. PL intensity values were also collected in the lifetime measurement set-up using both 1490 and 980 nm pumps.

Figure 6.4 shows the PL spectra of the bulk glasses with different erbium ion concentrations excited with an 830 nm continuous wave laser. All the spectra have similar line shape and band positions. The emission peak lays at 1538 nm, which is slightly red-shifted from the 1532 nm usually observed in oxide glass hosts [314], also was observed in Er^{3+}:As$_2$S$_3$ films (see Section 3.3.2(c)). The long wavelength shoulder on the PL spectrum is growing slightly with the increase of Er^{3+} concentration, which is also plotted in the inset for the normalized PL spectra. Shoulder growth accompanied by increasing emission bandwidth has previously been observed in a number of studies, e.g.[120], and is believed to be associated with reabsorption of the emitted 1540 nm light in highly doped materials. In this work, however, there is no sign of bandwidth increase, which suggests a different mechanism is in play, perhaps relates to the higher order ~1550 nm transition ($^4H_{11/2}\rightarrow{}^4I_{9/2}$ transition), possible due to the 830 nm pump wavelength.

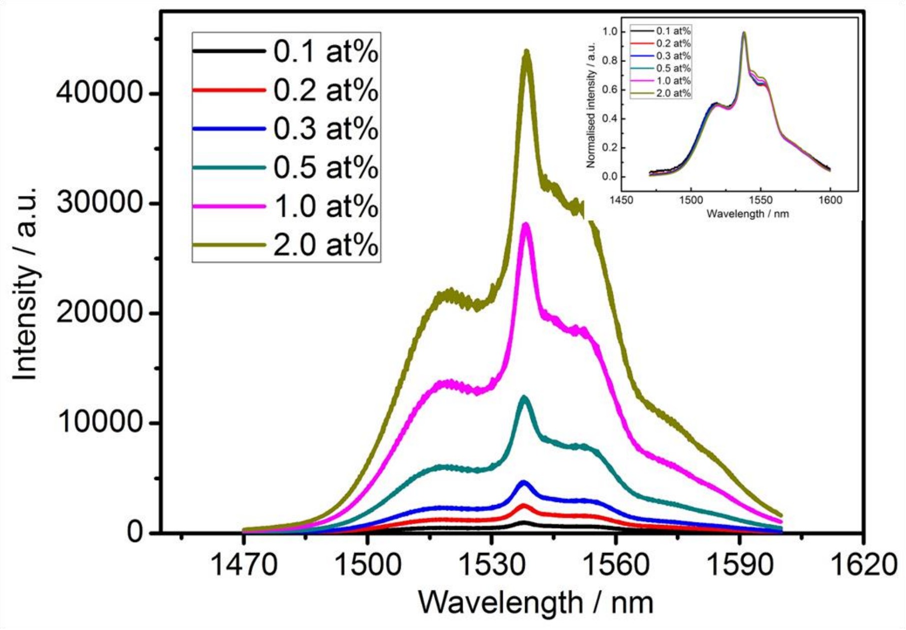

Figure 6.4 PL spectra of Er^{3+}:Ge$_{25}$Ga$_{10}$Se$_{65}$ (at%) bulk glasses with different Er^{3+} concentrations ranging from 0.1 at% to 2 at% excited at 830 nm. The insert is the normalised PL spectra.

The PL intensity at 1538 nm versus erbium ion concentration for the 830 nm pump is presented in Figure 6.5(a). It shows an initial supra-linear increased in PL with erbium ion concentration before becoming sub-linear at high concentrations, as would be expected from ion-ion effects. Figure 6.5(b) shows the PL intensity with a 1490 nm pump laser which displays the normally expected behaviour of reducing PL efficiency with increasing Er^{3+} concentration, as seen with a 980 nm pump. The linear relationship between absorption and erbium ion concentration (see Figure 6.3(b)) verifies that the supra-linear curvature in the 830 nm PL result is not due to errors in the Er^{3+}

concentration at low values. The origin of this effect remains uncertain and needs further investigation. However, it is clear that the performance is beginning to decline at Er^{3+} concentration beyond 1 at%, which for this glass composition could be considered optimal on the basis of the data presented. While considering the 10 at% Ga concentration in all the glasses and the optimal ratio of Ga^{III}/Er^{3+} at 10:1 noted in prior work [120], the limit of the homogeneous distribution of erbium ion in this host should be ~1 at%. Therefore it is reasonably expected that erbium ions start to form clusters at an erbium ion concentration more than 1 at%, leading to the gradual quenching of PL emission at 1550 nm [315, 316] which fits with the measured data.

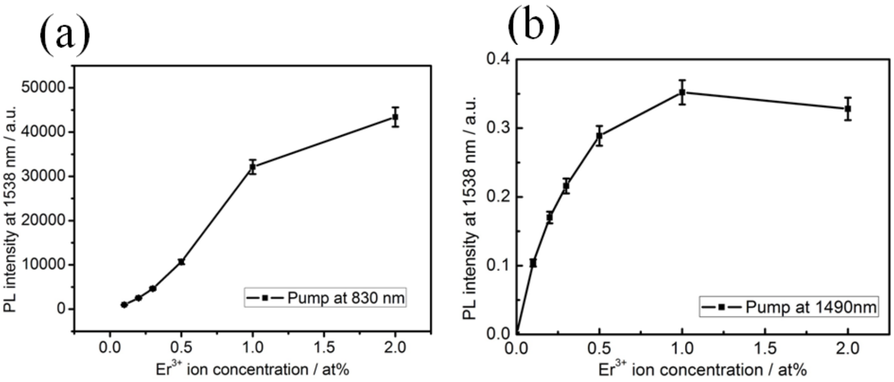

Figure 6.5 PL intensity at 1538 nm with 830 nm excitation (a), and PL intensity at 1538 nm excited at 1490 nm (b) of Er^{3+}:$Ge_{25}Ga_{10}Se_{65}$ (at%) bulk glasses with erbium ion concentration ranging from 0.1 at% to 2 at%.

6.1.5 Absorption and emission cross-section of erbium ion doped Ge-Ga-Se bulk glasses

Based on the absorption spectrum of the 0.1 at% (~3×10^{19} ion/cm^3) Er^{3+}:$Ge_{25}Ga_{10}Se_{65}$ (at%) glass sample, McCumber theory [161] was employed to calculate the emission cross-section, and the results are shown in Figure 6.6. The McCumber theory and measured emission cross-section agree well except for the minor deviation in the 1520 nm tail region. Also in Figure 6.6, a maximum pump efficiency curve is plotted which represents the maximum inversion possible versus pump wavelength as described by equation 2.14. With 1490 nm excitation, the inversion efficiency is around 71%. At shorter wavelengths, the efficiency is higher, but the absorption cross-section reduces further leading to lower overall pump absorption. The results also indicate that for a highly doped short waveguide amplifier, the optimum pump wavelength lays in the 1500-1510 nm region where the absorption is approaching half its peak value whilst the inversion efficiency remains above 60%, as has been successfully employed in for example TeO_2 based waveguide amplifiers [152]. This is a significantly longer pump wavelength than in silica or other oxide based hosts.

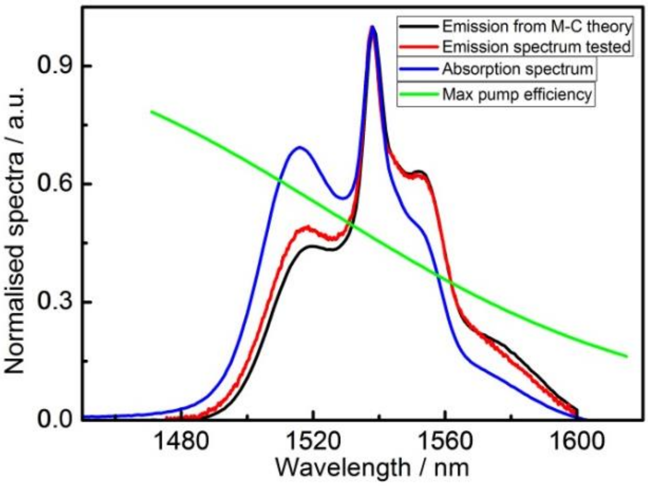

Figure 6.6 Normalised absorption, emission spectra and simulated emission cross-section based on M-C theory, and max pump efficiency with pump at 1490 nm of the 0.1 at% Er^{3+}:$Ge_{25}Ga_{10}Se_{65}$ bulk glass.

The dependence of PL intensity on pump power was investigated for high and low erbium ion doped samples (0.1 at% (~3×10^{19} ion/cm^3) and 2 at% (~6×10^{20} ion/cm^3)), with excitation at 1490 nm, and the results are shown in Figure 6.7. It is clear in both samples that PL intensity is increasing with the increase of pump intensity, but with different trends. For the 0.1 at% Er^{3+} doped glass, the PL intensity increases linearly with pump intensity in the measured range which is low enough in intensity that there is still a significant fraction of Er^{3+} in the ground state and no saturation of the emitted 1550 nm radiation occurred. For the 2 at% Er^{3+} doped sample, there is instead an approximately quadratic relationship over the same pump power range. This quadratic trend in the highly doped glass results from radiative and non-radiative ion-ion energy exchange interactions which are not present in the lower doped samples due to the larger average distance between Er^{3+} ions.

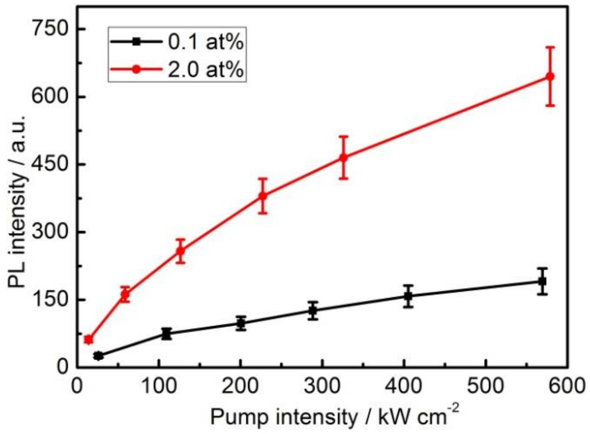

Figure 6.7 PL intensity at 1538 nm versus pump intensity (at 1490 nm) in low (0.1 at%) and high (2 at%) Er^{3+} doped $Ge_{25}Ga_{10}Se_{65}$ bulk glass.

Due to the low phonon energy in chalcogenide glasses, the multiphonon relaxation rate of Er^{3+} between the $^4I_{11/2}$ state and the $^4I_{13/2}$ state is low and the $^4I_{11/2}$ state has a long lifetime, comparable to that of the $^4I_{13/2}$ state [46]. Therefore, the lifetime of the $^4I_{13/2}$ state when pumped with a 980 nm laser would be expected to be significantly longer than that with a 1490 nm laser, due to energy storage at the $^4I_{11/2}$ state. To avoid this issue, a 1490 nm laser was employed to probe the $^4I_{13/2}$ state lifetime of the Er^{3+}, using the confocal experimental configuration described in Section 3.3.2, to avoid reabsorption and stimulated emission artifacts [152]. It is well known that as the Er^{3+} concentration increases that the average distance between neighbouring ions diminishes, enabling a variety of energy transfer effects to become relevant. As many of these effects occur between two or more Er^{3+} ions in the $^4I_{13/2}$ metastable state, these excited ions do not contribute to creating photons in the desired state. Therefore, this reduces the PL efficiency and also results in a decrease of the lifetime of the desired state with increasing ion concentration, as the energy transfer is a fast ion-ion interaction. Typically these effects have been found to follow an empirical formula first proposed in [189]:

$$\tau^{obs} = \frac{\tau_0}{1+(\rho/Q)^p} \tag{6.1}$$

where τ_{obs} is the observed fluorescence lifetime, τ_0 is the ideal fluorescence lifetime with zero concentration, ρ is the Er^{3+} concentration, Q is the quenching concentration and p referred as phenomenological parameter characterizing the steepness of the corresponding quenching curve. As several of the effects encapsulated in this relationship also depend (sometimes) nonlinearly on the number of excited ions, there is also a dependence of the parameters on pump power.

The photoluminescence decay curves were measured for the glass samples over a range of different pump intensities (from ~10 to ~600 kW/cm^2), the parameters recorded being the measured 1/e lifetime, and the intrinsic lifetime (ie the supposed radiative lifetime, see Section 3.3.2). The lifetimes versus pump power for each glass were then fitted with suitable polynomials to extrapolate the data back to ‘zero pump power’ to enable the effective ‘zero pump power lifetimes’ to be extracted. Figure 6.8 presents the data for both the 1/e and intrinsic lifetimes of the $^4I_{13/2}$ metastable state of Er^{3+} at effective ‘zero power’ and at ~600 kW/cm^2 pump intensity.

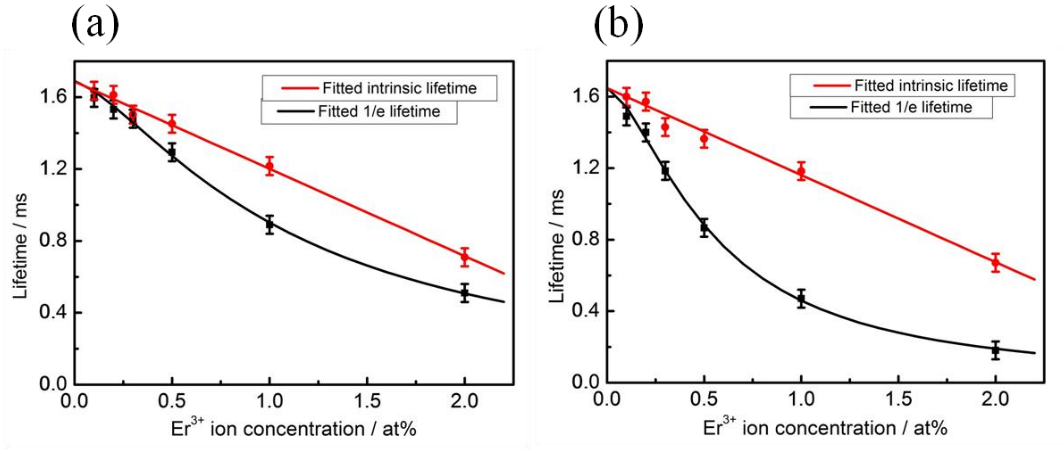

Figure 6.8 1/e and intrinsic lifetime of the $^4I_{13/2}$ metastable state of Er^{3+} with different doping concentrations, at extrapolated zero pump power (a); also at high pump power (~600 kW/cm^2 intensity) (b), of Er^{3+} doped $Ge_{25}Ga_{10}Se_{65}$ bulk glass.

There are a number of clear trends from the data in Figure 6.8. Looking first at the intrinsic lifetime in Figure 6.8(a) & (b), it is independent of the pump power (as expected) and had a clear linear dependence on concentration with a slope of -0.48 ms/at% erbium ion. The slope of the line is also significantly lower than the -0.7 ms/mol% (Er_2S_3) reported in [295]. However this improvement in performance still lags the better oxide glasses where essentially concentration independent radiative lifetimes have been observed up to about 2 at% Er^{3+} [317]. It also needs to be reinforced that sufficient gallium was present to ensure erbium ion clustering did not occur according to prior research [120]. The concentration quenching present is therefore more intrinsic in nature, occurring even at low erbium ion doping and high Ga:Er^{3+} ratios, and reasons for this relatively strong dependence contrary to those in some oxide glasses remain to be elucidated.

Both the ‘zero power’ and high power 1/e lifetimes show a more significant dependence on concentration and can be fitted well by the empirical formula mentioned above as shown in Figure 6.8. The Q value, referred to as quenching concentration, is 1.1 for the zero pump power case and 0.545 for the high pump power, based on the fitting. This indicates that mechanisms that depend upon the inverted population (co-operative upconversion and/or excited state absorption process for example) are strongly active in these glasses. The relatively strong power dependence indicates that care is required in the design of amplifier devices using these materials where the pump intensity has to be considered relative to the erbium ion concentration, and the likely trade-offs thus will impose. Of particular concern is the considerable lifetime shortening at high power and high concentrations, the region of operation often used in planar waveguide amplifiers. Further study is needed to determine the dominant mechanism at play and potential remedies for this behaviour. The high power lifetime shortening in particular suggests that concentrations below 1 at% Er^{3+} are strongly preferable for waveguide amplifier devices, though a trade-off with the propagation loss then will determine the optimum concentration and design. Concentrations in the range of 0.5-0.75 at% Er^{3+} might be considered optimum as they would be expected to show up to about a factor of two reduction in the 1/e lifetime under high pumping compared to the radiative value (which is tolerable), and this also lies in the high efficiency part of the PL intensity versus pump power density curve as shown in Figure 6.5.

6.1.6 Erbium ion doped $Ge_{25}Ga_{10}Se_{65}$ bulk glass summary

Broad PL emission band centred at 1538 nm was observed from a series of Er^{3+}: $Ge_{25}Ga_{10}Se_{65}$ bulk glasses with erbium ion concentration ranging from 0.1 at% to 2.0 at%. The dependence of PL intensity and lifetime with increasing erbium ion concentration was presented and discussed, clear concentration dependences being present leading to continuous monotonic decay of the lifetime with increasing erbium ion concentration. Based on the results, a concentration in the range of 0.5-0.75 at% could be considered as optimum, and in the following film fabrication part, the erbium ion concentration was controlled carefully to reside in this range.

6.2 Erbium ion doped Ge-Ga-Se film deposition and characterization

6.2.1 Erbium ion doped Ge-Ga-Se film deposition

Despite erbium ion doped Ge-Ga-Se glasses being intensively studied, only a few reports on erbium ion doped Ga-containing chalcogenide films were published so far. Takahiko et al. reported the properties of Er^{3+} doped Ga-Ge-Se films on fused silica substrates deposited using RF sputtering, and lifetimes of 1.8-2.6 ms for the Er^{3+} $^4I_{13/2}$ state were observed when excited at 973 nm [219]. In Nazabal et al.'s reports, Er^{3+} doped Ga-Ge-Sb-S(Se) films were fabricated using pulsed laser deposition (PLD) and RF sputtering, and both physical and optical properties of the films were investigated [318]. The lifetime of the $^4I_{13/2}$ state of Er^{3+} decreased from 1.6 ms to 1.1 ms in the sputtered films as the erbium ion concentration increased from 0.3 to 1.5 at% ($3.4\text{x}10^{19}$ to $1.65\text{x}10^{20}$ ions/cm^3) without mentioning the pumping wavelength. A lifetime of 1.8 ms (equal to the values calculated using Judd-Ofelt theory) was achieved on a piece of Ga-Ge-Sb-S(Se) bulk glass with 0.05 at% Er^{3+} concentration after 60 minutes annealing [318].

A large part of the difficulty in film/waveguide amplifier fabrication, particularly in gallium containing chalcogenide glasses, relates to the difficulties in fabricating high quality erbium ion doped films. Thermal evaporation is perhaps the simplest, and therefore, most widely used method of preparing chalcogenide glasses films. However, many ternary and quaternary chalcogenide glasses display the undesirable property of forming phase separated molecular liquids on melting, with the different phases boiling off at different temperatures and rates. This can result in films with often quite different composition to the starting materials e.g. [213, 225]. Barely un-doped films obtained from rare-earth ion doped bulk targets using thermal evaporation were mentioned in Fick and Lyubin's papers [128, 130]. The weight percentage of gallium was found to be significantly reduced from the value in the starting material in films deposited using standard thermal evaporation [319]. Among all the chalcogenide glass film deposition methods, elemental co-thermal evaporation provides a solution to this issue as it offers the possibility of controlling the evaporation rate of each element in the film independently. Thus, the final composition of the film can be controlled precisely.

For this reason, co-thermal evaporation was employed in this work, where each element had its own source and evaporation rate monitor, and thus the evaporation rate of each element could be controlled accurately and independently to select any desired film composition. High purity Ge, Ga, Se and Er elements (5*N*) were used as starting materials, and evaporation was performed at a vacuum level ~1x10^{-5} Pa using the previously described chamber manufactured by Angstrom Sciences (in Section 3.2). Procedure of the Er^{3+}:Ge-Ga-Se film evaporation was similar to the procedure of Er^{3+}:As_2S_3 film thermal evaporation, which was described in Section 3.2.3. The film thickness and linear refractive index (n) were measured using a dual angle spectroscopic reflectometer (SCI FilmTek 4000) using a Tauc-Lorentz model. The final film composition was determined by energy dispersive X-ray spectroscopy (EDS).

6.2.2 Erbium ion doped Ge-Ga-Se film characterisation

A film with a thickness of 1062±5 nm and refractive index of 2.433±0.002 at 1550 nm was deposited. Its composition was measured to be 24.60 at% Ge, 10.94 at% Ga, 63.74 at% Se and 0.71 at% (~2×10^{20} ion/cm^3) Er which is in the optimal region based on the PL and lifetime measurements of the bulk glasses as noted in Section 6.1.6. An issue encountered during film evaporations was “spitting” of gallium particles out of the evaporation crucible. As will be discussed in this section, this led to a significant density of small particles in the films.

The Raman spectrum of the obtained films was measured with a Horiba Jobin Yvon 64000 spectrometer utilizing a 632 nm laser as the excitation source and a 50x near infrared objective with NA of 0.75. The obtained spectrum of an Er^{3+}:Ge-Ga-Se film and a reference Raman spectrum of a 0.5 at% Er^{3+}:$Ge_{25}Ga_{10}Se_{65}$ bulk glass are shown in Figure 6.9. Although the spectrum from the film is much noisier than that from the bulk glass due to the low film thickness, the main features at 202 cm^{-1} with a shoulder near 217 cm^{-1} and the lower intensity broad band from 270-330 cm^{-1} remain unchanged, implying the microstructure in film is similar to its bulk counterpart. The small extended band at ~450 cm^{-1} of the film arises from the thermally oxidized silicon (TOX) substrate upon which the film was deposited.

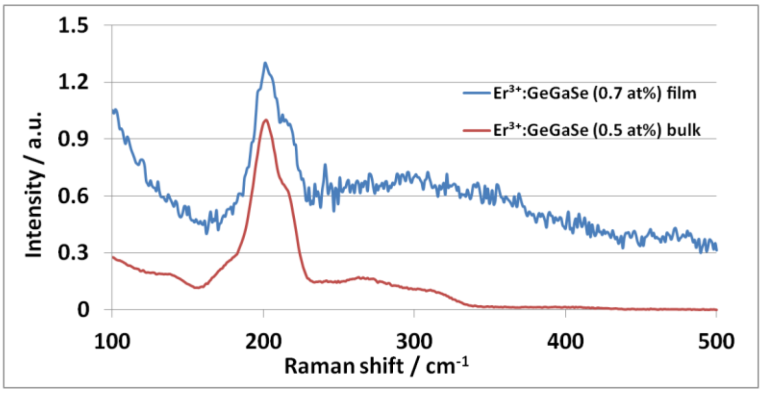

Figure 6.9 Raman spectra of co-thermal evaporated Er^{3+}:Ge-Ga-Se film and 0.5 at% $Er^{3+}:Ge_{25}Ga_{10}Se_{65}$ bulk glass with excitation at 632nm.

The lifetime of the $^4I_{13/2}$ state of Er^{3+} of this Er^{3+}:Ge-Ga-Se film was measured using the all fibre confocal set up mentioned in Section 3.3.2 with a 1490 nm pump. The intrinsic lifetime of this film was 0.87 ms, which is somewhat shorter than the ~1.35 ms observed in the corresponding bulk glass. Several factors could account for this. Firstly, the film was fabricated under non-equilibrium conditions in which a population of homopolar and ‘wrong’ bonds could be created, and these ‘wrong’ bonds may change the local environment for the erbium ions thereby degrading the performance. Secondly, local erbium ion clusters may also be formed during the evaporation as pure erbium metal was used as a source (i.e. polyatomic evaporation could occur as discussed with $Er^{3+}:As_2S_3$ in Section 3.5), leading to quenching of the emission [131]. Thirdly, the nanoscale homogeneity of the films was uncertain compared to the bulk glasses. The bulk glasses which were quenched from a metastable equilibrium melt were expected to be located in a region of the phase diagram where the glass was essentially single phase, rather than nanoscale phase separated. Given the clear issues with the gallium source and the non-equilibrium nature of the film growth, the film homogeneity cannot be guaranteed, and the “granular” nature often observed in evaporated thin films may also be relevant here [320]. Lastly, the erbium metal oxidisation and impurities introduced in the film during film evaporation may also cause a shorter lifetime.

The dependence of PL intensity and 1/e lifetime of Er^{3+} on pump power was also investigated in the obtained Er^{3+}:Ge-Ga-Se films, which is shown in Figure 6.10(a). The emission has approximately quadratic pump power dependence in the measured range, which is similar to the bulk glasses. The 1/e lifetime of the $^4I_{13/2}$ state of Er^{3+} in Ge-Ga-Se film also decay with increase of pump intensity as seen in the bulk glasses. To compare the 1/e lifetime of film and bulk glass, the observed lifetime empirical formula (equation 6.1) was employed again to estimate the 1/e lifetime of a bulk sample with 0.7 at% Er^{3+} at a pump intensity around 300 kW/cm^2. This produced an expected 1/e lifetime in the 0.7 at% Er^{3+} doped glass of 0.74 ms compared to the 0.52 ms measured in the film. The lifetime reduction in the film under pumping is smaller than that seen in the radiative lifetime (27% vs. 35%), and the shape of the decay curve in Figure 6.10(b) indicates that further reductions at the highest pump intensities expected in a typical waveguide device (up to ~1MW/cm^2) will be modest leaving a workable lifetime around 0.5 ms.

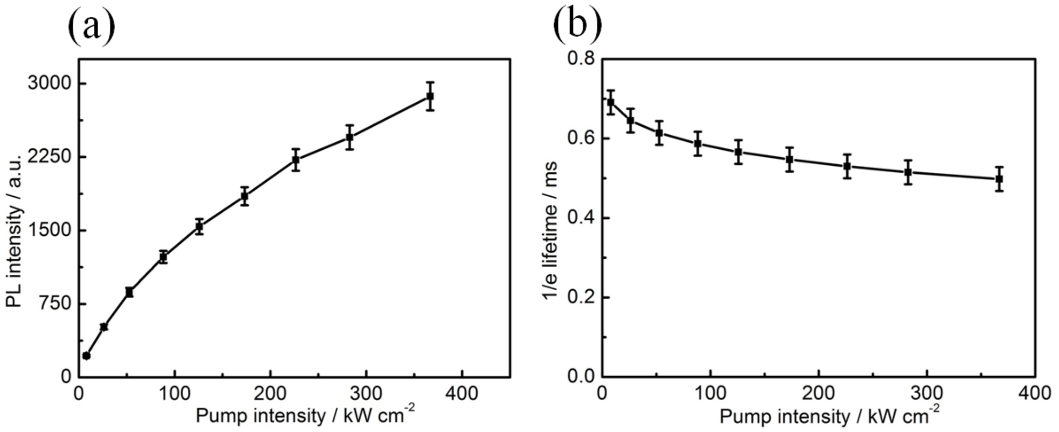

Figure 6.10 PL intensity (a), and 1/e lifetime of the $^4I_{13/2}$ state of Er^{3+} in the Er^{3+}:Ge-Ga-Se film (b) versus pump intensity in co-thermal evaporated films.

Measurements of film loss and erbium ion absorption in this Er^{3+}:Ge-Ga-Se film were performed using a Metricon 2010 prism coupler, and the detail of this method can be found in Section 3.3.2. The resulting optical loss of the film, as well as a fitted absorption curve based on the absorption curve of the Er^{3+}:$Ge_{25}Ga_{10}Se_{65}$ (0.1 at%) bulk glass are shown in Figure 6.11.

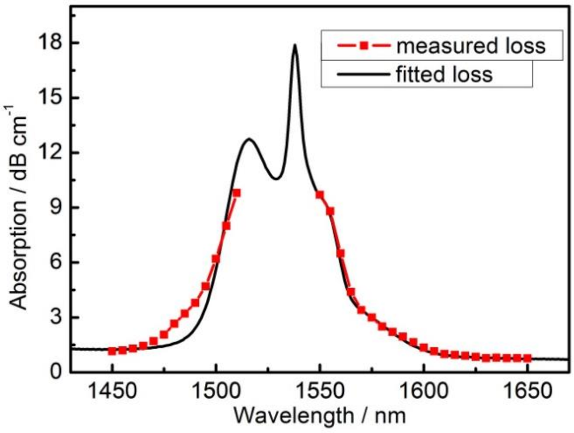

Figure 6.11 Absorption spectrum of Er^{3+} doped Ge-Ga-Se films measured using prism coupler, with a fitted curve based on the absorption curve of the Er^{3+}:$Ge_{25}Ga_{10}Se_{65}$ (0.1 at%) bulk glass.

A minimum value of 0.8 dB/cm at 1650 nm is found outside the erbium ion absorption band. Given the observed particles in the as deposited film, it is likely that the loss is dominated by scattering off particulates. To investigate the film quality and particle induced scattering loss, the deposited film was inspected using dark field microscopy with x20 and x100 magnifications to estimate the particle density and size. Optical micrographs of these particles taken in dark field is shown in Fig 6.12. Custom software was used to count the particles in numerous images to ascertain an average particle density and also to estimate the size distribution. The density of particles was ~0.01 particles/μm^2, with a mean particle diameter from 1.0 to 1.1 μm. The size distribution was always tightly bounded though with varying shape but the upper and lower bounds were 0.9 and 1.15 μm diameter based on multiple measurements of different parts of the wafer. Mie scattering would be expected to dominate in this size range, and here the r/λ (r is the radius of particle, and λ is the wavelength) ratio ranges from 0.3 in the 1550 nm band up to around 0.5 at 1000 nm. Mie scattering is a complex phenomenon requiring careful modelling for accurate predictions, but using the example of water droplets in air [321], this range of size parameter would result in a scattering cross-section that reduced by about a factor of two going from 1000 nm to 1550 nm. Additionally, the density of particles (i.e. a 1 mm wide beam typical of the set-up used would encounter 10,000 particles per mm of propagation length) and their likely metallic nature of the gallium droplets would be expected to induce non-negligible loss. It is expected that the particles could be eliminated with further refinement of the evaporation set-up, most likely by using a baffled evaporation source that has no line of sight between the evaporant and the wafer.

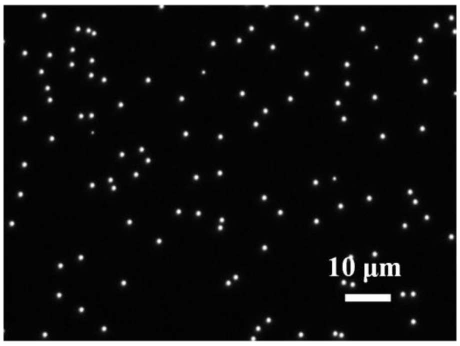

Figure 6.12 Particles on the Er^{3+} doped Ge-Ga-Se film, which was taken with microscopy in dark field mode. The micro-sized particles has diameters ranging from 0.9 µm to 1.15 µm.

As it was established that the particles from gallium spitting cause a significant part of the propagation loss of the film, a modification of the film evaporation facility was implemented to resolve this issue and will be detailed in the following section.

6.3 Erbium ion doped Ge-Ga-Se film modification and waveguide characterisation

6.3.1 Modification on erbium ion doped Ge-Ga-Se film deposition

So far, erbium ion doped Ge-Ga-Se film with controllable film composition was achieved by co-thermal evaporation. Intrinsic lifetime of 0.9 ms of the $^4I_{13/2}$ state of Er^{3+} in a 0.7 at% erbium ion doped Ge-Ga-Se film showed the potential erbium ion solubility of this host material. However, a high density of particles with diameter of ~1 µm was observed on the film surface, which resulted in non-negligible propagation loss. The formation of these particles was suspected to be due to the spitting from gallium source.

To eliminate the particulates in the Er^{3+}:Ge-Ga-Se film, a refinement of the evaporation set-up was proposed. A baffled source that had no direct line of sight between the evaporant and the wafer was used. After Er^{3+}:Ge-Ga-Se film deposition, the film needed to be patterned into waveguides using dry etching, the difficulty in directly etching erbium ion containing films due to the involatile erbium compounds, as described in Section 4.2.1, still existing. Therefore, a top layer of As_2S_3 was added on the Er^{3+}:Ge-Ga-Se film and then etched to get the designed ridge structure see Figure 6.16(a).

Erbium ion doped Ge-Ga-Se films were deposited using co-thermal evaporation on 100 mm Thermally Oxidised Silicon wafers at room temperature in a vacuum of ~10^{-5} Pa. A strip loaded geometry was adopted using a 450 nm As_2S_3 layer atop a 650 nm erbium ion doped Ge-Ga-Se layer. After deposition, this bilayer film was subjected to thermal post-treatment at 130 °C for 24 hours under vacuum to bring the As_2S_3 film back closer to its bulk state. Thickness and refractive index of this two layer-film were then measured using a spectroscopic reflectometer (SCI FilmTek 4000) using a Tauc-Lorentz model. The first 650 nm erbium ion doped Ge-Ga-Se layer had a refractive index of 2.43 at wavelength of 1550 nm, while the 450 nm As_2S_3 layer had a refractive index of 2.41 at 1550 nm after thermal treatment. This minor difference in refractive index made it possible to design and fabricate ridge waveguide.

The obtained erbium ion doped Ge-Ga-Se film was carefully inspected under an optical microscope using an x100 objective in dark field mode. A significant reduction in particle density was observed, indicating the baffled furnace effectively stopped the gallium spiting that was previously problematic in Section 6.2.2.

The composition of the Ge-Ga-Se layer was determined as $Ge_{2.6}Ga_{27.7}Se_{69.7}$ (at%) by EDS. This was a considerable difference to the film obtained previously and the desired composition ($Ge_{25}Ga_{11}Se_{64}$ at%). It was not possible to tune back to the desired composition as the Ge furnace was operating close to its temperature limit and so the Ge flux could not be increased, and slowing the rate of the other evaporants was not possible as the Er rate became unstable at the low values required for the desired doping after reducing the rates of the other furnaces. Due to the limited compositional resolution of EDS, the low erbium ion concentration could not be read accurately from the EDS results directly. However, comparing the optical erbium ion absorption band in the final waveguides with an erbium ion doped films with a similar host, the erbium ion concentration in this film was estimated at 0.5 at% (~1.5×10^{20} ion/cm^3).

The all-fibre confocal set-up as described previously (see Section 3.3.2) was employed to measure the PL intensity and the lifetime of the $^4I_{13/2}$ excited state with laser excitation at 1490 nm. An intrinsic lifetime of 0.99 ms was obtained from this film under an excitation intensity of 350 kW/cm^2. The dependence of lifetime and PL intensity versus pump power had also been investigated for this film with excitation at 1490 nm, and the results are shown in Figure 6.15. Intrinsic lifetime remained at 0.99

ms showing no dependence with pump intensity ranging from 15 kW/cm^2 to 1100 kW/cm^2 as expected. The 1/e lifetime dropped from 0.88 ms at 15 kW/cm^2 to 0.80 ms at 1100 kW/cm^2 pump intensity, indicating interactions between pump photons and excited ions or ion-ion effects, but the 1/e lifetime even at low pump powers, is only slightly less than the intrinsic lifetime. Whilst a difference between the 1/e and intrinsic lifetimes was observed in bulk glasses at this concentration, in the film sample the difference was greater than the bulk glass. This likely indicates that either other parasitic effects are occurring or that the erbium ions are not homogeneously distributed in the film. Nevertheless, the lifetime was sufficient to build a reasonable amplifier. The approximately quadratic trend of PL intensity versus pump intensity shown in Figure 6.15(b), also implies either or both of the occurrence of energy exchange effects and/or the PL intensity saturation under high pumping intensity.

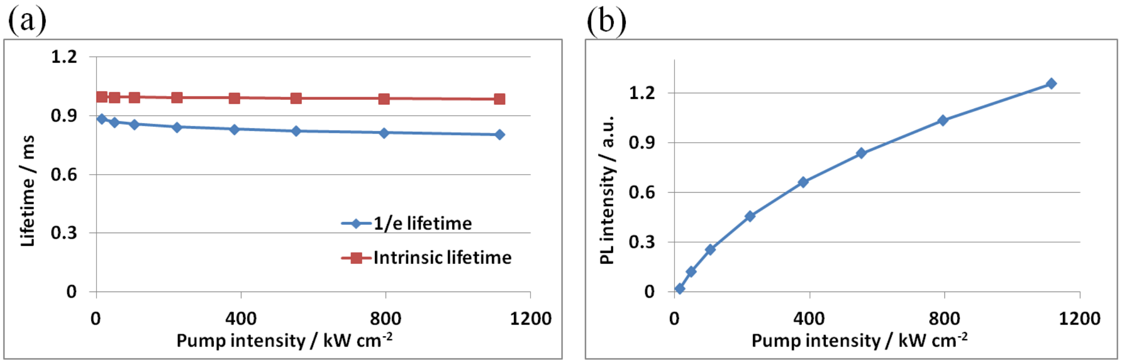

Figure 6.15 1/e and intrinsic lifetime of the $^4I_{13/2}$ state of Er^{3+} (a); PL intensity (b) versus pump intensity at 1490 nm of a Er^{3+}:Ge-Ga-Se film.

A longer intrinsic lifetime of 1.34 ms could be achieved by thermally post-treating Er^{3+} doped Ge-Ga-Se films at 280 °C for 24 hours, indicating the erbium ion was going into solution better as expected from the solubility of erbium ion in Ga-containing hosts [119, 198]. The T_g of the obtained film could not be directly measured, but from the literature, glasses with similar composition ($Ge_5Ga_{20}Se_{75}$ (at%)) had a T_g of 270 °C [322], and T_g increased with increasing Ga content due to rise in mean bond energy of the system. Thus, it was expected that film used in this experiment had a T_g higher than 270 °C. The large T_g difference between the layers (As_2S_3 layer had T_g of 180 °C), limited annealing to only 130 °C to protect the As_2S_3 layer and consequently potentially lowered Er^{3+} performance in the waveguides [133].

6.3.2 Erbium ion doped Ge-Ga-Se waveguides characterization

The ridge waveguides were structured using contact lithography with AZ MIR 701 positive Photoresist and Reactive Ion Etching (RIE) with CHF_3 gas [13]. 400 nm of the 450 nm As_2S_3 was etched away without touching the erbium ion doped layer to provide a smooth top surface. The cross-section of the designed structure for a 2 µm waveguide is shown in Figure 6.16. With this structure, the overlaps for both the TE and the TM fundamental modes and the Er^{3+} doped area were around 70%, thereby promising effective use of both the pump energy and the excited erbium ions.

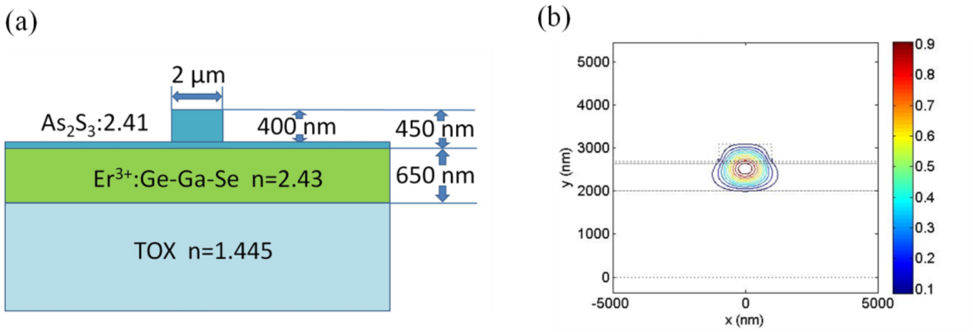

Figure 6.16 Details of the designed structure (a), and the simulated TE fundamental mode for the 2 µm wide Er^{3+}:Ga-Ge-Se waveguide (b).

Cut-back measurements were performed in the TE mode at 1650 nm which was away from the erbium ion absorption band to ensure the accuracy of the propagation loss. The results of four waveguides from the same set with 2 µm width are shown in Figure 6.17. The waveguide was originally 63 mm long and was then cleaved into a 22 mm section and a 41 mm section. The minimum loss among the 2 µm waveguides is 1.67 dB/cm, while the average number for these four waveguides is 1.97 dB/cm with a standard deviation of 0.23 dB/cm. Two loss data points from 22 mm long waveguides are absent in the figure, due to a bad cleaved edge that could be clearly seen under microscope. It is worth noting that this propagation loss value is much higher than the typical 0.35 dB/cm from As_2S_3 waveguides (in Section 4.5.1) with similar dimensions [133].

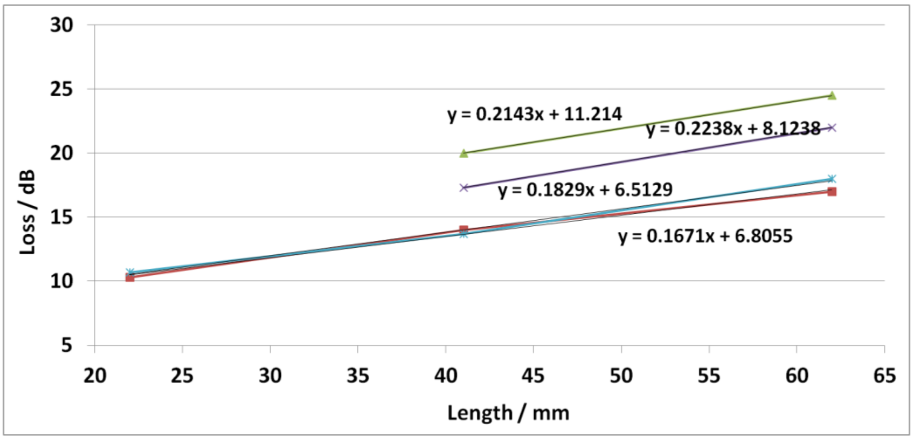

Figure 6.17 Cut-back method for the loss measurement of 2 µm wide Er^{3+}:Ge-Ga-Se waveguides in the TE mode at 1650 nm.

The wavelength dependence of the propagation loss in a 2 µm wide Er^{3+}:Ge-Ga-Se waveguide was measured using a supercontinuum source and optical spectrum analyser and is shown in Figure 6.18. As stated in Section 4.5.1, propagation loss following a $1/\lambda^2$ dependence is expected for sidewall scattering (λ is the wavelength), whilst a $1/\lambda^4$ dependence is indicative of scattering off nanoscale inhomogeneities as Rayleigh scattering. Good propagation loss fitting was obtained for the measured waveguides with the $1/\lambda^2$ formula, indicating the sidewall roughness in the film was the main contributor to propagation loss. The sidewall scattering component was higher than "normal" for one clear reason and one likely option. This waveguide had an air top cladding, resulting in larger scattering losses from the larger refractive index difference compared the polysiloxane clad (n=1.535 at 1550 nm) all As_2S_3 devices. Sidewall scattering is often approximated as scaling with the square of the core-clad index difference [323], which would implied a sidewall roughness loss of ~0.8 dB/cm might be expected in this device if the etch quality was up to the standards of the all As_2S_3 waveguides and scaling from the 0.3 dB/cm figure there.

Nanoscale phase separation is one process that is known to occur in chalcogenide glasses [250] that can produce the nanoscale inhomogeneities that manifest as Rayleigh scattering. Erbium ion clustering or the growth of different structures around the erbium ion itself can also produce similar effects as was observed in the case of previous work on Er^{3+}:As_2S_3 film (see Section 4.5.1). In waveguides measured in this work, the Rayleigh scattering component is so small that is almost absent from our fitting results shown in Figure 6.18, indicating there are far less film growth issues. Also as will be shown shortly, based upon the pumping results obtained from this waveguide, little of the erbium ions are clustered in this film and this is consistent with the result of the above analysis that scattering caused by doped erbium ion is unlikely in this waveguide. Therefore it appears that the etching in this device is not as good, and in fact given the square dependence on roughness and the acute sensitivity to the correlation length in this region of operation [324], then only a small change is required to degrade the loss to the levels observed.

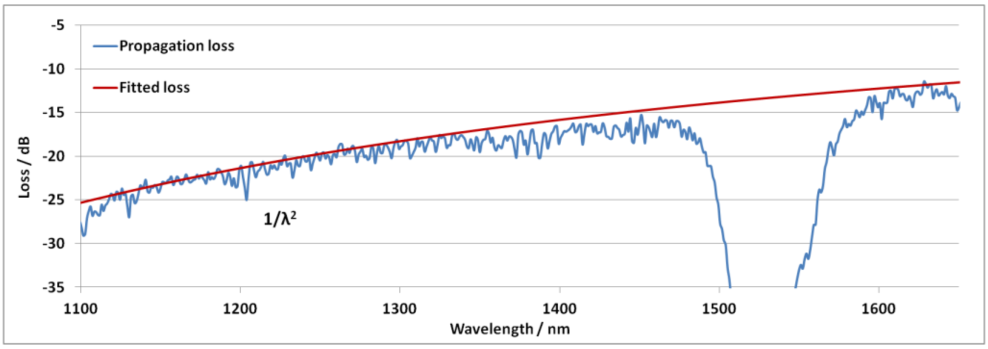

Figure 6.18 Measured optical propagation loss spectrum of a 2 µm wide Er^{3+}:Ge-Ga-Se waveguide with $1/\lambda^2$ fitted data.

6.4 Optical enhancement and photoinduced absorption of erbium ion doped Ge-Ga-Se waveguides

Excitation experiments were performed on an Er^{3+}:Ge-Ga-Se waveguide. Given the low Er^{3+} absorption at 1490 nm evident in Figure 6.18, a diode laser operating at 1505 nm was employed as an excitation source. The scheme of the optical set-up for this experiment is similar to the one shown in Figure 4.20. A heavily attenuated supercontinuum source (<-30 dBm to avoid exciting the erbium ions) with range from 600-2000 nm was used as the signal source. The pump source and signal were combined together through a 90/10 coupler (pump on 90% port) and then delivered to a 26 mm long Er^{3+}:Ge-Ga-Se waveguide via a lensed fibre with a 2.5 µm $1/e^2$ diameter. The emerging light was collected by another lensed fibre and then recorded on an optical spectrum analyser (Ando AQ 6317). The resulting optical enhancement curve and its dependence on excitation power are shown in Figure 6.19 as a function of pump power.

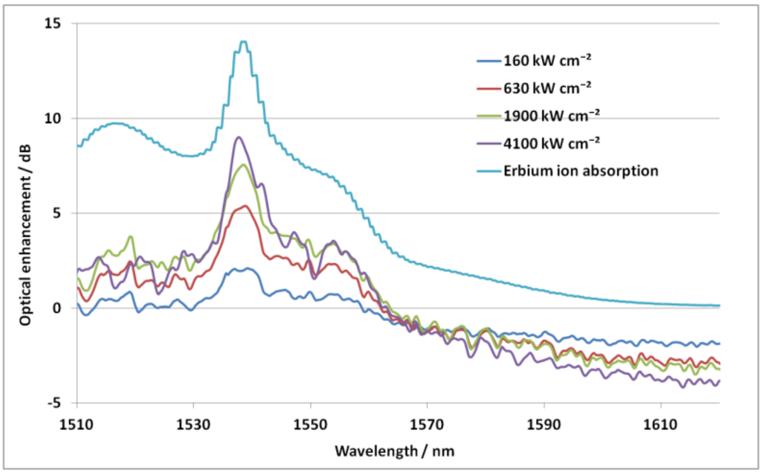

Figure 6.19 Erbium ion absorption curve and optical enhancement spectra of an Er^{3+}:Ge-Ga-Se waveguide under different excitation intensity at 1505 nm.

From the optical enhancement curve in Figure 6.19, about 9 dB enhancement is achieved with the available maximum 130 mW pump power at the input of the lensed fibre (and ~50 mW launched into the waveguide). However, it is clear from looking at the data at 1620 nm, where no enhancement would be expected, that the whole level of the curve drops by up to 4 dB at maximum pump power. Increased loss is also seen across the whole transmission spectrum of the device and so does not just represent excited state absorption on the long wavelength side of the erbium ion absorption. This loss was completely and relatively rapidly reversible (~1 minute) by turning off the pump, and was also verified to be associated with the erbium ion as injecting high power at 1430 nm (where the erbium ion absorption was negligible) had no effect.

The correlation with pumping the erbium ion strongly suggested an effect connected with upconversion to shorter wavelengths, especially as such processes will be enhanced in chalcogenide glasses compared to oxide hosts due to the much longer upper state lifetimes resulting from much lower multiphonon recombination rates [117]. Illumination with light at and above the band gap has previously been established to result in photoinduced wideband absorption in some materials [325]. Whilst most of the previous study was on As_2S_3 and As-S-Se based fibre and showed relatively weak absorption at 1550 nm (<0.2 dB/m at 10 mW/cm^2 of transverse bandgap light [325]), effects were also noted in Ge-As-Se glasses but little data presented. With this in mind, 1550 nm light was propagated through waveguides made from un-doped $Ge_3Ga_{28}Se_{69}$, As_2S_3, $Ge_{33}As_{12}Se_{55}$ (AMTIR-1, unannealed) and $Ge_{11.5}As_{23.5}Se_{65}$ (unannealed) whilst exposing them to ~10 mW/cm^2 red and green LED based light from above. The As_2S_3

waveguide exhibited a change of <0.01 dB/cm propagation loss, whereas all the Ge containing waveguides showed much stronger effects. The effect was most dramatic in the $Ge_{33}As_{12}Se_{55}$ waveguide which exhibited an increase in propagation losses approaching 10 dB/cm, compared to ~0.5 dB/cm in the $Ge_{11.5}As_{23.5}Se_{65}$ and ~1 dB/cm in the $Ge_3Ga_{28}Se_{69}$ for red illumination and ~2 dB/cm for green. The bandgap of this erbium ion doped Ge-Ga-Se film is about 1.75 eV (708 nm) based upon the results from FilmTek measurements. The photo-induced loss change in a 28 mm long Ge-Ga-Se waveguide with green light was recorded and is displayed in Figure 6.20. At point A, the green light LED (~550 nm) with ~10 mW/cm^2 intensity was turned on, and at point B, the LED was turned off. The time response of the photoinduced absorption in the materials was best fitted with a triple exponential decay. For the Ge-As-Se glasses, recovery was completed within 2 seconds, whereas in the Ge-Ga-Se glass complete recovery required ~90 s with fitted exponential time constants of ~0.1 s, ~1.5 s, and ~30 s. In all cases the presence of a fast decay component indicating a free carrier component was checked for, but no response faster than ~50 ms could be found even when looking with a 1MHz bandwidth detection system. The much increased decay time may indicate a higher density of defect states in the sub bandgap region where the carriers move between them as a result of thermalisation thereby surviving longer.

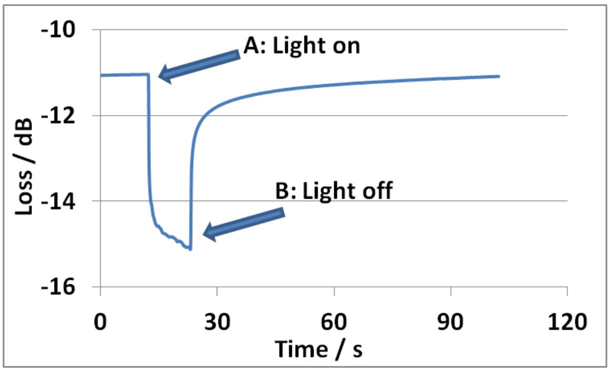

Figure 6.20 Photo-induced loss (at 1550 nm) change with time in a 28 mm length Ge-Ga-Se waveguide. At point A the green light was turned on, and at point B the green light was turned off.

Up-conversion related emissions at 980 nm, 800 nm, 670 nm, 540 nm and 520 nm, associated with radiative decay from the $^4I_{9/2}$, $^4F_{9/2}$, $^4S_{3/2}$ and $^2H_{11/2}$ states, respectively, to the ground state, are all located in the bandgap or Urbach tail of this Ge-Ga-Se host material. Due to the small mode area (~2 μm^2) of the waveguides, the intensity of up-conversion related emissions in the waveguides could certainly be high enough to induce photoinduced absorption, and this coupled with the insensitivity to high power 1430 nm light suggested strongly this is the cause of the increased loss. In addition, Er^{3+} excited to states with energy equal to or higher than the bandgap energy of the glass matrix may directly transfer energy to the electronic states of the glass matrix [147, 148]. This may also be a contributor for the observed photoinduced loss.

To obtain an accurate erbium ion population inversion ratio, the effects of photoinduced loss should be eliminated from the calculation of enhancement. Andriesh [326] found an exponential fit to the photoinduced absorption in the above bandgap and Urbach tail region, but the dependence then became non-exponential beyond ~1100 nm. Given that the data being used was in the >1100 nm region and that a different material was being considered, a phenomenological approach was adopted. The photoinduced losses were extracted from the wideband difference between the zero-excitation and 130 mW-excitation curves and empirically found to be well fitted by the formula: loss=$k/(\lambda^4+b)$, where k and b are fitting coefficients and λ is the wavelength. At this stage no interpretation could be placed on this dependence. Figure 6.21 illustrates the excellent fit afforded by this relationship.

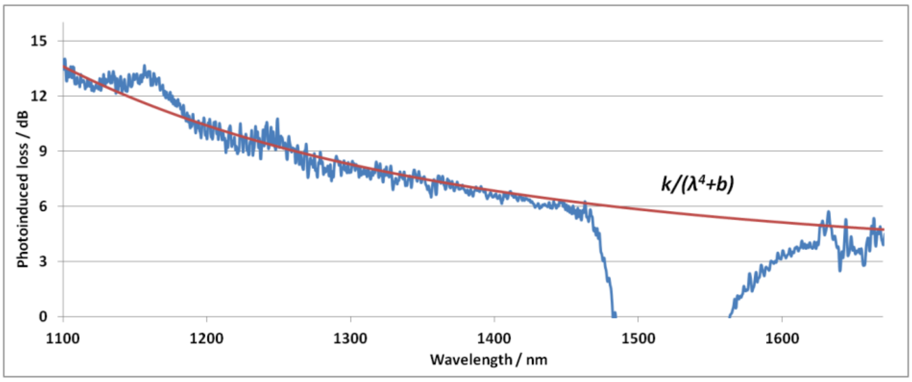

Figure 6.21 Loss increment curve of an Er^{3+}:Ge-Ga-Se waveguide due to photoinduced absorption effect and the fitted curve.

With the fitted photoinduced loss curve in Figure 6.21, the real signal enhancement curve under 4100 kW/cm^2 pumping was obtained and is shown in Figure 6.22(a) as the solid line. Optical enhancements corresponding to different population inversion ratios from 10% up to 65% were calculated and is also shown in Figure 6.22(a) as dashed lines. From these curves, the experimental enhancement curve fits with the calculated line having 50% population inversion. This is far higher than obtained in the best previous measurement and would produce internal gain (see in Section 4.5.3) across most of the spectrum, as shown in Figure 6.22(b). The sharp peak and big power fluctuation around 1505 nm in Figure 6.22(b) is the residual pump power centred at 1505 nm. The maximum inversion versus wavelength curve is plotted in Figure 6.23(a), which was calculated according to the method described in Section 2.2.2. The maximum possible inversion calculated for 1505 nm pumping is 65%. To attain reasonable gain requires an inversion of 60-65% as is evident from Figure 6.22(a) where more than another 4 dB of enhancement is available at the peak, and of course more actual gain with higher doping.

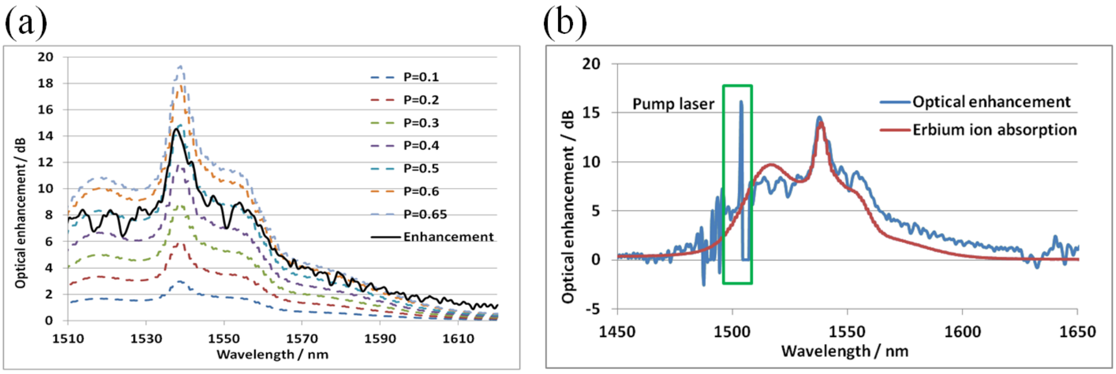

Figure 6.22 Calculated optical enhancement as a function of the population inversion and experimental optical enhancement (a); experimental optical enhancement and the erbium ion absorption (b) of a 26 mm Er^{3+}:Ge-Ga-Se waveguide.

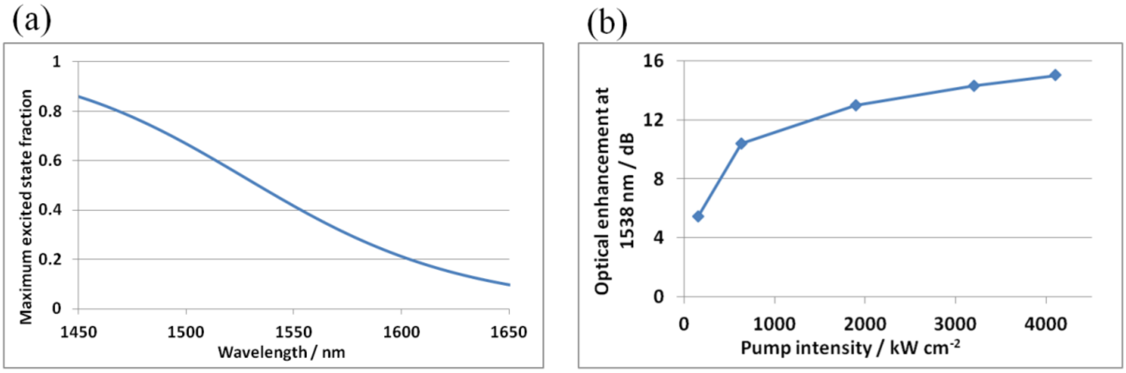

Figure 6.23 Calculated maximum pump efficiency versus pump wavelength (a); measured peak enhancement at 1538 nm as a function of pump power (measured at fibre connector) (b) of a 26 mm Er^{3+}:Ge-Ga-Se waveguide.

Peak enhancement at 1538 nm was extracted from each measured enhancement curve in Figure 6.19 and its dependence on pump power is plotted in Figure 6.23 (b). It is clear that the saturation region has almost been reached and further increases in the enhancement will be small (~1 dB) corresponding to a further small increase in the inversion to perhaps 55%. Note that with overlap loss and reflection the expected power coupled into the waveguide was ~50 mW and so it was not pumped especially strongly but no further pump power was available to push it to saturation. This is, to the Author's knowledge, the first time population inversion at these levels in erbium ion has been attained in a chalcogenide glass host waveguide, and indicates that sufficient population inversion for high gain amplification can be achieved with erbium ions. The saturation at levels below the theoretical maximum indicates that a small proportion of erbium ions are still clustered, in energy contact, or are optically inactive in this host material as grown, consistent with the low power lifetime shortening compared to the intrinsic lifetime noted in Section 6.3.1. Further improvement in both deposition and/or more effective thermal post-treatment is required to match the theoretical performance. This, however, requires a change of the waveguide design to use a higher T_g strip glass, or the use of waveguide fabrication methods such as lift off [274] or hot embossing [280, 327]. A practical device also requires much lower passive waveguide losses (should be achievable with improved processing and film growth with appropriate compositions) and also the resolution of the photoinduced losses. It remains to be seen whether the photoinduced loss also occurs in films with the desired composition of gallium doped germanium selenide, or whether a different composition with a higher bandgap will be more advantageous.

6.5 Conclusion

In this chapter, high quality erbium ion doped Ge-Ga-Se films were deposited and ridge waveguides based on these films were patterned. Significant signal enhancement at 1.5 µm was observed and 50% erbium ion population inversion was obtained, with a saturation maximum of ~55% being possible, in waveguides with 1.5×10^{20} Er^{3+} ion/cm^3. This is the highest level of inversion ever demonstrated for erbium ions in a chalcogenide glass host waveguide and is an important step towards future devices operating at 1550 nm and on the MIR transitions in erbium ion. Photoinduced absorption loss caused by upconversion products in the waveguides was the remaining hurdle to achieving net gain. Further research is needed to find suitable compositions that possess high rare-earth ion solubility whilst avoiding the detrimental photoinduced losses.

Chapter 7

Conclusions and recommendations

7.1 Conclusions

This work focused on the fundamentals of fabrication and characterisation of erbium ion doped chalcogenide glass planar waveguide amplifiers. There have been a number of important achievements that advance the field. Erbium ion doped chalcogenide films were deposited using co-thermal evaporation and RF sputtering based on As_2S_3 and Ge-Ga-Se host materials. Waveguides were patterned with standard photolithography and reactive ion plasma etching. In erbium ion doped As_2S_3 waveguides made using co-thermal evaporation, internal gain from 1570 to 1630 nm was observed for the first time in a chalcogenide glass host. Erbium ion doped As_2S_3 films deposited through RF sputtering showed even more promising results in terms of PL lifetime and PL intensity of Er^{3+}. Significant signal enhancement at 1.5 µm was observed and 50% erbium ion population inversion was obtained in an erbium ion doped Ge-Ga-Se waveguides fabricated using co-thermal evaporated film. To the Author's knowledge this is the highest level of inversion ever demonstrated for erbium ions in a chalcogenide host and is an important step towards future devices operating at 1.5 µm and on the MIR transitions in erbium ion in chalcogenide planar devices.

This work had extensively investigated the fabrication methods for high quality erbium ion doped chalcogenide thin films. Co-thermal evaporation was employed in erbium ion doped As_2S_3 deposition for its precise control of each element's evaporation rate and thus the final film composition. Both physical and optical properties of obtained film were investigated carefully. Films with erbium ion concentration from 0.15 at% (0.45×10^{20} ions/cm^3) to 0.6 at% (1.8×10^{20} ions/cm^3) were deposited and studied to optimise the erbium ion concentration. Film doped with 0.15 at% Er^{3+} was shown to have the best performance in terms of the $^4I_{13/2}$ state lifetime and 1.5 µm PL efficiency. However, results from high temperature thermal post-treatment showed the solubility of erbium ion in As_2S_3 film is even lower than 0.15 at%. Likewise it was shown that the clustering of erbium ion in the films resulted from polyatomic evaporation, a difficult matter to resolve using liquid metal sources whilst still making highly doped films in an acceptable time frame. With the low loss waveguide (~0.35

dB/cm) patterned on 0.15 at% Er^{3+} doped As_2S_3 film, internal gain was observed from 1570 to 1630 nm for the first time.

Different approaches to fabricate erbium ion doped As_2S_3 films were investigated. Promising results on intrinsic lifetime were achieved in $ErCl_3$ doped As_2S_3 (2.6 ms), however no waveguide was fabricated on these films due to poor film quality. Films fabricated using RF sputtering showed promising lifetime (2 ms after thermal post-treatment) and strong PL intensity (stronger than the PL intensity from the previous co-thermal Er^{3+}:As_2S_3 film with internal gain at similar erbium ion concentration), but its emission performance was sensitive to green light and moisture. Due to the existence of green light from up-conversion in erbium ion doped waveguide when high pumping intensity was applied, the PL performance of this sputtered film was unstable and decayed to a level that is not suitable for an amplification device.

Host chalcogenide material other than As_2S_3, Ge-Ga-Se glass, was also investigated for its high rare-earth ion solubility property. Emission properties of Er^{3+} doped Ge-Ga-Se bulk glasses were studied as a function of erbium ion doping concentration from 0.1 at% up to 2 at%. A clear concentration quenching effect in the Ge-Ga-Se glasses was observed for the first time even when sufficient gallium was present to ensure homogeneous distribution of the erbium ions. A region between approximately 0.5 and 0.8 at% of Er^{3+}, however, was shown to provide sufficient doping, good photoluminescence and adequate lifetime to envisage practical planar waveguide amplifier devices. Micron-size particles in erbium ion doped Ge-Ga-Se caused by spitting of the gallium was observed and eliminated using a modification to the deposition equipment. High quality erbium ion doped Ge-Ga-Se films were achieved and ridge waveguides based on these films were patterned. Significant signal enhancement at 1.5 µm was observed and ~50% Er^{3+} population inversion was obtained, with a saturation maximum of ~55% being possible in waveguides with 1.5×10^{20} Er^{3+} ion/cm^3. To the Author's knowledge this is the highest level of population inversion ever demonstrated for erbium ion in a chalcogenide glass host. However, photoinduced absorption loss caused by upconversion products in the waveguides showed up and remained a hurdle to achieving net gain.

7.2 Recommendations for future work

Despite achieving internal gain in erbium ion doped As_2S_3 by co-thermal evaporation, and more than 50% population inversion in erbium ion doped Ge-Ga-Se host, so far no practical planar waveguide amplifier was realised. On the positive side, according to the results obtained, it is reasonable to conclude that there is no intrinsic barrier in making rare-earth ion doped chalcogenide waveguide amplifiers. The problem to be resolved is in attaining unclustered erbium ion doping and moisture immunity.

Likely the best way forward for evaporated As_2S_3 is to move to Er_2S_3 as the dopant, which requires some modification to the evaporation system so that the Er_2S_3 can be evaporated from a tungsten or molybdenum boat without heating the film during deposition. This should then conceptually prevent the erbium ion clustering during the deposition, and if the thermal post-treatment is restricted, allow for high concentrations to be introduced into the films and for net gain to be achieved.

Since the RF sputtered film had almost the best optical performance, excepting the PL decay, therefore it is worth looking for a way to overcome this issue. Columnar structure in films due to the growth habit of RF sputtering and was reported in different host materials. Optimising the film deposition parameters such RF power and gas pressure might be a possible way to eliminate columnar structure. A successful example was reported in [2] in TeO_2 films (though with reactive sputtering) where net gain optical amplification was achieved. However, the As_2S_3 target is quite fragile, thus cracking may occur when the RF power is high, which leads to a poor film quality. Considering this, little space is left for increasing the RF power, but control of the gas pressure may be a viable alternative and should be investigated. A moisture barrier could also be employed, though work is required to establish exactly how to totally prevent moisture penetration.

More than 50% population inversion was achieved in an erbium ion doped Ge-Ga-Se waveguide, but strong photo-induced loss prevented internal gain being observed. It was also noticed that with different glass compositions, the amplitude of photo-induced loss varies considerably. For example, $Ge_{33}As_{12}Se_{55}$ (AMTIR-1) had a much bigger photo-induced loss than the Ge-Ga-Se glass used here, and $Ge_{11}As_{24}Se_{65}$ (at%) had a smaller one under the same condition. Therefore, it is reasonable to ask if there is a possible composition in Ge-Ga-Se family that has good rare-earth ion solubility but without significant photo-induced loss. In this case, materials research into Ge-Ga-Se to find a better composition that has a better photo-induced loss resistance is necessary. On the other hand, the photo-induced loss reported in Chapter 6 was thought bandgap related, and the up-conversion emissions from erbium ion had a huge overlap with Ge-Ga-Se's bandgap which brought the issue confronted here. Thus, rare-earth ions without any strong visible emissions and up-conversion related emissions in Ge-Ga-Se's bandgap wavelength may work fine with this host.

Also, the glasses this thesis focused on are only two members of the big chalcogenide glass family. Other materials such as Ge-Ga-S, Ga-As-S, Ga-La-S etc., may offer better opportunity than these two, in this perspective, a comprehensive study of chalcogenide materials is necessary.

References

1. S. E. Miller, "Integrated Optics - an Introduction," At&T Tech J **48**, 2059-2069 (1969).
2. K. T. Vu, "Fabrication and characterisation of nonlinear tellurite planar waveguides," Doctoral dissertation, The Australian National University, Australia (2011).
3. R. Nagarajan, M. Kato, J. Pleumeekers, P. Evans, S. Corzine, S. Hurtt, A. Dentai, S. Murthy, M. Missey, R. Muthiah, R. A. Salvatore, C. Joyner, R. Schneider, M. Ziari, F. Kish, and D. Welch, "InP Photonic Integrated Circuits," IEEE J Sel Top Quant **16**, 1113-1125 (2010).
4. B. J. Eggleton, B. Luther-Davies, and K. Richardson, "Chalcogenide photonics," Nat Photonics **5**, 141-148 (2011).
5. T. D. Vo, H. Hu, M. Galili, E. Palushani, J. Xu, L. K. Oxenlowe, S. J. Madden, D. Y. Choi, D. A. P. Bulla, M. D. Pelusi, J. Schroder, B. Luther-Davies, and B. J. Eggleton, "Photonic chip based transmitter optimization and receiver demultiplexing of a 1.28 Tbit/s OTDM signal," Opt Express **18**, 17252-17261 (2010).
6. A. Choudhary, B. Morrison, I. Aryanfar, S. Shahnia, M. Pagani, Y. Liu, K. Vu, S. Madden, D. Marpaung, and B. J. Eggleton, "Advanced integrated microwave signal processing with giant on-chip Brillouin gain," J Lightwave Technol **PP**, 1-1 (2016).
7. M. Pelusi, F. Luan, T. D. Vo, M. R. E. Lamont, S. J. Madden, D. A. Bulla, D. Y. Choi, B. Luther-Davies, and B. J. Eggleton, "Photonic-chip-based radio-frequency spectrum analyser with terahertz bandwidth," Nat Photonics **3**, 139-143 (2009).
8. J. Schroder, F. Wang, A. Clarke, E. Ryckeboer, M. Pelusi, M. A. F. Roelens, and B. J. Eggleton, "Aberration-free ultra-fast optical oscilloscope using a four-wave mixing based time-lens," Opt Commun **283**, 2611-2614 (2010).
9. M. D. Pelusi, V. G. Ta'eed, L. B. Fu, E. Magi, M. R. E. Lamont, S. Madden, D. Y. Choi, D. A. P. Bulla, B. Luther-Davies, and B. J. Eggleton, "Applications of highly-nonlinear chalcogenide glass devices tailored for high-speed all-optical signal processing," IEEE J Sel Top Quant **14**, 529-539 (2008).
10. X. Gai, Y. Yu, B. Kuyken, P. Ma, S. J. Madden, J. Van Campenhout, P. Verheyen, G. Roelkens, R. Baets, and B. Luther-Davies, "Nonlinear absorption and refraction in crystalline silicon in the mid-infrared," Laser Photonics Rev **7**, 1054-1064 (2013).
11. X. Gai, S. Madden, D. Y. Choi, D. Bulla, and B. Luther-Davies, "Dispersion engineered $Ge_{11.5}As_{24}Se_{64.5}$ nanowires with a nonlinear parameter of $136W^{-1}m^{-1}$ at 1550nm," Opt Express **18**, 18866-18874 (2010).
12. Y. L. Ruan, W. T. Li, R. Jarvis, N. Madsen, A. Rode, and B. Luther-Davies, "Fabrication and characterization of low loss rib chalcogenide waveguides made by dry etching," Opt Express **12**, 5140-5145 (2004).
13. S. J. Madden, D. Y. Choi, D. A. Bulla, A. V. Rode, B. Luther-Davies, V. G. Ta'eed, M. D. Pelusi, and B. J. Eggleton, "Long, low loss etched As_2S_3 chalcogenide waveguides for all-optical signal regeneration," Opt Express **15**, 14414-14421 (2007).
14. J. Chiles, M. Malinowski, A. Rao, S. Novak, K. Richardson, and S. Fathpour, "Low-loss, submicron chalcogenide integrated photonics with chlorine plasma etching," Appl Phys Lett **106**(2015).
15. K. P. Yap, A. Delage, J. Lapointe, B. Lamontagne, J. H. Schmid, P. Waldron, B. A. Syrett, and S. Janz, "Correlation of Scattering Loss, Sidewall Roughness and Waveguide Width in Silicon-on-Insulator (SOI) Ridge Waveguides," J Lightwave Technol **27**, 3999-4008 (2009).
16. K. K. Lee, D. R. Lim, H. C. Luan, A. Agarwal, J. Foresi, and L. C. Kimerling, "Effect of size and roughness on light transmission in a Si/SiO_2 waveguide: Experiments and model," Appl Phys Lett **77**, 2258-2258 (2000).
17. S. Madden, Z. Jin, D. Choi, S. Debbarma, D. Bulla, and B. Luther-Davies, "Low loss coupling to sub-micron thick rib and nanowire waveguides by vertical tapering," Opt Express **21**, 3582-3594 (2013).
18. A. K. Mishra, X. Yang, D. Lenstra, G. D. Khoe, and H. J. S. Dorren, "Wavelength conversion employing 120-fs optical pulses in an SOA-based nonlinear polarization switch," IEEE J Sel Top Quant **10**, 1180-1186 (2004).
19. E. Tangdiongga, Y. Liu, H. de Waardt, G. D. Khoe, A. M. J. Koonen, H. J. S. Dorren, X. Shu, and I. Bennion, "All-optical demultiplexing of 640 to 40 Gbits/s using filtered chirp of a semiconductor optical amplifier," Opt Lett **32**, 835-837 (2007).
20. M. Matsuura, O. Raz, F. Gomez-Agis, N. Calabretta, and H. J. S. Dorren, "Error-free 320-to-40-Gbit/s optical demultiplexing based on blueshift filtering in a quantum-dot semiconductor optical amplifier," Opt Lett **38**, 238-240 (2013).
21. Y. Liu, E. Tangdiongga, Z. Li, H. de Waardt, A. M. J. Koonen, G. D. Khoe, X. W. Shu, I. Bennion, and H. J. S. Dorren, "Errior-free 320-Gb/s all-omtical wavelength conversion using a single semiconductor optical amplifier," J Lightwave Technol **25**, 103-108 (2007).
22. G. Contestabile, Y. Yoshida, A. Maruta, and K. I. Kitayama, "Coherent wavelength conversion in a quantum dot SOA," IEEE Photonic Tech L **25**, 791-794 (2013).
23. B. Filion, W. C. Ng, A. T. Nguyen, L. A. Rusch, and S. LaRochelle, "Wideband wavelength conversion of 16 Gbaud 16-QAM and 5 Gbaud 64-QAM signals in a semiconductor optical amplifier," Opt Express **21**, 19825-19833 (2013).
24. R. J. Mears, L. Reekie, I. M. Jauncey, and D. N. Payne, "Low-noise erbium-doped fiber amplifier operating at 1.54 μm," Electron Lett **23**, 1026-1028 (1987).

25. P. G. Kik and A. Polman, "Erbium doped optical-waveguide amplifiers on silicon," Mrs Bull **23**, 48-54 (1998).
26. J. D. B. Bradley and M. Pollnau, "Erbium-doped integrated waveguide amplifiers and lasers," Laser Photonics Rev **5**, 368-403 (2011).
27. T. Kitagawa, K. Hattori, M. Shimizu, Y. Ohmori, and M. Kobayashi, "Guided-wave laser based on erbium-doped silica planar lightwave circuit," Electron Lett **27**, 334-335 (1991).
28. R. Brinkmann, W. Sohler, and H. Suche, "Continuous-wave erbium-diffused $LiNbO_3$ wave-guide laser," Electron Lett **27**, 415-417 (1991).
29. G. N. vandenHoven, R. J. I. M. Koper, A. Polman, C. vanDam, J. W. M. vanUffelen, and M. K. Smit, "Net optical gain at 1.53 μm in Er-doped Al_2O_3 waveguides on silicon," Appl Phys Lett **68**, 1886-1888 (1996).
30. C. R. Petersen, U. Moller, I. Kubat, B. B. Zhou, S. Dupont, J. Ramsay, T. Benson, S. Sujecki, N. Abdel-Moneim, Z. Q. Tang, D. Furniss, A. Seddon, and O. Bang, "Mid-infrared supercontinuum covering the 1.4-13.3 μm molecular fingerprint region using ultra-high NA chalcogenide step-index fibre," Nat Photonics **8**, 830-834 (2014).
31. Y. Yu, X. Gai, T. Wang, P. Ma, R. P. Wang, Z. Y. Yang, D. Y. Choi, S. Madden, and B. Luther-Davies, "Mid-infrared supercontinuum generation in chalcogenides," Opt Mater Express **3**, 1075-1086 (2013).
32. Y. Yu, X. Gai, P. Ma, D. Y. Choi, Z. Y. Yang, R. P. Wang, S. Debbarma, S. J. Madden, and B. Luther-Davies, "A broadband, quasi-continuous, mid-infrared supercontinuum generated in a chalcogenide glass waveguide," Laser Photonics Rev **8**, 792-798 (2014).
33. Y. Yu, B. Zhang, X. Gai, C. C. Zhai, S. S. Qi, W. Guo, Z. Y. Yang, R. P. Wang, D. Y. Choi, S. Madden, and B. Luther-Davies, "1.8-10 μm mid-infrared supercontinuum generated in a step-index chalcogenide fiber using low peak pump power," Opt Lett **40**, 1081-1084 (2015).
34. Y. Yu, X. Gai, P. Ma, K. Vu, Z. Y. Yang, R. P. Wang, D. Y. Choi, S. Madden, and B. Luther-Davies, "Experimental demonstration of linearly polarized 2-10 μm supercontinuum generation in a chalcogenide rib waveguide," Opt Lett **41**, 958-961 (2016).
35. S. D. Jackson, "Towards high-power mid-infrared emission from a fibre laser," Nat Photonics **6**, 423-431 (2012).
36. C. K. N. Patel, "High power infrared QCLs: advances and applications," SPIE 8268, Quantum Sensing and Nanophotonic Devices IX **8268**, 13 (2012).
37. Y. H. Shen, S. U. Alam, K. K. Chen, D. J. Lin, S. S. Cai, B. Wu, P. P. Jiang, A. Malinowski, and D. J. Richardson, "PPMgLN-based high-power optical parametric oscillator pumped by Yb^{3+}-doped fiber amplifier incorporates active pulse shaping," IEEE J Sel Top Quant **15**, 385-392 (2009).
38. IPG photonics, retrieved 30 June, 2017, http://www.ipgphotonics.com/laser/view/102/Lasers/Mid_IR_Hybrid_Lasers/.
39. A. B. Seddon, Z. Q. Tang, D. Furniss, S. Sujecki, and T. M. Benson, "Progress in rare-earth-doped mid-infrared fiber lasers," Opt Express **18**, 26704-26719 (2010).
40. J. S. Sanghera, L. B. Shaw, and I. D. Aggarwal, "Chalcogenide glass-fiber-based Mid-IR sources and applications," IEEE J Sel Top Quant **15**, 114-119 (2009).
41. J. S. Sanghera and I. D. Aggarwal, "Active and passive chalcogenide glass optical fibers for IR applications: a review," J Non-Cryst Solids **256**, 6-16 (1999).
42. R. Reisfeld and A. Bornstein, "Absorption and emission-spectra in chalcogenide glass of composition $0.7Ga_2S_3 \cdot 0.27La_2S_3 \cdot 0.03Nd_2S_3$," Chem Phys Lett **47**, 194-196 (1977).
43. A. Bornstein and R. Reisfeld, "Laser emission cross-section and threshold power for laser operation at 1077 nm and 1370 nm; chalcogenide mini-lasers doped by Nd^{3+}," J Non-Cryst Solids **50**, 23-27 (1982).
44. R. Reisfeld and A. Bornstein, "Fluorescence of Er^{3+} doped $La_2S_3 \cdot 3Ga_2S_3$ glasses," J Non-Cryst Solids **27**, 143-145 (1978).
45. R. Reisfeld, "Chalcogenide glasses doped by rare-earths-structure and optical-properties," Ann Chim-Sci Mat **7**, 147-160 (1982).
46. C. C. Ye, D. W. Hewak, M. Hempstead, B. N. Samson, and D. N. Payne, "Spectral properties of Er^{3+}-doped gallium lanthanum sulphide glass," J Non-Cryst Solids **208**, 56-63 (1996).
47. L. Brandon Shaw, D. Schaafsma, J. Moon, B. Harbison, J. Sanghera, I. E. D. K. D. V. G. C.-H. C. Aggarwal, and W. Knox, "Evaluation of the IR transitions in rare-earth-doped chalcogenide glasses," in *Conference on Lasers and Electro-Optics*, OSA Technical Digest (Optical Society of America, 1997), CWF48.
48. T. Schweizer, B. N. Samson, J. R. Hector, W. S. Brocklesby, D. W. Hewak, and D. N. Payne, "Infrared emission and ion-ion interactions in thulium- and terbium-doped gallium lanthanum sulfide glass," J Opt Soc Am B **16**, 308-316 (1999).
49. Y. B. Shin, W. Y. Cho, and J. Heo, "Multiphonon and cross relaxation phenomena in Ge-As(or Ga)-S glasses doped with Tm^{3+}," J Non-Cryst Solids **208**, 29-35 (1996).
50. A. Guhur and S. D. Jackson, "Efficient holmium-doped fluoride fiber laser emitting 2.1 μm and blue upconversion fluorescence upon excitation at 2 μm," Opt Express **18**, 20164-20169 (2010).
51. J. F. Li, H. Y. Luo, L. L. Wang, Y. Liu, Z. J. Yan, K. M. Zhou, L. Zhang, and S. K. Turistsyn, "Mid-infrared passively switched pulsed dual wavelength Ho^{3+}-doped fluoride fiber laser at 3 μm and 2 μm," Sci Rep-Uk **5**(2015).
52. Y. B. Shin, J. N. Jang, and J. Heo, "Mid-infrared light emission characteristics of Ho^{3+}-doped chalcogenide and heavy-metal oxide glasses," Opt Quant Electron **27**, 379-386 (1995).

53. L. B. Shaw, B. B. Harbison, B. Cole, J. S. Sanghera, and I. D. Aggarwal, "Spectroscopy of the IR transitions in Pr^{3+} doped heavy metal selenide glasses," Opt Express **1**, 87-96 (1997).
54. L. B. Shaw, B. Cole, P. A. Thielen, J. S. Sanghera, and I. D. Aggarwal, "Mid-wave IR and long-wave IR laser potential of rare-earth doped chalcogenide glass fiber," IEEE J Quantum Elect **37**, 1127-1137 (2001).
55. T. Schweizer, D. W. Hewak, B. N. Samson, and D. N. Payne, "Spectroscopy of potential mid-infrared laser transitions in gallium lanthanum sulphide glass," J Lumin **72-74**, 419-421 (1997).
56. H. M. Pask, R. J. Carman, D. C. Hanna, A. C. Tropper, C. J. Mackechnie, P. R. Barber, and J. M. Dawes, "Ytterbium-doped silica fiber lasers - versatile sources for the 1-1.2 μm Region," IEEE J Sel Top Quant **1**, 2-13 (1995).
57. O. Henderson-Sapir, S. D. Jackson, and D. J. Ottaway, "Versatile and widely tunable mid-infrared erbium doped ZBLAN fiber laser," Opt Lett **41**, 1676-1679 (2016).
58. J. Schneider, "Fluoride fibre laser operating at 3.9 μm," Electron Lett **31**, 1250-1251 (1995).
59. V. G. Ta'eed, N. J. Baker, L. B. Fu, K. Finsterbusch, M. R. E. Lamont, D. J. Moss, H. C. Nguyen, B. J. Eggleton, D. Y. Choi, S. Madden, and B. Luther-Davies, "Ultrafast all-optical chalcogenide glass photonic circuits," Opt Express **15**, 9205-9221 (2007).
60. J. A. Savage, "Optical-properties of chalcogenide glasses," J Non-Cryst Solids **47**, 101-116 (1982).
61. I. D. Aggarwal and J. S. Sanghera, "Development and applications of chalcogenide glass optical fibers at NRL," J Optoelectron Adv M **4**, 665-678 (2002).
62. D. Y. Choi, S. Madden, D. A. Bulla, R. Wang, A. Rode, and B. Luther-Davies, "Submicrometer-thick low-loss As_2S_3 planar waveguides for nonlinear optical devices," IEEE Photonic Tech L **22**, 495-497 (2010).
63. M. Galili, J. Xu, H. C. H. Mulvad, L. K. Oxenlowe, A. T. Clausen, P. Jeppesen, B. Luther-Davies, S. Madden, A. Rode, D. Y. Choi, M. Pelusi, F. Luan, and B. J. Eggleton, "Breakthrough switching speed with an all-optical chalcogenide glass chip: 640 Gbit/s demultiplexing," Opt Express **17**, 2182-2187 (2009).
64. K. Tan, D. Marpaung, R. Pant, F. Gao, E. B. Li, J. Wang, D. Y. Choi, S. Madden, B. Luther-Davies, J. Q. Sun, and B. J. Eggleton, "Photonic-chip-based all-optical ultra-wideband pulse generation via XPM and birefringence in a chalcogenide waveguide," Opt Express **21**, 2003-2011 (2013).
65. X. Gai, D. Y. Choi, S. Madden, and B. Luther-Davies, "Polarization-independent chalcogenide glass nanowires with anomalous dispersion for all-optical processing," Opt Express **20**, 13513-13521 (2012).
66. B. J. Eggleton, T. D. Vo, R. Pant, J. Schroder, M. D. Pelusi, D. Y. Choi, S. J. Madden, and B. Luther-Davies, "Photonic chip based ultrafast optical processing based on high nonlinearity dispersion engineered chalcogenide waveguides," Laser Photonics Rev **6**, 97-114 (2012).
67. J.S. Wang, E.M. Vogel, and E. Snitzer, "Tellurite glass: a new candidate for fiber devices," Optical Materials **3**, 17 (1994).
68. B. Gleason, K. Richardson, L. Sisken, and C. Smith, "Refractive index and thermo-optic coefficients of Ge-As-Se chalcogenide glasses," Int J Appl Glass Sci **7**, 374-383 (2016).
69. H. X. Li, J. Lousteau, W. N. MacPherson, X. Jiang, H. T. Bookey, J. S. Barton, A. Jha, and A. K. Kar, "Thermal sensitivity of tellurite and germanate optical fibers," Opt Express **15**, 8857-8863 (2007).
70. T. Toyoda and M. Yabe, "The temperature-dependence of the refractive-indexes of fused-silica and crystal quartz," J Phys D Appl Phys **16**, L97-L100 (1983).
71. M. Daimon and A. Masumura, "High-accuracy measurements of the refractive index and its temperature coefficient of calcium fluoride in a wide wavelength range from 138 to 2326 nm," Appl Optics **41**, 5275-5281 (2002).
72. ISO 20473:2007(E), "Optics and photonics-spectral bands," (2007).
73. L. M. Miller and P. Dumas, "Chemical imaging of biological tissue with synchrotron infrared light," Bba-Biomembranes **1758**, 846-857 (2006).
74. P. Honzatko, Y. Baravets, I. Kasik, and O. Podrazky, "Wideband thulium-holmium-doped fiber source with combined forward and backward amplified spontaneous emission at 1600-2300 nm spectral band," Opt Lett **39**, 3650-3653 (2014).
75. A. Halder, M. C. Paul, S. W. Harun, S. M. M. Ali, N. Saidin, S. S. A. Damanhuri, H. Ahmad, S. Das, M. Pal, and S. K. Bhadra, "1880-nm broadband ASE generation with bismuth-thulium codoped fiber," IEEE Photonics J **4**, 2176-2181 (2012).
76. L. B. Shaw, B. J. Cole, J. S. Sanghera, I. D. Aggarwal, F. H. Kung, S. S. Bayya, R. Mossadegh, P. A. Thielen, J. R. Kircher, and R. L. Murrer, "Development of IR-emitting infrared fibers at the Naval Research Laboratory," Proc. SPIE 4366, Technologies for Synthetic Environments: Hardware-in-the-Loop Testing, 6 (2001).
77. X. Wang, X. X. Jin, P. Zhou, X. L. Wang, H. Xiao, and Z. J. Liu, "High power, widely tunable, narrowband superfluorescent source at 2 μm based on a monolithic Tm-doped fiber amplifier," Opt Express **23**, 3382-3389 (2015).
78. S. Tokita, M. Murakami, S. Shimizu, M. Hashida, and S. Sakabe, "Liquid-cooled 24 W mid-infrared Er:ZBLAN fiber laser," Opt Lett **34**, 3062-3064 (2009).
79. M. A. Khalighi and M. Uysal, "Survey on free space optical communication: A communication theory perspective," IEEE Commun Surv Tut **16**, 2231-2258 (2014).
80. H. Henniger and O. Wilfert, "An introduction to free-space optical communications," Radioengineering **19**, 203-212 (2010).
81. Healthline, retrieved 30 June, 2017 ,http://www.healthline.com/health/laser-therapy#Overview1.

82. R. Kaufmann, A. Hartmann, and R. Hibst, "Cutting and skin-ablative properties of pulsed midinfrared laser-surgery," J Dermatol Surg Onc **20**, 112-118 (1994).
83. J. T. Walsh, T. J. Flotte, R. R. Anderson, and T. F. Deutsch, "Pulsed CO_2-laser tissue ablation-effect of tissue-type and pulse duration on thermal-damage," Laser Surg Med **8**, 108-118 (1988).
84. L. J. Mortensen, C. Alt, R. Turcotte, M. Masek, T. M. Liu, D. C. Cote, C. Xu, G. Intini, and C. P. Lin, "Femtosecond laser bone ablation with a high repetition rate fiber laser source," Biomed Opt Express **6**, 32-42 (2015).
85. Kayvan Shokrollahia, Elizabeth Raymondb, and M. S. C. Murisona, "Lasers: principles and surgical applications," The Journal of Surgery **2**, 7 (2004).
86. M. A. Mackanos, D. M. Simanovskii, K. E. Schriver, M. S. Hutson, C. H. Contag, J. A. Kozub, and E. D. Jansen, "Pulse-duration-dependent Mid-infrared laser ablation for biological applications," IEEE J Sel Top Quant **18**, 1514-1522 (2012).
87. C. Gonzalez, W. P. van de Merwe, M. Smith, and L. Reinisch, "Comparison of the erbium-yttrium aluminum garnet and carbon dioxide lasers for in vitro bone and cartilage ablation," Laryngoscope **100**, 14-17 (1990).
88. C. L. Canedy, W. W. Bewley, J. R. Lindle, J. A. Nolde, D. C. Larrabee, C. S. Kim, M. Kim, I. Vurgaftman, and J. R. Meyer, "Interband cascade lasers with wavelengths spanning 2.9 μm to 5.2 μm," J Electron Mater **37**, 1780-1785 (2008).
89. C. L. Canedy, J. R. Lindle, W. W. Bewley, C. S. Kim, M. Kim, J. A. Nolde, I. Vurgaftman, and J. R. Meyer, "Interband cascade lasers with wavelengths spanning 3.2-4.2 μm," J Electron Mater **38**, 1948-1951 (2009).
90. P. Q. Liu, A. J. Hoffman, M. D. Escarra, K. J. Franz, J. B. Khurgin, Y. Dikmelik, X. J. Wang, J. Y. Fan, and C. F. Gmachl, "Highly power-efficient quantum cascade lasers," Nat Photonics **4**, 95-98 (2010).
91. Wikipedia, retrieved 30 June, 2017, https://en.wikipedia.org/wiki/MIRACL.
92. Y. Kalisky and O. Kalisky, "The status of high-power lasers and their applications in the battlefield," Opt Eng **49**(2010).
93. L. Becker, "Influence of IR sensor technology on the military and civil defense" Quantum Sensing and Nanophotonic Devices III **6127**, S1270-S1270 (2006).
94. H. Kaushal and G. Kaddoum, "Applications of lasers for tactical military operations," IEEE Access **5**, 20736-20753 (2017).
95. C. Maccarley, B. M Hemme, and L. Klein, "Evaluation of infrared and millimeter-wave Imaging technologies applied to traffic management," SAE 2000 World Congress Technical Paper Series, Warrendale, Pa., (2000).
96. G. A. Kumar, R. E. Riman, L. A. D. Torres, O. B. Garcia, S. Banerjee, A. Kornienko, and J. G. Brennan, "Chalcogenide-bound erbium complexes: Paradigm molecules for infrared fluorescence emission," Chem Mater **17**, 5130-5135 (2005).
97. W. J. Miniscalco, "Erbium-doped glasses for fiber amplifiers at 1500 nm," J Lightwave Technol **9**, 234-250 (1991).
98. G. C. Righini, C. Arnaud, S. Berneschi, M. Bettinelli, M. Brenci, A. Chiasera, P. Feron, M. Ferrari, M. Montagna, G. N. Conti, S. Pelli, H. Portales, C. Siligardi, A. Speghini, and L. Zampedri, "Integrated optical amplifiers and microspherical lasers based on erbium-doped oxide glasses," Optical Materials **27**, 1711-1717 (2005).
99. A. Jha, S. X. Shen, L. H. Huang, B. Richards, and J. Lousteau, "Rare-earth doped glass waveguides for visible, near-IR and mid-IR lasers and amplifiers," J Mater Sci-Mater El **18**, S315-S320 (2007).
100. E. M. Yeatman, M. M. Ahmad, O. McCarthy, A. Vannucci, P. Gastaldo, D. Barbier, D. Mongardien, and C. Moronvalle, "Optical gain in Er-doped SiO_2-TiO_2 waveguides fabricated by the sol-gel technique," Opt Commun **164**, 19-25 (1999).
101. K. Maeda, T. Sakai, K. Sakai, T. Ikari, M. Munzar, D. Tonchev, S. O. Kasap, and G. Lucovsky, "Effect of Ga on the structure of Ge-Se-Ga glasses from thermal analysis, Raman and XPS measurements," J Mater Sci-Mater El **18**, S367-S370 (2007).
102. M. Munzar, C. Koughia, D. Tonchev, K. Maeda, T. Ikari, C. Haugen, R. Decorby, J. N. McMullin, and S. O. Kasap, "Optical properties of Er-doped $Ga_x(Ge_{0.3}Se_{0.7})_{(100-x)}$ glasses," Optical Materials **28**, 225-230 (2006).
103. J. S. Sanghera, L. B. Shaw, L. E. Busse, V. Q. Nguyen, P. C. Pureza, B. C. Cole, B. B. Harbison, I. D. Aggarwal, R. Mossadegh, F. Kung, D. Talley, D. Roselle, and R. Miklos, "Development and infrared applications of chalcogenide glass optical fibers," Fiber Integrated Opt **19**, 251-274 (2000).
104. Z. X. Li, T. F. Xu, X. A. Shen, S. X. Dai, X. S. Wang, Q. H. Nie, and X. H. Zhang, "Investigation of 2.9 μm luminescence properties and energy transfer in Tm^{3+}/Dy^{3+} co-doped chalcohalide glasses," J Rare Earth **29**, 105-108 (2011).
105. T. Schweizer, D. W. Hewak, D. N. Payne, T. Jensen, and G. Huber, "Rare-earth doped chalcogenide glass laser," Electron Lett **32**, 666-667 (1996).
106. T. Schweizer, B. N. Samson, R. C. Moore, D. W. Hewak, and D. N. Payne, "Rare-earth doped chalcogenide glass fibre laser," Electron Lett **33**, 414-416 (1997).
107. H. Tawarayama, E. Ishikawa, K. Yamanaka, K. Itoh, K. Okada, H. Aoki, H. Yanagita, Y. Matsuoka, and H. Toratani, "Optical amplification at 1.3 μm in a praseodymium-doped sulfide-glass fiber," J Am Ceram Soc **83**, 792-796 (2000).
108. A. K. Mairaj, C. Riziotis, A. M. Chardon, P. G. R. Smith, D. P. Shepherd, and D. W. Hewak, "Development of channel waveguide lasers in Nd^{3+}-doped chalcogenide (Ga:La:S) glass through photoinduced material modification," Appl Phys Lett **81**, 3708-3710 (2002).

109. G. R. Elliott, G. S. Murugan, J. S. Wilkinson, M. N. Zervas, and D. W. Hewak, "Chalcogenide glass microsphere laser," Opt Express **18**, 26720-26727 (2010).
110. L. Mescia, F. Smektala, and F. Prudenzano, "New trends in amplifiers and sources via chalcogenide photonic crystal fibers," International Journal of Optics **2012**, 8 (2012).
111. T. J. Carrig, A. Zakel, G. J. Wagner, and W. J. Alford, "Chromium-doped chalcogenide lasers," IEEE Leos Ann Mtg, 260-261 (2005).
112. S. B. Mirov, V. V. Fedorov, D. Martyshkin, I. S. Moskalev, M. Mirov, and S. Vasilyev, "Progress in Mid-IR lasers based on Cr and Fe-doped II-VI chalcogenides," IEEE J Sel Top Quant **21**(2015).
113. U. Demirbas and A. Sennaroglu, "Intracavity-pumped Cr^{2+}: ZnSe laser with ultrabroad tuning range between 1880 and 3100 nm," Opt Lett **31**, 2293-2295 (2006).
114. N. Tolstik, E. Sorokin, and I. T. Sorokina, "Graphene mode-locked Cr:ZnS laser with 41 fs pulse duration," Opt Express **22**, 5564-5571 (2014).
115. M. P. Frolov, Y. V. Korostelin, V. I. Kozlovsky, V. V. Mislavskii, Y. P. Podmar'kov, S. A. Savinova, and Y. K. Skasyrsky, "Study of a 2-J pulsed Fe:ZnSe 4- µm laser," Laser Phys Lett **10**(2013).
116. N. Coluccelli, M. Cassinerio, P. Laporta, and G. Galzerano, "100 kHz linewidth Cr^{2+}:ZnSe ring laser tunable from 2.12 to 2.58 µm," Opt Lett **37**, 5088-5090 (2012).
117. T. Schweizer, D. J. Brady, and D. W. Hewak, "Fabrication and spectroscopy of erbium doped gallium lanthanum sulphide glass fibres for mid-infrared laser applications," Opt Express **1**, 102-107 (1997).
118. D. T. Tonchev, C. J. Haugen, R. G. DeCorby, J. N. McMullin, and S. O. Kasap, "Thermal and photoluminescence properties of Er^{3+}-doped $(GaSe)_{(x)}(As_2Se_3)_{(1-x)}$ glasses," J Non-Cryst Solids **326**, 364-368 (2003).
119. T. W. Allen, M. M. Hawkeye, C. J. Haugen, R. G. DeCorby, J. N. McMullin, D. Tonchev, K. Koughia, and S. O. Kasap, "Photoluminescence measurements of Er-doped chalcogenide glasses," J Vac Sci Technol A **22**, 921-924 (2004).
120. K. Koughia, M. Munzar, D. Tonchev, C. J. Haugen, R. G. Decorby, J. N. McMullin, and S. O. Kasap, "Photoluminescence in Er-doped Ge-Ga-Se glasses," J Lumin **112**, 92-96 (2005).
121. S. Kasap, K. Koughia, G. Soundararajan, and M. G. Brik, "Optical and photoluminescence properties of erbium-doped chalcogenide glasses (GeGaS:Er)," IEEE J Sel Top Quant **14**, 1353-1360 (2008).
122. D. J. Coleman, P. Golding, T. A. King, and S. D. Jackson, "Spectroscopic and energy-transfer parameters for Er^{3+}-doped and Er^{3+}, Pr^{3+}-codoped GeGaS glasses," J Opt Soc Am B **19**, 1982-1989 (2002).
123. K. Kadono, T. Yazawa, S. B. Jiang, J. Porque, B. C. Hwang, and N. Peyghambarian, "Rate equation analysis and energy transfer of Er^{3+}-doped Ga_2S_3-GeS_2-La_2S_3 glasses," J Non-Cryst Solids **331**, 79-90 (2003).
124. L. G. Li, J. Y. Bian, Q. Jiao, Z. J. Liu, S. X. Dai, and C. G. Lin, "GeS_2-In_2S_3-CsI chalcogenide glasses doped with rare earth ions for near- and mid-IR luminescence," Sci Rep-Uk **6**(2016).
125. Z. X. Wang, H. T. Guo, X. S. Xiao, Y. T. Xu, X. X. Cui, M. Lu, B. Peng, A. P. Yang, Z. Y. Yang, and S. X. Gu, "Synthesis and spectroscopy of high concentration dysprosium doped GeS_2-Ga_2S_3-CdI_2 chalcohalide glasses and fiber fabrication," J Alloy Compd **692**, 1010-1017 (2017).
126. S. Q. Gu, Q. Xu, E. E. Reuter, J. T. Verdeyen, and S. G. Bishop, "Photoluminescence and excitation spectroscopy in Er-As_2s_3 glass," Leos '93 Conference Proceedings, 206-207 (1993).
127. S. Q. Gu, S. Ramachandran, E. E. Reuter, D. A. Turnbull, J. T. Verdeyen, and S. G. Bishop, "Novel broad-band excitation of Er^{3+} luminescence in chalcogenide glasses," Appl Phys Lett **66**, 670-672 (1995).
128. V. Lyubin, M. Klebanov, B. Sfez, and B. Ashkinadze, "Photoluminescence and photodarkening effect in erbium-doped chalcogenide glassy films," Mater Lett **58**, 1706-1708 (2004).
129. C. Vigreux-Bercovici, A. Pradel, A. Fuchs, and J. Fick, "Effect of annealing on the photoluminescence in sputtered films of Er-doped chalcogenide glasses," Phys Chem Glasses-B **47**, 162-166 (2006).
130. J. Fick, E. J. Knystautus, A. Villeneuve, F. Schiettekatte, S. Roorda, and K. A. Richardson, "High photoluminescence in erbium-doped chalcogenide thin films," J Non-Cryst Solids **272**, 200-208 (2000).
131. Z. G. Ivanova, K. Koughia, D. Tonchev, J. C. Pivin, and S. O. Kasap, "Photoluminescence in Er-implanted amorphous Ge-S-Ga thin films," J Optoelectron Adv M **7**, 1271-1276 (2005).
132. Z. G. Ivanova, V. S. Vassilev, E. Cernoskova, and Z. Cernosek, "Physicochemical, structural and fluorescence properties of Er-doped Ge-S-Ga glasses," J Phys Chem Solids **64**, 107-110 (2003).
133. K. Yan, K. Vu, and S. Madden, "Internal gain in Er-doped As_2S_3 chalcogenide planar waveguides," Opt Lett **40**, 796-799 (2015).
134. V. Moizan, V. Nazabal, J. Troles, P. Houizot, J. L. Adam, J. L. Doualan, R. Moncorge, F. Smektala, G. Gadret, S. Pitois, and G. Canat, "Er^{3+}-doped GeGaSbS glasses for mid-IR fibre laser application: Synthesis and rare earth spectroscopy," Optical Materials **31**, 39-46 (2008).
135. T. H. Lee, J. Heo, B. J. Park, Y. G. Choi, and K. H. Kim, "Spectroscopic properties of Ho^{3+}-doped chalcogenide glasses for 1.6 m (U-band) fiber-optic amplifiers," International Symposium on Photonic Glass (Ispg 2002) **5061**, 72-76 (2003).
136. Y. B. Shin, J. N. Jang, and J. Heo, "Midinfrared light-emission characteristics of Ho^{3+}-doped chalcogenide and heavy-metal oxide glasses," Opt Quant Electron **27**, 379-386 (1995).
137. T. Schweizer, B. N. Samson, J. R. Hector, W. S. Brocklesby, D. W. Hewak, and D. N. Payne, "Infrared emission from holmium doped gallium lanthanum sulphide glass," Infrared Phys Techn **40**, 329-335 (1999).

138. A. Galstyan, S. H. Messaddeq, V. Fortin, I. Skripachev, R. Vallee, T. Galstian, and Y. Messaddeq, "Tm^{3+} doped Ga-As-S chalcogenide glasses and fibers," Optical Materials **47**, 518-523 (2015).
139. S. X. Dai, B. Peng, P. J. Zhang, T. F. Xu, W. Xunsi, Q. H. Nie, and X. H. Zhang, "The near- and mid-infrared emission properties of Tm^{3+}-doped GeGaS-CsI chalcogenide glasses," J Non-Cryst Solids **356**, 2424-2428 (2010).
140. J. Heo and Y. B. Shin, "Absorption and mid-infrared emission spectroscopy of Dy^{3+} in Ge-As(or Ga)-S glasses," J Non-Cryst Solids **196**, 162-167 (1996).
141. J. Heo, W. Y. Cho, and W. J. Chung, "Sensitizing effect of Tm^{3+} on 2.9 μm emission from Dy^{3+}-doped $Ge_{25}Ga_5S_{70}$ glass," J Non-Cryst Solids **212**, 151-156 (1997).
142. M. J. Zhang, A. P. Yang, Y. F. Peng, B. Zhang, H. Ren, W. Guo, Y. Yang, C. C. Zhai, Y. W. Wang, Z. Y. Yang, and D. Y. Tang, "Dy^{3+}-doped Ga-Sb-S chalcogenide glasses for mid-infrared lasers," Mater Res Bull **70**, 55-59 (2015).
143. S. Q. Gu, S. Ramachandran, E. E. Reuter, D. A. Turnbull, J. T. Verdeyen, and S. G. Bishop, "Photoluminescence and excitation spectroscopy of Er-doped As_2S_3 Glass - novel broad-band excitation mechanism," J Appl Phys **77**, 3365-3371 (1995).
144. D. A. Turnbull and S. G. Bishop, "Rare earth dopants as probes of localized states in chalcogenide glasses," J Non-Cryst Solids **223**, 105-113 (1998).
145. S. Ramachandran and S. G. Bishop, "Excitation of Er^{3+} emission by host glass absorption in sputtered films of Er-doped $Ge_{10}As_{40}Se_{25}S_{25}$ glass," Appl Phys Lett **73**, 3196-3198 (1998).
146. T. Y. Ivanova, A. A. Man'shina, A. V. Kurochkin, Y. S. Tver'yanovich, and V. B. Smirnov, "Er^{3+} to glass matrix energy transfer in Ga-Ge-S : Er^{3+} system," J Non-Cryst Solids **298**, 7-14 (2002).
147. T. Y. Ivanova, A. A. Man'shina, A. V. Kurochkin, T. S. Tver'yanovich, and V. B. Smirnov, "Non-radiative energy transfer from Er^{3+} ions to the electronic states of the chalcogenide glass matrix," J Non-Cryst Solids **326**, 320-324 (2003).
148. T. Y. Ivanova, A. A. Manshina, A. V. Povolotskiy, Y. S. Tver'yanovich, S. K. Liaw, and Y. S. Hsieh, "Erbium-mediated photoconductivity of Ga-Ge-S-Se:$Er^{(3+)}$ chalcogenide glasses," J Phys D Appl Phys **41**(2008).
149. F. Auzel, "Upconversion and anti-stokes processes with f and d ions in solids," Chem Rev **104**, 139-173 (2004).
150. Y. G. Choi, K. H. Kim, S. H. Park, and J. Heo, "Comparative study of energy transfers from Er^{3+} to Ce^{3+} in tellurite and sulfide glasses under 980 nm excitation," J Appl Phys **88**, 3832-3839 (2000).
151. X. B. Liu, M. Naftaly, and A. Jha, "Spectroscopic evidence for oxide dopant sites in GeS_2-based glasses using visible photoluminescence from Pr^{3+} probe ions," J Lumin **96**, 227-238 (2002).
152. K. Vu and S. Madden, "Tellurium dioxide erbium doped planar rib waveguide amplifiers with net gain and 2.8dB/cm internal gain," Opt Express **18**, 19192-19200 (2010).
153. P. C. de Sousa, J. F. Lima, and O. A. Serra, "From lighting to photoprotection: Fundamentals and applications of rare earth materials," J Brazil Chem Soc **26**, 2471-2495 (2015).
154. A. J. Kenyon, "Recent developments in rare-earth doped materials for optoelectronics," Prog Quant Electron **26**, 225-284 (2002).
155. J. B. Gruber, J. R. Henderson, M. Muramoto, K. Rajnak, and J. G. Conway, "Energy levels of single-crystal erbium oxide," J Chem Phys **45**, 477-482 (1966).
156. D. E. Mccumber, "Einstein relations connecting broadband emission and absorption spectra," Phys Rev a-Gen Phys **136**, A954-A957 (1964).
157. D. E. Mccumber, "Theory of phonon-terminated optical masers," Phys Rev **134**, A299-+ (1964).
158. C. B. Layne, W. H. Lowdermilk, and M. J. Weber, "Multiphonon relaxation of rare-earth ions in oxide glasses," Phys Rev B **16**, 10-20 (1977).
159. R. Reisfeld and M. Eyal, "Possible ways of relaxations for excited-states of rare-earth ions in amorphous media," J Phys-Paris **46**, 349-355 (1985).
160. V. G. Truong, B. S. Ham, A. M. Jurdyc, B. Jacquier, J. Leperson, V. Nazabal, and J. L. Adam, "Relaxation properties of rare-earth ions in sulfide glasses: Experiment and theory," Phys Rev B **74**(2006).
161. W. J. Miniscalco and R. S. Quimby, "General procedure for the analysis of Er^{3+} cross-sections," Opt Lett **16**, 258-260 (1991).
162. J. N. Sandoe, P. H. Sarkies, and S. Parke, "Variation of Er^{3+} cross-section for stimulated emission with glass composition," J Phys D Appl Phys **5**, 1788-1799 (1972).
163. T. Schweizer, D. W. Hewak, B. N. Samson, and D. N. Payne, "Spectroscopic data of the 1.8-, 2.9-, and 4.3- μm transitions in dysprosium-doped gallium lanthanum sulfide glass," Opt Lett **21**, 1594-1596 (1996).
164. K. Koughia, D. Saitou, T. Aoki, M. Munzar, and S. O. Kasap, "Photoluminescence lifetime spectrum in erbium doped Ge-Ga-S glasses," J Non-Cryst Solids **352**, 2420-2424 (2006).
165. B. R. Judd, "Optical absorption intensities of rare-earth ions," Phys Rev **127**, 750-761 (1962).
166. G. S. Ofelt, "Intensities of crystal spectra of rare-earth ions," J Chem Phys **37**, 511-520 (1962).
167. U. R. Rodriguez-Mendoza, E. A. Lalla, J. M. Caceres, F. Rivera-Lopez, S. F. Leon-Luis, and V. Lavin, "Optical characterization, 1.5 μm emission and IR-to-visible energy upconversion in Er^{3+}-doped fluorotellurite glasses," J Lumin **131**, 1239-1248 (2011).
168. W. T. Carnall, P. R. Fields, and K. Rajnak, "Electronic energy levels in the trivalent lanthanide aquo ions. I. Pr^{3+}, Nd^{3+}, Pm^{3+}, Sm^{3+}, Dy^{3+}, Ho^{3+}, Er^{3+}, and Tm^{3+}," The Journal of Chemical Physics **49**, 4424-4442 (1968).

169. H. T. Sun, S. Q. Xu, S. X. Dai, L. Wen, J. J. Zhang, L. L. Hu, and Z. H. Jiang, "Efficient frequency upconversion emission in Er^{3+}-doped novel strontium lead bismuth glass," J Non-Cryst Solids **351**, 288-292 (2005).
170. I. S. Sharova, T. Y. Ivanova, and A. A. Man'shina, "Analysis of the spectroscopic parameters of chalcogenide glasses in the Ga-Ge-S : Er^{3+} system," Glass Phys Chem+ **32**, 38-46 (2006).
171. V. Moizan, V. Nazabal, J. Troles, P. Houizot, J.-L. Adam, F. Smektala, J.-L. Doualan, R. Moncorgé, G. Canat, and J.-P. Cariou, "Mid-infrared fiber laser application: Er^{3+} doped chalcogenide glasses," Optical Components and Materials IV **6469**, 11 (2007).
172. A. Polman, "Erbium implanted thin film photonic materials," J Appl Phys **82**, 1-39 (1997).
173. N. A. O. P. C. Becker, and J. R. Simpson, "Erbium-doped fiber amplifiers: fundamentals and technology," Academic Press, San Diego, CA (1997).
174. C. E. Chryssou, F. Di Pasquale, and C. W. Pitt, "Er^{3+}-doped channel optical waveguide amplifiers for WDM systems: A comparison of tellurite, alumina and Al/P silicate materials," IEEE J Sel Top Quant **6**, 114-121 (2000).
175. G. N. vandenHoven, E. Snoeks, A. Polman, C. vanDam, J. W. M. vanUffelen, and M. K. Smit, "Upconversion in Er-implanted Al_2O_3 waveguides," J Appl Phys **79**, 1258-1266 (1996).
176. S. Brovelli, A. Galli, R. Lorenzi, F. Meinardi, G. Spinolo, S. Tavazzi, V. Sigaev, S. Sukhov, P. Pernice, A. Aronne, E. Fanelli, and A. Paleari, "Efficient 1.53 μm erbium light emission in heavily Er-doped titania-modified aluminium tellurite glasses," J Non-Cryst Solids **353**, 2150-2156 (2007).
177. Y. D. Hu, S. B. Jiang, G. Sorbello, T. Luo, Y. Ding, B. C. Hwang, J. H. Kim, H. J. Seo, and N. Peyghambarian, "Numerical analyses of the population dynamics and determination of the upconversion coefficients in a new high erbium-doped tellurite glass," J Opt Soc Am B **18**, 1928-1934 (2001).
178. M. F. Churbanov, A. N. Moiseev, G. E. Snopatin, V. V. Dorofeev, V. G. Pimenov, A. V. Chilyasov, A. S. Lobanov, T. V. Kotereva, V. G. Plotnichenko, V. V. Koltashev, and Y. N. Pyrkov, "Production and properties of high purity glasses of TeO_2-WO_3, TeO_2-ZnO systems," Phys Chem Glasses-B **49**, 297-300 (2008).
179. L. Wetenkamp, G. F. West, and H. Tobben, "Optical-properties of rare earth-doped ZBLAN glasses," J Non-Cryst Solids **140**, 35-40 (1992).
180. S.-c. Zheng, Y.-w. Qi, S.-x. Peng, D.-d. Yin, Y.-x. Zhou, and S.-x. Dai, "Structure and spectroscopic properties of Er^{3+}/Ce^{3+} co-doped TeO_2-Bi_2O_3-TiO_2 glasses modified with various WO_3 contents for 1.53 μm emission," Optoelectronics Letters **9**, 461-464 (2013).
181. Y. Dwivedi, A. Rai, and S. B. Rai, "Energy transfer in Er:Eu:Yb co-doped tellurite glasses: Yb as enhancer and quencher," J Lumin **129**, 629-633 (2009).
182. D. L. Dexter, "A theory of sensitized luminescence in solids," J Chem Phys **21**, 836-850 (1953).
183. R. I. Laming, S. B. Poole, and E. J. Tarbox, "Pump excited-state absorption in erbium-doped fibers," Opt Lett **13**, 1084-1086 (1988).
184. R. Soulard, B. Xu, J. L. Doualan, P. Camy, and R. Moncorge, "Ground- and excited-state absorption and emission spectroscopy of Nd:GGG," J Lumin **132**, 2521-2524 (2012).
185. G. M. Salley, R. Valiente, and H. U. Gudel, "Phonon-assisted cooperative sensitization of Tb^{3+} in $SrCl_2$: Yb, Tb," J Phys-Condens Mat **14**, 5461-5475 (2002).
186. W. P. Qin, Z. Y. Liu, C. N. Sin, C. F. Wu, G. S. Qin, Z. Chen, and K. Z. Zheng, "Multi-ion cooperative processes in Yb^{3+} clusters," Light-Sci Appl **3**(2014).
187. B. D. Bartolo, "Advances in nonradiative processes in solids," **249**(1991).
188. M. J. F. Digonnet, "Rare-earth-doped fiber lasers and amplifiers, revised and expanded," (2001).
189. X. Orignac, D. Barbier, X. M. Du, R. M. Almeida, O. McCarthy, and E. Yeatman, "Sol-gel silica/titania-on-silicon Er/Yb-doped waveguides for optical amplification at 1.5 μm," Optical Materials **12**, 1-18 (1999).
190. S. E. Stokowski, R. A. Saroyan, and M. J. Weber, "Nd-doped laser glass spectroscopic and physical properties," Lawrence Livermore National Laboratory, University of California, (1981).
191. J. L. Wagener, P. F. Wysocki, M. J. F. Digonnet, H. J. Shaw, and D. J. Digiovanni, "Effect of concentration on the efficiency of erbium-doped silica fiber lasers," Fiber Laser Sources and Amplifiers Iv **1789**, 80-89 (1993).
192. J. E. Roman, P. Camy, M. Hempstead, W. S. Brocklesby, S. Nouh, A. Beguin, C. Lerminiaux, and J. S. Wilkinson, "Ion-exchanged Er/Yb waveguide laser at 1.5 μm pumped by laser diode," Electron Lett **31**, 1345-1346 (1995).
193. O. Lumholt, T. Rasmussen, and A. Bjarklev, "Modelling of extremely high concentration erbium-doped silica waveguides," Electron Lett **29**, 495-496 (1993).
194. F. Auzel, "Erbium doped glasses for laser," Doctoral dissertation, University of Paris, France (1968).
195. T. Ohtsuki, "Rare-earth doped glass waveguides for amplifers and lasers," Doctoral dissertation, The University of Arizona (1996).
196. R. Fairman and B. Ushkov, "Semiconducting Chalcogenide Glass III: Applications of Chalcogenide Glasses", Elsevier Science, (2004).
197. V. K. Kudoyarova, S. A. Kozyukhin, K. D. Tsendin, and V. M. Lebedev, "Photoluminescence and composition of amorphous As_2Se_3 films modified with Er(thd)(3) complex compound," Semiconductors **41**, 914-920 (2007).
198. J. Ikuta, K. Maeda, T. Sakai, T. Ikari, K. Koughia, M. Munzar, and S. O. Kasap, "Optical and photoluminescence properties of Er-doped $(GeSe_2)_{(1-x)}(Ga_2Se_3)_{(x)}$ bulk glasses," J Mater Sci-Mater El **18**, S231-S234 (2007).

199. K. Koughia, M. Munzar, T. Aoki, and S. O. Kasap, "Photoluminescence spectra and lifetimes of $^4I_{13/2}$ -> $^4I_{15/2}$ and $^4I_{11/2}$ -> $^4I_{15/2}$ transitions in erbium doped GeGaSe and GeGaS glasses," J Mater Sci-Mater El **18**, S153-S157 (2007).
200. R. Frerichs, "New optical glasses with good transparency in the infrared," J Opt Soc Am **43**, 1153-1157 (1953).
201. A. R. HILTON, "Optical properties of chalcogenide glasses," J Non-Cryst Solids **2**, 28-39 (1970).
202. N. S. Kapany and R. J. Simms, "Recent developments in infrared fiber optics," Infrared Phys **5**, 69-76 (1965).
203. T. Kanamori, Y. Terunuma, S. Takahashi, and T. Miyashita, "Chalcogenide glass-fibers for mid-infrared transmission," J Lightwave Technol **2**, 607-613 (1984).
204. M. J. Collins, A. S. Clark, J. K. He, D. Y. Choi, R. J. Williams, A. C. Judge, S. J. Madden, M. J. Withford, M. J. Steel, B. Luther-Davies, C. L. Xiong, and B. J. Eggleton, "Low Raman-noise correlated photon-pair generation in a dispersion-engineered chalcogenide As_2S_3 planar waveguide," Opt Lett **37**, 3393-3395 (2012).
205. I. V. Kabakova, R. Pant, D. Y. Choi, S. Debbarma, B. Luther-Davies, S. J. Madden, and B. J. Eggleton, "Narrow linewidth Brillouin laser based on chalcogenide photonic chip," Opt Lett **38**, 3208-3211 (2013).
206. A. Byrnes, R. Pant, E. B. Li, D. Y. Choi, C. G. Poulton, S. H. Fan, S. Madden, B. Luther-Davies, and B. J. Eggleton, "Photonic chip based tunable and reconfigurable narrowband microwave photonic filter using stimulated Brillouin scattering," Opt Express **20**, 18836-18845 (2012).
207. A. Zoubir, M. Richardson, C. Rivero, A. Schulte, C. Lopez, K. Richardson, N. Ho, and R. Vallee, "Direct femtosecond laser writing of waveguides in As_2S_3 thin films," Opt Lett **29**, 748-750 (2004).
208. L. Su, C. J. Rowlands, T. H. Lee, and S. R. Elliott, "Fabrication of photonic waveguides in sulfide chalcogenide glasses by selective wet-etching," Electron Lett **44**, 472-473 (2008).
209. T. Han, S. Madden, S. Debbarma, and B. Luther-Davies, "Improved method for hot embossing As_2S_3 waveguides employing a thermally stable chalcogenide coating," Opt Express **19**, 25447-25453 (2011).
210. Amorphous Materials Inc, retrieved 30 June, 2017, http://www.amorphousmaterials.com/products/.
211. W. S. Rodney, I. H. Malitson, and T. A. King, "Refractive index of arsenic trisulfide," J Opt Soc Am **48**, 633-636 (1958).
212. M. R. E. Lamont, B. Luther-Davies, D. Y. Choi, S. Madden, and B. J. Eggleton, "Supercontinuum generation in dispersion engineered highly nonlinear (gamma=10/W/m) As_2S_3 chalcogenide planar waveguide," Opt Express **16**, 14938-14944 (2008).
213. R. P. Wang, S. J. Madden, C. J. Zha, A. V. Rode, and B. Luther-Davies, "Annealing induced phase transformations in amorphous As_2S_3 films," J Appl Phys **100**(2006).
214. R. J. Kobliska and S. A. Solin, "Raman spectrum of vitreous As_2S_3," J Non-Cryst Solids **8-10**, 5 (1972).
215. M. S. Iovu, S. D. Shutov, A. M. Andriesh, E. I. Kamitsos, C. P. E. Varsamis, D. Furniss, A. B. Seddon, and M. Popescu, "Spectroscopic studies of bulk As_2S_3 glasses and amorphous films doped with Dy, Sm and Mn," J Optoelectron Adv M **3**, 443-454 (2001).
216. V. K. Tikhomirov, M. Barj, S. Turrell, J. Kobelke, N. Idrissi, M. Bouazaoui, B. Capoen, and A. B. Seddon, "Non-linear Raman effects and photodarkening in chalcogenide glass As_2S_3," Europhys Lett **76**, 312-317 (2006).
217. A. Fuchs, J. Fick, V. Balan, C. Vigreux, and A. Pradel, "Photoluminescence and waveguiding in sputtered films of Er-doped chalcogenide glasses," P Soc Photo-Opt Ins **5451**, 327-336 (2004).
218. J. Z. Tang, S. Liu, Q. D. Zhu, Y. A. Sun, G. Li, Z. Y. Yang, X. H. Zhang, X. S. Wang, P. Q. Zhang, S. X. Dai, and Y. S. Xu, "$As_{40}S_{59}Se_1/As_2S_3$ step index fiber for 1-5 µm supercontinuum generation," J Non-Cryst Solids **450**, 61-65 (2016).
219. T. Imai, K. Maeda, M. Fujita, and N. Saito, "Photoluminescence properties of erbium-doped amorphous gallium-germanium-selenium films fabricated by RF sputtering," Phys Status Solidi C **6**, S106-S109 (2009).
220. R. A. Jarvis, R. P. Wang, A. V. Rode, C. Zha, and B. Luther-Davies, "Thin film deposition of $Ge_{33}As_{12}Se_{55}$ by pulsed laser deposition and thermal evaporation: Comparison of properties," J Non-Cryst Solids **353**, 947-949 (2007).
221. M. Frumar, B. Frumarova, P. Nemec, T. Wagner, J. Jedelsky, and M. Hrdlicka, "Thin chalcogenide films prepared by pulsed laser deposition - new amorphous materials applicable in optoelectronics and chemical sensors," J Non-Cryst Solids **352**, 544-561 (2006).
222. A. Abrutis, V. Plausinaitiene, M. Skapas, C. Wiemer, O. Salicio, M. Longo, A. Pirovano, J. Siegel, W. Gawelda, S. Rushworth, and C. Giesen, "Chemical vapor deposition of chalcogenide materials for phase-change memories," Microelectron Eng **85**, 2338-2341 (2008).
223. S. S. Song, N. Carlie, J. Boudies, L. Petit, K. Richardson, and C. B. Arnold, "Spin-coating of $Ge_{23}Sb_7S_{70}$ chalcogenide glass thin films," J Non-Cryst Solids **355**, 2272-2278 (2009).
224. S. S. Song, J. Dua, and C. B. Arnold, "Influence of annealing conditions on the optical and structural properties of spin-coated As_2S_3 chalcogenide glass thin films," Opt Express **18**, 5472-5480 (2010).
225. D. A. P. Bulla, R. P. Wang, A. Prasad, A. V. Rode, S. J. Madden, and B. Luther-Davies, "On the properties and stability of thermally evaporated Ge-As-Se thin films," Appl Phys a-Mater **96**, 615-625 (2009).
226. O. Nordman, N. Nordman, and N. Peyghambarian, "Electron beam induced changes in the refractive index and film thickness of amorphous As_xS_{100-x} and As_xSe_{100-x} films," J Appl Phys **84**, 6055-6058 (1998).

227. N. Ho, J. M. Laniel, R. Vallee, and A. Villeneuve, "Photosensitivity of As_2S_3 chalcogenide thin films at 1.5 μm," Opt Lett **28**, 965-967 (2003).

228. J. J. Hu, M. Torregiani, F. Morichetti, N. Carlie, A. Agarwal, K. Richardson, L. C. Kimerling, and A. Melloni, "Resonant cavity-enhanced photosensitivity in As_2S_3 chalcogenide glass at 1550 nm telecommunication wavelength," Opt Lett **35**, 874-876 (2010).

229. T. Han, "Nano-Moulding of Integrated Optical Devices," Doctoral dissertation, The Australian National University, Australia (2011).

230. A. L. Dawar, P. K. Shishodia, G. Chauhan, J. C. Joshi, C. Jagadish, and P. C. Mathur, "Effect of UV exposure on optical-properties of amorphous As_2S_3 Thin-Films," Appl Optics **29**, 1971-1973 (1990).

231. D. Y. Choi, S. Maden, A. Rode, R. P. Wang, and B. Luther-Davies, "Plasma etching of As_2S_3 films for optical waveguides," J Non-Cryst Solids **354**, 3179-3183 (2008).

232. D. Y. Choi, S. Madden, D. Bulla, A. Rode, R. P. Wang, and B. Luther-Davies, "SU-8 protective layer in photo-resist patterning on As_2S_3 film," Physica Status Solidi C: Current Topics in Solid State Physics, Vol 8, No 11-12 **8**(2011).

233. D. Y. Choi, S. Madden, D. Bulla, R. P. Wang, A. Rode, and B. Luther-Davies, "Thermal annealing of arsenic tri-sulphide thin film and its influence on device performance," J Appl Phys **107**(2010).

234. D. Y. Choi, A. Wade, S. Madden, R. P. Wang, D. Bulla, and B. Luther-Davies, "Photo-induced and thermal annealing of chalcogenide films for waveguide fabrication," Physcs Proc **48**, 196-205 (2013).

235. M. Frumar, Z. Polak, and Z. Cernosek, "Raman spectra and photostructural changes in the short-range order of amorphous As-S chalcogenides," J Non-Cryst Solids **256**, 105-110 (1999).

236. K. Palka, T. Syrovy, S. Schroter, S. Bruckner, M. Rothhardt, and M. Vlcek, "Preparation of arsenic sulfide thin films for integrated optical elements by spiral bar coating," Opt Mater Express **4**, 384-395 (2014).

237. J. Cook, S. Slang, R. Golovchak, H. Jain, M. Vlcek, and A. Kovalskiy, "Structural features of spin-coated thin films of binary As_xS_{100-x} chalcogenide glass system," Thin Solid Films **589**, 642-648 (2015).

238. K. L. Yan, R. Wang, K. Vu, S. Madden, K. Belay, R. Elliman, and B. Luther-Davies, "Photoluminescence in Er-doped Ge-As-Se chalcogenide thin films," Opt Mater Express **2**, 1270-1277 (2012).

239. C. Strohhofer and A. Polman, "Absorption and emission spectroscopy in Er^{3+}-Yb^{3+} doped aluminum oxide waveguides," Optical Materials **21**, 705-712 (2003).

240. S. Ivanova and F. Pelle, "Strong 1.53 μm to NIR-VIS-UV upconversion in Er-doped fluoride glass for high-efficiency solar cells," J Opt Soc Am B **26**, 1930-1938 (2009).

241. F. F. Sene, J. R. Martinelli, and L. Gomes, "Optical and structural characterization of rare earth doped niobium phosphate glasses," J Non-Cryst Solids **348**, 63-71 (2004).

242. Z. G. Ivanova, M. Jayasimhadri, and M. Kincl, "Optical properties of Er-doped GeS_2-Ga_2S_3 glasses," J Optoelectron Adv M **11**, 1269-1272 (2009).

243. R. E. Collin, "Foundations for microwave engineering, 2ed ED," Wiley India Pvt. Limited, (2007).

244. A. W. Snyder and J. Love, "Optical Waveguide Theory," Springer US, (1983).

245. R. Scarmozzino, A. Gopinath, R. Pregla, and S. Helfert, "Numerical techniques for modeling guided-wave photonic devices," IEEE J Sel Top Quant **6**, 150-162 (2000).

246. E. Schweig and W. B. Bridges, "Computer-analysis of dielectric waveguides - a finite-difference method," IEEE T Microw Theory **32**, 531-541 (1984).

247. M. Stern and W. P. Huang, "Finite-difference analysis of planar optical waveguides," PIER 10 (Progress in Electromagnetic Research 10) **10**, 64 (1995).

248. B. M. A. Rahman, F. A. Fernandez, and J. B. Davies, "Review of finite-element methods for microwave and optical wave-guides," P IEEE **79**, 1442-1448 (1991).

249. M. Irannejad, M. Pasha, G. Jose, P. Steenson, T. T. Fernandez, A. Jha, Q. Jiang, Z. Y. Zhang, R. A. Hogg, C. Evans, Z. Ikonic, and P. Harrison, "Active glass waveguide amplifier on GaAs by UV-pulsed laser deposition and femtosecond laser inscription," Laser Phys Lett **9**, 329-339 (2012).

250. D. Y. Choi, S. Madden, A. Rode, R. P. Wang, and B. Luther-Davies, "Nanoscale phase separation in ultrafast pulsed laser deposited arsenic trisulfide (As_2S_3) films and its effect on plasma etching," J Appl Phys **102**(2007).

251. P. Bienstman, E. Six, M. Roelens, M. Vanwolleghem, and R. Baets, "Calculation of bending losses in dielectric waveguides using eigenmode expansion and perfectly matched layers," IEEE Photonic Tech L **14**, 164-166 (2002).

252. Webelements, retrieved 30 June, 2017, https://www.webelements.com/erbium/.

253. A. B. Fallahkhair, K. S. Li, and T. E. Murphy, "Vector finite difference modesolver for anisotropic dielectric waveguides," J Lightwave Technol **26**, 1423-1431 (2008).

254. I. D. Rukhlenko, M. Premaratne, and G. P. Agrawal, "Effective mode area and its optimization in silicon-nanocrystal waveguides," Opt Lett **37**, 2295-2297 (2012).

255. M. Yamada, M. Shimizu, M. Okayasu, T. Takeshita, M. Horiguchi, Y. Tachikawa, and E. Sugita, "Noise characteristics of Er^{3+}-doped fiber amplifiers pumped by 0.98 and 1.48 μm laser-diodes," IEEE Photonic Tech L **2**, 205-207 (1990).

256. R. G. Smart, J. L. Zyskind, and D. J. Digiovanni, "Experimental comparison of 980 nm and 1480 nm-pumped saturated in-line erbium-doped fiber amplifiers suitable for long-haul soliton transmission-systems," IEEE Photonic Tech L **5**, 770-773 (1993).

257. F. Prudenzano, L. Mescia, L. Allegretti, V. Moizan, V. Nazabal, and F. Smektala, "Theoretical study of cascade laser in erbium-doped chalcogenide glass fibers," Optical Materials **33**, 241-245 (2010).

258. Optiwave Systems Inc, retrieved 30 June, 2017, https://optiwave.com/category/products/system-and-amplifier-design/optisystem/.
259. J. J. Hu, N. N. Feng, N. Carlie, L. Petit, A. Agarwal, K. Richardson, and L. Kimerling, "Optical loss reduction in high-index-contrast chalcogenide glass waveguides via thermal reflow," Opt Express **18**, 1469-1478 (2010).
260. V. V. Zigel, A. A. Litvinenko, G. K. Ulyanov, and G. A. Chalabyan, "Ultrasonic dispersive waveguide with a layer of chalcogenide glass on lithium-niobate," Sov Phys Acoust **21**, 77-77 (1975).
261. Y. Ohmachi, "Acoustooptical light diffraction in thin-films," J Appl Phys **44**, 3928-3933 (1973).
262. S. Zembutsu and S. Fukunishi, "Waveguiding properties of (Se,S)-based chalcogenide glass-films and some applications to optical-waveguide devices," Appl Optics **18**, 393-399 (1979).
263. D. A. Turnbull, J. S. Sanghera, V. Nguyen, and I. D. Aggarwal, "Fabrication of waveguides in sputtered films of GeAsSe glass via photodarkening with above bandgap light," Mater Lett **58**, 51-54 (2004).
264. N. Ho, M. C. Phillips, H. Qiao, P. J. Allen, K. Krishnaswami, B. J. Riley, T. L. Myers, and N. C. Anheier, "Single-mode low-loss chalcogenide glass waveguides for the mid-infrared," Opt Lett **31**, 1860-1862 (2006).
265. O. M. Efimov, L. B. Glebov, K. A. Richardson, E. Van Stryland, T. Cardinal, S. H. Park, M. Couzi, and J. L. Bruneel, "Waveguide writing in chalcogenide glasses by a train of femtosecond laser pulses," Optical Materials **17**, 379-386 (2001).
266. M. A. Hughes, W. J. Yang, and D. W. Hewak, "Spectral broadening in femtosecond laser written waveguides in chalcogenide glass," J Opt Soc Am B **26**, 1370-1378 (2009).
267. J. L. Wang, B. R. He, S. X. Dai, J. F. Zhu, and Z. Y. Wei, "Waveguide in Tm^{3+}-doped chalcogenide glass fabricated by femtosecond laser direct writing," IEEE Photonic Tech L **27**, 237-240 (2015).
268. M. Dubov, S. R. Natarajan, J. A. R. Williams, and I. Bennion, "Mask-less lithography for fabrication of optical waveguides," Commercial and Biomedical Applications of Ultrafast Lasers Viii **6881**, 88110-88110 (2008).
269. A. K. Mairaj, P. Hua, H. N. Rutt, and D. W. Hewak, "Fabrication and characterization of continuous wave direct UV (lambda=244 nm) written channel waveguides in chalcogenide (Ga:La:S) glass," J Lightwave Technol **20**, 1578-1584 (2002).
270. L. E. Zou, B. X. Chen, H. S. Lin, H. Hamanaka, and M. Iso, "Fabrication and propagation characterization of As_2S_8 chalcogenide channel waveguide made by UV irradiation annealing," Appl Optics **48**, 6442-6447 (2009).
271. C. Meneghini, K. Le Foulgoc, E. J. Knystautas, A. Villeneuve, T. Cardinal, and K. A. Richardson, "Ion implantation: an efficient method for doping or fabricating channel chalcogenide glass waveguides," Materials Modification by Ion Irradiation **3413**, 146-153 (1998).
272. F. Qiu and T. Narusawa, "Application of swift and heavy ion implantation to the formation of chalcogenide glass optical waveguides," Optical Materials **33**, 527-530 (2011).
273. R. G. DeCorby, N. Ponnampalam, M. M. Pai, H. T. Nguyen, P. K. Dwivedi, T. J. Clement, C. J. Haugen, J. N. McMullin, and S. O. Kasap, "High index contrast waveguides in chalcogenide glass and polymer," IEEE J Sel Top Quant **11**, 539-546 (2005).
274. J. A. Frantz, L. B. Shaw, J. S. Sanghera, and I. D. Aggarwal, "Waveguide amplifiers in sputtered films of Er^{3+}- doped gallium lanthanum sulfide glass," Opt Express **14**, 1797-1803 (2006).
275. J. J. Hu, V. Tarasov, N. Carlie, N. N. Feng, L. Petit, A. Agarwal, K. Richardson, and L. Kimerling, "Si-CMOS-compatible lift-off fabrication of low-loss planar chalcogenide waveguides," Opt Express **15**, 11798-11807 (2007).
276. J. S. Sanghera, P. C. Pureza, and I. D. Aggarwal, "Method of forming waveguides with ion exchange of halogen ions," U.S. Patent 5,294,240 (1994).
277. V. A. G. Rivera, E. Rodriguez, E. F. Chillcce, C. L. Cesar, and L. C. Barbosa, "Waveguide produced by fiber on glass method using Er^{3+}-doped tellurite glass," J Non-Cryst Solids **353**, 339-343 (2007).
278. V. Balan, C. Vigreux, A. Pradel, A. Llobera, C. Dominguez, M. I. Alonso, and M. Garriga, "Chalcogenide glass-based rib ARROW waveguide," J Non-Cryst Solids **326**, 455-459 (2003).
279. N. S. Abdel-Moneim, C. J. Mellor, T. M. Benson, D. Furniss, and A. B. Seddon, "Fabrication of stable, low optical loss rib-waveguides via embossing of sputtered chalcogenide glass-film on glass-chip," Opt Quant Electron **47**, 351-361 (2015).
280. T. Han, S. Madden, D. Bulla, and B. Luther-Davies, "Low loss chalcogenide glass waveguides by thermal nano-imprint lithography," Opt Express **18**, 19286-19291 (2010).
281. D. G. Georgiev, P. Boolchand, and K. A. Jackson, "Intrinsic nanoscale phase separation of bulk As_2S_3 glass," Philos Mag **83**, 2941-2953 (2003).
282. K. Vu, K. L. Yan, Z. Jin, X. Gai, D. Y. Choi, S. Debbarma, B. Luther-Davies, and S. Madden, "Hybrid waveguide from As_2S_3 and Er-doped TeO_2 for lossless nonlinear optics," Opt Lett **38**, 1766-1768 (2013).
283. K. Vu, S. Farahani, and S. Madden, "980nm pumped erbium doped tellurium oxide planar rib waveguide laser and amplifier with gain in S, C and L band," Opt Express **23**, 747-755 (2015).
284. A. Mori, Y. Ohishi, T. Kanamori, and S. Sudo, "Optical amplification with neodymium-doped chalcogenide glass fiber," Appl Phys Lett **70**, 1230-1232 (1997).
285. B. Dussardier, W. Blanc, and G. Monnom, "Luminescent ions in silica-based optical fibers," Fiber Integrated Opt **27**, 484-504 (2008).
286. Y. L. Xue, P. Wu, Y. Liu, X. Zhang, L. Lin, and Q. Jiang, "Highly efficient near-IR photoluminescence of Er^{3+} immobilized in mesoporous SBA-15," Nanoscale Res Lett **5**, 1952-1961 (2010).

287. B. J. Ainslie, S. P. Craig, R. Wyatt, and K. Moulding, "Optical and structural-analysis of neodymium-doped silica-based optical fiber," Mater Lett **8**, 204-208 (1989).

288. M.Ya.Gen and Yu.l.Petrov, "Disperse condensates of metal vapour," Russian Chemical Reviews **38**(1969).

289. G. Verhaegen, F. E. Stafford, M. Ackerman, and P. Goldfinger, "Correlation of dissociation energies of gaseous molecules and of heats of vaporization of solids .1. Homonuclear diatomic molecules," T Faraday Soc **58**, 1926-1938 (1962).

290. A. Durandet, R. Boswell, and D. Mckenzie, "New plasma-assisted deposition technique using helicon activated reactive evaporation," Rev Sci Instrum **66**, 2908-2913 (1995).

291. M. Shojiya, M. Takahashi, R. Kanno, Y. Kawamoto, and K. Kadono, "Up-conversion luminescence of Er^{3+} in chloride glasses based on $ZnCl_2$ or $CdCl_2$," Appl Phys Lett **65**, 1874-1876 (1994).

292. F. Q. Zeng, G. Z. Ren, X. N. Qiu, and Q. B. Yang, "Effect of different Er^{3+} compounds doping on microstructure and photoluminescent properties of oxyfluoride glass ceramics," Physica B **403**, 2417-2422 (2008).

293. G. Soundararajan, C. Koughia, A. Edgar, C. Varoy, and S. Kasap, "Optical properties of erbium-doped fluorochlorozirconate glasses," J Non-Cryst Solids **357**, 2475-2479 (2011).

294. D. Tonchev and S. O. Kasap, "Influence of Cl doping on the thermal properties of amorphous Se," Phys Chem Glasses **43**, 66-71 (2002).

295. D. T. Tonchev, K. V. Koughia, Z. G. Ivanova, and S. O. Kasap, "Thermal and optical properties of erbium doped $(GeS_2)_{75}(Ga_2S_3)_{25}$ glasses," J Optoelectron Adv M **9**, 337-340 (2007).

296. K. Bourhis, J. Massera, L. Petit, H. Ihalainen, A. Fargues, T. Cardinal, L. Hupa, M. Hupa, M. Dussauze, V. Rodriguez, C. Boussard-Pledel, B. Bureau, C. Roiland, and M. Ferraris, "Influence of P_2O_5 and Al_2O_3 content on the structure of erbium-doped borosilicate glasses and on their physical, thermal, optical and luminescence properties," Mater Res Bull **63**, 41-50 (2015).

297. A. B. Corradi, V. Cannillo, M. Montorsi, and C. Siligardi, "Influence of Al_2O_3 addition on thermal and structural properties of erbium doped glasses," J Mater Sci **41**, 2811-2819 (2006).

298. P. Lopez-Iscoa, L. Petit, J. Massera, D. Janner, N. G. Boetti, D. Pugliese, S. Fiorilli, C. Novara, F. Giorgis, and D. Milanese, "Effect of the addition of Al_2O_3, TiO_2 and ZnO on the thermal, structural and luminescence properties of Er^{3+}-doped phosphate glasses," J Non-Cryst Solids **460**, 161-168 (2017).

299. J. Li, X. Shen, J. Q. Sun, K. Vu, D. Y. Choi, R. P. Wang, B. Luther-Davies, S. X. Dai, T. F. Xu, and Q. H. Nie, "Fabrication and characterization of $Ge_{20}Sb_{15}Se_{65}$ chalcogenide glass rib waveguides for telecommunication wavelengths," Thin Solid Films **545**, 462-465 (2013).

300. V. Nazabal, A. M. Jurdyc, P. Nemec, M. L. Brandily-Anne, L. Petit, K. Richardson, P. Vinatier, C. Bousquet, T. Cardinal, S. Pechev, and J. L. Adam, "Amorphous Tm^{3+} doped sulfide thin films fabricated by sputtering," Optical Materials **33**, 220-226 (2010).

301. K. L. Yan, K. Vu, Z. Y. Yang, R. P. Wang, S. Debbarma, B. Luther-Davies, and S. Madden, "Emission properties of erbium-doped Ge-Ga-Se glasses, thin films and waveguides for laser amplifiers," Opt Mater Express **4**, 464-475 (2014).

302. M. Knadel, R. A. V. Rossel, F. Deng, A. Thomsen, and M. H. Greve, "Visible-near infrared spectra as a proxy for topsoil texture and glacial boundaries," Soil Sci Soc Am J **77**, 568-579 (2013).

303. V. Chawla, R. Jayaganthan, and R. Chandra, "Structural characterizations of magnetron sputtered nanocrystalline TiN thin films," Mater Charact **59**, 1015-1020 (2008).

304. E. Alfonso, G. Cubillos, and J. Olaya, "Thin Film Growth Through Sputtering Technique and Its Applications," INTECH Open Access Publisher, (2012).

305. V. Balan, C. Vigreux, and A. Pradel, "Chalcogenide thin films deposited by radio-frequency sputtering," J Optoelectron Adv M **6**, 875-882 (2004).

306. A. Galstyan, S. H. Messaddeq, I. Skripachev, T. Galstian, and Y. Messaddeq, "Role of iodine in the solubility of Tm^{3+} ions in As_2S_3 glasses," Opt Mater Express **6**, 230-243 (2016).

307. Q. Jiao, G. Li, L. N. Li, C. G. Lin, G. X. Wang, Z. J. Liu, S. X. Dai, T. F. Xu, and Q. Y. Zhang, "Effect of gallium environment on infrared emission in Er^{3+}-doped gallium-antimony-sulfur glasses," Sci Rep-Uk **7**(2017).

308. M. M. Li, Y. S. Xu, X. M. Jia, L. Yang, N. B. Long, Z. J. Liu, and S. X. Dai, "Mid-infrared emission properties of Pr^{3+}-doped Ge-Sb-Se-Ga-I chalcogenide glasses," Opt Mater Express **8**, 992-1000 (2018).

309. Y. Shpotyuk, "Effect of rare-earth doping on free-volume nanostructure of Ga-codoped glassy $(As/Sb)_2Se_3$," Nanoscale Res Lett **12**(2017).

310. G. Tang, C. M. Liu, Z. Y. Yang, L. Luo, and W. Chen, "Micro-structural studies of $GeSe_2$-Ga_2Se_3-MX (MX = CsI and PbI_2) glasses using Raman spectra," J Non-Cryst Solids **355**, 1585-1589 (2009).

311. P. Nemec, B. Frumarova, and M. Frumar, "Structure and properties of the pure and Pr^{3+}-doped $Ge_{25}Ga_5Se_{70}$ and $Ge_{30}Ga_5Se_{65}$ glasses," J Non-Cryst Solids **270**, 137-146 (2000).

312. V. B. Petrovic, D. D. Strbac, I. O. Gut, and S. R. Lukic, "Optical properties of Er-doped As-S-Ge chalcogenide glasses," J Optoelectron Adv M **11**, 2035-2038 (2009).

313. V. B. Petrović, I. O. Gúth, and S. R. Lukić-Petrović, "Raman spectra of quasi-binary As_2S_3-GeS_2 doped with Er," Journal of Research in Physics The Journal of University of Novi Sad **37**, 6 (2014).

314. S. L. Li, G. Fu, and Y. K. Ye, "1.54 µm photoluminescence emission from Er-implanted SiO_2 crystal and SiO_2 glass," Nucl Instrum Meth B **307**, 434-437 (2013).

315. F. Auzel and P. Goldner, "Towards rare-earth clustering control in doped glasses," Optical Materials **16**, 93-103 (2001).

316. Y. Guimond, J. L. Adam, A. M. Jurdyc, H. L. Ma, J. Mugnier, and B. Jacquier, "Optical properties of antimony-stabilised sulphide glasses doped with Dy^{3+} and Er^{3+} ions," J Non-Cryst Solids **256**, 378-382 (1999).
317. S. X. Shen, A. Jha, X. B. Liu, M. Naftaly, K. Bindra, H. J. Bookey, and A. K. Kar, "Tellurite glasses for broadband amplifiers and integrated optics," J Am Ceram Soc **85**, 1391-1395 (2002).
318. V. Nazabal, P. Camy, P. Nemec, H. Lhermite, J. Charrier, J. L. Doualan, S. Zhang, M. Frumar, and J. L. Adam, "Erbium doped germanium based sulphide optical waveguide amplifier for near and mid-IR," Proc Spie **7366**(2009).
319. E. Barthelemy, C. Vigreux-Bercovici, P. Yot, and A. Pradel, "Co-thermal evaporation: a new method to deposit telluride films," Optoelectron Adv Mat **1**, 487-490 (2007).
320. D. Y. Choi, S. Madden, A. Rode, R. P. Wang, A. Ankiewicz, and B. Luther-Davies, "Surface roughness in plasma-etched As_2S_3 films: Its origin and improvement," IEEE T Nanotechnol **7**, 285-290 (2008).
321. R. Penndorf, "Mie scattering coefficient for water droplets in air," J Meteorol **13**, 219-220 (1956).
322. S. M. Salem, M. B. S. Osman, A. M. Salem, H. M. Hashem, and H. A. Saleh, "Physical properties and structural characterization of thermally evaporated $Ge_{25-x}Ga_xSe_{75}$ System," Current Science International **04**, 12 (2015).
323. P. K. Tien, "Light waves in thin films and integrated optics," Appl Optics **10**, 2395-2413 (1971).
324. F. P. Payne and J. P. R. Lacey, "A theoretical-analysis of scattering loss from planar optical waveguides," Opt Quant Electron **26**, 977-986 (1994).
325. A. Andriesh, M. Iovu, O. Shpotiuk, and I. Culeac, "Optical losses and photo-induced absorption in chalcogenide glass fibers," J Optoelectron Adv M **11**, 2172-2178 (2009).
326. A M Andriesh, I. P. Culeac, and V. M. Loghin, "Photoinduced changes of optical absorption in chalcogenide glass fibres," Pure Appl. Opt. **1**, 12 (1992).
327. Z. G. Man, W. J. Pan, D. Furniss, T. M. Benson, A. B. Seddon, T. Kohoutek, J. Orava, and T. Wagner, "Embossing of chalcogenide glasses: monomode rib optical waveguides in evaporated thin films," Opt Lett **34**, 1234-1236 (2009).